Geochemistry International, Vol. 42, Suppl. 2, 2004, pp. S159–S324.

Preface

This contribution by D.V. Grichuk addresses the development of methods of the thermodynamic modeling of hydrothermal processes, and application of these methods to the investigation of very intriguing natural objects, ocean-floor hydrothermal systems.

Theoretical modeling is now the main tool of physical geochemistry. The past 50 years have seen considerable advances in the development of general principles and exploration of some particular reactions to the quantitative investigation of complex multicomponent systems closely correlated with natural prototypes. The Geochemistry Department of Moscow State University actively participates in the development of thermodynamic modeling. Studies by Grichuk and his colleagues, M.V. Borisov, Yu.V. Shvarov, and others, have greatly contributed to the theory and application of this method. Grichuk's paper is the result of many years of investigation aimed at the creation of a model for hydrothermal systems with an endogenous source of energy and ore matter and an exogenous source of solutions.

The subject of his study, ocean-floor hydrothermal systems, shows a number of unique features. The most interesting among them for geologists is that it provides an opportunity to directly observe the formation of economic-scale ore mineralization. Although the economic value of ore occurrences in mid-ocean ridges is currently estimated rather pessimistically, the investigation of oceanic hydrothermal systems sheds light on the formation of ancient massive sulfide deposits. Hydrothermal vents on the ocean floor are very complex objects. Notwithstanding over 25 years of investigative research, there are still some unresolved problems, especially concerning the deep parts of hydrothermal systems. The development of theoretical models allows one to collect diverse pieces of information to obtain a comprehensive picture, which is clearly demonstrated by the study presented in this issue.

A characteristic feature of Grichuk's study, which characterizes the current stage of the development of physical geochemistry, is that a theoretical model is used as a tool for the solution of geological problems. The conclusions drawn in this study regarding the evolution of ore composition owing to metasomatic processes in the interiors of the system, the mechanism of formation of zoning in the ore body, and the influence of boiling on ore mineralization provide new insights into the existing data and considerable progress in the theory of hydrothermal processes.

Head of the Geochemistry Department
of Moscow State University
academician Vilen A. Zharikov

Thermodynamic Models of Submarine Hydrothermal Systems

D. V. Grichuk

Faculty of Geology, Moscow State University, Vorob'evy gory, Moscow, 119992 Russia
e-mail: grichuk@geol.msu.ru

Received March 3, 2004

Abstract—This contribution presents a method for constructing thermodynamic models of convective hydrothermal systems with an exogenous source of solutions. With the example of a simulation of modern hydrothermal systems on the ocean floor, the prospects of such a method for the interpretation and forecasting of hydrothermal mineralization are discussed. A procedure for constructing isotopic chemical models is described using sulfur isotopes as an example. The role of boiling within oceanic hydrothermal systems in the formation of metalliferous deposits is evaluated. This paper is intended for geologists who specialize in hydrothermal ore deposits, geochemists, and marine geologists and can be used by students as a guide for the simulation of ore-forming processes.

CONTENTS

INTRODUCTION

This paper summarizes the investigations that have been carried out by the author in 1979–2003 at the Geochemistry Department of Moscow State University. When this work was initiated, the thermodynamic modeling of geochemical processes had already developed into a branch of the geosciences. Efforts of outstanding researchers, R.M. Garrels, H.C. Helgeson, I.K. Karpov, I.L. Khodakovskii, B.N. Ryzhenko, and others, provided a theoretical basis for the method, algorithms, and program codes for the calculation of equilibria in multicomponent systems. The application of thermodynamic modeling to the investigation of geologic objects required the development of simulation techniques adequately reflecting the complexity of geologic processes.

The goal of this work was to develop methods for the thermodynamic modeling of convective hydrothermal systems, devise a model for a hydrothermal ore-forming system in the oceanic crust, and characterize, with the aid of this model, hydrothermal ore-forming processes in a submarine environment.

I am very grateful to academician V.A. Zharikov, head of the Geochemistry Department, for his help and support during the entire period of this study. Of particular significance over the years was the creative cooperation of my colleagues B.N. Ryzhenko, M.V. Borisov, Yu.V. Shvarov, S.G. Krasnov, and M.Yu. Korotaev. The author acknowledges the assistance, valuable discussions, and advices by Yu.V. Alekhin, L.A. Bannikova, E.N. Baranov, L.V. Dmitriev, A.V. Zotov, A.I. Krivtsov, A.Yu. Lein, V.I. Mal'kovskii, A.A. Pek, V.S. Savenko, N.M. Sushchevskaya, and A.A. Yaroshevskii. Assistance by A.Yu. Bychkov, A.V. Tutubalin, E.E. Abramova, and G.L. Mel'nikova is greatly appreciated.

Various stages of this study were financially supported by grants of the Special Federal Program *World Ocean*, the program *Universities of Russia* (Geomodel project UR 09.003.003), the International Scientific Foundation, the Russian Foundation for Basic Research (project nos. 94-05-17301a, 96-05-64887, 99-05-64868, and 02-05-64282), the Federal Program for the Support of Leading Scientific Schools (project nos. 96-15-98338 and NSh-491.2003.5), and contracts of the Ministry for Natural Resources of the Russian Federation.

CHAPTER 1. GENERAL FORMULATION OF THE PROBLEM

1.1. Methodology of Thermodynamic Modeling

Recent advances in geology, as well as in other sciences, have arisen through the introduction of a new methodological approach, which can be termed the model approach. For a long time, geology developed by way of empirical generalizations. The expansion of our knowledge of nature and, more importantly, the introduction of methods of exact sciences (including physical chemistry) disclosed the limited possibilities of the empirical approach. This motivated researchers in geology, in general, and geochemistry, in particular, to pursue studies of another type using theoretical models.

Problems related to the utilization of theoretical models have been discussed in a number of publications on the philosophy of science. Without going into detail, the essence of the model approach can be briefly presented as follows: this method replaces a study object by its model, which is simpler and more accessible for investigation and corresponds to the object in some principal aspects; the results of the investigation of the model are transferred to the properties of the object.

Two important points must be noted. First, an object and its model cannot be exactly isomorphic; otherwise, model substitution for the object would not provide any advantages. The choice of key aspects depends on the purposes of an investigation and is based on subjective judgments, and it is not known *a priori* if they are sufficient for goal attainment. Therefore, a necessary step is to check their correspondence to the object, i.e., to verify the model. Second, the main stage of research is not the construction of a model but the investigation of its properties. The model is a tool rather than the goal of the work. When the model approach was being introduced into geology, this necessary property was somewhat blurred, but now such a perception of models is of special significance. A model must have predictive capabilities, and some of its consequences must correspond to the as yet unknown properties of its natural prototype.

The general scheme of a study utilizing the model approach is depicted in Fig. 1. The results of an investigation of the properties of a natural object or objects (prototype) are used to perform a schematization, i.e., the properties of the prototype essential for further investigations are distinguished, and a logical scheme is constructed from them. A theoretical model is created on the basis of the logical scheme using the tenets of exact sciences. The theoretical model is explored, and its properties (model consequences) are determined. Some of the consequences are used to assess the efficiency of the model (verification), and others can be employed to predict unknown properties of the natural prototype.

It is obvious from this scheme that at least some of the model consequences must be suitable for a comparison with the object during model verification. However, if all the consequences of a model are used for verification, the predictive capacity of the model vanishes, and the model is useless. Note that the process of verification is two-sided; the results of simulation may indicate a need for a refinement of some properties of the natural prototype. It is even possible that some essential parameters of the natural object will be unraveled only

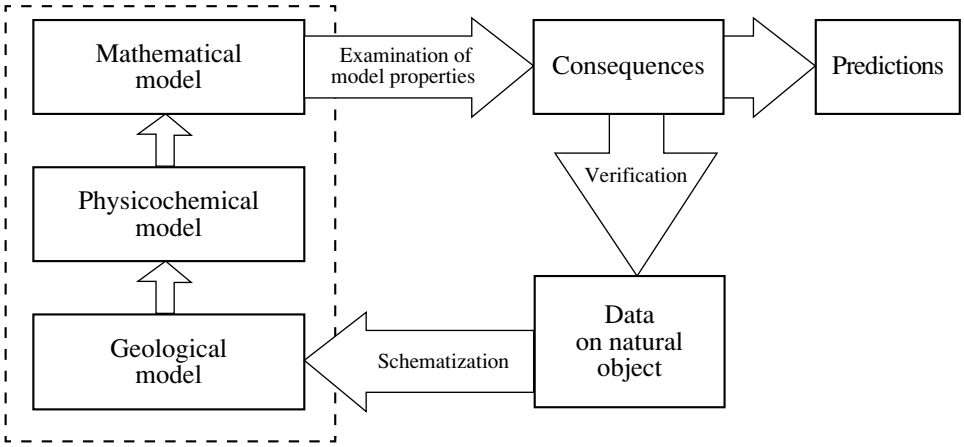

Fig. 1. Methodology of a simulation study.

during the construction of its theoretical model (e.g., Bychkov, 1995).

Based on the above considerations, the problems addressed in model investigations can be divided into two groups: type I problems are external with respect to the method of modeling, and type II problems are internal issues of the model.

Type I comprises the following problems:

—prediction of the unknown properties of natural objects and

—establishing causal and correlation relationships between the known properties of objects.

Type II comprises the following problems:

—choosing the most adequate logical scheme for the object from several alternative hypotheses,

—demonstration of the plausibility of the accepted logical scheme or revealing contradictions in it, and

—demonstration of the internal consistency and efficiency of the theoretical model.

The problems are listed in order of descending scientific importance. However, in terms of methodology, in a particular study, problems should be considered from simple to complex, or in ascending order in the above lists.

Theoretical models in modern geochemical investigations are primarily related to the application of quantitative physicochemical methods, and the progress in the development of the model approach during the past decades was related to the utilization of computer techniques. Therefore, three "layers" can be distinguished within the majority of thermodynamic models of geochemical processes (*Methods of…*, 1988) (Fig. 1):

—a geological model (logical scheme),

—a physicochemical model and

—a mathematical model (a means of obtaining consequences).

The geological model defines the spatial and temporal scales and *P–T* conditions of the process; matter sources and their mineral and chemical compositions; the mechanisms and characteristics of mass transfer; and the chemistry, mineralogy, and spatial distribution of the products of the process.

The physicochemical model describes the chemical composition of the geological model in terms of a physicochemical system. If the methods of equilibrium thermodynamics are utilized, the physicochemical model includes the thermodynamic properties of newly formed compounds, equations for the calculation of thermodynamic equilibria, and expressions describing reaction kinetics and the dynamics of mass transfer.

The mathematical model provides a tool for the quantitative solution of physicochemical model equations (computation algorithm) and a computer code for its implementation.

Although such a three-layer division is obvious and even trivial, each of the constituents of the thermodynamic model uses specific laws and methods and introduces its own set of simplifications and approximations and corresponding sources of errors. It should be noted also that within-layer approximations (for instance, the use of the Debye–Hückel equation for the calculation of activity coefficients) are often universally accepted and even unified, whereas across-layer transitions are usually subjective and specific in each investigation.

The application of equilibrium thermodynamic methods, which deal with the states of a system, for the construction of models for natural processes results in an intrinsic contradiction. This contradiction was first resolved by Helgeson (1968). This paper is still one of the most cited geochemical publications. Using the partial equilibrium concept of P. Barton, Helgeson proposed consideration of a nonequilibrium process as a sequence of equilibrium states of the system, whose composition changes depending on the progress of an irreversible reaction. The Helgeson approach (method of the degree of reaction progress) was extended and

developed by other authors (e.g., Karpov, 1981). It is inherently applicable to the development of a process in time and ignores the movement of materials in space (this issue is discussed in more detail in Chapter 2). The spatial variability of a process can be described using the principle of local equilibrium proposed by Korzhinskii (1951, 1969). In this approach, the variability of a process in space and time is approximated by a series of equilibrium states of the systems whose compositions are interconnected by both kinetic and dynamic relationships, which are the conditions of mass transfer between domains of the geological model. The models of this class are referred to as equilibrium dynamic models (*Methods of…*, 1988). Such models are used in this study.

In the past three decades, the thermodynamic modeling of geochemical processes has been extensively developed in Russia and other countries. Considerable progress in this branch of geochemistry was related to the efforts of Helgeson and his colleagues (Helgeson, 1968; Helgeson *et al.*, 1969, 1970), Karpov's school in Irkutsk (Karpov *et al*., 1976; Kashik and Karpov, 1978; Karpov, 1981; etc.), I.L. Khodakovsky (Khodakovsky *et al.*, 1978), B.N. Ryzhenko, Vikt.L. Barsukov, M.V. Borisov, R.P. Rafal'skii, B. Fritz (1975, 1981), and many other researchers. The success of their studies was connected with the creation of efficient computer programs, including SELECTOR (Karpov *et al.*, Siberian Institute of Geochemistry), GIBBS (Yu.V. Shvarov, Moscow State University), EQ3/6 (T.J. Wolery, Lawrence Livermore National Laboratory), and CHILLER (M. Reed, US Geological Survey). The investigations relied on the development of banks and bases of thermodynamic data embracing a considerable portion of geologically important substances and a wide range of conditions. The most widely used databases are SUPCRT92 (Johnson *et al.*, 1992), DIANIK (Vernadsky Institute of Geochemistry and Analytical Chemistry), THERMINEOS (Siberian Institute of Geochemistry), UNITHERM (Moscow State University), and some others.

Thermodynamic modeling is used in modern geochemistry for the description of diverse processes, from weathering to magmatism and protoplanetary differentiation. This study focuses on the methods of thermodynamic modeling of hydrothermal processes by the example of modern mid-ocean ridge systems.

1.2. Correlation of Ancient and Modern Hydrothermal Processes

The first ore-forming seafloor hydrothermal system was discovered in 1963 in the axial part of the Red Sea by an American expedition of the R/V *Atlantis-II* (*Hot Brines…*, 1969). This system (and similar adjacent systems, which were later discovered) showed some very distinctive features owing to the influence of Miocene evaporates intersected by the Red Sea rift, and the question of its ancient analogues remains to be solved. The discovery of this system and a series of subsequent studies developing the hypothesis of the hydrothermal–sedimentary origin of massive sulfide ores as a result of seawater circulation in the hot crust (Ohmoto and Rye, 1974; Sakai and Matsubaya, 1974; Lister, 1972; Spooner *et al.*, 1977; Solomon and Walshe, 1979) have generated considerable interest in this problem.

Evidence for hydrothermal activity was found in the Mid-Atlantic Ridge (MAR), the East Pacific Rise (EPR), and the Galapagos Spreading Center (GSC). The first high-temperature hydrothermal system was found at 21° N on the EPR at the end of 1979 (*RISE Project…*, 1980). During subsequent American, French, Russian, and international expeditions, new hydrothermal systems have been found on the ocean floor almost each year. Up to now, such occurrences have been reported from many localities in the EPR, MAR, the system of the Juan de Fuca Ridge, and back-arc basins of the southwestern Pacific Ocean. Although it soon became clear that economic ore deposits could hardly be discovered on the ocean floor, the impact of the data obtained on the theory of hydrothermal processes, marine geology and geochemistry, and even biochemistry and ecology (related to the discovery of peculiar populations of organisms near hydrothermal vents) was so significant that the number of publications relevant to this problem has long exceeded 1000. The geology and geochemistry of oceanic hydrothermal systems were addressed in a number of books; thematic issues of the *Marine Mining*, the *Canadian Mineralogist,* the *Economic Geology*, and the *Journal of Geophysical Research*; and several special symposia. Oceanic hydrothermal systems are among the most comprehensively studied geologic objects.

These studies demonstrated a close resemblance of modern sulfide occurrences on the ocean floor to ancient massive sulfide ores. The factual information collected during this work supported the possibility of formation of hydrothermal–sedimentary ores by the thermal convection of surface (marine) waters in crustal rocks near a magma chamber, which serves as a heat source (recycling model, Krivtsov, 1981). Many characteristics of oceanic sulfide ores were found in ancient deposits (Zaikov, 1991; Maslennikov, 1999). Some differences were revealed simultaneously, primarily in geodynamic settings: almost all seafloor sulfide occurrences are related to spreading zones in mid-ocean ridges or back-arc basins, whereas an island-arc environment is reconstructed for ancient copper massive sulfide deposits (*Hydrothermal Sulfide…*, 1992).

Thus, the reason for the compositional similarity of the ores is related to the similar physicochemical mechanisms and conditions of ore formation, which are probably universal. Such a convergence of ore formation mechanisms provides an opportunity to use the data on oceanic hydrothermal systems for the construction of a model of ore-generating processes, whose

application will be much wider than spreading zone environments.

The following problems were considered in this study

—development of methods for the simulation of infiltration metasomatic processes and elaboration of necessary thermodynamic and program tools;

—construction and exploration of a thermodynamic model of a hydrothermal system in the oceanic crust and verification of this model;

—development of methods for the simulation of hydrothermal–sedimentary ore formation and construction on this basis of a model for the formation of a massive sulfide ore body;

—development of the thermodynamic modeling of isotopic chemical systems and application of this method for the investigation of the sulfur isotopic model of ore formation in the ocean; and

—development of simulation procedures, construction of a model, and assessment of the influence of boiling within a hydrothermal system on the processes of ore formation.

CHAPTER 2. METHODS OF THERMODYNAMIC MODELING OF HYDROTHERMAL AND METASOMATIC PROCESSES

Problem formulation. Water–rock interaction is of prime importance for the geologic processes involving aqueous solutions, both hydrothermal and low-temperature. This phenomenon is responsible for the formation of the chemical composition of metalliferous hydrothermal solutions and hydrothermal and metasomatic ore deposition. Therefore, the development of methods for the simulation of water–rock interaction is crucial for the construction of thermodynamic models for hydrothermal processes.

The methods of modeling are currently developed in two directions. One of them is aimed at simulation procedures involving the dynamics of mass transfer and kinetics of chemical reactions (macrokinetic approach of Zaraiskii *et al.*, 1989). Considerable progress has been achieved in the development of the theoretical background of this approach (Lichtner and Balashov, 1993; Steefel and Lasaga, 1994). Unfortunately, as was shown by Rafal'skii (1993), the paucity of data on kinetic constants hampers the wide use of macrokinetic models. The application of this approach to models with sufficiently large numbers of components, allowing sophisticated geological interpretation, is a research topic of the distant future.

Another direction concerns the construction of models combining the dynamics of mass transfer and imitation of the kinetics of chemical reactions through a series of equilibrium states of the system (equilibrium dynamic approach according to *Methods of...*, 1988). This approach was employed in the majority of modern studies on the simulation of hydrothermal processes. In accordance with the principles of local equilibrium (Korzhinskii) or partial equilibrium (Barton), the equilibrium dynamic approach implies that the development of a process in space and/or time is considered as a series of equilibrium states of chemical systems, whose compositions are defined by dynamic and kinetic relationships.

The calculation of equilibrium dynamic models includes two phases: (a) prescribing a series of states of the systems (dynamic phase) and (b) calculation of the equilibrium states of these systems (equilibrium phase). There are sophisticated methods for the calculation of equilibria in multicomponent multisystems (Karpov, 1981; Reed, 1982; *Methods of...*, 1988). There are also highly efficient computer programs (SELECTOR, HCh, EQ3/6, CHILLER, etc.) allowing equilibrium calculations for systems of any complexity. The input thermodynamic information provided by modern thermodynamic data banks (SUPCRT92, UNITHERM, etc.) is sufficient to obtain important geological results.

The main problem with this method is currently refinement of the dynamic parts of the models. Since the dynamic characteristics of a model depend on the properties of the geologic process considered, it is hardly possible to create a universal method appropriate for all processes. Studies conducted at the Geochemistry Department of Moscow State University demonstrated that different methods (scenarios) have to be used for the simulation of processes occurring in various parts of hydrothermal ore-forming systems. In this chapter we evaluate methods for the simulation of several geologic situations most common in current model studies: (a) formation of infiltration metasomatic columns, (b) formation of ore-bearing solutions in extended hydrothermal systems with prevailing fracture percolation, and (c) ore deposition during cooling of hydrothermal solutions.

Some characteristic features of the methods of equilibrium dynamic simulation of hydrothermal and metasomatic processes are illustrated by the example of seawater interaction with tholeiitic basalts. This interaction has been comprehensively studied by experimental and computation techniques (Chapter 3). In the simulation of metasomatic processes, this problem yields rather complicated results and displays some relationships that are rarely observed in problems with simpler mineral compositions, for example, in the simulation of acid leaching of granitoids. Ore deposition during cooling is examined in oceanic hydrothermal systems, which provide typical examples of hydrothermal–sedimentary ore formation (Chapters 3, 4).

The application of various methods is illustrated in this chapter by calculations in the 15-element multisystem H–O–K–Na–Ca–Mg–Fe–Al–Si–C–S–Cl–Cu–Zn–Pb including 45 minerals of fixed composition and 55 solution species.[1] This system is described in detail

[1] Mineral symbols used in the diagrams of this chapter are given in Table 18.

Table 1. Compositions of the basalt, alaskite granite, and solutions that were used for the numerical simulation of infiltration metasomatic columns and ore deposition during cooling

Component	Basalt	Alaskite granite	Seawater	Seawater modified by heating	Hydrothermal solution
H	0	0	0.002114	0.01535	0.117295
O	27.32542	30.4	0.120401	0.098189	0.060188
K	0.0382	2.3	0.0099	0.009904	0.028856
Na	0.7936	–	0.468	0.468079	0.467921
Ca	2.0837	–	0.0103	0.00539	0.024077
Mg	1.9606	–	0.0532	0.046397	1.0×10^{-7}
Fe	1.4364	–	0	0.000154	0.001175
Al	2.9756	2.3	0	2.51×10^{-8}	8.11×10^{-6}
Si	8.4231	12.9	0	0.000027	0.013992
C	0.0088	–	0.002327	0.002328	0.006694
S	0.0209	–	0.02823	0.023114	0.008247
Cl	0	0	0.5459	0.5459	0.5459
Cu	0.00116	–	0	2.16×10^{-7}	1.3×10^{-6}
Zn	0.0011	–	0	2.1×10^{-7}	0.000025
Pb	0.000012	–	1.01×10^{-7}	1.0×10^{-7}	3.0×10^{-7}
H_2O	–	–	55.51	55.49722	54.59447

Note: The composition of modified seawater was obtained by calculating the equilibrium 1 kg seawater +0.1 g basalt at 350°C and 500 bar. The composition of the hydrothermal solution was calculated within the model of an oceanic hydrothermal system at $T_{max} = 350$°C, $P = 500$ bar, and $R/W = 0.496$ (Section 4.1.1).

in section 3.4.2. For the calculation of isothermal models ($T = 350$°C and $P = 500$ bar), the initial solution was represented by seawater modified to reach an equilibrium state under these conditions (accounting for anhydrite and brucite precipitation from seawater under such conditions). The models of hydrothermal solution cooling used reconstructed smoker solutions as an initial hydrothermal solution. The compositions of rocks and solutions used in calculations are shown in Table 1.

Classification of chemical reactors. The equilibrium dynamic models considered here have much in common with apparatuses used in chemical processes. The theory of chemical reactors is thoroughly developed in chemical engineering (Denbig, 1968; *General Chemical…,* 1977) and some of its aspects can be used for the simulation of geologic processes. In particular, the classification of chemical reactors is important for the following discussion.

Chemical reactors are classified with respect to a number of criteria, including method of filling, character of movement of the reaction medium, thermal regime, etc. By the method of filling, chemical reactors are divided into periodic, which are filled before the beginning of the chemical process and emptied after its completion, and continuous (flow) reactors, which involve the input and output of substances in the course of the process. By the character of material movement, the continuous reactors are subdivided into mixed and replacement reactors. The ultimate cases are referred to as ideal mixing and ideal replacement (plug) flow reactors. Real replacement reactors differ from the ideal pattern for many reasons: along-axis diffusion, hydrodynamic dispersion, hydrodynamic wall effects, etc. By the thermal regime, isothermal, polythermal, adiabatic, and other types of reactors are distinguished. There is a class of composite reactors, whose construction is either represented by cascades of reactors or separated into steps (cells, rectification plates, etc.). Figure 2 presents the principal structure of main reactor types.

Processes in each type of reactors are described by a specific system of equations. It is supposed (*Principles of…*, 1991, p. 79) that continuous replacement flow reactors (Fig. 2c) can be approximated by a cellular model, as a cascade of ideal mixed reactors (Fig. 2d) with a great number of cells.

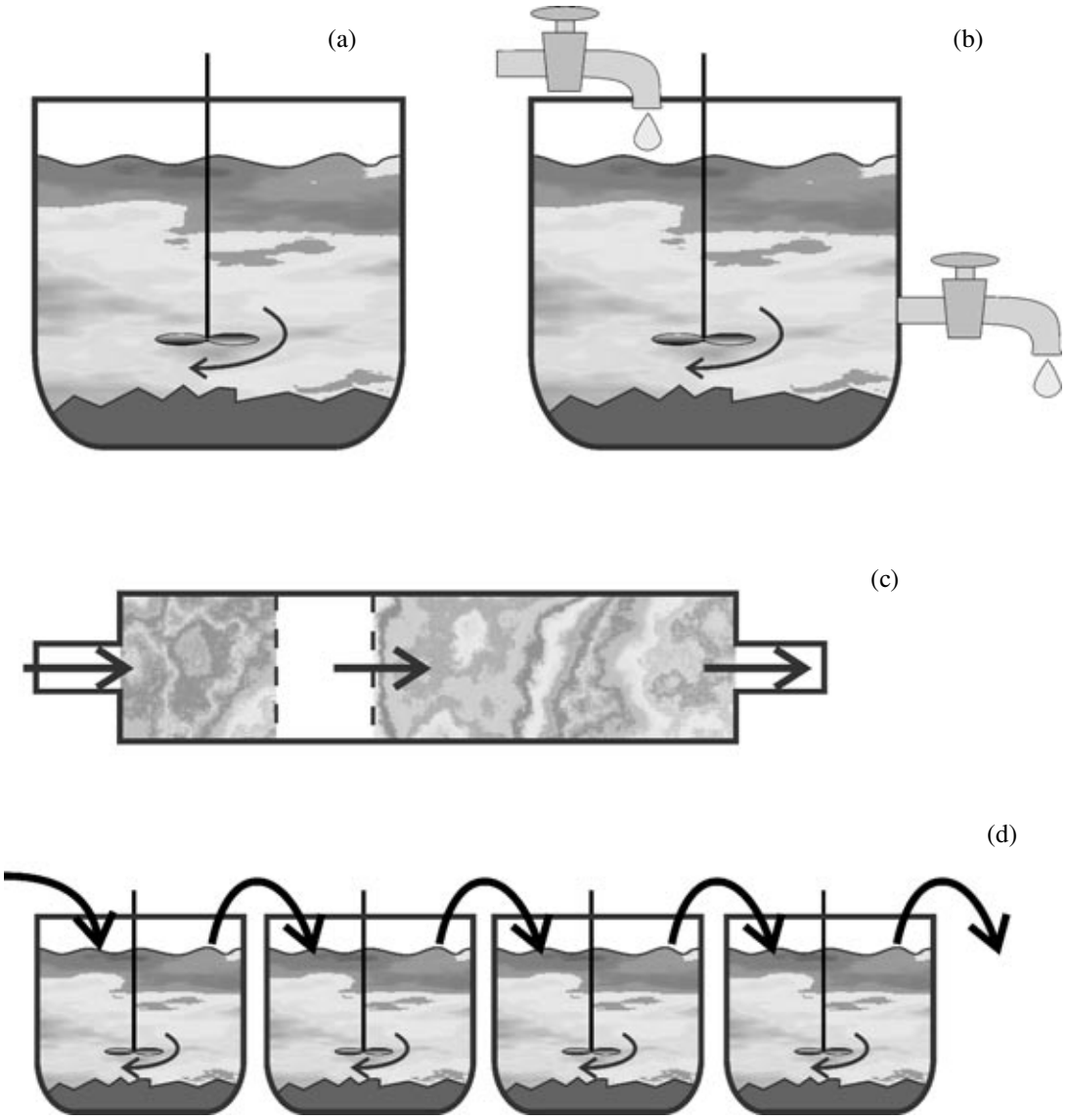

Fig. 2. Classification of chemical reactors with respect to the method of filling and the character of reaction medium movement. (a) Periodic reactor, (b) continuous (flow-through) reactor with ideal mixing, (c) continuous (flow-through) reactor with ideal replacement, (d) cascade of reactors (step reactor) with ideal mixing.

Note also that a steady-state regime in continuous reactors differs from start and stop regimes, which are described by different systems of equations.

2.1. Methods of Simulation of Infiltration Metasomatic Processes

2.1.1. Infiltration metasomatism and its properties in the Korzhinskii theory

In modern petrology and geochemistry, the interpretation of infiltration metasomatism is based on the theory of metasomatic zoning developed by Korzhinskii (1969). He postulated a few main features of infiltration metasomatism (logical scheme) and analyzed the system of equations (theoretical model) describing this scheme. This analysis revealed a number of consequences that must control the properties of metasomatic columns produced by fluid infiltration. If a thermodynamic model of hydrothermal and metasomatic processes is aimed at reproducing metasomatic zoning, and its parameters correspond to the postulates of the Korzhinskii theory, its consequences must be satisfied in the numerical model.

The following conditions were postulated by Korzhinskii for the development of the theory.

I Solution percolates through a permeable homogeneous medium. Solution movement is laminar and corresponds to plug replacement, and there is no hydrodynamic dispersion.

II The solution reacts instantaneously with solid phases, and all portions of solid phases are equally accessible for the reaction.

In addition, it was implicitly assumed that the amounts of dissolved components per unit volume of the porous medium are negligible compared with their contents in the solid phase.

These conditions implied the following traits of an isothermal metasomatic column without minerals of variable composition (this case is the most appropriate for testing the methods of thermodynamic modeling).

1 At the onset of infiltration, a metasomatic column is immediately formed in its complete and final form and only subsequently expands.

2 Metasomatic zones grow linearly with time. The propagation rate of each boundary is higher than that of the preceding one, which provides the stable structure of the column.

3 The percentages of minerals are constant over the whole length of each metasomatic zone.

4 The composition of the pore solution changes abruptly at the boundaries between zones and is constant within any metasomatic zone.

Such a peculiar dynamic regime was referred to as the conditionally steady-state system (Korzhinskii, 1979). Its properties are constant when scaled by x/t, where x is the distance from the beginning of the column, and t is the time.

The simulation of infiltration metasomatic zoning, if it satisfies conditions I and II, must yield a column with certain properties specified by consequences *1–4*.[2] This provides an opportunity to test the internal consistency and applicability of the methods of numerical modeling.

2.1.2. Method of the degree of reaction progress by Helgeson

A computer method for the thermodynamic modeling of irreversible water–rock interactions was first proposed by Helgeson (1968). He applied the principle of partial equilibrium by Barton. The global parameter of the irreversible process was represented by the degree of progress (ξ) of the reaction limiting the rate of the entire process (this is usually a reaction with initial minerals or initial rock on the whole), whereas all other reactions were regarded as equilibrium ones and could, consequently, be calculated by the methods of equilibrium thermodynamics. The rate-limiting reaction changes the composition of the equilibrium portion of the system in accordance with the stoichiometry of the initial substances in it. This relation was explicitly described by Karpov (1981, pp. 124–126). The quantity ξ is an implicit function of time; this function is monotonous, which allows us to calculate the chemical pathway of the process in m_i versus ξ coordinates, where m_i are the amounts of dissolved substances and mineral products of the process. Figure 3 shows a pathway of seawater–basalt interaction calculated by this procedure for 350°C and 500 bar.

Analysis of the method of thermodynamic modeling that was described in detail by Helgeson (1979) shows that it deals with systems closed with the respect to the solution and does not account for any spatial movement of material. In terms of equilibrium dynamic models, the Helgeson method can be considered as a series of equilibrium states of a multisystem whose composition is changed by the continuous addition of initial rock. In terms of the theory of chemical reactors, it corresponds to a periodic (i.e., not flow-through) reactor (Fig. 2a). The Helgeson method is thus not designed for the calculation of metasomatic processes, which include mass transfer in space as one of the most important properties. The results of calculations shown in Fig. 3 do not correspond to metasomatic zones but rather describe mineral associations changing in time within a fixed reaction volume, for instance, in an autoclave. Therefore, condition I of the Korzhinskii theory is not met in such a model, and the results of application of this method are not consistent with all its consequences. It can be clearly seen in Figs. 3a and 3b that the proportions of minerals and the composition of the solution vary with ξ within the stability field of a certain mineral assemblage. The interpretation of this method *sensu lato* as a means to reproduce spatial and temporal relations in metasomatic processes may lead to controversies and even, as will be shown below, erroneous conclusions. Attempts of such expanded interpretations appeared in the literature and even gained some popularity (Karpov, 1981; Kashik, 1989).

This problem was first explored by Fritz (1975), who pointed out the main factor hampering the application of the Helgeson method to spatial problems. In this method the products of previous reaction steps remain in the sphere of interaction and can react during the following steps with the altered solution (back-reaction), whereas the mineral products of reactions are left behind and do not further react with the solution portion that formed them in the infiltration metasomatic process. The importance of this difference depends on the chemistry of a particular system, and this problem will be discussed below.

2.1.3. Method of a step flow-through reactor

In order to adapt the Helgeson approach to the simulation of infiltration metasomatism, Fritz (1975) proposed a method referred to as *systeme reversale*. He modified the algorithm of the degree of reaction progress method. At each step of calculation, the bulk composition of the system changed not only at the expense of the limiting reaction proportionally to ξ, but also by the removal from the system of the solid phases formed during the previous step of calculation. In such

[2] The conditions and consequences were not numbered by Korzhinskii (1969), but was done in this paper to facilitate description.

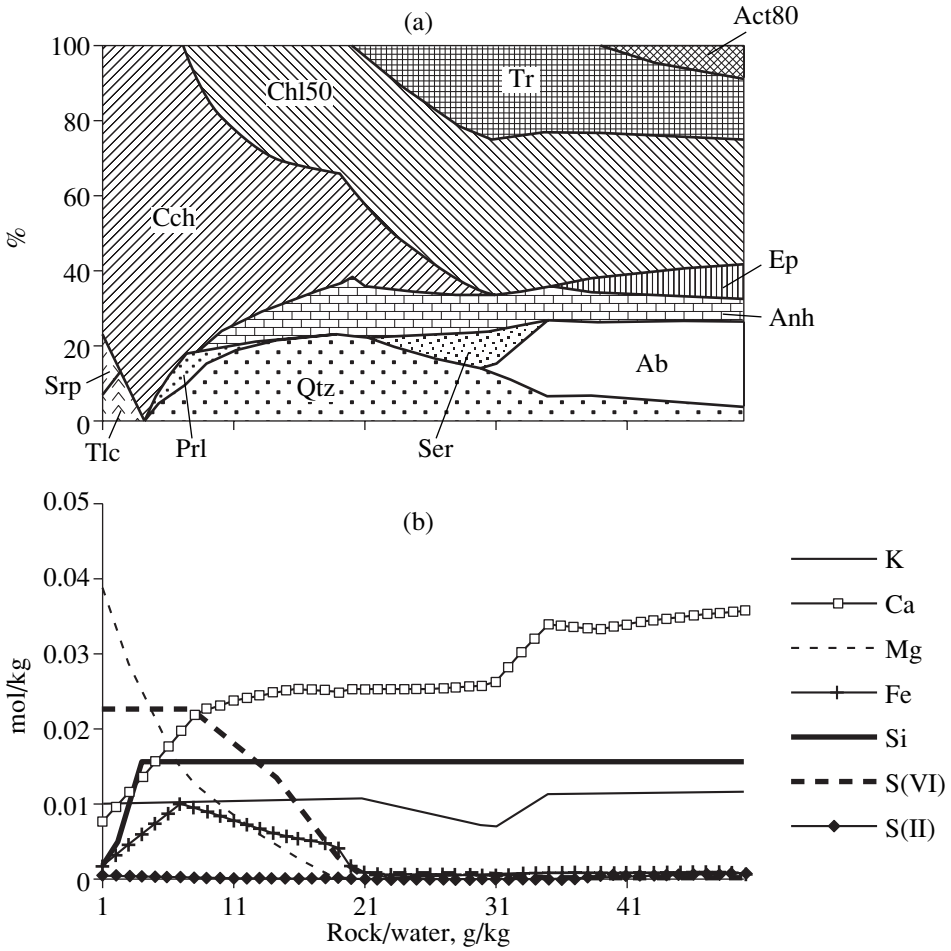

Fig. 3. Calculation of seawater–basalt interaction by the Helgeson method at $T = 350°C$ and $P = 500$ bar. (a) Mineral assemblages and (b) solution composition.

a way, the solid and liquid products of interaction were separated, which is characteristic of an infiltration process. With such a separation of reaction products, the Fritz method does not correspond to a periodic reactor or a continuous completely mixed reactor (Figs. 2a, 2b). The system of differentiation equations used by Fritz (1975) is analogous to that proposed by Helgeson (1968) and implies infinitely small ξ increments, which corresponds to a process in a continuous flow reactor (Fig. 2c). A numerical implementation of the method with finite, although small, ξ increments is equivalent to a step flow reactor (Fig. 2d). It is essential that a material of fixed composition (rock) is added to the system at each ξ increment. Hence the process simulated in this method corresponds to the movement of a single (first) portion of solution through a step reactor filled with fresh rock, i.e., to the regime of an incipient flow reactor.

The results obtained by such a method for the model of infiltration metasomatism in the seawater–basalt system are shown in Fig. 4. A comparison of Figs. 3 and 4 reveals some differences between the model results (ignoring the fact that the variable ξ has a different physical meaning in the Helgeson and Fritz methods, and they are, strictly speaking, not comparable). The most important difference is related to the ξ range of anhydrite stability, which extends in the Helgeson method up to $\xi > 200$ g/kg. In addition, the Helgeson method implies much higher sulfur contents at high ξ. This discrepancy is related to the fact that sulfur is rapidly removed from the system as a solid product (anhydrite) in the case considered by the Fritz method, whereas it is retained in the reaction sphere in the Helgeson approach. There are also differences in the sequence of mineral assemblages (in the example considered, the Helgeson method yields a larger stability field of sericite, Fig. 3a, but produces no hematite and magnetite, which are predicted by the Fritz method), and in some minor details. In general, the fields of phase assemblages calculated by the Helgeson method are more extended along the ξ axis compared with the Fritz method.

The two methods must yield identical results under certain conditions, which can be easily estimated from

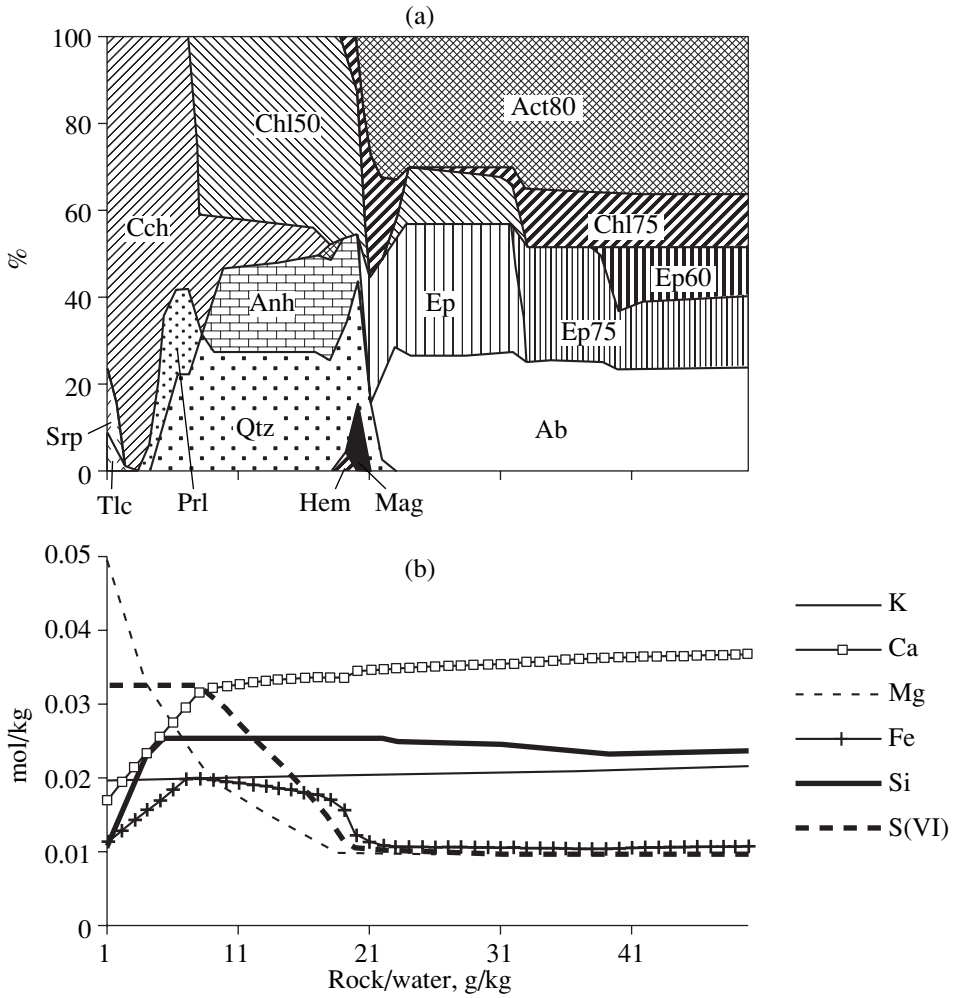

Fig. 4. Calculation of seawater–basalt interaction by the Fritz method at $T = 350°C$ and $P = 500$ bar. (a) Mineral assemblages and (b) solution composition.

the analysis of the reason for the aforementioned discrepancies. The Helgeson and Fritz methods are identical with respect to solution composition and sequence of mineral assemblages when all the minerals occurring in the initial rock dissolve congruently and the components introduced with the solution do not precipitate (canonical column according to Shvarov *et al.*, 2000). Under such conditions, nothing is lost from the solution moving through the flow reactor as minerals left behind. However, even in such a case, the percentages of minerals calculated by the Helgeson and Fritz method are different, because the mineral composition in the former approach is summed over all the previous zones of the column for the given step.

Metasomatic zoning produced by acid leaching approaches the canonical column. Figure 5 presents an example of calculations for the interaction of granite (chemical composition of the rock is given in Table 1) with sulfuric acid solution. This example almost completely satisfies the aforementioned necessary conditions, but it can be clearly seen that the percentages of minerals in the assemblages calculated by the Helgeson model are variable (Fig. 5a), and the muscovite stability fields have different sizes in Figs. 5a, 5c.

Thus, there is a simple criterion (necessary but not sufficient, as will be shown below) for the applicability of the Helgeson method to simulate at least the qualitative structure of an infiltration metasomatism column: the absence of incongruently dissolving minerals and phase replacement in the model column. The majority of published model columns obtained by the Helgeson method for weathering and hydrothermal alteration do not meet this criterion.

The Fritz method complies with condition II of the Korzhinskii theory and does not violate condition I. However, it can be readily seen that the results of calculations shown in Figs. 4a, 4b, and 5d are not consistent with consequences *3* and *4*: the proportions of minerals and the compositions of solutions change within individual metasomatic zones, i.e., the columns are not conditionally steady-state. For instance, an example with alaskite granite (Fig. 5d) shows distinct variations

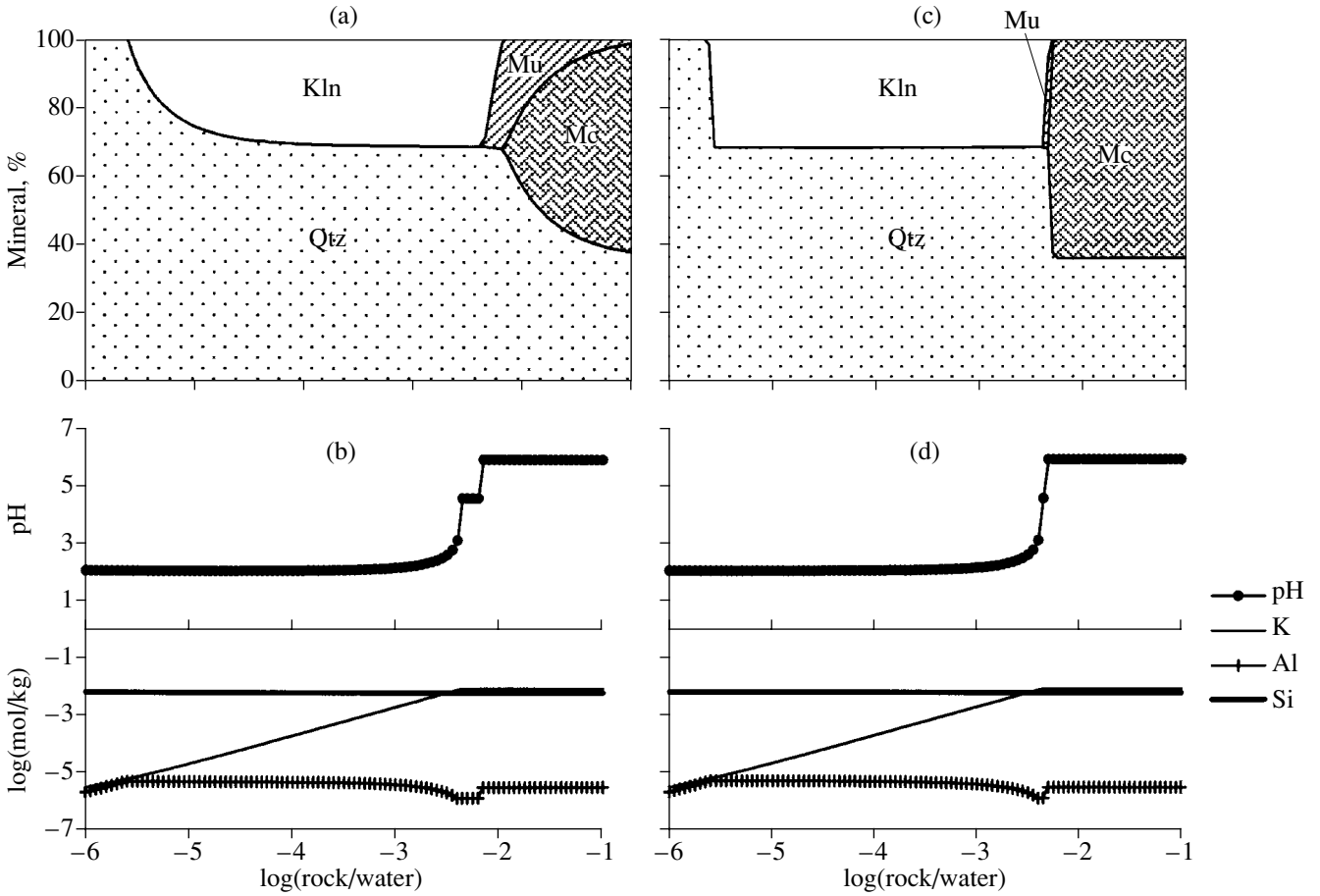

Fig. 5. Interaction of an alaskite granite with hydrochloric acid solution at $T = 250°C$, $P = 500$ bar, and 0.001 mol/kg HCl. (a) Helgeson method, mineral assemblages; (b) Helgeson method, solution composition; (c) Fritz method, mineral assemblages; and (d) Fritz method, solution composition.

in pH and K concentration in the solution within the field of the quartz–kaolinite assemblage. Consequence *2* (column growth with time) is in principle not reproduced by this method. The physical presentation of the method as a movement of a portion of solution through a rock suggests that consequence *1* (instantaneous formation of the whole metasomatic column) is also not provided. The fundamental reason for this discrepancy is related to the fact that condition II of the Korzhinskii theory implies instantaneous equilibrium between the first infinitely small portion of solution and the initial rock (frontal zone of the column), i.e.,

$$\lim_{\xi \to 0} (R/W) = \infty, \quad (1)$$

where R/W is the mass ratio of the reacting rock and water. The use of the Fritz method in its analytical form is equivalent to

$$\lim_{\xi \to 0} (R/W) = \text{const}, \quad (2)$$

and for numerical solutions with finite ξ increments:

$$\lim_{\xi \to 0} (R/W) = 0. \quad (3)$$

In the simulation by the Fritz method, a moving batch of solution reacts with new rock portions and accumulates components partitioning into solution (for instance, potassium, in the calculations illustrated by Figs. 4b and 5d), which is in conflict with consequence *4*. This results in variability in the proportions of minerals within an individual metasomatic zone (contrary to consequence *3*). Thus the Fritz method does not reproduce any consequence of the Korzhinskii theory.

Note finally that the physical presentation of a flow reactor was not used in Fritz's study. A step flow reactor was first explicitly used for the thermodynamic modeling of the hydrothermal process by Grichuk and Borisov (1983). However the reactor considered by these authors was a polythermal one, and condition *1*, plug replacement, was not met in the problem formulation.

2.1.4. Method of multiwave step flow reactor (MSFR)

An obvious limitation of the Fritz method is that interaction between a single portion of solution with fresh rock (initial regime) is simulated. One way to

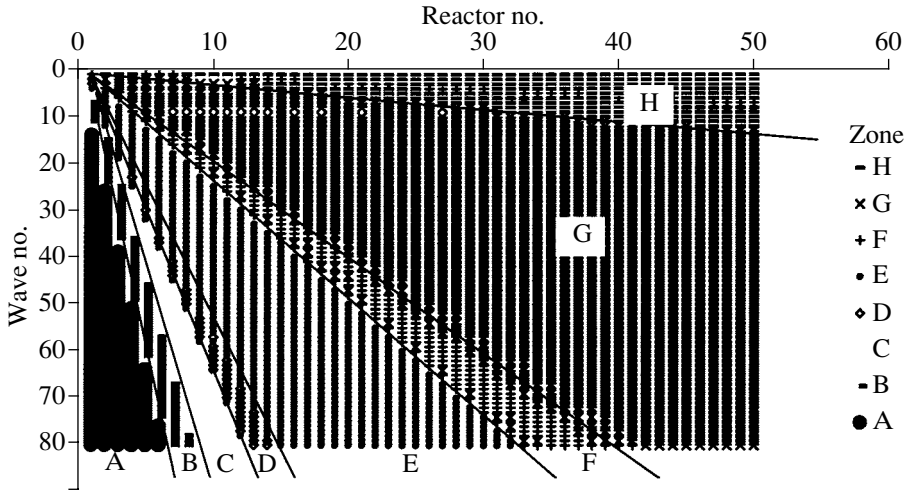

Fig. 6. Growth of metasomatic zones with time calculated by the method of a multiwave flow step reactor (MFSR) for the interaction of seawater with basalt at $T = 350°C$, $P = 500$ bar, 50 steps, and 80 waves (solution portions). Symbols are calculated points. Metasomatic zones: (A) Cch + Srp; (B) Cch + Qtz + Prl; (C) Chl50 + Qtz + Prl + Hem; (D) Chl50 + Qtz + Hem + Anh; (E) Chl50 + Qtz + Hem + Prl + Anh; (F) Chl75 + Qtz + Ep + Act80 + Ab; (G) Chl75 + Ep + Act80 + Wai; and (H) Chl75 + Ep + Act80 + Ab + Wai.

overcome this limitation is to use the method of a multiwave step flow reactor (the term wave is used synonymously with the term solution batch by Heinrich, 1990). The idea of simulating metasomatic alterations by passing many portions of solution through a system of cells (steps of a flow reactor) containing certain amounts of rock was first used by Fouillac *et al.* (1977). This method was referred to as *systeme renouvelle.* These authors modified Helgeson's algorithm representing a weathering profile as an array of 20 cells through which solution was transported. They assumed that only part of the solution occurring in a given cell was moved to the next cell during the next calculation step (the fraction of solution transported was specified by the parameter ζ), and the ratio ζ/ξ was used as a similarity criterion in their modeling. Fouillac *et al.* (1977) did not discuss the physical meaning of this feature of their approach, but it is reasonable to suggest that the variable ζ reflects the influence of hydrodynamic dispersion. In terms of the theory of chemical reactors, such a method corresponds to a cascade of partially mixed reactors. Fouillac *et al.* (1977) demonstrated that the results obtained in their *systeme renouvelle* are qualitatively different from those of the Helgeson and Fritz approaches. Since the introduction of hydrodynamic dispersion violates condition I of the Korzhinskii theory, it is impossible to test the applicability of this method by the agreement with the consequences of the theory. It should also be noted that the use of a logarithmic scale for ζ/ξ in a cell array violates the condition of flow continuity and cannot be physically interpreted.[3]

A multiwave flow reactor was first explicitly used in a thermodynamic model by Grichuk (1988), who simulated convection in hydrothermal systems rather than in a metasomatic column (Section 2.2).

The MSFR method simulates a metasomatic column by passing many solution portions (waves) through the reactor, and, in contrast to the Fritz method, it has to be free of the effect of accumulation of easily mobilized components in the solution. Moreover, since the column is divided into an increasing number of steps affected by a great number of waves, the model is reminiscent of a continuous reactor (*General Chemical...*, 1977), which must give better agreement with the Korzhinskii theory.

Figures 6 and 7 present the results of MSFR application to the calculation of an infiltration column in the seawater–basalt system. Figure 6 shows that the movement of the boundaries of metasomatic zones is approximately linear with time (i.e., with the number of solution portions passing through the column) (consequence *2*). The calculation produced continuous growth of a series of eight metasomatic zones.[4] As can be seen from Fig. 7b, the composition of the solution changes at the boundaries of metasomatic zones, which is in agreement with consequence *4* of the Korzhinskii theory. However, the calculation of mineral composition (Fig. 7a) revealed, in this case, unexpected variations in the proportions of minerals within a zone. A comprehensive analysis of these results showed that such variations are artifacts of the computation method.

[3] The study of Foullac *et al*. (1977) was unfortunately not continued. According to the Science Citation Index, it has been cited 16 times between its publication in 1977 and 1995, and always in sections containing overviews of previous work.

[4] There is an additional zone, *Chl + Qtz + Hem + Anh + Tr*, but it is represented in all waves by no more than one reactor and is probably a ghost zone.

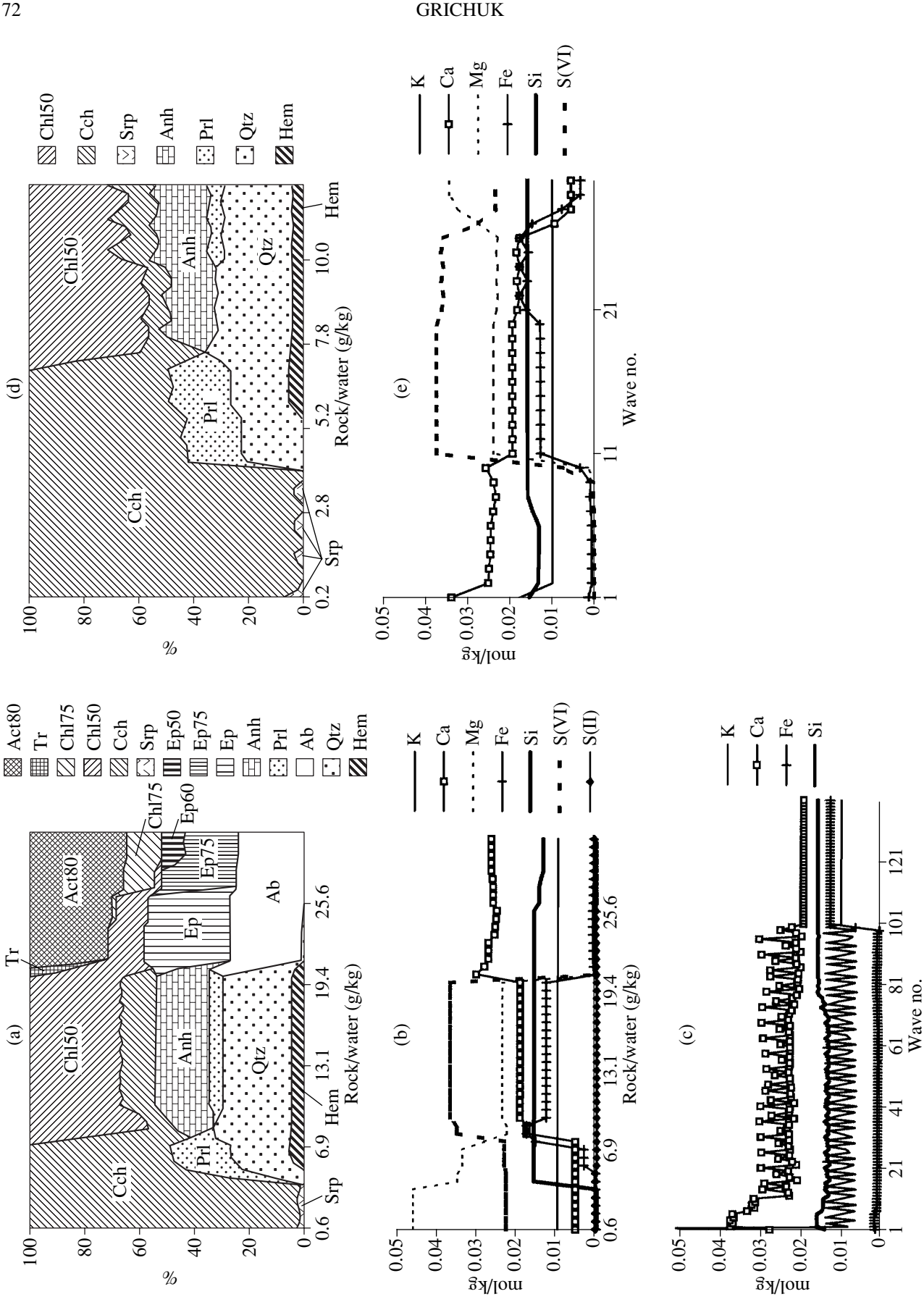
(a)
(b)
(c)
(d)
(e)
Act80
Tr
Chl75
Chl50
Cch
Srp
Ep50
Ep75
Ep
Anh
Prl
Ab
Qtz
Hem
Ep60
%
Rock/water (g/kg)
mol/kg
Wave no.
K
Ca
Mg
Fe
Si
S(VI)
S(II)

Fig. 7. Calculation of seawater–basalt interaction by the method of a multiwave flow step reactor (MFSR) at $T = 350°C$ and $P = 500$ bar. (a) Mineral assemblages, metasomatic zones for the case with 50 g of rock on reactor steps and wave no. 80; (b) changes in the composition of the 80th solution portion during its passage through the metasomatic column; (c) compositions of solution portions passing through the 40th step of the reactor, the mass of rock in each reactor step is 50 g; (d) mineral assemblages for the case with 5 g of rock in each reactor step and wave no. 20; and (e) compositions of solution portions passing through the 40th step of the reactor for the case with 1 g of rock in each reactor step.

The reason for these variations lies in the fact that reactor steps have fixed dimensions (i.e., the masses of initial rock) in the MFSR method. The mineral and chemical compositions of a step containing a boundary between metasomatic zones appear to be combined from the compositions of the contacting metasomatic zones. The solution passing across the boundary should be out of contact with the minerals of the previous zone, but equilibrium is calculated for the bulk composition of such a reactor step, which results in the occurrence of a back-reaction (though small-scale). The calculation of equilibrium for such a boundary step will yield a spurious result in two cases: (a) if incongruent dissolution or replacement of phases takes place on the boundary, and (b) for a dissolution boundary, if the amount of the dissolved phase is not sufficient for the saturation of the given amount of water (in such a case, the boundary will move to the next reactor step in the following stage of calculations). This feature causes oscillations in the composition of a solution passing through a fixed cross-section of the reactor, even if this cross-section stays within a single metasomatic zone (Fig. 7c). In other words, although the composition of each model water portion passing through a metasomatic zone remains constant, the adjacent water portion occurring simultaneously in the same zone may have a different composition.

An increase in the number and a decrease in the size of steps (the fraction of boundary steps yielding spurious results should diminish) do not in fact improve the stability of calculated results, because the probability of solution undersaturation increases owing to reason (b), and reason (a) is not fully eliminated. As can be seen from Figs. 7d and 7e, in such a case variations in the solution composition decrease, but variations in the proportions of minerals in the zones become more pronounced. This may even produce spurious repeated zones (intercalation of monomineralic clinochlore and clinochlore + serpentine zones in the left part of Fig. 7d). An increase in the prescribed mass of rock per step reduces the variability in mineral composition (Fig. 7b), but this lengthens the computation time for the following reason. The MSFR method may provide spurious mineral assemblages for initial waves, if several metasomatic zones appear to be combined in a single step of the reactor. Only after the passage of several waves of solution will the column expand, these spurious assemblages vanish, and the movement of zone boundaries become linear in time (Fig. 6). An increase in the mass of rock per step protracts the initial nonsteady-state period of calculations, sometimes very significantly (calculations may appear physically impossible on a personal computer).

Thus, the use of the MSFR method for the simulation of an infiltration metasomatic column fulfils consequence *2* and, approximately, consequences *3* and *4*. The computational scheme is not sufficiently efficient, because a great number of waves must be calculated. These disadvantages are intrinsic properties of the method and cannot be avoided. The only regulated parameter of the method is the initial mass of rock per step. An increase in this mass is physically equivalent to an enhancement of hydrodynamic dispersion, which violates the condition of plug replacement (condition I of the Korzhinskii theory), and a decrease in the mass leads to the limiting transition expressed by Eq. (3), which violates condition II.

2.1.5. Direct use of consequences of the Korzhinskii theory in algorithms of the simulation of infiltration metasomatism

The properties of infiltration metasomatic columns described by the Korzhinskii theory can be directly used to construct an algorithm for equilibrium dynamic modeling. For instance, Ivanov and Borisov (1980) used the qualitative stability of zone sequence in a column as a criterion in the reconstruction of the composition of a metasomatic solution.

Alexeyev (1985) proposed an approach to the calculation of metasomatic columns by means of the thermodynamic simulation of reactions at zone boundaries and determination of the rate of zone boundary movement as the main parameter of comparison according to consequence *2* of the Korzhinskii theory (method of boundary reactions, Shvarov *et al.*, 2000). In fact, the method proposed by Alexeyev represents a metasomatic column as a step flow reactor (though the term was not used in his study), but reactions are calculated only in those elementary volumes (steps) where the boundaries of metasomatic zones are situated at the given step of the simulation. In such a way, consequences *3* and *4* are automatically satisfied. The stepwise method of computation employed by Alexeyev (1985) is formally not consistent with consequence *1*.

The application of this method was illustrated by the example of acid leaching of alaskite granites, which gives rise to a simple metasomatic column with three or four metasomatic zones depending on the composition of the initial solution. The simulation of more complex systems leads to some problems that were not considered by Alexeyev (1985). For instance, if a solution of

complex composition reacts with an excess amount of initial rock, the first step of calculations by the Alexeyev method often does not provide the correct set of minerals in the back zone (compare with the above-described method of the degree of reaction progress at $\xi > 1$, Fig. 3). As a result, the subsequent calculation of the structure of the whole column will be erroneous, and Alexeyev did not provide a way to recognize such a discrepancy.

The method of boundary reactions was further developed by Shvarov *et al.* (2000). These authors showed that a zone boundary reaction can be written as

$$tL_i + S_{i+1} \longrightarrow tL_{i+1} + S_i, \quad (4)$$

where L and S denote the compositions of the solution and solid phase, respectively, and the subscripts i and $i + 1$ refer to the zone numbers, back and frontal with respect to the given boundary. Reaction (4) reflects the condition of formation of the back zone during the instantaneous reaction of L_i with the mineral substances of the frontal zone.

Shvarov *et al.* (2000) showed that there are two types of boundaries between zones in a metasomatic column and reactions on these boundaries must be calculated differently.

(1) If the mineral assemblage of S_{i+1} includes all the minerals of S_i (congruent dissolution), then L_{i+1} is in equilibrium with S_{i+1} and S_i simultaneously (condition of equilibrium downflow). It can be easily shown that the number of minerals in S_{i+1} is higher by one than that in S_i. The boundaries that comply with this condition are referred to as simple, and the columns including only simple boundaries are termed canonical columns. In the case of a simple boundary, the calculation of equilibrium for the chemical system composed of L_i and S_{i+1} (excess solid phase) yields a solution corresponding to S_{i+1}. A comparison of the compositions of phases defines the parameter t:

$$t = \frac{S_i - S_{i+1}}{L_i - L_{i+1}}. \quad (5)$$

The reciprocal parameter (i.e., 1/t) is the ratio of the rate of zone boundary movement to the velocity of solution flow.

(2) If the mineral assemblage of the back zone contains at least one mineral missing in the frontal zone (indicating incongruent dissolution), the zone boundary is referred to as a reaction boundary, and the column with such boundaries is noncanonical. The reaction boundary is associated with two (or more) coupled reactions. The mineral products of one of these reactions are initial compounds for another reaction. For such a boundary, the calculation of equilibrium in the (L_i + excess S_{i+1}) system results in extra mineral species and an incorrect t value.

The following algorithm was proposed for the calculation of a canonical column composed of n zones ($S_0 = 0$):

$$\begin{matrix} L_0|L_1|L_2|\ldots|L_n \\ S_0|S_1|S_2|\ldots|S_n \end{matrix}.$$

(1) Equilibrium is calculated for the system (L_0 + excess S_n). The t value of the disappearance of the first mineral from the phase assemblage of the frontal zone is determined. The obtained solid phase is regarded as zone ($n - 1$). This operation is repeated for zone ($n - 1$) and all the following zones to obtain a first approximation for the mineral assemblages of all zones of the column.

(2) Passing from the back zone to the frontal one, the composition of the solution is calculated for each zone.

(3) Passing from the frontal zone to the back one, the amounts of minerals in the mineral assemblages of zones are calculated.

The appearance of new mineral assemblages is checked in stages (2) and (3). If they do form, the calculation returns to the previous step in order to refine the zone sequence.

The correctness of the resulting column is generally controlled by t values. The following condition must be met for all boundaries within the column:

$$t_i \le t_{i+1}. \quad (6)$$

If this condition is not met, the column is not canonical, i.e., there are reaction boundaries. The violation of condition (6) implies that there is a ghost zone in the calculated model column (Lichtner and Balashov, 1993), whose back boundary moves faster than the frontal one. Shvarov developed a special procedure for the calculation of such boundaries taking into account the incompleteness of reactions occurring on the back boundary of a ghost zone. It should be noted that the overwhelming majority of infiltration metasomatic columns contain reaction boundaries and are not canonical.

Shvarov *et al.* (2000) and Grichuk and Shvarov (2002) compared the results of calculations of metasomatic columns and showed that, with respect to computational efficiency, the method of boundary reactions is far superior to the MSFR method. It is devoid of artifacts related to the stepwise treatment of the process in the MFSR method. This can be illustrated by the example presented in the paper. In particular, even for wave no. 1000, the column calculated by the MFSR method contained an extra zone (probably a ghost zone), which was lacking in the strict solution obtained by the method of boundary reactions.

2.2. Modeling of Metasomatic Processes in Extended Hydrothermal Systems

With respect to the character of processes, extended hydrothermal systems with percolation through frac-

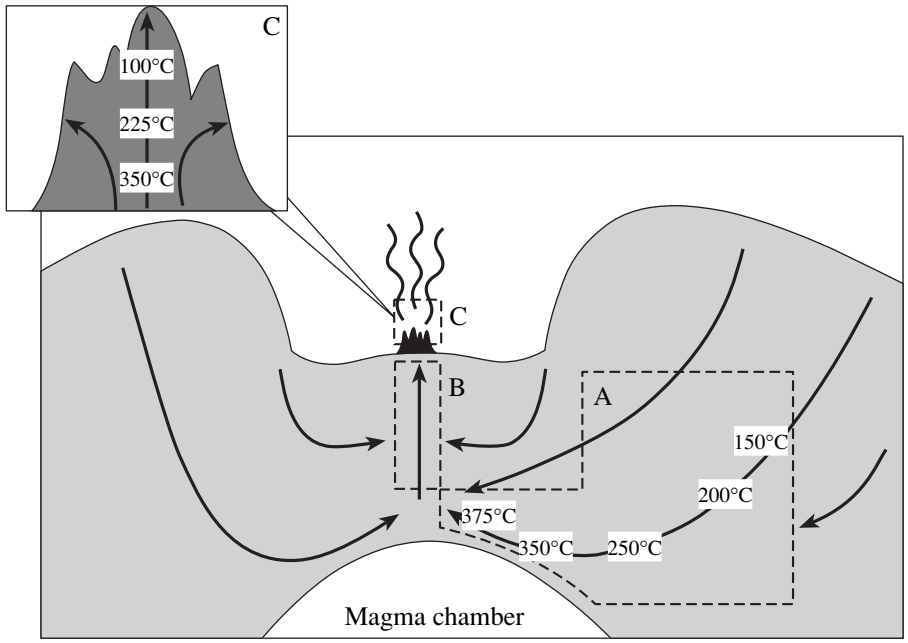

Fig. 8. Simplified model of a hydrothermal system as a flow step reactor: (A) region of the downwelling limb, (B) region of the upwelling limb, and (C) zone of ore deposition.

ture networks are remarkably different from the above-described process of formation of infiltration metasomatic columns. The most fundamental difference is that conditions I and II of the Korzhinskii theory are not applicable for large-volume systems. Indeed, percolation through fractures in rocks with a strongly varying permeability gives rise to significant hydrodynamic dispersion, and plug replacement (condition I) is not realized. The velocity of solution movement in fractures can be much higher than the rate of penetration into the blocks of rock and metasomatic alteration of the inner parts of the blocks. This results in the formation of relicts of unaltered rocks and concentric zoning of metasomatic alterations in the blocks (violation of condition II). Therefore, metasomatic processes in such hydrothermal systems are in fact a superposition of infiltration metasomatism in the direction of solution flow and diffusion metasomatism in the perpendicular direction, complicated by strong hydrodynamic dispersion. This situation obviously cannot be reduced to the formation of an ideal infiltration metasomatic column. The rigorous analysis of such processes presents considerable difficulties, and, when necessary, the simulation of such geologic processes is carried out using various approximations.

A specific class of problems of simulating processes in extended systems is the model of formation of ore-bearing solutions in convective hydrothermal systems with an exogenous source of solution (atmospheric or marine) and an endogenous source of energy. In such a case, the metal loading of solution is controlled by water–rock interaction in a thermally heterogeneous medium with prevailing fracture percolation. The best studied example of such problems is the model of hydrothermal systems in the oceanic crust (Section 3.1.4); similar characteristics display the models of epithermal and stratiform deposits (Heinrich *et al.*, 1995; Ilchik and Barton, 1997) and even of the greisen process (Korotaev *et al.*, 1992).

Grichuk and Borisov (1983) and Grichuk (1988) proposed use of the MSFR method for the simulation of such systems. A convective hydrothermal system is presented in this method as a polythermal step reactor (Fig. 8 analogous to Fig. 2d), in which a partial equilibrium is reached in each step between the solution and the rock. The solution flow path is divided into steps with a fixed temperature increment (10–50°C). A parameter of partial equilibrium has to be prescribed for each step. This parameter specifies irreversible interactions between the solution and rock and is represented by the rock/water ratio (R/W). This is, in fact, a similarity criterion of the model, equal to the mass proportion of fresh rock reacting with the given solution portion at the given step to the mass of this portion.

The mass of the water portion is given by the expression

$$W = S_{\varnothing} v \rho_w \Delta t = Q \Delta t, \quad (7)$$

where $S_{\varnothing}$ is the effective section, v is the velocity of solution movement, ρ_w is the density of the solution, Δt is the time of passage through the reactor step (temperature zone along the flow path), and Q is the solution discharge rate. The mass of reacted rock is

$$R = v_r S_{fr} \Delta t, \quad (8)$$

where S_{fr} is the total surface of fractures within the rock block (reaction step), and v_r is the specific rate of reaction between the solution and fresh rock. It can be easily seen that the R/W value is not directly dependent on Δt and the models utilizing this parameter can be scaled by time.

The parameters of Eqs. (7) and (8) cannot yet be precisely determined, especially v_r, and they cannot be used as a basis for the construction of quantitative models (Rafal'sky, 1993). Grichuk and Borisov (1983) and Grichuk (1988) proposed a method to circumvent this difficulty. The R/W values can be constrained by indirect geochemical methods, in particular, from isotopic systematics (Spooner *et al.*, 1977; Norton and Knight, 1977; etc.). In particular, for modern oceanic hydrothermal systems, a procedure was developed for the estimation of the integral $\Sigma R/W$ value that was reached in the hydrothermal system as a whole from the concentrations of mobile elements (see Section 3.2.1 for more detail). For the hydrothermal systems studied, these values are between 0.5 and 2.0 kg of rock per one kilogram of solution. In the context of the MSFR method, a drawback of such estimates is that the $\Sigma W/R$ value must be divided in the model between the contributions of each step. Moreover, the $\Sigma W/R$ of the system can vary with time.

The following simplifying assumptions can be made for the model of a convective hydrothermal system: (a) the model is steady-state with respect to the position of temperature zones and velocities of solution movement; (b) the times of passage of temperature zones are approximately equal, and the time of solution passage through the ith step, Δt_i, is proportional to ΔT_i; and (c) the permeabilities of rocks do not vary significantly in space and time. Given these assumptions, the parameters Q and S_{fr} can be taken to be equal in the reactor steps and time-invariant (although their exact values are not known). The only time- and temperature-dependent parameter appearing in the expression for R/W is then the specific rate of reaction with fresh rock, v_r.

The temperature dependence of R/W can be written in the notation used in this work as

$$\Sigma R/W = \frac{S_{fr}}{Q}\int_{T_0}^{T_f} v_r(T)dT = \frac{S_{fr}}{Q}\sum_{i=1}^{n}[\overline{v_{ri}}(T)\Delta T_i], \quad (9)$$

where T_0 and T_f are the temperatures of the beginning and end of the process in the descending flow, ΔT is the temperature increment between the reactor steps, $\overline{v_{ri}}$ is the average rate of the reaction in the temperature interval corresponding to step i, and n is the number of steps in the reactor. The temperature dependence of the rate of the solution–rock reaction can be specified by the empirical equation of Wood and Walther (1983) and Walther and Wood (1989), who demonstrated that, under far from equilibrium conditions, the rate of aluminosilicate dissolution in near neutral solutions normalized to the number of oxygen atoms in the formula is governed by an Arrhenius-type equation:

$$\log k = \frac{2900}{T} - 6.85 \text{ (g-atom O/cm}^2\text{ s)}, \quad (10)$$

where k is equivalent to v_r in our notations. The first term of Eq. (10) corresponds to the quantity $2.301E_a/RT$ in the Arrhenius equation, which gives an activation energy of 10.5 kJ/g-atom O. The numerical integration[5] of this expression over temperature intervals allows us to obtain the v_{ri} values and then distribute the value $\Sigma R/W$ between the reactor steps using the simple expression

$$(R/W)_i = \Sigma(R/W)\frac{v_{ri}}{\sum_{i=1}^{n} v_{ri}}. \quad (11)$$

The dependency corresponding to Eq. (11) is shown in Fig. 9. A more rigorous hydrodynamic calculation of these relations for a convective system (Tutubalin and Grichuk, 1997a) without assumptions (a) and (b) yielded rather similar results.

Time dependence of R/W. A metasomatic zone propagates linearly with time normal to the fracture surfaces, if its growth is controlled by the rate of a surface reaction, as was supposed above. However, it is obvious that along with the expansion of the layer of metasomatized rocks, diffusion mass transfer in this layer will play an increasing role and the process of interaction with fresh rock will be slowed down. The theory of diffusion metasomatism (Korzhinskii, 1969) implies a parabolic growth law: the width of metasomatic zones increases proportionally to the square root of time, τ. In general it is impossible to predict a transition from a linear growth regime to a parabolic one. For a model of a hydrothermal system of considerable volume and discharge rate with a $\Sigma(R/W)$ of about 1, it can be suggested that the linear stage is already completed after the passage of a few solution portions. Therefore, the growth rate of the layer of metasomatic rocks near fracture walls will decrease:

$$v_r = \frac{\partial x}{\partial \tau} = v_r^0\frac{\partial(\sqrt{\tau})}{\partial \tau} = v_r^0\frac{1}{\sqrt{\tau}}, \quad (12)$$

where v_r^0 is the rate in the initial moment of the process, and x is the thickness of the altered layer. The stepwise approximation of the interaction process used in the MSFR method implies that an increase in R/W in each reactor step can be described for the jth wave by the simple expression

$$(R/W)_j = (R/W)_1(\sqrt{j} - \sqrt{j-1}). \quad (13)$$

[5] An Arrhenius equation of the form $v = k^0\exp(-E_a/RT)$ cannot be integrated analytically.

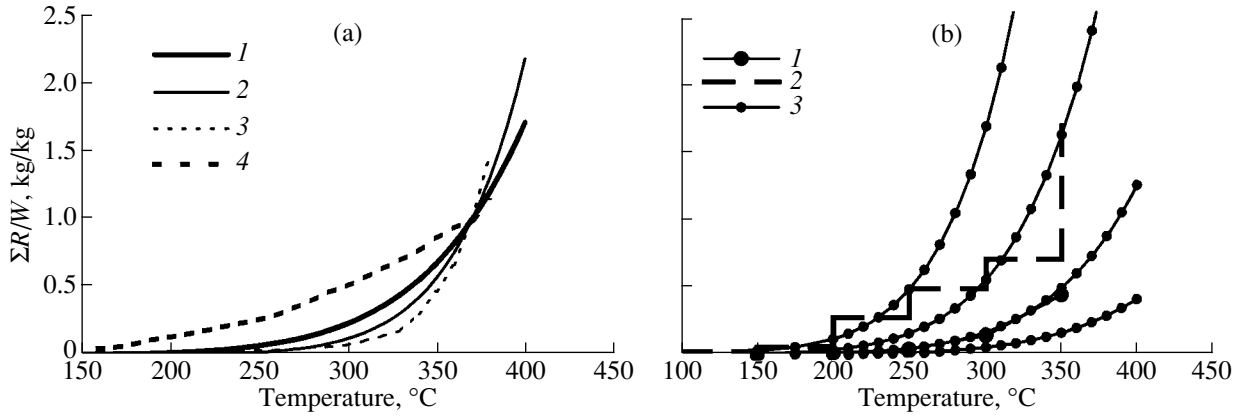

Fig. 9. Temperature dependencies of $\Sigma R/W$. (a) (*1*) Calculated by Eq. (11) in an approximation of continuous movement (normalized to 1 kg/kg at 370°C); (*2*) calculated for a diffusion-controlled process at E_a = 16 kJ/g-at; (*3*) minimum and (*4*) maximum $\Sigma R/W$ values obtained in the hydrodynamic model of Tutubalin and Grichuk (1997a). (b) Dependencies of $\Sigma R/W$ on T used in the thermodynamic models of (*1*) Grichuk *et al.* (1985), (*2*) Bowers and Taylor (1985), and (*3*) model calculations of this study.

A comparison of Eqs. (8) and (12) shows that Eq. (13) assumes a constant interaction surface area, which is equal to S_{fr}. This is true for a system of plane-parallel fractures, whereas other geometries of rock blocks (spherical jointing or hexagonal systems of fractures due to thermal contraction) result in a more rapid v_r decrease with time than that predicted by Eqs. (12) and (13).

The limiting case is the exhaustion of fresh rock at a reactor step when R/W falls to zero. Equations (12) and (13) do not account for such a possibility, and any simulation algorithm must include a special constraint on the total volume of rock that is allowed to react with solution in the given reactor step, which follows from the relation

$$n_{\mathrm{cr}} \sum_{j=1}^{n_{\mathrm{cr}}} (R/W)_j = (R/W)_1 \sqrt{n_{\mathrm{cr}}} \le \frac{1}{\Phi} \frac{\rho_r}{\rho_w}, \qquad (14)$$

where n_{cr} is the number of the solution portion under which fresh rock is exhausted; Φ is the fracture porosity; and ρ_r and ρ_w are the densities of the rock and water, respectively. For $\Sigma R/W$ values of 0.5–2.0 measured in oceanic hydrothermal systems (Von Damm, 1990) and a fracture porosity of basalt of about 3% (Hyndman and Drury, 1976), fresh rock is exhausted in the high-temperature reactor steps at a wave number of $n \times 1000$, i.e., in long-lived model systems. This is in agreement with observations in ophiolitic sequences (Richardson *et al.*, 1987; Nehlig *et al.*, 1994), where the complete alteration of rocks to epidosite occurs at the boundary of dike complexes with isotropic gabbro marking the position of the roof of a magma chamber (i.e., the hottest and chemically most active part of the convective system), whereas the overlying rocks are weakly altered.

Limitations of the model. The above-described procedure of the simulation of a hydrothermal system as a polythermal step flow reactor involves implicit assumptions which must be taken into account during the interpretation of computational results.

(1) The model assumes that the layer of metasomatic rock is uniform, whereas it is a diffusion metasomatic column according to the theory of diffusion metasomatism. Ignoring this phenomenon implies equal migration abilities for all the components that did not form solid phases under the given $\Sigma R/W$ values in the model, whereas the natural situation will be more complicated with differentiated mobility of elements in the direction normal to the fissure channels. Since the method of determining $\Sigma R/W$ from the compositions of natural solutions (Von Damm *et al.*, 1985) is based on the most mobile alkali elements, model calculations for oceanic hydrothermal systems may overestimate the removal of some other elements from rocks (S, Pb, and Zn); the model implicitly implies their removal up to the frontal zone of the diffusion column, which may not correspond to the natural situation.

(2) The model suggests that fresh rock reacts with solution as a homogenous material. This is imposed by the use of Eq. (10), which was obtained for a nonequilibrium state solution–aluminosilicate interaction. However, as a result, the mineral composition of the initial rock and, more importantly, the composition of solution do not affect the rate of this reaction.[6]

(3) The $(R/W)_1$ value used in Eq. (13) concerns a diffusion-controlled process, and its distribution with temperature may not be identical to that defined by Eq. (10), which was obtained for a process controlled by a surface reaction. The temperature dependency in the Wood–Walther equation corresponds to an activa-

[6] It should be noted that the rates of solution reactions with other mineral classes (oxides, sulfides, carbonates, and sulfates) are higher than for aluminosilicates (Rafal'sky, 1993), and their interaction with water will be controlled to a large extent by armoring with an aluminosilicate matrix.

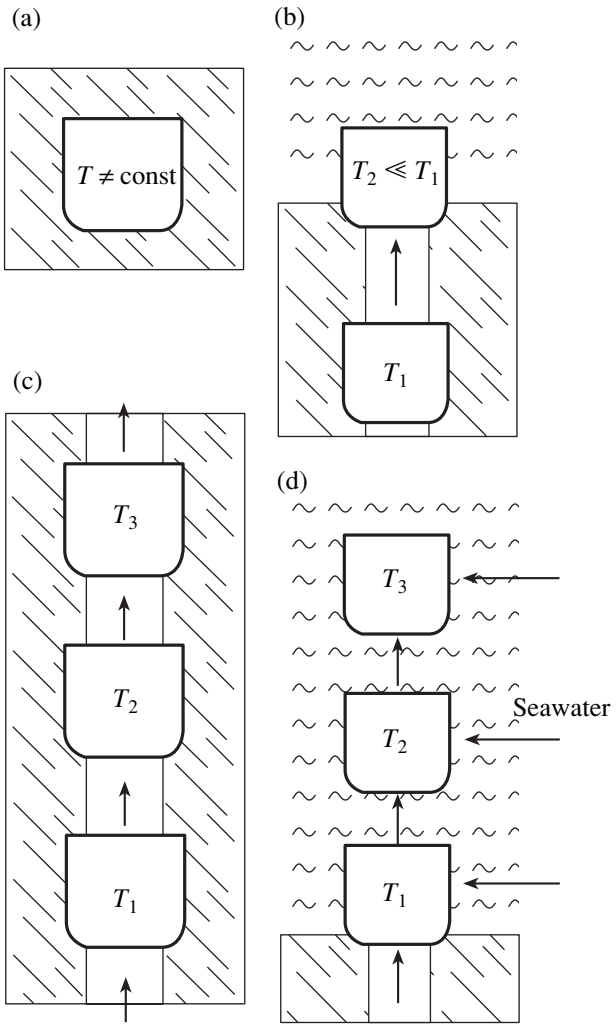

Fig. 10. Cartoons showing the construction of models for ore deposition. (a) Model of slow cooling in a closed system; (b) model of rapid cooling; (c) model of slow cooling in a flow-through system; and (d) model of sequential cooling with mixing.

tion energy (E_a) of 10.5 kJ/g-at O for a heterogeneous reaction. This value is comparable to the activation energies of ion diffusion in aqueous solutions (16–19 kJ/at; Erdey-Gru, 1974) and the activation energies of diffusion-controlled reactions in an aqueous environment (<20 kJ/mol; Lasaga, 1981).

The replacement of the constant in the integrand of Eq. (9) by the value characteristic of a diffusion process does not significantly change the R/W dependency (Fig. 9a). The deviations in the distribution of R/W will be smaller than other model uncertainties, and accounting for these features in Eq. (11) makes the model more complicated but does not improve its quality.

(4) The procedure accepted in the model for the division of the solution flow pipe into temperature segments assumes a complete mixing within any segment, owing to hydrodynamic dispersion and the absence of more considerable processes of solution mixing with different thermal prehistories within the hydrothermal system. These conditions are not always satisfied in natural convective systems. While the former condition can be optimized by choice of the temperature increment in the model (in fact, the size of the rock block is distinguished as a reactor step), the second condition requires a hydrodynamic model of the process and the division of the thermodynamic model into a spatial mesh (Tutubalin and Grichuk, 1997b).

(5) Similar to the above-described isothermal column (Fig. 7), the polythermal model based on the MSFR method is prone to artifacts, including the variability in solution composition at a change in the composition of mineral assemblages in previous reactor steps.

The above-described method is used in this paper for the simulation of convective hydrothermal systems in the oceanic and island-arc crust (Section 4.1).

2.3. Modeling of Ore Deposition during Cooling of Hydrothermal Solutions

Modeling of ore deposition is of special interest for researchers, because it is closely connected with practical geological tasks. A considerable number of studies on the thermodynamic modeling of ore formation have been published up to now. They make use of various approaches, from the calculation of phase diagrams for ore minerals and assemblages (Garrels and Christ, 1965) to dynamic models (Averkin, 1987). Analysis of all the proposed methods of modeling is not possible in this contribution, and, similar to the previous section, we restrict ourselves to the models of the dynamic equilibrium class.

All the models that interpret cooling-related ore deposition in the context of the local equilibrium approximation can be divided into two groups depending on whether the system considered is open or closed. Open-system models can be further subdivided into two subgroups: without input of substances into the system (its composition can be changed by mass removal during spatial separation of solution and precipitated phases) and with such addition (for instance, systems involving solution mixing). Modern methods of thermodynamic calculations allow one to obtain rather precise (in the physicochemical sense) solutions for such models. As will be shown below, a major challenge is the geological interpretation of model results, i.e., the determination of natural processes that can be correlated with a particular model scenario. The principal schemes of several scenarios considered in this section are shown in Fig. 10.

2.3.1. Scenario of closed-system cooling

In cooling scenarios a series of equilibrium states is calculated for a system of given composition at decreasing temperature and pressure. The main property of the

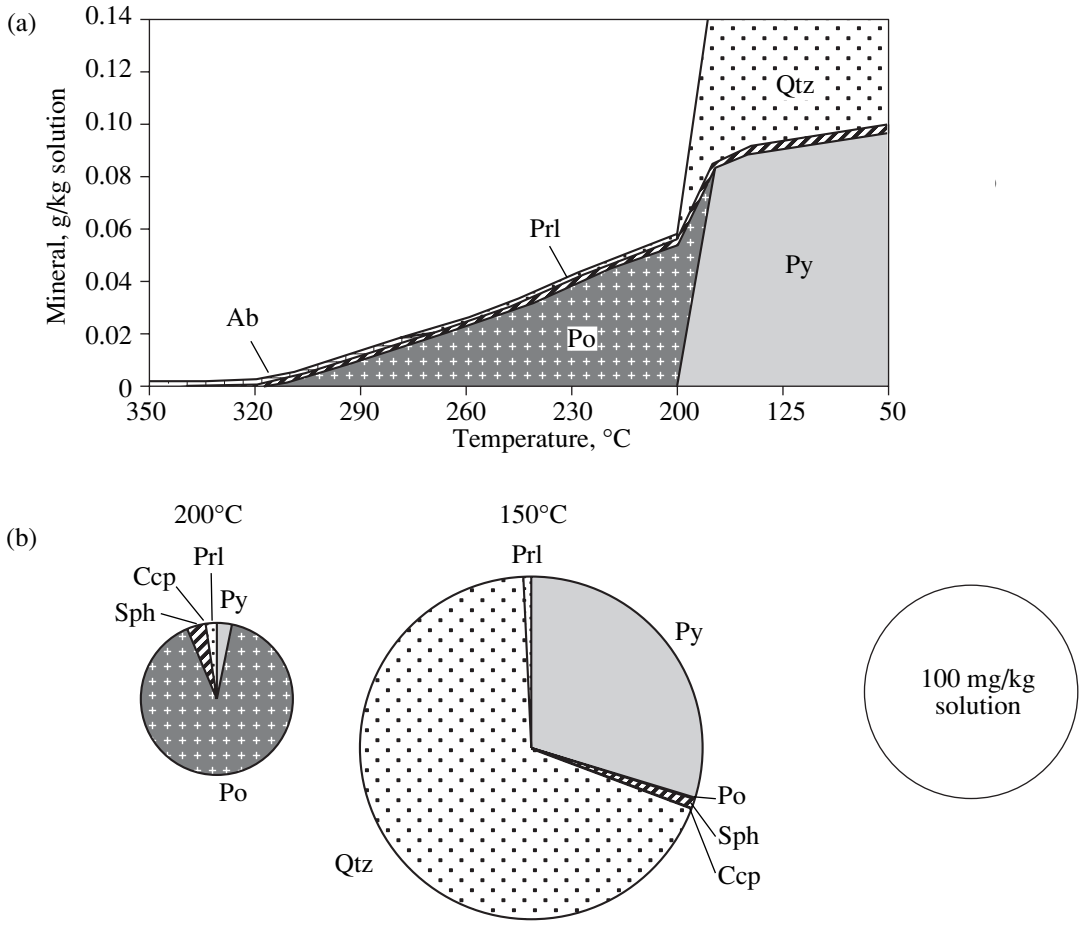

Fig. 11. Calculation of ore deposition during cooling at a feeder reactor temperature of 350°C and P = 500 bar. (a) The mineralogy of cooling products in a closed system of a given composition as a function of temperature. (b) Rapid cooling in a closed system as a function of quenching temperature (quenching pressure of 200 bar). The circle area is proportional to the mass of precipitate.

closed-system scenario is that the state of the system in each computation step is independent of the character of previous equilibrium states of the system under different equilibrium parameters.

The closest prototype of such a process is the calculation of slow cooling of a gas–liquid inclusion in an inert crystal (Fig. 10a). If some phases become unstable in response to changes in conditions (for instance, a temperature decrease), they disappear from the equilibrium assemblage. When a series of states is considered, it is equivalent to the occurrence of back-reactions, i.e., replacement of previously formed minerals.

Figure 11a illustrates the calculation of the composition of solid phases in a closed system of given composition (Table 1, hydrothermal solution) as a function of decreasing temperature. It can be clearly seen in this diagram that, when certain temperatures are reached, previously precipitated minerals are replaced (pyrrhotite is replaced by pyrite at 175°C, and albite is replaced by pyrophyllite at 270°C). Since the system is closed, it cannot be regarded as a sequence of minerals deposited from a solution moving along a fracture or a channel. Moreover, the correspondence of such a model to some real situation is dubious, because the reactions of recrystallization of previously formed minerals are inhibited at low temperatures. In contrast to the equilibrium model, the ore phases formed in nature can be "quenched" and will not be subsequently altered. Thus, the closed-system cooling scenario has limited applications for the simulation of processes in the interiors of hydrothermal systems.

The closed-system cooling scenario was used by Bowers *et al.* (1985) for oceanic hydrothermal systems. Although, owing to the geochemical characteristics of the initial composition, the results of this study were rather reasonable, some details clearly show that the use of a closed-system scenario is not justified for flow-through systems. For instance, the calculation of solution composition in the Guaymas Basin hydrothermal system yielded an increase in Mn concentration owing to back-reactions during solution cooling at temperatures below 200°C.

Surprisingly, the closed-system cooling scenario has found application for simulation of the process of very

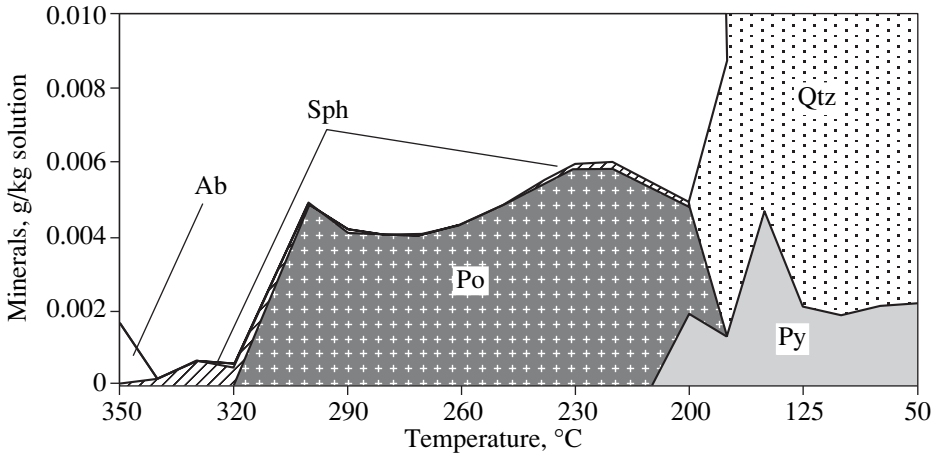

Fig. 12. Results of the simulation of fractional ore deposition during solution cooling in a flow-through system with a temperature increment of 10°C.

fast hydrothermal and sedimentary ore deposition, when the temperature of a hydrothermal solution decreases abruptly during its venting on the ocean floor. If the ore phases are rapidly cooled and quenched and they have no time to react with the components of bottom water, the closed-system model (Fig. 10b) yields the desired assemblage. Such a scenario was used by Grichuk *et al.* (1985) for the calculation of ore deposition in smokers.

The model of rapid cooling has its own stumbling blocks. It is necessary to define final quenching temperature, and this temperature is probably different for different reactions. Some thermodynamically stable minerals may be missing in similar natural associations, and metastable phases may occur (for instance, amorphous silica instead of quartz). Thus, the model of rapid ore deposition requires *a priori* natural information.

The average quenching temperature can be approximately estimated by calculations similar to those shown in Fig. 11a. The best agreement with smoke emitted by seafloor smokers, i.e., a suspension of hydrothermal minerals formed during the rapid discharge of hot solutions into cold seawater, was attained at a quenching temperature of 150–200°C. In order to emphasize the discontinuous character of solution cooling, pie diagrams of quench products appeared to be especially convenient (Grichuk *et al.*, 1985). These diagrams allow presentation of additional dependencies from the parameters of the model. Figure 11b shows the composition of hydrothermal precipitates as a function of quenching temperature. Similar results are described in Section 4.3.1.

2.3.2. Fractional precipitation in a flow-through system

If the natural prototype of the cooling model is a flow-through system, the principle of a flow reactor must be used in the model. Considering the available computer programs for numerical simulation, it appears reasonable to use a step flow reactor instead of a continuous one (Fig. 10c). If the reactor contains a sufficiently large number of steps, the influence of back-reactions will be small and the model results will be quite adequate.

Figure 12 displays the simulation of solution cooling in a flow-through system. It can be seen that the major portion of ore phases (pyrrhotite with minor sphalerite) is deposited within 300–200°C. Although this diagram appears similar to Fig. 11a, the results are significantly different. The main ore phase during fractional precipitation is pyrrhotite rather than pyrite, which was obtained in the closed-system model (Table 2).

The temperature increment used in calculations is an indefinite parameter of the step flow reactor model. In practice, a decrease in the temperature increment lengthens computations and makes the preparation of input data and the interpretation of model results more laborious and time-consuming. The choice of increment value is a compromise between computation time and the quality of results. Table 2 compares the results of calculations obtained with different temperature increments. The similarity in the qualitative and quantitative compositions of the bulk precipitate was used as a criterion. These results show that there are no real differences between the models with increments smaller than 10°C. It was found that calculations with reduced temperature steps are reasonable in the intervals of the most extensive ore precipitation. The calculation procedure can be optimized using a variable temperature increment. The results of such calculations are presented in the next to last column of the table.

The last column of the table presents the results of simulation of closed-system cooling. A comparison with the models of step flow reactors reveals considerable differences between the results of ore precipitation obtained in various model scenarios. This suggests that

Table 2. Simulation of the fractional deposition of ore matter during cooling of a hydrothermal solution from 350 to 50°C (mg/kg of solution); the composition of the initial solution is shown in Table 1

Mineral	Cooling step				Closed system
	50°C	20°C	5°C	optimized*	
Pyrite	230.8	230.9	230.9	230.9	819.6
Pyrrhotite	601.9	601.7	601.5	601.5	0
Galena	0.327	0.327	0.327	0.327	0.327
Sphalerite	24.7	24.7	24.7	24.7	24.7
Chalcopyrite	1.25	1.25	1.25	1.25	1.25
Quartz	10582	10581	10581	10581	10588
Albite	6.6	6.8	7.1	7.1	0
Pyrophyllite	0.77	0.64	0.52	0.52	4.06
Actinolite-80	0.024	0.024	0.024	0.024	0

*The optimized increment is 10°C within 350–200°C and 25°C within 200–50°C.

it is inappropriate to use closed-system models for the problems imitating flow-through systems. Among such problems is, for instance, the simulation of formation of mineralized stockworks in the ascending channels of a hydrothermal system.

2.3.3. Scenarios of cooling with mixing

The mixing of solutions of different compositions is one of the main mechanisms of ore deposition in hydrothermal systems. Since the temperatures of mixed solutions are in general different and the hotter solution is usually more metalliferous, temperature is also a factor of ore deposition during mixing.

The analysis of previously published results shows that several scenarios have been invoked to simulate such processes. They differ in the style of introduction of the second (cold) solution and the way they account for metastable reactions.

The first thermodynamic model of ore deposition during mixing was calculated by Janecky and Seyfried (1984). These authors addressed the problem of reproducing processes accompanying smoker discharge into bottom seawater. In contrast to the above-described scenario of rapid discharge, they assumed that the substances of hydrothermal solutions had enough time to react chemically with seawater (completely or partially). Taking temperature as the main parameter of the model and using heat balance conditions, these authors obtained an equation for the calculation of mixing proportions of hydrothermal solution (m_{HS}) and seawater (m_{SW}). If the average heat capacities of these solutions are not significantly different, this equation is written as

$$m_{SW}/m_{HS} = \frac{T_{HS} - T_{mix}}{T_{mix} - T_{SW}}, \quad (15)$$

where T_{mix} is the temperature of the mixture. The examination of their simulation method shows that it is a modification of the method of the degree of reaction progress by Helgeson, in which the main component of the system is 1 kg of hydrothermal solution and cold seawater is gradually added to it. Thus, it is a peculiar titration procedure of hydrothermal solution with simultaneous cooling. However, the Janecky–Seyfried model does not involve the removal of solid reaction products. Therefore, some precipitated minerals could be dissolved and replaced by other phases during following cooling steps. Figure 13 shows the results of simulation by this scenario for the mixing of smoker solution and cold seawater. It can be seen that, according to these calculations, newly formed anhydrite is not retained upon further cooling and talc is partly replaced by dolomite. Chalcopyrite precipitates at 350°C and disappears at lower temperatures. Bornite forms and is subsequently replaced by chalcocite. At temperatures below 100°C, the amounts of copper-bearing minerals are the same as at the beginning of the process. The confinement of copper mineralization to the hottest parts of hydrothermal systems, which is among the most persistent features of oceanic ore formation, is not described by such a scenario. This method cannot in principle reproduce spatial differentiation of ore components.

Since the nature of the aforementioned flaws in this scenario is known, the mixing model can be easily modified to be applied to the sequential mixing scenario (Fig. 10d). In this scenario, at each cooling stage, small batches of cold solution are added to the previously formed mixture and the solid products of mixing are swept from the system. In essence, this scenario is a nonisothermal case of the Fritz method. The addition

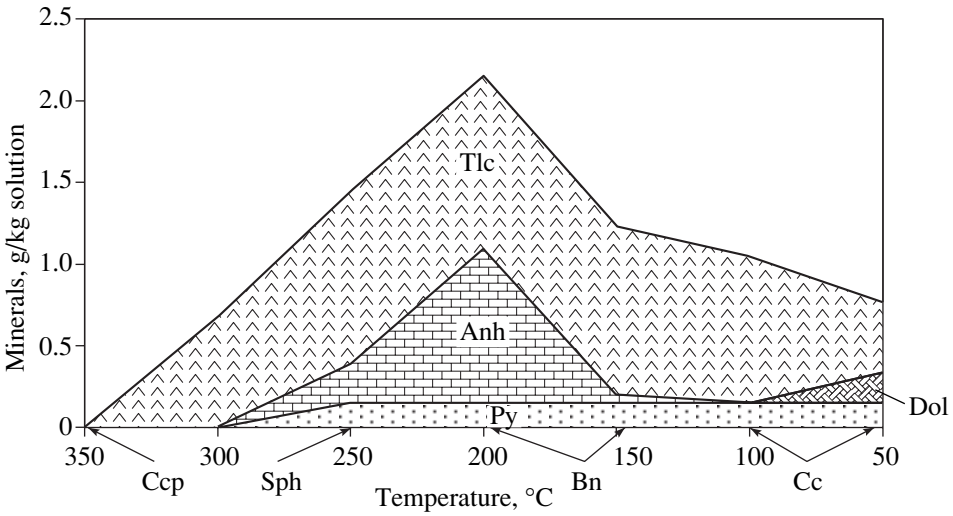

Fig. 13. Calculation of the mixing of hydrothermal solution with cold seawater using the Janecky–Seyfried model. Here, after the occurrence of minor quantities of ore minerals is shown with arrows.

of cold solution is described by an equation identical to Eq. (15). For the *i*th step of cooling, we have

$$\Delta m_i = m_{i-1}\frac{T_{i-1} - T_i}{T_i - T_{SW}}, \quad (16)$$

where Δm_i is the portion of seawater added to the solution. Figure 14a shows the results of calculations for the scenario of sequential mixing of hydrothermal solution and seawater. A comparison with the Janecky–Seyfried model (Fig. 13) shows that the compositions of sediments are different both quantitatively and qualitatively (in the association and temperature intervals of precipitation).

One important merit of Janecky and Seyfried's (1984) study was the evaluation of the role of metastable states for such a rapid process as hydrothermal venting. They demonstrated that ignoring the reaction of seawater sulfate with reducers occurring in hydrothermal solution provides better agreement with natural observations. This approach appeared to be very promising and was subsequently used by many authors. In addition to sulfur compounds, the metastable character of ore deposition processes is evidently reflected in some other hydrothermal components. In particular, evidence from oceanic smokers suggests that the concentrations of silica in their solutions correspond to equilibrium with amorphous silica rather than with quartz (Wells and Ghiorso, 1991). The equilibrium dynamic approach provides no criteria for the distinguishing of metastable constituents of the system, and this can be done only by comparison with natural prototypes.

Figure 14b shows the results of simulation for a metastable case of the sequential mixing scenario. It differs from the equilibrium case in the association of newly formed minerals and ranges of their precipitation. In particular, the order of precipitation changes from talc–pyrite–anhydrite in the equilibrium case to anhydrite–talc–pyrite in the metastable case; there is a low-temperature deposition of magnesium carbonates, brucite, etc. The geochemical aspects of this problem are discussed in more detail in Section 4.3.1.

2.4. Conclusions

The scenarios described in this chapter do not obviously include all aspects of the simulation of hydrothermal processes. Natural situations are certainly much more diverse. For instance, scenarios of processes involving a gas phase were not considered in this chapter (some examples of such models are given in Chapter 6). As the techniques of geochemical modeling are being developed, more sophisticated methods can also appear for those interactions that were considered in this chapter.

Significant progress has been made in the development of combined scenarios for processes including various successive elementary interactions from those considered above. A spectacular example of such combined scenarios is the model of self-mixing developed for the formation of hydrothermal lode ores (Barsukov and Borisov, 1982a, 1982b; Borisov, 2003). This model reproduced the generation of pore solutions in a hydrothermal metasomatic halo at the expense of hydrothermal solution interaction with rocks (using the MSFR method) and ore deposition due to mixing in the areas where solutions percolating through the rock are focused into a fissure conduit. Another example of combined scenarios is given in Section 4.3.2 with application to the simulation of formation of a large sulfide edifice on the seafloor.

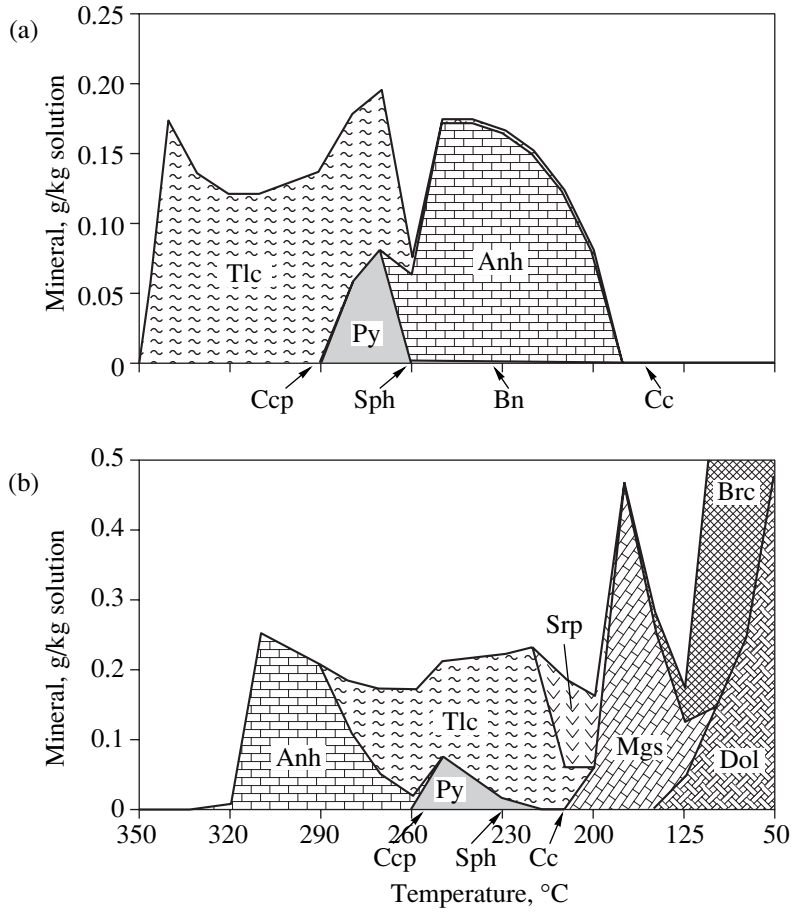

Fig. 14. Results of calculations for the scenario of sequential mixing. (a) Equilibrium mixing; (b) metastable mixing with "frozen" reactions of sulfate reduction, methane oxidation, and quartz precipitation.

The MSFR method has found intriguing application in the study by Borisov (2003) on vein mineralization related to conductive cooling. He considered two scenarios referred to as the reaction and layered models. The reaction model describes a prolonged process involving metasomatic alteration of previously deposited vein material by the solution of subsequent portions. The layered model inhibits metasomatic replacements, and newly formed sediments joined those of previous stages. A comparison with natural prototypes (deposits of the Sadon ore region) showed that the layered model is in better agreement with nature.

One of the most promising directions in the development of equilibrium dynamic models for hydrothermal systems is a synthesis of hydrodynamic and thermodynamic models. It is reasonable to expect that this work will give rise to a new class of models allowing a correlation of chemical interactions with space and time coordinates, which is of special interest for geology. Some pilot studies in this direction have already been published (Steefel and Lasaga, 1994; Tivey, 1995; Tutubalin and Grichuk, 1997a, 1997b).

With the advent of diverse modeling techniques, there is a need to choose the best method for the solution of particular problems. The analysis performed in this chapter suggests that errors of two types may associate with this choice.

Errors of the first type arise in the schematization stage (Section 1.1), when the logical scheme constructed on the basis of natural data appears to be inadequate to the problem formulated. This situation can be exemplified by the choice of a stable scenario for ore deposition during mixing instead of metastable one (Sections 2.3.3 and 4.3.1). First-type errors can be revealed by comparing the results of simulation with the natural prototype.

Errors of the second type originate in the internal inconsistency of the model that appears during the transition from a logical scheme to a physicochemical and mathematical model. Among such errors is the application of the method of the degree of reaction progress to flow-through systems. In many cases such defects of the method can be unraveled by the logical analysis of the model construction (Fritz, 1975). A comparison with natural prototypes does not usually permit recognition of second-type errors. The only reliable way to distinguish them is a comparison with an independent alternative model that reproduces, at least qualitatively,

the logical scheme of the process. An example of such an analysis is given in Section 2.1, where the qualitative solution of the problem of formation of infiltration metasomatic zoning obtained in the Korzhinskii theory was used to control quantitative simulation methods.

CHAPTER 3. THERMODYNAMIC MODEL OF A CONVECTIVE HYDROTHERMAL SYSTEM IN A MID-OCEAN RIDGE

3.1. Geologic Setting and Composition of High-Temperature Oceanic Hydrothermal Systems

The discovery of high-temperature hydrothermal activity on the ocean floor is one of the most significant breakthroughs in geology in recent decades. Advances in the understanding of oceanic hydrothermal systems are related to studies by many researchers from various countries. The development of innovative techniques in oceanology and marine geology, the advent of manned submersibles operating at great depths, played a crucial role in this process. The use of submersibles, side-looking sonar systems, deep-tow cameras, samplers, and high-precision navigation systems enabled detailed investigation of such in accessible and small-sized objects as submarine hydrothermal vents and related sulfide edifices.

The investigation of oceanic hydrothermal systems involves a great diversity of techniques and methods and rival in this respect any studies of modern geology. This resulted in considerable progress in the understanding of the nature of these amazing objects. The history of the discovery and investigation of oceanic hydrothermal systems was described in the publications of leaders and members of research teams (Rona, 1984; Lisitsin *et al.*, 1990; *Hydrothermal Sulfide…,* 1992; Bogdanov, 1997). This section does not attempt to give a chronologically ordered record of ideas and the results of investigations.

The goal of this section is to provide a synopsis of modern knowledge on the geologic structure of hydrothermal systems in the oceanic crust, the chemical and mineral compositions of products of this activity (ores and solutions), the genetic schemes of this process, and their experimental and theoretical substantiation; some controversial issues are analyzed in more detail.

3.1.1. Geologic setting

There are a number of compilations on the hydrothermal activity in the world ocean (Rona, 1984; *Hydrothermal Sulfide…*, 1992). The results obtained in recent years were reviewed by Rona and Scott (1993) and Bogdanov (1997). Figure 15 shows the locations of the high-temperature objects whose geochemistry was best characterized. The majority of currently known submarine hydrothermal systems occur in the modern spreading zones of mid-ocean ridges. High-temperature hydrothermal systems were found at spreading centers in the back-arc basins of the southwestern Pacific (Manus, Woodlark, Lau, and North Fiji basins), island-arc troughs (Mariana and Okinawa troughs), hotspot-related submarine volcanoes (Loihi, Teahitia, and Macdonald). A group of similar objects is represented by submarine hydrothermal vents in the coastal regions of New Zealand, New Guinea, Iceland, the Kuril Islands, Italy, and Japan. New discoveries are continuous. The geologic setting and properties of hydrothermal systems have been most comprehensively studied in mid-ocean ridges. This group of systems was used as a natural prototype for the construction of a thermodynamic model.

All the known active hydrothermal systems of this group are located in the axial valleys of mid-ocean ridges on a very young crust. They are usually found either in the axial (neovolcanic) zone or at the base of valley-wall faults (Fouquet *et al.*, 1988, 1996; Lisitsin *et al.*, 1990; etc.). Such a correlation with the morphologically distinct elements of the geologic structure considerably facilitates the search for hydrothermal systems. Hydrothermal systems are unevenly distributed along mid-oceanic ridges. Within fast-spreading ridge segments bounded by transform faults, active hydrothermal systems are most frequently observed in topographic highs in the central parts of the segments and are less common at their ends (Ballard and Francheteau, 1982; Crane, 1985; Macdonald and Fox, 1988). Such a distribution is currently interpreted as reflecting a greater magma chamber thickness and a hotter crust beneath the central part of the segment.

This pattern of hydrothermal system distribution is not universal. The Logachev hydrothermal field, which was found on the slow-spreading Mid-Atlantic Ridge at 15° N (Akimtsev *et al.*, 1991), is situated in an uplifted block of ultrabasic rocks near a transform fault. Several other systems related to blocks of ultrabasic rocks were subsequently found on the Mid-Atlantic Ridge. The Axial Seamount vent field on the Juan de Fuca Ridge is confined to the caldera of a submarine volcano sitting directly on the ridge axis. Evidence for ancient hydrothermal activity was detected at several off-axis volcanoes at 13° and 21° N on the East Pacific Rise (EPR) (Alt *et al.*, 1987; Fouquet *et al.*, 1988; Hekinian *et al.*, 1989; *Hydrothermal Sulfide…*, 1992).

A particular group of hydrothermal systems with specific geologic structures, mineralogy, and chemical compositions develops in the segments where mid-ocean ridges are overlain by thick sedimentary covers. Three such systems have been found up to now: in the Guaymas Basin in the Gulf of California, Escanaba Trough, and Middle Valley (Fig. 15). Their peculiarities are related to the interaction of hydrothermal solutions with sediments, and they are not considered in this paper.

The hydrothermal systems of back-arc basins do not form a compact group. Some of them (North Fiji, Woodlark, and Manus basins) are related to back-arc

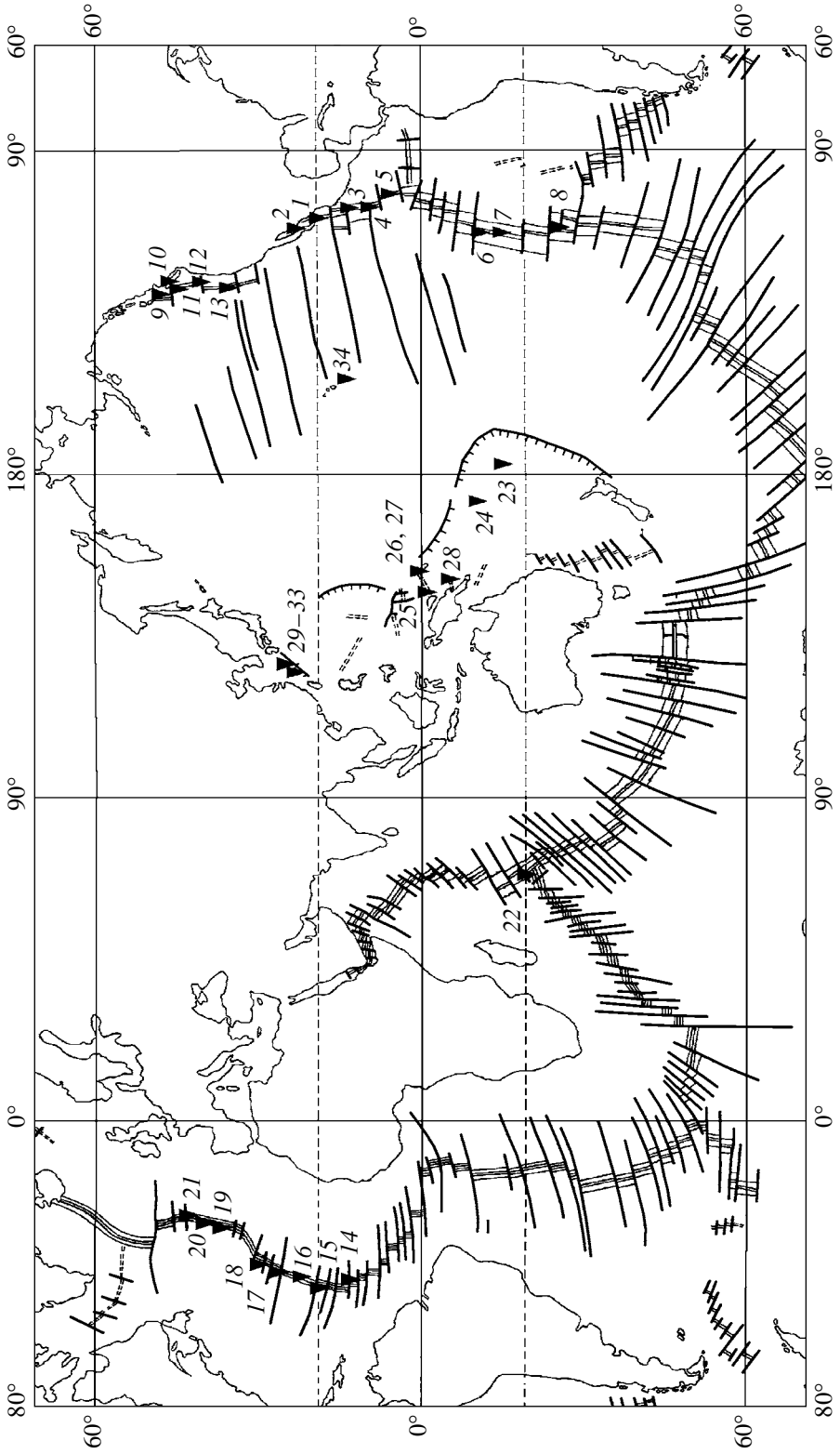

Fig. 15. Schematic distribution of geochemically characterized submarine hydrothermal systems. Numerals correspond to those in Table 6.

spreading centers in a basaltic crust and are geochemically similar to the systems of mid-ocean ridges. Intermediate and silicic igneous rocks occur at the hydrothermal sites of the Lau and eastern Manus basins (Fouquet *et al.*, 1993; Binns and Scott, 1993). The JADE hydrothermal field occurring in a submarine caldera in the Okinawa Trough is considered as a modern analogue of Kuroko-type deposits (Halbach *et al.*, 1989, 1993; Marumo and Hattori, 1999; Glasby and Notsu, 2003), and its geochemical characteristics are significantly different from those of mid-ocean ridge systems.

The energy of mid-ocean ridge hydrothermal systems is usually supplied by magma bodies. Early studies supposed the existence of linear magma chambers, about 20 km wide, beneath ridge axes. They were regarded as sources of considerable heat flows and generation of a new oceanic crust. This view evolved gradually as new comprehensive geophysical data became available. The existence of wide magma chambers was not confirmed, instead, they appeared to be much narrower. Moreover, there is often no evidence for the presence of magma bodies under slow-spreading ridges (i.e., either there is no magma chamber or it is narrow and not detectable by geophysical methods). It is currently thought that magma chambers beneath fast-spreading ridges are no wider than 2–4 km and pinch out toward transform faults (Phinney and Odom, 1983; McClain *et al.*, 1985; Macdonald and Fox, 1988; Wilcock and Delaney, 1996). The depth of chamber roofs is determined from seismoacoustic data and microseism records by bottom seismographs (Riedesel *et al.*, 1982) and is usually 1–3 km. Beneath slow-spreading ridges, magma chambers are even narrower and probably exist sporadically.

The structure of the oceanic crust was reconstructed on the basis of investigations of ophiolitic complexes and is supported by the results of deep-sea drilling. The upper layer is made up of pillow lavas produced by submarine eruptions. The underlying dike complex is formed through filling of extensional fractures, which served as crustal conduits for submarine eruptions. The dike complex rests on a layer of isotropic gabbro, which is interpreted as the result of melt freezing on the roof of magma chambers. A layered intrusive complex beneath it was formed at the bottom of a magma chamber during the crystallization differentiation of melt. The intrusive complex is underlain by ultrabasic upper mantle rocks. Hydrothermal alteration occurs in the rocks of the upper section including the isotropic gabbro layer, and the degree of alteration increases downward (Coleman, 1977; Gillis and Robinson, 1990; Anderson *et al.*, 1990; Gillis, 1995).

The igneous rocks of the oceanic crust show fairly stable petrochemical characteristics. They are classified as tholeiitic basalts and are collectively referred to as mid-ocean ridge basalts (MORB). The differentiation trend of these basalts shows an enrichment of residual melts in iron and titanium. Their extensive differentiation in the oceanic crust occasionally produces ferroandesites and ferrorhyolites, which is exemplified by igneous complexes of the Galapagos Spreading Center (e.g., Perfit *et al.*, 1983; Embley *et al.*, 1988). The analysis of such occurrences suggests that Fe–Ti basalts as well as ferroandesites and ferrorhyolites can be formed in small residual magma chambers before the complete solidification of magma bodies. The EPR and MAR segments hosting active hydrothermal systems are composed of relatively weakly differentiated basalts (Stakes *et al.*, 1984; Davis and Clague, 1987; Hekinian and Walker, 1987).

The compositions of newly formed mineral associations in the country rocks near hydrothermal systems were studied by many authors, reviewed by Mottl (1983), Silantyev (1984), and Kurnosov (1986). In the beginning of these studies, Humphris and Thompson (1978) pointed out the existence of two types of basalt alterations characterized by the occurrence of chlorite and epidote, respectively. The mineral association of the former type includes chlorite, mixed-layer chlorite/smectite, quartz, occasionally hematite and anhydrite. The association of the second type includes epidote, chlorite, albite, actinolite, and minor quartz. The recharge area of a convective hydrothermal system (downwelling limb of convection) is characterized by the magnesian and ferromagnesian compositions of chlorite. It was shown that the mineral association correlates with temperature: epidotized rocks are usually related to higher interaction temperatures, and chloritized rocks correspond to moderate temperatures. For low-temperature conditions, Kurnosov (1986) distinguished zeolite and smectite metamorphic facies, but these processes are characterized by very low rates and are probably related to halmyrolysis rather than to hydrothermal events. Strictly speaking, the chlorite and epidote assemblages of secondary minerals are metasomatic rather than metamorphic, because the compositions of altered rocks are significantly different from those of initial basalts, which suggests a substantial loss or gain of major elements (Humphris and Thompson, 1978). Both associations are typical of metasomatically altered basic rocks and correspond to the chlorite and propylite facies, respectively (Plyusnina, 1983).

There is still limited evidence on the character of metasomatic alteration in the upwelling limb of a convection cell for oceanic hydrothermal systems. The relevant data were mainly obtained by dredging extinct systems where feeder channels had been exposed by tectonic processes. In the TAG hydrothermal field, a footwall zone of metasomatic alteration was drilled during Leg 158 of the Ocean Drilling Program (Humphris *et al.*, 1995; Herzig *et al.*, 1998). The zone of metasomatic alteration near the feeder conduit of oceanic hydrothermal systems is no wider than a few hundred meters (Jonasson *et al.*, 1986; Ridley *et al.*, 1994). According to available observations, basalts undergo greenschist alteration and propylitization in this zone, producing a characteristic assemblage of

chlorite with epidote and albite (Mottl, 1983; Bideau *et al.*, 1985; Embley *et al.*, 1988). A zone of paragonite development was documented in the TAG field, in the upper part of a channel immediately below a sulfide body (Humphris *et al.*, 1998). In this respect, oceanic hydrothermal systems are different from ancient massive sulfide deposits, where quartz–sericite metasomatic rocks passing to chlorite rocks are commonly formed around the channel (Franklin *et al.*, 1981; *Metasomatism and…*, 1998).

3.1.2. Compositions and properties of sulfide edifices and hydrothermal solutions

Mid-ocean ridges are significantly different with respect to the mode of occurrence of ore-forming process. The fast-spreading EPR (up to 18 mm/y) comprises hydrothermal fields with numerous small hydrothermal vents (up to 130 in the segment between 12°41′ N and 12°52′ N; *Hydrothermal Sulfide…*, 1992), most of which are already inactive. The masses of individual bodies are $n \times 10^3$–$n \times 10^4$ t. The ridges spreading at a moderate rate comprise fields with a smaller number of larger edifices. Only several very large hydrothermal mounds were found in the TAG and MARK fields on the slow-spreading Mid-Atlantic Ridge (spreading rate <2 cm/y) and the Galapagos Spreading Center. Their masses are estimated from the apparent sizes as several million tons (Bogdanov, 1997; Herzig *et al.*, 1998). Isotopic investigations suggest that the characteristic growth time of a small sulfide body on the EPR is $n \times 10^2$–$n \times 10^3$ y, whereas the large structures of the TAG and MARK fields experienced a long and complex evolutionary history (Lalou *et al.*, 1993, 1995).

The morphology of sulfide edifices was comprehensively described by Lisitsin *et al.* (1990) and Bogdanov (1997). Small edifices are usually steep-sided cones, several meters high (occasionally, up to 20 m), with the chimney of an active hydrothermal vent on top. Combinations of several conical edifices are common. The basements of the edifices are built up of clastic material composed of cemented products of destruction and oxidation of pipelike chimneys. Large hydrothermal edifices are gently sloping conical mounds, up to 60 m high and up to 250 m and even more in diameter. The tops of such edifices are often truncated and host groups of active hydrothermal vents (Lisitsin *et al.*, 1990, Figs. 21–23, 25). Small hydrothermal edifices often show rather complicated shapes.

Of special interest are the sizes of sulfide bodies occurring in the sedimentary cover. Deep-sea drilling in the Middle Valley region (Davis *et al.*, 1992) confirmed the suggestion by Lisitsin *et al.* (1990) on the extension of such bodies into sedimentary layers. During Leg 139 of the Ocean Drilling Program, an ore body was penetrated to a depth of 94 m.

The mineral composition of oceanic hydrothermal edifices was discussed in a number of publications (see *Hydrothermal Sulfide…*, 1992 for a review). There are a limited number of major minerals accounting for more than 10% of the rock volume: the ore constituents are pyrite, marcasite, chalcopyrite, sphalerite, and wurtzite; and the gangue minerals are opal, anhydrite, and barite. Isocubanite and talc were occasionally found in significant amounts. Sulfide edifices developing on a sedimentary sequence (Guaymas Basin, Escanaba Trough, and Middle Valley) show peculiar mineral compositions with considerable amounts of pyrrhotite; the Middle Valley assemblage also includes magnetite (Krasnov *et al.*, 1994; Krasnov and Stepanova, 1996). Some hydrothermal systems of back-arc basins and island arcs are enriched in chalcophile trace elements (Pb, Ag, As, Sb, etc.), which results in the formation of a number of silver (Mozgova *et al.*, 1993) and arsenic minerals (Halbach *et al.*, 1989, 1993). Table 3 lists all the minerals detected in oceanic hydrothermal edifices.

The mineralogy of hydrothermal sulfide bodies is rather diverse, and various authors distinguished different types of sulfide ores on the basis of mineral composition (up to 10 types or even more; Fouquet *et al.*, 1988). The simplest classification was proposed in *Hydrothermal Sulfide…* (1992), where the two most widespread mineral assemblages were distinguished among the objects studied: (a) pyrite–marcasite–sphalerite ores with opal, characteristic of small sulfide bodies and outer parts of large edifices, which are often highly porous; and (b) massive pyrite and pyrite–chalcopyrite ores with quartz, which are probably more common in the inner parts of large sulfide mounds. Their mineralogical characteristics have been studied in detail only in the outer parts of hydrothermal sulfide edifices, whereas the interior structure and mineralogical zoning of large bodies remain poorly known.[7] Probable schemes of mineralogical zoning in the sulfide bodies and their evolution in time are discussed in Section 3.2.

The chemical composition of oceanic sulfide ores in general mirrors their mineralogy. Based on the proportions of the major ore elements Fe, Cu, and Zn, Krasnov (*Hydrothermal Sulfide…*, 1992) distinguished four geochemical types of ores: (1) massive pyrite (Cu < 4.5% and Zn < 1%), (2) copper sulfide (Cu > 4.5% and Zn < 1%), (3) zinc sulfide (Cu < 4.5% and Zn > 1%),

[7] Up to now, drilling operations have been performed at four hydrothermal locations. Drilling in the Snake Pit hydrothermal mound at 23° N on the MAR (Detrick *et al.*, 1986) resulted in very low recovery. In 1994 drilling operations were carried out on an active edifice of the TAG field (Humphris *et al.*, 1995; Herzig *et al.*, 1998), and its geochemical structure was characterized in detail. A sulfide body at Middle Valley (Davis *et al.*, 1992; Krasnov and Stepanova, 1996) showed a peculiar composition, which is related to its occurrence in the sedimentary sequence. Drilling during ODP Leg 193 was carried out at the Pacmanus hydrothermal vent field, which developed in dacitic rocks, but only some preliminary results have been reported (Paulick *et al.*, 2004).

Table 3. Minerals found in the sulfide hydrothermal edifices on the ocean floor, mainly after *Hydrothermal Sulfide…* (1992) with some additional data from other sources (Shadlun *et al.*, 1992; Bogdanov, 1997; Mozgova *et al.*, 1998; Lein *et al.*, 2003)

Pyrite	Proustite	Calcite	Realgar*
Chalcopyrite	Pearceite	Aragonite	Orpiment*
Sphalerite	Stannite	Anhydrite	Cinnabar*
Wurtzite	Franckeite	Gypsum	Kermesite*
Marcasite	Alabandite	Barite	Jalpaite*
Pyrrhotite	Stibnite	Caminite	Silver*
Isocubanite	Pyrargyrite	Smectites	Pb–As sulfosalts*
Bornite	Polybasite	Talc	Enargite*
Covellite	Miargyrite	Nontronite	Rhodochrosite*
Chalcocite	Stephanite	Lizardite	Imogolite*
Digenite	Cobaltite		
Idaite	Millerite	Fe hydroxides	
Tennantite	Pentlandite	Lepidocrocite	
Tetrahedrite	Coloradoite	Mn hydroxides	
Galena	Gold	Hematite	
Jordanite	Bismuth	Starkeyite	
Acanthite	Brass	Anglesite	
Arsenopyrite	Cadmium	Cerussite	
Loellingite	Sulfur	Chalcanthite	
Diaphorite	Opal	Jarosite	
Fe-freibergite	Quartz	Natrojarosite	
Boulangerite	Magnetite	Copiapite	
Ag–Hg sulfosalts	Anatase	Goslarite	
Freieslebenite	Brucite	Atacamite	

* Minerals identified in ores from the hydrothermal fields of the Okinawa Trough (Halbach *et al.*, 1989, 1993; Glasby and Notsu, 2003).

and (4) mixed copper–zinc sulfide (Cu > 4.5% and Zn > 1%). The data set studied by Krasnov (262 samples) included 46% of type 3 samples, 24% of type 2 samples, 15% of type 1 samples, and 15% of type 4 samples. The chemical compositions of these ore types are shown in Table 4. Copper and zinc are negatively correlated in most objects and show strong local variations within individual hydrothermal edifices and even their segments.

The relative proportions of metals in the ores are correlated with the size and tectonic setting of bodies. Small edifices in the axial zones of ridges with high and medium spreading rates are strongly enriched in zinc. Larger bodies from the same setting show higher iron contents. The largest sulfide structures from the MAR, axial volcanoes of the EPR, and the Galapagos rift show the maximum iron content and copper enrichment relative to zinc, mainly at the expense of zinc depletion (Krasnov, 1990; *Hydrothermal Sulfide…*, 1992). New data by Hannington *et al.* (1998) supported these relationships.

The minor elements of the ores show ubiquitous correlations with major components. The pyrite and copper sulfide types are relatively rich in Co, Se, and Mo (high-temperature association), whereas zinc sulfide ores have higher Pb, Cd, As, Sb, Ag, and Au concentrations (medium-temperature association) (Hannington *et al.*, 1991; *Hydrothermal Sulfide…*, 1992). The investigations by Krasnov and his colleagues on the chemical compositions of individual minerals showed that zinc sulfides are the main carriers of Cd, Ni, and Ag; pyrite, of As and Co; and chalcopyrite, of Se. As, Sb, Ag, and Au form their own mineral phases in oceanic deposits (Table 3).

High-temperature venting into bottom oceanic water is the most remarkable manifestation of hydrothermal processes in the oceanic crust. Mixing of the discharged solution with cold seawater almost immediately produces a suspension of mineral particles (smoke). That is why the hydrothermal vents were named smokers (*RISE Project…*, 1980). Smoke columns rise a few hundred meters above the seafloor, merging with each other and dispersing gradually. Based on the color of the smoke, which depends on its mineral composition, black smokers (pyrrhotite and other sulfides) and white smokers (amorphous silica and anhydrite) were recognized. Gray and even transparent smokers were also described (Craig *et al.*, 1987; Kastner *et al.*, 1987; Lisitsin *et al.*, 1992). The character of a smoker appeared to be closely related to the temperature of the hydrothermal system. Black smokers are the hottest and show an issue temperature of up to 350–360°C, whereas the temperature of white smokers is no higher than 330°C and usually 200–300°C. In addition to focused discharge through chimneys, large ore edifices may show diffuse venting, which was observed during submersible dives as water shimmering.

The maximum measured temperatures of hydrothermal systems are remarkably uniform. Most of the hydrothermal systems of the EPR and the Juan de Fuca Ridge have temperatures no higher than 350–355°C. Temperatures up to 360–365°C were determined in three most extensively studied systems of the Mid-Atlantic Ridge. Noteworthy is a correlation between these values and ocean depth. Hydrothermal systems are discharged at depths of 3600–3100 m in the Atlantic Ocean and 2500–2600 m in the EPR. Note that the relatively shallow hydrothermal system of Axial Seamount on the Juan de Fuca Ridge (1900 m) shows a maximum temperature of 328°C (Butterfield *et al.*, 1990).

The existence of hydrothermal solutions with temperatures higher than 350–360°C has been discussed

Table 4. Average chemical compositions of oceanic sulfide ores (*Hydrothermal Sulfide…*, 1992)

Element, %	Massive iron sulfide type	Massive copper sulfide type	Massive zinc sulfide type	Copper–zinc type	Average for all ores
Fe	37.40	34.28	22.90	24.44	27.60
Cu	0.26	10.42	0.45	6.08	1.36
Zn	0.26	0.21	12.33	4.32	2.23
S	38.59	37.98	31.84	29.87	32.0
Mg	–	0.10	0.12	0.02	0.09
Al	0.26	0.34	0.08	0.14	0.15
Si	3.72	1.97	3.61	2.82	2.83
Ca	2.39	2.38	0.32	0.45	0.30
Ba	0.35	0.047	0.23	0.30	0.21
Mn	0.11	0.014	0.035	0.016	0.07
Pb	0.0608	0.0168	0.1188	0.0495	0.0659
ppm					
Co	325	448	20	49	66
Ni	54	28	19	47	31
As	782	102	525	252	348
Se	226	118	13	25	29
Mo	90	251	37	98	62
Cd	8.6	17.4	287	250	101
Sb	81	3.5	80	21	37
Ag	30	15	100	73	57
Au	0.093	0.49	1.44	1.8	1.0

extensively in the literature (Delaney *et al.*, 1989; Tivey *et al.*, 1990) in connection with the problem of boiling in oceanic hydrothermal systems (Chapter 6). By 1989 four reliable temperature measurements between 375 and 405°C had been documented, including one vent of the Endeavor hydrothermal field, where a temperature monitoring experiment was carried out over 46 days (Tivey *et al.*, 1990). Similar experiments of longer duration have been conducted at 9°50′ N on the EPR (Fornari *et al.*, 1998), in the Cleft segment of the Juan de Fuca Ridge (Tivey *et al.*, 2002), and in the active TAG edifice after drilling (Goto *et al.*, 2002). These measurements demonstrated that oceanic hydrothermal vents are characterized by prolonged periods of steady temperatures of 350–365°C. They may be disturbed by volcanic and seismic events resulting in short-term temperature variations. The maximum temperature of 405°C was measured at 21°33′ S on the EPR (Von Damm *et al.*, 2003) (see also Chapter 6).

The nature of the temperature uniformity of hydrothermal systems remains elusive. The reason for the constancy of temperature could be related to the properties of water rather than to the internal structure of hydrothermal systems. According to the hypothesis of Cann *et al.* (1985/1986), this phenomenon is caused by the heat removal efficiency, which passes through a maximum near the aforementioned temperatures owing to concurrent changes in the heat capacity and viscosity of water.

Many researchers attempted to estimate discharge rates and heat fluxes for individual hydrothermal vents and whole hydrothermal fields. The discharge rates of hot springs were estimated from the visual determinations of flow velocity and chimney diameter, but the accuracy of such estimates is not high. There is a significant discrepancy between the data of various authors, which is probably related to the methods of determination and the considerable natural variability of discharge rate values (Table 5). In large hydrothermal structures, solutions are usually emitted through numerous vents forming groups of smokers (Lisitsin *et al.*, 1990), and the total discharge rate of such groups may be 1–2 orders of magnitude higher than that of individual smokers. Another complex problem is the assessment of relative discharge rates of localized and diffuse venting in large edifices. According to Rona *et al.* (1993), the total heat flux for an active edifice from the TAG field appeared to be 5–10 times higher than that through the group of smokers on top of the edifice. This suggests a prevalence of diffuse discharge in large sulfide bodies.

Table 5. Discharge rates and heat flows of hydrothermal systems

Hydrothermal system	No. in Fig. 15	Discharge rate of solution, kg/s		Heat flow, MW		Reference
		single source	whole system	single source	whole system	
21° N EPR	1	–	–	$6 \pm 2 \times 10^7$ cal/s	–	MacDonald *et al*., 1980
"	"	0.7–11	150	0.5–2.5	220	Converse *et al*., 1984
11° N EPR	4	1–5	–	3.7 ± 0.8	–	Little *et al*., 1987
Juan de Fuca Ridge, Endeavor segment	10	–	–	6.2 (average)	364 ± 73 (main field) 122 ± 61 (Tubeworm)	Ginster *et al*., 1994
Juan de Fuca Ridge, Cleft segment	12	–	–	3.1 (average)	49 ± 13	"
MAR, TAG field	16	–	–		225 ± 25 (active mound)	Rona *et al*., 1993

The chemical composition of oceanic hydrothermal solutions has been a subject of many studies. Early publications were reviewed by Von Damm (1990). Taking into account recent data, it is now possible to characterize to a varying extent the geochemistry of more than 30 hydrothermal systems (Fig. 15). Tables 6–9 summarize data on the major and trace component compositions of solutions, their isotopic parameters, and dissolved gases.

The main technical problem in the geochemical investigation of hydrothermal solutions is sampling of almost point-sized targets at great depths. This problem was solved only by the introduction of submersible diving and special samplers. However, even these sampling methods could not exclude bottom water. Even under the most favorable conditions, the fraction of seawater in a sample is several percent and, more frequently, several tens of percent. Edmond *et al.* (1982) proposed a method to circumvent this difficulty: a series of samples is collected in a hydrothermal vent, and a line of mixing with seawater is constructed for each component using solution analyses. Edmond proposed use of the magnesium concentration as a mixing parameter, because its concentration is very low in the hydrothermal vents of mid-ocean ridges. Compositions extrapolated to the concentration Mg = 0 using the mixing diagrams are interpreted as pure hydrothermal solutions (end-member). The validity of the assumption on zero magnesium content was confirmed using other components (SO_4, U, and Mo). Small negative values for the SO_4 concentration occasionally obtained by such an extrapolation are probably related to the precipitation of anhydrite and barite during the period between sampling and analysis.

Unfortunately, the method proposed by Edmond *et al.* (1982) cannot be used to process the data obtained from vents in ultrabasic blocks (Lein *et al.*, 2000). The concentration of Mg in water from these vents decreases less rapidly than in fluids emanating from the basaltic crust. There is still no reliable method of extrapolation for such solutions.

The analysis of chalcophile elements poses a special problem, because they may precipitate owing to cooling during sampling. These losses must be taken into account (Von Damm, 1990; Trefry *et al.*, 1994). Furthermore, rapidly moving hydrothermal solutions can transport mechanical suspensions from the feeder channel and the sulfide body, and it is not possible to reliably discriminate them from the suspension formed in response to sample cooling.

Despite considerable variations in numerical values, the oceanic solutions display stable compositional trends relative to seawater. These trends were established in the earliest studies (Edmond *et al.*, 1982; Michard *et al.*, 1984; Von Damm *et al.*, 1985), and the subsequent work only provided further detail. Hydrothermal solutions differ from seawater in having much lower concentrations of Mg, SO_4, U, and Mo. They are significantly enriched in the major components K, Ca, and Si and the lithophile trace elements Li, Rb, Cs, Be, and Al. Their Sr content may be both higher and lower than that of seawater. Hydrothermal solutions are probably enriched in Ba and Ra (which is suggested by the data on ^{226}Ra and its daughter isotopes ^{222}Rn and ^{210}Pb; Kadko and Moore, 1988), but these elements are extensively precipitated during mixing with seawater in the course of sampling. The hydrothermal systems occurring in areas with thick sedimentary covers produce solutions enriched in NH_4 and I, and, to a smaller extent, in Br and B.

Hot springs from oceanic hydrothermal systems are characterized by high concentrations of ore elements (Fe, Mn, and Zn) and a number of chalcophile trace elements (Cu, Pb, Cd, Co, Ag, As, Sb, and Se), which are enriched by 3–7 orders of magnitude relative to seawater. These elements (especially trace elements) show a considerable scatter, and the observed variations are correlated mainly with vent temperatures. The concentrations shown in Tables 6 and 7 represent the highest temperature vents of hydrothermal fields and probably most adequately characterize the solutions ascending to the seafloor surface.

Table 6. Chemical compositions of high-temperature solutions from oceanic hydrothermal systems extrapolated to the end-member with Mg = 0

Region		Seawater	East Pacific Rise											
Hydrothermal system			21° N				Guaymas Basin		13° N			11° N	9°17′ N, Vent "F"	
No. in Fig. 15			1				2		3			4	5	
Vent			NGS	OBS	SW	HG	3	4		1	3	4	1991	1994
No.			1	2	3	4	5	6	7	8	9	10	11	12
component, parameter	unit													
t	°C	2	273	350	355	351	285	315	317	–	(380)	347	388	351
pH(25°C)		7.8	3.8	3.4	3.6	3.3	5.9	5.9	3.2	3.2	3.3	3.1	2.8	2.6
Cl	mmol/kg	541	579	489	496	496	637	599	740	718	760	563	46.5	846
Na	″	464	510	432	439	443	513	485	560	587	596	472	38.4	683
K	″	9.8	25.8	23.2	23.2	23.9	37.1	40.1	29.6	29.8	28.8	32.0	1.16	41.5
Ca	″	10.2	20.8	15.6	16.6	11.7	41.5	34.0	55.0	44.6	54.8	22.5	1.83	45.6
SiO_2	″	0.16	19.5	19.5	17.3	15.6	13.5	13.8	22.0	21.9	17.9	18.8	5.93	20
Alk	mg-eq/kg	2.3	–0.19	–0.40	–0.30	–0.50	6.50	8.10	–	–0.638	–0.398	–1.021	–1.4	–1.8
CO_2	mmol/kg	2.3	5.72	–	–	–	–	–	10.8–16.7	–	–	–	15.5	11.4
H_2S	″	0	6.6	7.3	7.5	8.4	5.2	4.8	–	2.9	4.5	8.0	41	8.71
SO_4	″	27.9	0.00	0.50	0.60	0.40	–0.34	0.06	–	–	–	–	–1.04	0.86
Fe	″	$<10^{-6}$	0.871	1.664	0.750	2.429	0.180	0.077	1.450	3.98	10.76	6.47	1.49	12.1
Mn	″	$<10^{-6}$	1.002	0.960	0.699	0.878	0.236	0.139	1.000	1.689	2.035	0.766	0.174	3.28
Zn	μmol/kg	0.01	40	106	89	104	40	19	–	102	2	105	–	–
Cu	″	0.007	<0.02	35	9.7	44	<0.02	1.10	–	–	–	–	–	–
Pb	″	1×10^{-5}	0.183	0.308	0.194	0.359	0.652	0.230	–	0.135	0.014	0.050	–	–
Reference			Von Damm, 1990						Michard *et al.*, 1984	Bowers *et al.*, 1988			Von Damm *et al.*, 1997	

Table 6. (Contd.)

Region		East Pacific Rise				Juan de Fuca Ridge				
Hydrothermal system		17°25′ S	18°15′ S	Rapa Nui Vent Field, 21°34′ S, Brandon vent		Explorer Ridge	Endeavour segment, 47°57′ N			
No. in Fig. 15		6	7	8		9	10			
Vent		Nadir	Akorta	brine	vapor	Vent 12d	Hulk	Lobo	Peanut	North
No.		13	14	15	16	17	18	19	20	21
component, parameter	unit									
t	°C	340	>305	376	401	276	353	346	350	356
pH(25°C)		3	3.25	3.26	3.1	4.62	4.5	4.25	–	4.5
Cl	mmol/kg	190	848	557	297	559	505	428	253	477
Na	″	125	686	441	242	–	391	336	216	378
K	″	6.7	20.3	13.8	6.87	31.13	27.6	24.5	13.5	29.1
Ca	″	5.2	47	32.8	15.8	22.37	42.9	33.0	13.8	34.3
SiO_2	″	10.6	16.8	12.5	8.69	4.40	17.0	15.9	11.0	16.8
Alk	mg-eq/kg	–	–	–0.685	–0.815	0.68	–0.06	–0.06	–1.1	0.192
CO_2	mmol/kg	13.1	8.5	–	–	–	8.4	11.7	22.0	22.0
H_2S	″	8.6	8.4	6.86	7.93	0.964	2.9	5.0	8.1	2.1
SO_4	″	–	–	(–0.5)	2.63	12.79	–	–	–	–
Fe	″	0.59	12.2	12.3	6.97	5.500	0.533	0.646	–	0.177
Mn	″	0.25	1.73	1.3	0.622	0.155	0.194	0.263	0.325	0.271
Zn	μmol/kg	90	314	121	100	0.077	32	28	–	–
Cu	″	10	88	105	45	0.015	9	14	–	–
Pb	″	–	–	–	–	–	–	0.145	–	–
Reference		Charlou *et al.*, 1996		Von Damm *et al.*, 2003		Tunnicliffe *et al.*, 1986*[1]	Butterfield *et al.*, 1994			

Table 6. (Contd.)

Region		Juan de Fuca Ridge									
Hydrothermal system		Axial Volcano, ASHES field				Southern Juan de Fuca Ridge, Cleft segment, 45° N					Escanaba Trough, 41° N
No. in Fig. 15		11				12					13
Vent		Inferno	Hell	Crack	Virgin Mound	Plume	Vent 1	Vent 3	Pipe Organ	Monolith	
No.		22	23	24	25	26	27	28	29	30	31
component, parameter	unit										
t	°C	328	301	217	299	224	285	–	262	327	217
pH(25°C)		3.5	3.5	–	4.4	–	–	–	2.8	2.8	5.4
Cl	mmol/kg	624	550	258	176	1087	896	951	1245	908	668
Na	″	499	446	209	148	796	661	784	695	695	560
K	″	26.8	24.6	11.5	6.98	51.6	37.3	45.6	58.7	41.0	40.4
Ca	″	46.8	38.9	18.9	10.2	96.4	84.7	77.3	109	79.0	33.4
SiO_2	″	15.1	–	–	13.5	23.3	22.8	22.7	24.0	21.0	6.91
Alk	mg-eq/kg	–0.48	–0.51	0.4	0.66	–	–	–	–2.05	–0.82	3.1
CO_2	mmol/kg	50	(90)	179	285	4.46	4.34	–	–	–	–
H_2S	″	7.1	–	–	(18)	3.5	2.69	4.4	1.99	3.7	1.1
SO_4	″	–	–	–		–0.50	–1.30	–1.70	–4.14	–0.68	–
Fe	″	1.065	0.868	0.0133	0.012	18.739	10.349	17.770	16.4	4.9	0.01
Mn	″	1.150	1.136	0.287	0.142	3.585	2.611	4.480	4.25	1.94	0.01–0.021
Zn	μmol/kg	111	134	2.6	2.2	780	374	469	520	580	<0.1
Cu	″	9.9	1.2	0.1	0.4	1.5	15.5	2	1.4	7.8	<0.1
Pb	″	0.302	–	–	0.101	1.63	0.73	1	0.98	1.090	–
Reference		Butterfield *et al.*, 1990				Von Damm, 1990; Evans *et al.*, 1988; Trefry *et al.*, 1994; Metz and Trefry, 2000			Butterfield and Massoth, 1994; Trefry *et al.*, 1994		Zierenberg *et al.*, 1993

Table 6. (Contd.)

Region		Mid–Atlantic Ridge											
Hydrothermal system		Logatchev, 14°45′ N	MARK, 23° N		TAG, 26° N		Broken Spur, 29° N	Lost City, 30° N	Rainbow, 36°14′ N	Lucky Strike, 37°17′ N			Menez Gwen, 37°50′ N
No. in Fig. 15		14	15		16		17	18	19	20			21
Vent			1	Snake Pit	Black smokers	White smokers	4			2608 Vent	Y3	Eiffel	Menez flank
No.		32	33	34	35	36	37	38	39	40	41	42	43
component, parameter	unit												
t	°C	353	350	345	366	273–320	364	45–70	365	328	324	324	284
pH(25°C)		3.3	3.9	3.8	3.35	3	–	9–9.8	2.8	3.78	3.7	3.7	4.2
Cl	mmol/kg	515	559	559	636	–	469	544–551	750	526	472	417	313
Na	″	438	510	546	557	–	419	465–512	553	406	402	347	381
K	″	22	23.6	24	17.1	17.1	18.8	–	20	27.4	24.8	21.6	23.0
Ca	″	28	9.9	10	30.8	27	12.8	19.4–24.1	67	42.1	36.7	32.3	33.1
SiO_2	″	8.2	18.2	18	20.75	19.1	–	–	6.9	17.5	15.4	13.3	10.3
Alk	mg-eq/kg	–	–0.064	–0.563	–0.45	–1.1	–	–	–	–0.58	–	–	–
CO_2	mmol/kg	10.1	5.2–6.7	–	2.9–3.4	–	–	–	16	–	28.4	23.0	20.1
H_2S	″	0.8	5.9	2.7	2.5–6.7	0.5	8.5–11.0	0.064	1.0–1.2	4.64	3.0	2.1	1.7
SO_4	″	–	–	–	–	–	6.0–7.1	5.9–12.9	–	0.327	13–28	–	–
Fe	″	2.5	2.180	2.121	5.590	3.830	2.156	0.0008	24.0	0.749	0.863	0.624	0.0282
Mn	″	0.33	0.491	0.443	0.680	0.750	0.260		2.25	0.389	0.446	0.289	0.068
Zn	μmol/kg	25–30	50	47	46	300–400	88	0.2–6.9	160	–	37	26	4.2
Cu	″	15–50	17	12	120–150	3	68.6	0.2–0.7	140	–	15	16.5	2.7
Pb	″	0.086	0.265	–	0.110	–	0.376	0.07–0.12	0.148	–	0.130	–	0.056
Reference		Douville *et al.*, 2002; Charlou *et al.*, 2002	Campbell *et al.*, 1988; Douville *et al.*, 2002	Jean–Baptiste *et al.*, 1991	Edmond *et al.*, 1995; Douville *et al.*, 2002; Charlou *et al.*, 2002		James *et al.*, 1995; Charlou *et al.*, 2002	Kelley *et al.*, 2001*[2]; Lein *et al.*, 2004*[3]	Douville *et al.*, 2002; Charlou *et al.*, 2002	Von Damm *et al.*, 1998	Charlou *et al.*, 2000, 2002; Douville *et al.*, 2002		

Table 6. (Contd.)

Region		Indian Ocean	Back–arc basins of the Pacific					
Hydrothermal system		Rodrigues Triple Junction, Kairei Field	Lau Basin, Vai Lili field	N. Fiji Basin	Manus basin	East Manus basin, Desmos field	East Manus basin, Pacmanus field	Woodlark Basin, Franklin Seamount
No. in Fig. 15		22	23	24	25	26	27	28
Vent			VL–3	White Lady	Vienna Woods			
No.		44	45	46	47	48	49	50
component, parameter	unit							
t	°C	360	334	285	275	88–120	268	(270–350)
pH(25°C)		3.5	2	4.7	4.5	2.08	2.6	–
Cl	mmol/kg	642	790	250	712	486	572	626–737
Na	″	560	590	210	534	420	445	–
K	″	14.3	79	–	24	12.1	86	–
Ca	″	30	41.3	6.55	82	7.6	15.1	54
SiO_2	″	15.8	14.5	15	15	5.8	16.2	10.6–15.1
Alk	mg-eq/kg	–0.46	–	–	–0.11	–9.2	–	–
CO_2	mmol/kg	–	(7.6–15.6)	–	6	15	32	–
H_2S	″	4.0	(<0.2)	2	1.8	10	6.8	–
SO_4	″	0.3	–	–	–	32.8	–	–
Fe	″	5.4	2.50	~12	0.109	0.01	2.404	1.9–2.8
Mn	″	0.84	7.1	–	0.348	0.11	3.116	0.5–0.7
Zn	μmol/kg	–	3000	–	10	12	115	19–27
Cu	″	–	34	–	<2	<2	35.6	39–55
Pb	″	–	3.9	–	<0.004	0.022	7.08	58–82
Reference		Gamo *et al.*, 2001	Fouquet *et al.*, 1993	Grimaud *et al.*, 1989	Lisitsin *et al.*, 1992; Bach *et al.*, 2003	Gamo *et al.*, 1997; Bach *et al.*, 2003 *[4]	Bach *et al.*, 2003	Lisitsin *et al.*, 1991

Table 6. (Contd.)

Region		Island arcs and volcanoes of the Pacific					
Hydrothermal system		Okinawa Trough, Minami–Ensei Knoll	Okinawa Trough, CLAM field	Okinawa Trough, JADE field	Okinawa Trough, Iheya North Knoll	Okinawa Trough, Suiyo Seamount	Hawaiian Islands, Loihi Volcano
No. in Fig. 15		29	30	31	32	33	34
Vent							Pele's vents
No.		51	52	53	54	55	56
component, parameter	unit						
t	°C	265–278	100–216	320	238	296–311	31
pH(25°C)		4.9–5.1	5.2–5.6	4.72	4.6	3.7–3.9	5.6
Cl	mmol/kg	501–525	462–514	550	441–458	401–1000	522–538
Na	″	410–431	–	425	377–385	445	451–463
K	″	49–51	–	72	49–50	30	11.5–13.2
Ca	″	21–22	–	22	14–15	89	10.9–11.7
SiO_2	″	10–11	–	13	8	13	1.77
Alk	mg-eq/kg	3.0–3.5	2.5–10.3	1.9	0.5–3.6	–0.20	8.12–11.1
CO_2	mmol/kg	64–96	74–86	26–200	–	39	300
H_2S	″	1.6–2.4	9.27	13.7	–	1.3	2.1
SO_4	″	–	16.4	–	–	–	26.0–26.5
Fe	″	–	–	–	–	–	0.603–1.46
Mn	″	0.088–0.094	–	0.11	0.44–0.447	0.586	0.0206–0.0484
Zn	μmol/kg	–	–	–	–	–	–
Cu	″	–	–	–	–	–	–
Pb	″	–	–	–	–	–	–
Reference		Glasby, Notsu, 2003	Gamo *et al.*, 1991*[5]; Glasby and Notsu, 2003	Gamo *et al.*, 1991; Glasby and Notsu, 2003	Glasby and Notsu, 2003		Sedwick *et al.*, 1992*[6]

Data not extrapolated to the end-member: *[1] Mg = 22.37; *[2] Mg = 9–19; *[3] Mg = 11–18.8; *[4] Mg = 49; *[5] Mg = 34.3; and *[6] Mg = 49.5–51.1 mmol/kg.

Table 7. Trace-element compositions of high-temperature solutions from oceanic hydrothermal systems extrapolated to the end-member with Mg = 0

Region		Seawater	East Pacific Rise											
Hydrothermal system			21° N				Guaymas Basin		13° N			11° N	9°17′ N, Vent "F"	
No. in Fig. 15			1				2		3			4	5	
Vent			NGS	OBS	SW	HG	3	4		1	3	4	1991	1994
No. in Table 6			1	2	3	4	5	6	7	8	9	10	11	12
component	unit													
Li	μmol/kg	26	1033	891	899	1322	720	873	688	614	16	884	18	1620
Rb	″	1.3	31.0	28.0	27.0	33.0	57.0	66.0	14.1	18	–	24	–	–
Cs	nmol/kg	2	230	202	230	246	–	–	–	115	591	195	–	–
Be	″	0.02	37	15	10	13	42	29	–	–	20	–	–	–
Sr	μmol/kg	87	97	81	83	65	253	226	175	171	131	80	2.32	167
Ba	″	0.14	>16	>8	>10	>11	>15	>54	–	–	–	–	–	–
As	nmol/kg	27	30	247	214	452	1071	1074	–	–	–	–	–	–
Se	″	2.5	<0.6	72	70	61	38	103	–	–	–	–	–	–
Br	μmol/kg	840	929	802	877	855	–	1063	1163	–	–	–	74.8	1350
B	″	416	507	505	500	548	–	1570	–	–	–	–	–	–
Al	″	0.02	4.0	5.2	4.7	4.5	6.7	3.7	–	–	–	–	–	–
Co	nmol/kg	0.03	22	213	66	227	<5	<5	–	–	–	–	–	–
Cd	″	1	17	155	144	180	46	27	–	55	–	30	–	–
Ag	″	0.02	<1	38	26	37	24	2	–	–	–	–	–	–
I	μmol/kg	–	–	–	–	–	–	58	–	–	65	–	–	–
NH_4	″	<10	–	–	–	–	10300	12900	–	–	168	–	–	–
Reference		Von Damm, 1990	Von Damm, 1990; Palmer and Edmond,1989				Von Damm, 1990; Campbell and Edmond, 1989		Michard *et al.*, 1984	Bowers *et al.*, 1988; Palmer and Edmond, 1989			Von Damm *et al.*, 1997	

Table 7. (Contd.)

Region		East Pacific Rise				Juan de Fuca Ridge				
Hydrothermal system		17°25′ S	18°15′ S	Rapa Nui Vent Field, 21°34′ S, Brandon vent		Explorer Ridge	Endeavour segment, 47°57′ N			
No. in Fig. 15		6	7	8		9	10			
Vent		Nadir	Akorta	Brine	Vapor	Vent 12d	Hulk	Lobo	Peanut	North
No. in Table 6		13	14	15	16	17	18	19	20	21
component	unit									
Li	µmol/kg	183	690	488	270	472	439	379	160	438
Rb	″	2	6.8	–	–	32.9	38.0	33.6	–	–
Cs	nmol/kg	–	–	–	–	–	364	331	–	–
Be	″	–	–	–	–	–	–	–	–	–
Sr	µmol/kg	13.3	187	93.5	47.2	120	153	135	60	149
Ba	″	6.1	17.4	–	–	–	–	–	–	–
As	nmol/kg	–	–	–	–	–	–	–	–	–
Se	″	–	–	–	–	–	–	–	–	–
Br	µmol/kg	318	1320	890	490	–	–	–	–	–
B	″	–	–	465	429	–	698	755	723	725
Al	″	–	–	–	–	–	–	–	–	–
Co	nmol/kg	–	–	–	–	–	–	–	–	–
Cd	″	–	–	–	–	–	–	–	–	–
Ag	″	–	–	–	–	–	–	–	–	–
NH_4	µmol/kg	–	–	–	–	18.2	500	563	577	–
Reference		Charlou *et al.*, 1996		Von Damm *et al.*, 2003		Tunnicliffe *et al.*, 1986*[1]	Butterfield *et al.*, 1994			

Table 7. (Contd.)

Region		Juan de Fuca Ridge									
Hydrothermal system		Axial Volcano, ASHES field				Southern Juan de Fuca Ridge, Cleft segment, 45° N					Escanaba Trough, 41° N
No. in Fig. 15		11				12					13
Vent		Inferno	Hell	Crack	Virgin Mound	Plume	Vent1	Vent3	Pipe Organ	Monolith	
No. in Table 6		22	23	24	25	26	27	28	29	30	31
component	unit										
Li	µmol/kg	636	548	286	184	1718	1108	1808	2350	1570	1268
Rb	″	–	–	–	–	37.0	28.0	32.0	38.5	27.6	95–105
Cs	nmol/kg	–	–	–	–	–	–	–	248	217	7100–7700
Be	″	–	–	–	–	95	150	150	–	–	–
Sr	µmol/kg	192	–	81	46	312	230	267	348	236	209
Ba	″	26	–	–	6	–	–	–	8	90	–
As	nmol/kg	–	–	–	–	(650)	(260)	–	330	(370)	–
Se	″	–	–	–	–	–	–	–	–	–	–
Br	µmol/kg	956	856	401	250	1832	1580	1422	1880	1295	1179
B	″	590	–	–	450	496	–	–	524	482	1900–2160
Al	″	–	–	–	–	–	–	–	–	–	–
Co	nmol/kg	–	–	–	–	450	200	(180)	1430	57	–
Cd	″	–	–	–	–	470	910	(375)	550	700	–
Ag	″	–	–	–	–	48	120	–	40	88	–
Mo	″	–	–	–	–	31	6	–	–	30	–
Sb	″	–	–	–	–	11	18	–	7	15	–
I	µmol/kg	–	–	–	–	–	–	–	–	–	99
NH_4	″	–	–	–	–	–	–	–	–	–	5600
Tl	nmol/kg	–	–	–	–	(92)	(45)	(60)	74	(42)	110
Reference		Butterfield *et al*., 1990				Von Damm,1990; Trefry *et al*., 1994; Metz and Trefry, 2000			Butterfield, Massoth, 1994; Trefry *et al*., 1994; Metz and Trefry, 2000		Zierenberg *et al*., 1993

Table 7. (Contd.)

Region		Mid–Atlantic Ridge										
Hydrothermal system		Logatchev, 14°45′ N	MARK, 23° N		TAG, 26° N		Broken Spur, 29° N	Lost City, 30° N	Rainbow, 36°14′ N	Lucky Strike, 37°17′ N		Menez Gwen, 37°50″ N
No. in Fig. 15		14	15		16		17	18	19	20		21
Vent			1	Snake Pit	Black smokers	White smokers	4			Y3	Eiffel	Menez flank
No. in Table 6		32	33	34	35	36	37	38	39	41	42	43
component	unit											
Li	µmol/kg	245	843	1030	411	–	1035	–	340	357	286	274
Rb	″	28	10.0	11.9	9.1	9.4	13.6	–	37	39.1	22.7	25.6
Cs	nmol/kg	385	177	–	108	113	148	–	333	235	167	330
Be	″	–	38.5	–	–	–	–	–	–	–	–	–
Sr	µmol/kg	138	50	50	103	91	42.9	–	200	119	76	111
Ba	″	>4.5	>4.3	–	>19	–	>14.9	–	>67	9.4	42.4	22.6
As	nmol/kg		–	–	(70)	–	–	–				–
Br	µmol/kg	818	847	–	880–1045	–	749	–	1178	922	735	710
B	″		518	–	356	388	473	–	–	–	–	–
Al	″	4	5.3	–	–	–	–	–	2	11	–	6
Co	nmol/kg	–	–	–	(2570)	–	422	140–160	13000		–	–
Cd	″	63	–	–	66	–	145	–	130	79	–	12
Ag	″	11	–	–	51	–	–	–	47	25	–	17
Mo	″	1	–	–	5	–	–	–	2	84	–	–
Sb	″	–	–	–	3.9	–	–	–	3.1	6.3	–	4.7
Tl	nmol/kg	7	–	–	13	–	–	–	9	16	–	11
Ni	″	–	–	–	–	–	–	64–1260	3000	–	–	–
Reference		Douville *et al.*, 2002; Charlou *et al.*, 2002	Campbell *et al.*, 1988; Charlou *et al.*, 2002	Jean–Baptiste *et al.*, 1991	Von Damm, 1990; Edmond *et al.*, 1995; Metz and Trefry, 2000; Douville *et al.*, 2002; Charlou *et al.*, 2002		James *et al.*, 1995	Lein *et al.*, 2004*[2]	Douville *et al.*, 2002; Charlou *et al.*, 2002	Charlou *et al.*, 2000; Douville *et al.*, 2002		Charlou *et al.*, 2000

Table 7. (Contd.)

Region			Back-arc basins of the Pacific			Island arcs and volcanoes of the Pacific				
Hydrothermal system		Lau Basin, Vai Lili field	Manus basin	East Manus basin, Desmos field	East Manus basin, Pacmanus field	Okinawa Trough, Minami–Ensei Knoll	Okinawa Trough, JADE field	Okinawa Trough, Iheya North Knoll	Okinawa Trough, Suiyo Seamount	Hawaiian Islands, Loihi Volcano
No. in Fig. 15		23	25	26	27	29	31	32	33	34
Vent		VL–3	Vienna Woods							Pele's vents
No. in Table 6		45	47	48	49	51	53	54	55	56
component	unit									
Li	µmol/kg	623	1010	36	724	5400–5800	2500	800	–	46.1–57.6
Rb	″	68	11	3.5	75	–	–	–	–	3.19–4.81
Cs	nmol/kg	1560	–	–	–	–	–	–	–	–
Sr	µmol/kg	120	290	61	97	215–227	94	56–62	304	89–92.4
Ba	″	>39	17	0.9	3	53–56	59	10–12	100	0.61–0.88
As	nmol/kg	6	–	–	–	–	–	–	–	–
Br	µmol/kg	1140	1070	750	911	–	–	–	–	–
B	″	830	–	–	–	3700–4000	3400	–	–	–
Al	″	–	14	10	9.4	–	–	–	–	–
Co	nmol/kg	–	5.8	–	–	–	–	–	–	–
Cd	″	1500	8.9	–	–	–	–	–	–	–
Ag	″	–	6.5	–	–	–	–	–	–	–
Au	″	–	7.1	–	–	–	–	–	–	–
Bi	″	–	0.19	–	–	–	–	–	–	–
F	µmol/kg	–	31	135	337	–	–	–	–	–
NH_4	″	–	–	–	–	4600–4700	200–4900	1900–2600	<100	2.88–7.01
Ni	nmol/kg	–	–	–	–	–	–	–	–	39–80
Reference		Fouquet *et al.*, 1993	Lisitsin *et al.*, 1992; Bach *et al.*, 2003	Bach *et al.*, 2003*[3]	Bach *et al.*, 2003	Glasby, Notsu, 2003–				Sedwick *et al.*, 1992*[4]

Note: Data not extrapolated to the end-member: *[1] Mg = 22.37; *[2] Mg = 11.0–18.8; *[3] Mg = 49; and *[4] Mg = 49.5–51.1 mmol/kg.

The majority of hydrothermal solutions are weakly acidic (pH varies within 3–5 at 25°C). More acidic solutions with pH lower than 2.5 were found in hydrothermal sites in the Lau and East Manus back-arc basins (Table 6). Hydrothermal systems developing in the sedimentary cover usually produce solutions with pH higher than 5. Owing to the acidic pH values of hydrothermal solutions, the measurement of their alkalinity (*Alk*) usually yields negative values. All the high-temperature hydrothermal solutions of the ocean contain considerable amounts of hydrogen sulfide, from 1 to 12 mmol/kg (except for the Vai Lili vent field in the Lau back-arc basin, where H_2S was not reliably detected; Fouquet *et al.*, 1993).

A special problem is the behavior of Cl and Br in a number of hydrothermal systems. The chloride ion is one of the most conservative components of seawater, and no process in the oceanic water mass can significantly change its concentration. Elevated chlorinity was first discovered in a hydrothermal system at 13° N on the EPR (Michard *et al.*, 1984) and was actively debated in the literature. Michard *et al.* (1984) analyzed possible reasons for Cl accumulation including (a) water binding during hydration of crustal rocks, (b) extraction from basalts, (c) input of concentrated magma-derived fluids, and (d) boiling of hydrothermal solution in crustal levels. These authors concluded that solution boiling was the most plausible mechanism. Subsequent studies (Von Damm and Bischoff, 1987; Edmonds and Edmond, 1995; Edmond *et al.*, 1995) strengthened this conclusion by additional evidence, and this view is now universally accepted (this problem is considered in more detail in Chapter 6). The most convincing argument for the occurrence of fluid phase separation in the interiors of hydrothermal systems is the finding of vents with both high and low mineralization. The latter are products of vapor condensation. Such vents were found in hydrothermal systems at Axial Seamount and the Endeavor segment of the Juan de Fuca Ridge; in the North Fiji back-arc system; at 9°17′ N and 21°33′ S on the EPR; and Broken Spur, Lucky Strike, and Menez Gwen fields along the MAR (Table 6).

The concentrations of Br and Cl are strongly correlated and the Br/Cl ratio of hydrothermal solutions varies within a narrow range of $(1.44–1.68) \times 10^{-3}$ independent of chlorinity (Campbell and Edmond, 1989), which is similar to that of seawater (1.55×10^{-3}). These features are in agreement with the boiling mechanism. Br/Cl values as low as $(0.6–0.9) \times 10^{-3}$ were found during the investigation of very low-salinity high-temperature vents at 9°49′ N on the EPR (Oosting and Von Damm, 1996). The experimental test of existing hypotheses demonstrated that these variations are due to halite precipitation at almost complete boiling off of water and its subsequent dissolution under changing *P–T* conditions (Berndt and Seyfried, 1997).

The hydrogen and oxygen isotope composition of water was determined in several hydrothermal systems (Table 8). In all the objects studied, it was very similar to the isotopic composition of seawater, which is indicative of a marine water source in the oceanic hydrothermal systems (Welhan and Craig, 1983). According to calculations, a small positive shift of 1–2‰ relative to the local bottom water could be related to interaction with basalts (Bowers and Taylor, 1985). Strontium isotope ratios were determined in many hydrothermal system (Table 8) and lie between the isotopic characteristics of modern basalts (0.70280) and seawater (0.70917), which reflects strontium input from these two sources. The Pb isotope ratios of hydrothermal systems from 21° N EPR and the southern Juan de Fuca Ridge are identical to those of the host basalts, which are therefore regarded as a source of this element. A more radiogenic lead composition in solutions from the Guaymas Basin suggests Pb input from a sedimentary sequence (Chen *et al.*, 1986; Chen, 1987). The sulfur isotope composition of hydrogen sulfide was determined in solutions from more than a dozen hydrothermal systems (Table 8). The values obtained range from +0.5 to +7.8‰ reflecting a mixing of sulfur from magmatic (leached from basalts) and marine (reduction of sulfate sulfur of seawater by iron from basalts) sources (Bluth and Ohmoto, 1988). This topic is addressed in more detail in Chapter 5.

The data on dissolved gases show that the oceanic hydrothermal solutions are strongly enriched in hydrogen and methane, whose concentrations are very low in normal seawater (Table 9). The accumulation of ^3He was detected in hydrothermal solutions (Table 8): the $^3He/^4He$ ratios are higher than the atmospheric value (R_A) by a factor of 7–8 and approach the isotopic composition of helium from modern mid-ocean ridge basalts. According to the scarce measurements, the δD of dissolved hydrogen and methane corresponds to the temperature conditions within hydrothermal systems (Table 8). The abundances of dissolved gases are strongly affected by phase separation associated with boiling. The boiled off solutions show a high mineralization and low dissolved gas content (Evans *et al.*, 1988), whereas low-concentration hydrothermal solutions are usually enriched in gases, especially CO_2 and H_2S (Table 6).

Summarizing the available data on the chemical compositions of ore-forming solutions of oceanic hydrothermal systems, it should be pointed out that S, Fe, and Mn usually prevail over other ore components, and that most of the systems show elevated concentrations of Zn and minor Cu and Pb. With respect to S, Fe, and Zn content, these solutions correspond to reconstructions of ore-forming solutions of massive sulfide deposits (Kappel and Franklin, 1988). The data presented in Tables 6 and 7 indicate that the concentrations of ore elements in solutions from different systems are generally similar but not identical and may differ by more than an order of magnitude. Since ore element

Table 8. Isotopic characteristics of oceanic hydrothermal solutions

Region		Seawater	East Pacific Rise									
Hydrothermal system			21° N				Guaymas Basin		13° N			11° N
No. in Fig. 15			1				2		3			4
Vent			NBS	OBS	SW	HG	3	4		1	3	4
No. in Table 6			1	2	3	4	5	6	7	8	9	10
parameter	unit											
Sr	µmol/kg	87	97	81	83	65	253	226	175	188	189	86
$^{87}Sr/^{86}Sr$		0.7091	0.7030	0.7031	0.7033	0.7030	0.7052	0.7052	0.7041	0.70410	0.70405	0.70424
$\delta^{34}S(H_2S)$	‰ (CD)	–	3.4	1.3–1.5	2.7–5.5	2.3–3.2	–	–	–	–	–	–
$\delta D(H_2O)$	‰ (SMOW)	0	2.5	–	–	–	–	–	0.62…1.49	–	–	–
$\delta^{18}O(H_2O)$	‰ (SMOW)	0	1.6–2.0	–	–	–	–	–	0.39…0.66	–	–	–
$\delta^{11}B$	‰	39.5	32.7	32.2	31.5	30.0	–	23.2	–	–	–	–
$\delta^{13}C(CH_4)$	‰ (PDB)	–	–15.0	–17.4	–17.2	–	–	–	–19.5…–16.6	–	–	–
$\delta D(CH_4)$	‰ (SMOW)	–	–102; –126	–	–	–	–	–	–	–	–	–
$\delta D(H_2)$	‰ (SMOW)	–	–383; –396	–401	–373	–	–	–	–	–	–	–
$\delta^3He/^4He$	R_A		7.8	–	–	–	–	–	7.53	7.86	–	8.34
$\delta^{13}C(CO_2)$	‰ (PDB)	0	–7.0	–	–	–	–	–	–5.5…–4.1	–	–	–
Reference		Von Damm, 1990	Von Damm, 1990; Welhan and Craig, 1983				Von Damm, 1990		Michard *et al.*, 1984; Merlivat *et al.*, 1987	Palmer and Edmond, 1989; Kim *et al.*, 1984		

Table 8. (Contd.)

Region		East Pacific Rise						Juan de Fuca Ridge						
Hydrothermal system		9°17′ N, Vent "F"		17°25′ S	18°15′ S	Rapa Nui Vent Field, 21°34′ S, Brandon vent		Middle Valley	Axial Volcano, ASHES field		Cleft segment, 45° N			Escanaba Trough, 41° N
No. in Fig. 15		5		6	7	8			11		12			13
Vent		1991	1994	Nadir	Akorta	Brine	Vapor		Inferno	Virgin Mound	Plume	Vent1	Vent3	
No. in Table 6		11	12	13	14	15	16		22	25	26	27	28	31
parameter	unit													
Sr	µmol/kg	–	–	13.3	42.8	93.5	47.2	–	–	–	336	–	274	209
$^{87}Sr/^{86}Sr$		–	–	–	–			–	–	–	0.70370	–	0.70358	0.70988
$\delta^{34}S(H_2S)$	‰ (CD)	–	–	–	–	4.2	4.8	–	–	–	4.2… 7.3	4.0… 6.4	7.2… 7.4	7.8
$\delta D(H_2O)$	‰ (SMOW)	1.4	–0.1	–	–	2.9	1.7	–	–	–	–2.5… 0.5	–2… 0.5	–1.0… 0.5	–0.7
$\delta^{18}O(H_2O)$	‰ (SMOW)	1.46	1.54	0.53	0.5–0.6	0.82	0.77	–	0.8… 1.1	0.7… 0.9	0.65	0.6	0.8	0.43
$\delta^{11}B$	‰	–	–	–	–	–	–	–	(34.7)	–	34.2	–	–	10.1
$\delta^{13}C(CH_4)$	‰ (PDB)	–	–	–23.9	–22.0	–	–	–61.5… –52.2	–	–	–20.8	–18.2	–	–
$\delta D(CH_4)$	‰ (SMOW)	–	–	–	–	–	–	–153… –117.6	–	–	–	–	–	–
$\delta D(H_2)$	‰ (SMOW)	–	–	–	–	–	–	–	–	–	–	–	–	–
$\delta^3He/^4He$	R_A	–	–	8.34	8.3	–	–	–	–	–	–	–	–	–
$\delta^{13}C(CO_2)$	‰ (PDB)	–	–	–	–7.9	–	–	–33.0… –10.6	–	–	–4.4	–4.7	–	–
Reference		Von Damm *et al.*, 1997		Charlou *et al.*, 1996; Jean–Baptiste *et al.*, 1997, 1997a		Von Damm *et al.*, 2003		Taylor, 1990	Massoth *et al.*, 1989		Von Damm,1990; Palmer and Edmond, 1989; Shanks and Seyfried, 1987; Evans *et al.*, 1988			Zierenberg *et al.*, 1993; Palmer and Edmond, 1989

Table 8. (Contd.)

Region		Mid–Atlantic Ridge										
Hydrothermal system		Logatchev, 14°45′ N	MARK, 23° N		TAG, 26° N		Broken Spur, 29° N	Lost City, 30° N	Rainbow, 36°14′ N	Lucky Strike, 37°17′ N		Menez Gwen, 37°50′ N
No. in Fig. 15		14	15		16		17	18	19	20		21
Vent			1	Snake Pit	Black smokers	White smokers	4			Y3	Eiffel	Fontaine
No. in Table 6		32	33	34	35	36	37	38	39	41	42	
parameter	unit											
Sr	μmol/kg	138	50	–	103	91	42.9	–	42.9–48.0	119	76	111
$^{87}Sr/^{86}Sr$		–	0.7028	–	0.7038	0.7046	0.70347	–	–	–	–	–
$\delta^{34}S(H_2S)$	‰ (CD)	2.2–2.8	4.9	4.9–5.0	6.6–7.5; 8.6	–	0.5–1.0	–	2.4–3.1	–	–	–
$\delta D(H_2O)$	‰ (SMOW)	–	3.1	–	3.0	–	–	–	–	–	–	–
$\delta^{18}O(H_2O)$	‰ (SMOW)	–	1.9; 2.37	2.30	1.57	–	–	–	–	–	–	–
$\delta^{11}B$	‰	–	26.8	–	30.9	35	25	–	–	–	–	–
$\delta^{13}C(CH_4)$	‰ (PDB)	–14.6… –13.8	–	–	–8.0… –9.5	–	–18… –19	–17… –17.6	–13.4… –13.0	–13.0	–12.7	–19.6
		–13.6			–14.6				–15.8			
$\delta D(CH_4)$	‰ (SMOW)	–	–	–	–	–	–	–	–	–	–	–
$\delta D(H_2)$	‰ (SMOW)	–	–	–	–	–	–	–	–	–	–	–
$\delta^3He/^4He$	R_A	–	7.9–8.6	8.4	7.5	–	–	–	–	8.13	8.13	8.65
$\delta^{13}C(CO_2)$	‰ (PDB)	–4.3… +1	–	–9.0	–8.4… –10.0	–	–5.6	–	–4… +1	–7.2	–10.6	–9.1
					–4.3				–3.15			
Reference		Lein *et al.*, 2000; Charlou *et al.*, 2002	Campbell *et al.*, 1988; Gamo *et al.*, 2001	Jean–Baptiste *et al.*, 1991, 1997; Lein *et al.*, 2004	Edmond *et al.*, 1995; Jean–Baptiste *et al.*, 1997; Knott *et al.*, 1998; Lein, 2001; Gamo *et al.*, 2001; Charlou *et al.*, 2002		James *et al.*, 1995; Charlou *et al.*, 2002; Lein *et al.*, 2004	Lein *et al.*, 2004	Lein *et al.*, 2000; Charlou *et al.*, 2002	Jean–Baptiste *et al.*, 1998; Charlou *et al.*, 2000		

Table 8. (Contd.)

Region		Indian Ocean	Back-arc basins of the Pacific			Island arcs and volcanoes of the Pacific				
Hydrothermal system		Rodrigues Triple Junction, Kairei Field	Lau Basin, Vai Lili field	Mariana Trough	East Manus basin, Desmos field	Okinawa Trough, Minami–Ensei Knoll	Okinawa Trough, CLAM field	Okinawa Trough, JADE field	Okinawa Trough, Suiyo Seamount	Hawaiian Islands, Loihi Volcano
No. in Fig. 15		22	23		26	29	30	31	33	34
Vent			VL–3							
No. in Table 6		44	45		48	51	52	53	55	56
parameter	unit									
Sr	µmol/kg	77	120	78	–	215–227	–	94	310	100
$^{87}Sr/^{86}Sr$		0.7041	0.7044	0.70354	–	0.7100	–	0.7089	–	0.703
$\delta^{34}S(H_2S)$	‰ (CD)	6.9	–	–	–5.6	–	1.4	7.4	–	–
$\delta D(H_2O)$	‰ (SMOW)	4.8	–	–	–8.1	–	–	–	–	–
$\delta^{18}O(H_2O)$	‰ (SMOW)	1.9	0.85	–	0.3	–	–	–	–	–
$\delta^{11}B$	‰	–	26	–	–	–	–	–	–	–
$\delta^{13}C(CH_4)$	‰ (PDB)	–8.7	–	–	–	–	–41.2	–40.7…–36.1	–8.5	–
$\delta D(CH_4)$	‰ (SMOW)	–	–	–	–	–	–	–	–	–
$\delta D(H_2)$	‰ (SMOW)	–	–	–	–	–	–	–	–	–
$\delta^3He/^4He$	R_A	7.9	–	7.7–8.5	–	7.0–7.5	3.7–3.8	6.1–6.9	8.1	–
$\delta^{13}C(CO_2)$	‰ (PDB)	–6.2	–	–4.33	–	–4.0…–5.3	–3.8…–3.6	–5.0…–4.7	–1	–
Reference		Gamo *et al.*, 2001	Fouquet *et al.*, 1993; Jean–Baptiste *et al.*, 1997	Tsunogai *et al.*, 1994; Palmer and Edmond, 1989	Gamo *et al.*, 1997	Gamo *et al.*, 1991; Ishibashi *et al.*, 1995; Glasby and Notsu, 2003			Tsunogai *et al.*, 1994	Palmer and Edmond, 1989

Note: R_A is the atmospheric helium isotope ratio, 1.4×10^{-6}.

Table 9. Concentrations of dissolved gases in oceanic hydrothermal solutions

Region		East Pacific Rise									
Hydrothermal system		21° N			13° N		11° N	9°17′ N		17°25′ S	18°15′ S
No. in Fig. 15		1			3		4	5		6	7
Vent		NGS	OBS	SW				Vent “F”, 1991	Vent “F”, 1994	Nadir	Akorta
No. in Table 6		1	2	3	7	8–9	10	11	12	13	14
parameter	unit										
He	10^{-6} cm^3/kg	17.3	15.8	9.10	30–45	27–50	20–50	–	–	24	18
CH_4	cm^3/kg	1.24	0.548	0.411	0.62–1.24	1.15	1.5–2.6	–	–	7.5 µmol/kg	133 µmol/kg
H_2	cm^3/kg	30.5	37.5	9.9	–	3.2	10–11.2	1.8	0.30	150 µmol/kg	40 µmol/kg
Reference		Welhan and Craig, 1983			Merlivat *et al.*, 1987	Kim *et al.*, 1984		Von Damm *et al.*, 1997		Charlou *et al.*, 1996; Jean–Baptiste *et al.*, 1997a	

Region		Juan de Fuca Ridge					
Hydrothermal system		Endeavour segment, 47°57′ N	Axial Volcano, ASHES field			Cleft segment, 45° N	
No. in Fig. 15		10	11			12	
Vent		Lobo	Inferno	Crack	Virgin Mound	Plume	Vent1
No. in Table 6		19	22	24	25	26	27
parameter	unit						
He	µmol/kg	–	2.45	8.44	11.2	–	–
CH_4	″	–	25	–	–	84	118
H_2	″	166	–	–	–	351	527
C_2H_6	″	–	–	–	–	0.2	–
C_3H_8	″	–	–	–	–	0.049	–
Reference		Tivey, 1995	Butterfield *et al.*, 1990			Evans *et al.*, 1988	

Table 9. (Contd.)

Region		Mid–Atlantic Ridge								
Hydrothermal system		Logatchev, 14°45′ N	MARK, 23° N	TAG, 26° N	Broken Spur, 29° N	Lost City, 30° N	Rainbow, 36°14′ N	Lucky Strike, 37°17′ N		Menez Gwen, 37°50′ N
No. in Fig. 15		14	15	16	17	18	19	20		21
Vent			Snake Pit					Y3	Eiffel	Fontaine
No. in Table 6		32	34	35	37	38	39	41	42	
parameter	unit									
He	μmol/kg	–	2.0	–	–	–	–	12–26 (10^{-6} cm^3/kg)		–
CH_4	″	2100	62	124–147	65–130	130–280	2200	400	680	2150
						300–1200	2500			
H_2	″	12000	190–480	150–370	430–1030	250–430	13000	76.7	122	44.2
						930	16000			
C_2H_6	″	–	–	–	–	–	1.097	0.065	0.159	808
C_3H_8	″	–	–	–	–	–	0.048	–	0.009	0.018
Reference		Charlou *et al*., 2002	Jean–Baptiste *et al*., 1991; Charlou *et al*., 2002	Lein *et al*, 2000; Charlou *et al*., 2002		Kelley *et al*., 2001*[1]; Lein *et al*., 2004*[2]	Lein *et al*, 2000; Charlou *et al*., 2002	Jean–Baptiste *et al*., 1998; Charlou *et al*., 2000		

Region		Indian Ocean	Back-arc basins, island arcs, and volcanoes of the Pacific					
Hydrothermal system		Rodrigues Triple Junction, Kairei Field	Lau Basin, Vai Lili field	Okinawa Trough, Minami–Ensei Knoll	Okinawa Trough, CLAM field	Okinawa Trough, JADE field	Okinawa Trough, Suiyo Seamount	Hawaiian Islands, Loihi Volcano
No. in Fig. 15		22	23	29	30	28	33	34
Vent			VL–3					Pele's vents
No. in Table 6		44	45	51	52	53	55	56
parameter	unit							
He	μmol/kg	–	–	0.1–0.7	0.1	0.3–0.9	0.3; 0.6	–
CH_4	″	82	3–5	2600–7000	3100–4900	2500–7100	108; 140	7.254
H_2	″	–	25–34	12–13	110–150	10–50	25	–
Reference		Gamo *et al*., 2001	Fouquet *et al*., 1993	Glasby and Notsu, 2003	Glasby and Notsu, 2003*[3]	Ishibashi *et al*., 1995	Tsunogai *et al*., 1994; Glasby and Notsu, 2003	Karl *et al*., 1988*[4]

Note: Data not extrapolated to the end-member: *[1] Mg = 9–19; *[2] Mg = 11.0–18.8; *[3] Mg = 33–53; and *[4] Mg = 50.3 mmol/kg.

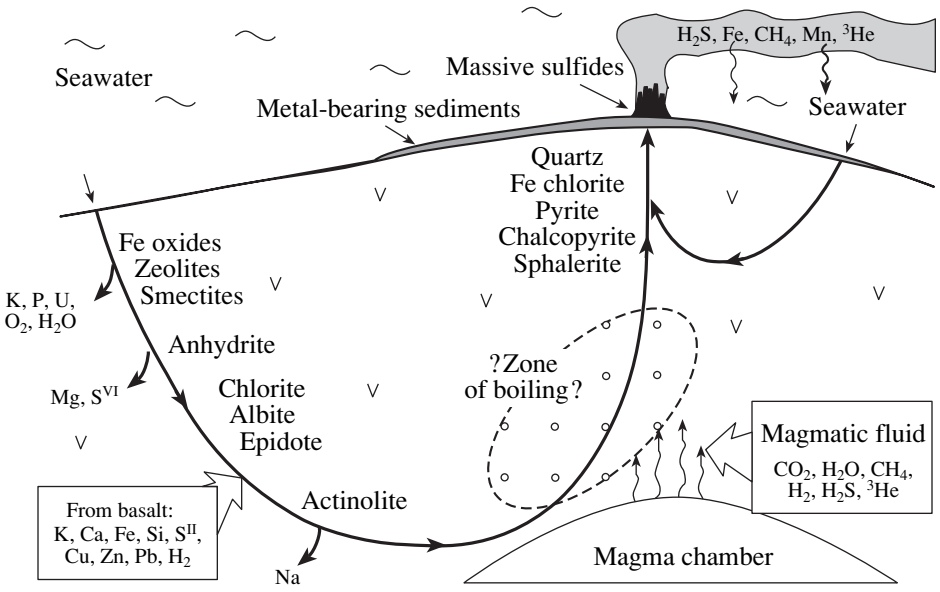

Fig. 16. Generalized relationships of geochemical processes in the hydrothermal system of a mid-ocean ridge.

abundances depend on many factors, the empirical description of such dependencies is not straightforward. The nature of many important chemical features of solutions remains controversial. Among them are the prevalence of Zn over Cu in the hydrothermal systems of 21° N EPR and the Juan de Fuca Ridge; Cu over Zn in the solutions of the TAG field; S over Fe in the 21° N EPR and some other systems; and Fe over S in solutions from TAG, 45° N on the Juan de Fuca Ridge, and the Explorer Ridge. These relationships are very important, because they create a mineralogical and geochemical portrait of the ores.

A comprehensive review of all the characteristics of oceanic hydrothermal processes is beyond the scope of this paper. Such very important geochemical problems as the role of hydrothermal processes in the mass fluxes and balances in the ocean, the activity of specific biological populations of hydrothermal systems, and some other problems were not considered. These complex problems, as well as the strategy and methods of prospecting for hydrothermal sulfide ores on the ocean floor, are not addressed in this work. A detailed discussion of these issues can be found in some general studies (e.g., Lisitsin *et al.*, 1990; *Hydrothermal Sulfide…*, 1992).

3.2. Logical Scheme of the Process and Its Experimental Substantiation

A geological and geochemical model for the hydrothermal process in the oceanic crust was developed in the 1970s and early 1980s. Its early variants were based on the results of investigations of ophiolitic complexes and metamorphic rocks recovered by deep-sea dredging and drilling, geophysical data, experimental simulation of seawater–basalt interactions, numerical models of convection systems, etc. (Spooner *et al.*, 1977; Humphris and Thompson, 1978; Wolery and Sleep, 1976; Lister, 1980; Rosenbauer and Bischoff, 1983). After the discovery and reconnaissance investigation of black smokers, the geochemical scheme of the process was revised and constrained by Edmond *et al.* (1982). Their results were repeatedly reproduced in the subsequent literature. Taking into account the most recent data, geochemical processes in an oceanic hydrothermal system are shown in a simplified form in Fig. 16.

Hydrothermal systems at mid-ocean ridges are convective systems with an endogenous heat source (magma body) and a fluid phase strongly dominated by the exogenous component (seawater). Seawater percolates through fractures in the tholeiitic basalts of the oceanic crust, is gradually heated, and reacts with the country rocks. The basalts are replaced by secondary mineral assemblages of smectite, chlorite, and propylite facies with increasing temperature. Some seawater components, including Mg, SO_4, K, U, and dissolved oxygen, are fixed in the solid phase. Simultaneously many components, including the ore elements Fe, S^{II}, Cu, Zn, and Pb, are extracted from the basalts. The most extensive water–rock interaction occurs in the hottest part (focus) of the hydrothermal system near contact with a magma chamber.

Magma-derived hydrothermal solutions released from the crystallizing melt may be introduced into the flow of hydrothermal solution in this zone. An area of boiling and separation of water and vapor phases may be formed near the magma body and in the lower part of the upwelling limb.

The movement of a hydrothermal solution in the upwelling limb of a convection system is rapid and

nearly adiabatic. Cold seawater can penetrate laterally into the upwelling flow, which results in the subsurface mixing and cooling of the hydrothermal solution. The hydrothermal solution emanates into the water column either as a localized jet (smoker) and/or by dispersed discharge typical of the flanks of large sulfide mounds (for instance, in the Mid-Atlantic and Juan de Fuca Ridge). Solid phases, including ore minerals, are precipitated from the hydrothermal solution owing to an abrupt temperature decrease and a change in composition due to mixing with bottom water. During active discharge, a considerable portion of ore substances is expelled into the water mass, forming hydrothermal plumes.

Sulfide edifices growing on the seafloor at hydrothermal vent sites show zonal internal structures and may have complex growth histories. The character of ore deposition changes during the growth of sulfide edifices (Krasnov *et al.*, 1988), because the role of slow percolation of hydrothermal solutions through the ore body increases gradually. The ore components of the solution are almost completely deposited within the large sulfide body, and the extent of metasomatic replacement of previously formed phases increases dramatically.

Several points of this logical scheme have been widely debated in the literature. Some important questions are not yet solved. Since the logical scheme is important for the construction of the thermodynamic model of the process, these problems must be analyzed in more detail in order to obtain comprehensively substantiated conclusions.

Hydrodynamic structure of circulation and heat and mass transfer in a convection cell. The existence of convective heat transfer in the oceanic crust was predicted from the results of geophysical surveys (Lister, 1972). Direct evidence for the occurrence of convection was obtained by deep-sea drilling. Water movement was documented in a number of boreholes near modern spreading centers. For instance, hot water inflow and a sharp increase in temperature at the borehole bottom were observed in Hole 482C (DSDP Leg 65) after the completion of drilling operations (Duennebier and Blackington, 1983). Seawater uptake at a rate of 6–7 m^3/h was revealed by hydrogeological measurements in comprehensively studied Hole 504B in the Costa Rica rift. The pressure deficit relative to the hydrostatic level was up to 10 atm (Becker *et al.*, 1983), i.e., this borehole penetrated the region of the descending flow of a convection cell.

There is little direct evidence on the distribution of temperature within hydrothermal systems. Only output temperatures were measured, and temperature at the base of the upwelling limb (focus of the system), which is probably the maximum in the system, can be reconstructed. For a typical measured value of 350–365°C (Campbell *et al.*, 1988a, 1988b; Von Damm, 1990) and a correction of 20–30°C for adiabatic cooling during ascent (Bischoff and Pitzer, 1985), the maximum temperature is 370–395°C.

Methods of mathematical modeling were widely used for the investigation of the character of water circulation in the oceanic crust. Early models were simplified and often considered as only one-dimensional problems (Lowell, 1975; Ribando *et al.*, 1976). The problem of heat transfer from rocks to solution has been explored on the basis of such models. It has long been established by observations of submarine eruptions that the duration of direct contact between seawater and melt must be very short and is of some importance only during magma intrusion and eruption, which can be exemplified by the observations of April 1991 at 9° N on the EPR (Von Damm *et al.*, 1995). Hydrothermal solutions are heated during contact with hot rocks. Of special importance for the understanding of this process was the cracking front hypothesis of Lister (1974, 1980). This hypothesis is based on the fact that cooling of a hot rock causes volume reduction and formation of a system of contraction fractures, which serve as pathways for water penetration into the hot rock body. The convective circulation of water enhances cooling, which results in the propagation of the cracking front, i.e., this process is self-supporting. It is limited only by the plasticity of hot rocks under lithostatic pressure. Under oceanic crust conditions, the position of the cracking front and, correspondingly, water penetration corresponds to the 400–450°C isotherm. However, the Lister model considered only heat removal from a solid rock and therefore overestimated the rate of cracking front propagation. This implied a very short-term existence of magma chambers even beneath fast-spreading ridges, which was in conflict with geological observations (Sleep, 1983). This controversy was resolved by Cann and Strens (1982). They argued that, in addition to water circulation in solid rocks, the thermal model of the process must take into account melt convection within the magma chamber. Owing to convective mixing within the chamber accompanying crystallization differentiation, heat is continuously conveyed to the roof and the chamber is solidified mainly at the expense of the cumulus pile (corresponding to the layered intrusive series of ophiolites). The roof of the chamber grows mainly by the freezing of melt against it, which produces a layer of isotropic gabbro. Cann *et al.* (1985/1986) demonstrated that the critical parameter of a thermal model is the thickness of the water-impermeable layer of hot plastic rocks above the chamber roof, where heat is only transferred by conduction. In order to explain the observed heat flux values, this layer has to be a few tens of meters thick. The position of the cracking front in the Cann model is relatively stable as long as melt is retained within the chamber. After the complete solidification of magma, the cracking front begins to move rapidly downward and hydrothermal convection ceases almost immediately. The Cann model implies that the rocks directly above the roof of the magma chamber must experience prolonged and

extensive hydrothermal alteration in a stable thermal regime. This is consistent with the data on the character and distribution of metasomatic alterations in the modern oceanic crust and ancient ophiolitic complexes.

The hydrodynamic structure of convective circulation of hydrothermal solutions near a magma chamber was elucidated by the calculation of two-dimensional models. Various authors examined variations in the structure of circulation under the influence of such factors as magma chamber geometry (Fehn and Cathles, 1979; Brikovski and Norton, 1989), nonuniform permeability of crustal rocks (Fisher and Narasimhan, 1991; Tutubalin *et al.*, 1995; Malkovskii and Pek, 1997; Tutubalin and Grichuk, 1997a, 1997b), formation of the zones of boiling and supercritical fluid states (Brikovski and Norton, 1989), etc. The general conclusion from this work is that the most intense flow in the convection cell is established near the contact with the magma chamber and almost parallel to its roof. Thus, the isotherms are concentrated near the magma chamber. At any given time, the zone of high-temperature water–rock interactions is limited to a relatively thin layer along the roof of the magma chamber and the vertical channel (Brikovski and Norton, 1989; Tutubalin *et al.*, 1995).

The geophysical data on the depth of magma chambers in the axial zones of mid-ocean ridges allow estimation of the depth of water circulation. The convection cells of axial hydrothermal systems have a characteristic vertical dimension of 1.5–3.0 km. According to the results of hydrodynamic modeling, their lateral extension is about 6 km (Brikovski and Norton, 1989).

After the discovery of significant variations in the salinity of oceanic hydrothermal solutions, Bischoff and Rosenbauer (1989) proposed an alternative model of two-layer convection in order to explain these observations and the accompanying geochemical effects. According to their model, the lower convection cell is filled with boiling brines, and the upper layer is a traditional cell recharged by seawater. Heat transfer between the cells occurs mainly by conduction, and there is almost no accompanying mass transfer. The authors assigned the formation of the lower brine cell to the initial phase of hydrothermal system development, during the intrusion of magmatic melt, which was probably accompanied by a large-scale vapor ejection. However, the investigation of a hydrothermal system at 9°47′ N on the EPR (Von Damm, 2000), which was affected by a magma body, did not confirm the existence of a long-lived brine reservoir within the oceanic crust. Hydrodynamic simulation demonstrated that a two-layer fluid system is unstable (Schoofs and Hansen, 2000).

Water–rock interaction and extent of metal extraction from basalts: natural and experimental data. The first high-temperature experiments on seawater–basalt interaction were reported several years before the discovery of seafloor hydrothermal systems (Bischoff and Dickson, 1975; Hajash, 1975; Seyfried and Bischoff, 1977; Mottl and Holland, 1978). The results of these investigations were important for an understanding of the geochemistry of processes occurring in the oceanic crust. It was found that during this interaction water becomes depleted in Mg and SO_4 and enriched in Si, Ca, K, Ba, Li, B, H_2S, Fe, and Mn, and the resulting solution shows acidic pH values (Seyfried and Bischoff, 1977; Mottl and Holland, 1978; Mottl *et al.*, 1979; Seyfried *et al.*, 1984). Anhydrite precipitates from the solution. Smectite, mixed-layer smectite/chlorite, and high-temperature actinolite, talc, albite, wairakite, magnetite, pyrite, and chalcopyrite develop after basalts. It was shown that the character of interaction strongly depends on the water/rock ratio (*W*/*R*), and there is a boundary *W*/*R* value of 50 ± 5 between the rock-dominated and water-dominated conditions of interaction (Mottl and Seyfried, 1980).

The experimental data were, in general, supported by the examination of natural objects, which was an important argument in favor of the model of seawater convection in the oceanic crust. On the other hand, the experiments exhibited some differences from the natural process, which were discussed in detail by Rosenbauer and Bischoff (1983). In particular, early experiments yielded considerable amounts of sulfide sulfur and low concentrations of chalcophile elements, which were not consistent with the natural prototypes. This effect appeared to be related to the experimental procedure: the seawater–basalt reaction in an autoclave differs from that in natural flow-through systems, where sulfate sulfur is fixed in anhydrite at the beginning of the downwelling limb of the convection system (see below). Therefore, modified seawater, a synthetic composition differing from seawater in the absence of sulfate species, has been used since 1980s as a starting solution in experiments.

Although very long experiments were conducted by Mottl *et al.* (1979), Seyfried and Bischoff (1979) (up to 1.5 y), and Janecky and Seyfried (1986) (almost two years), the natural assemblages of metasomatic minerals characteristic of altered basaltoids have not been completely reproduced. The most important difference is the lack of chlorite and epidote, which are the major minerals of metabasalts, in the experimental products. The reason is probably related to the very sluggish transformations of metastable smectites and mixed-layer smectite/chlorite that formed rapidly during the early stages of these experiments (Mottl, 1983). Even in the longest experiments, the system did not reach equilibrium and the composition of solutions continued to change.

When the general characteristics of seawater–basalt interactions were established, the experimenters focused their attention on the determination of conditions providing the observed metal concentrations in natural solutions and the estimation of reactions buffering solution compositions. Of crucial importance for the solution of these problems was a study by Seyfried

Table 10. Concentrations of ore metals and other components in hydrothermal solutions (H_2S, Fe, Mn, and SiO_2 are in mmol/kg; and Zn and Cu are in μmol/kg) from experiments under near critical conditions (Seyfried and Janecky, 1985)

Initial solid phase	Temperature, °C	Pressure, bar	Water/Rock	Duration, h	$pH_{25°C}$	H_2S	Fe	Mn	Zn	Cu	SiO_2
Basalt	350	400	1.0	212	4.8	6.76	0.192	0.125	16	0.6	14.1
″	″	″	″	626	4.4	6.17	0.247	0.167	19	0.9	19.67
Basalt	375	400	1.0	272	3.8	11.47	1.754	0.451	37	2.5	19.50
″	″	″	″	626	3.7	12.94	2.328	0.688	92	2.2	20.67
Basalt	400	400	1.0	579	3.3	17.68	8.684	1.202	121	22	22.17
″	″	″	″	2211	3.6	8.97	8.326	1.256	43	7	20.33
Basalt	425	400	0.5	32	2.8	30	25.07	3.677	45	0.8	14.3
″	″	″	″	846	2.7	30	26.95	4.40	32	0.6	11.19
″	″	″	″	2400	2.7	14	30.12	4.091	3.5	0.6	11.36
Diabase	425	400	0.5	55	3.2	21	12.75	3.277	25	2.5	13.67
″	″	″	″	317	2.9	18	15.28	3.623	23	0.5	11.92
″	″	″	″	1854	3.4	1.8	18.26	4.187	58	1.4	12.16
Diabase	400	400	1.0	821	3.9	5.94	1.369	0.514	6.1	1.5	14.62
″	″	″	″	1349	3.8	4.62	1.531	0.661	34	10	18.33
Basaltic glass	400	375	1.0	489	3.7	10.88	2.468	0.638	14	0.5	13.32
″	″	″	″	1350	3.5	11.76	2.613	0.655	–	1.6	13.18

and Janecky (1985), who demonstrated a strong pressure effect on the concentrations of metals in solution under near critical conditions. These authors obtained metal concentrations corresponding to those observed in oceanic hydrothermal systems (Table 10). Currently all major characteristics of the chemical composition of oceanic hydrothermal solutions have been experimentally reproduced.

In addition to basalts, seawater alteration was experimentally simulated with other rock types: peridotites (Seyfried and Dibble, 1980; Hajach and Chandler, 1981; Janecky and Seyfried, 1986), rhyolites and andesites (Dickson, 1977; Shiraki *et al.*, 1987), and sedimentary rocks (Bischoff *et al.*, 1981; Thornton and Seyfried, 1985, 1987).

It is important to note before further discussion that both the experimental and natural data indicate that all the rock-forming minerals of tholeiitic basalts (pyroxenes, plagioclases, and olivine phenocrysts) readily react with solution to produce secondary phases. Samples of metasomatized basalts (i.e., those with altered K, Na, Ca, and Mg contents) do not display a distinct zoning, which is characteristic of metasomatic rocks associating with ore veins.

Little is known about the mineral forms of ore element occurrence in fresh and hydrothermally altered basalts (Nesterenko and Al'mukhamedov, 1973; Heinrichs *et al.*, 1980; Bideau *et al.*, 1985; Doe, 1994; *Hydrothermal Sulfide…*, 1992). Both in fresh and altered basalts, copper usually forms its own mineral phase, chalcopyrite. In fresh basalts, lead usually substitutes for potassium in potassium feldspar. During metasomatic changes, lead is fixed in galena. The speciation of Zn in fresh basalts is dual: it occurs in approximately equal amounts in orthosilicates substituting for Mg and magnetite substituting for Fe. In altered basalts zinc probably forms its own phase, sphalerite, and can be incorporated in Mg-bearing hydrous silicates (chlorite and actinolite). Although the available data are fragmentary, they allow us to make an important conclusion concerning the model: ore elements do not occur in alteration-resistant mineral phases but do react with metasomatic solutions in approximately the same way as major components. This greatly simplifies the model and allows us to consider the initial rock as a homogeneous reactive material.

Anhydrite deposition. Experiments with seawater showed that its heating results in extensive anhydrite precipitation. This observation raised the question of the relation of these experiments and the geochemical scheme constructed on their basis to the natural process, because anhydrite was not found in metamorphosed basalts dredged from the ocean floor or recovered from shallow boreholes during the early stages of deep-sea drilling. Seyfried and Bischoff (1979) and other authors explained this controversy by anhydrite dissolution in cold water during the attenuation of convection in the hydrothermal system. This explanation is in agreement with the available data on a negative temperature dependency of anhydrite solubility in water. As a result, seawater is undersaturated in anhydrite at

temperatures below 150°C. When deep-sea boreholes penetrated the hot zones of active hydrothermal systems, vein anhydrite was systematically detected in drill cores (e.g., Alt *et al.*, 1983, 1989). Drilling in the TAG hydrothermal field revealed a surprising amount of anhydrite in the interior part of the edifice and the upper part of the stockwork zone. Mills *et al.* (1998) explained this fact by anhydrite formation through subsurface mixing with cold seawater.

Secondary mineral associations. Based on the analysis of experimental data and results of studies of natural objects, Mottl (1983) proposed a general scheme of secondary mineral assemblages formed by seawater–basalt interaction. The main parameter of this scheme is the *W*/*R* ratio, which is a measure of the metasomatic effect produced by seawater (mainly Mg introduction). High ratios (typical of the low-temperature part of the convection system) give rise to the quartz + smectites + chlorite ± talc assemblage, while Ca, Na, K, Mn, Cu, Zn, and Ba are completely removed from the rock, and the solution is weakly acidic to neutral. The excess of rock produces the chlorite + albite + epidote + actinolite + sphene ± quartz assemblage, which controls the major element composition of the solution. Conditions favorable for such an excess exist in the high-temperature part of the system.

Rock/water ratio. A fundamental parameter of the model of a flow-through hydrothermal system is the proportion of the rates of solution–rock interaction and mass transfer. In steady-state experiments, this factor is monitored by prescribing the proportion of basalt and solution. The influence of this parameter on the experimental results was described above. In the MSFR method for the model of an extended nonisothermal system with fissure percolation (Section 2.2), the similarity criterion is the ratio of effectively reacting masses of fresh water and solution summed over the flow line of solution, $\Sigma R/W$. This parameter was estimated by two methods in active oceanic hydrothermal systems: from the concentrations of mobile elements and from the Sr isotope ratios of emanating hydrothermal solutions.

The former method was proposed by Von Damm *et al.* (1985) and is based on the fact that some elements are almost completely extracted into solution during seawater–basalt interaction. Given their initial content in water and basalt and enrichment in the black-smoker solution, the amount of fresh basalt that reacted with the given solution portion can be calculated. If the element considered is not completely transported into solution, the value may be underestimated. Consequently, when $\Sigma R/W$ is determined from several elements, the maximum value should be used. Table 11 shows the data obtained by Von Damm *et al.* (1985) for the hydrothermal systems of 21° N EPR. It can be clearly seen that the alkali elements Li, K, and Rb, as well as H_2S, which are highly mobile in high-temperature hydrothermal systems, yield identical $\Sigma R/W$ estimates.

Table 11. Water/rock ratios in modern hydrothermal systems obtained from the investigation of the composition of smoker solutions (Von Damm *et al.*, 1985)

Indicator component	Water/rock	Rock/water
K	1.7–2.0	0.50–0.59
Li	1.1–1.8	0.56–0.9
Rb	0.27–1.9	0.53–3.7
H_2S	1.7–2.1	0.48–0.59

Note: The water/rock ratio is commonly used in the geochemical literature, and the inverse ratio is employed in thermodynamic models. In order to facilitate comparisons, the table presents both parameters.

The second method makes use of the fact that seawater and mid-ocean ridge basalts are significantly different in $^{87}Sr/^{86}Sr$ (0.70906 and 0.70280, respectively, according to Faure, 1986), and oceanic hydrothermal solutions show transitional characteristics. As there is no Sr isotope fractionation, and the concentrations of Sr in seawater and fresh tholeiitic basalts are relatively stable, the amount of rock reacting with the given solution portion can be calculated from the isotopic mass balance. This approach yields an approximate estimate, because it ignores the effect of Rayleigh exhaustion related to Sr partitioning from the moving solution into secondary minerals. Nonetheless, strontium isotope systematics and alkali element relationships yield similar estimates. Table 12 summarizes $\Sigma R/W$ estimates for oceanic hydrothermal systems. It can be seen that the oceanic hydrothermal systems show similar $\Sigma R/W$ values ranging within 0.5–2.0. The values determined on the basis of solution composition are the effective rock/water ratios integrated along the flow line of solution that are needed for construction of equilibrium dynamic models.

It is obvious from general considerations that the $\Sigma R/W$ values of hydrothermal systems may vary with time, but the period of observation of real oceanic objects is still very short, and no changes in solution composition have been yet reported (Campbell *et al.*, 1988a; Edmond *et al.*, 1995) (except for the cases of volcanic events discussed in chapters 6 and 7).

The *R*/*W* values of ancient analogues were estimated using the strontium and oxygen isotopic compositions of metasomatized rocks, and the balance relationships for their interaction with seawater. Such an estimate is integrated over time and corresponds to a given point. Hence, the values obtained for ancient and modern systems from the analyses of different materials cannot be directly correlated. As can be seen in Table 12, the *R*/*W* values of ancient massive sulfide deposits are systematically lower than those of oceanic hydrothermal systems. This difference probably reflects the longer duration of hydrothermal processes in the ancient objects as compared with the modern oceanic systems.

Table 12. Reconstruction of the water/rock ratios of hydrothermal systems

Region	Object	Method	Water/rock	Reference
Modern and recent systems in the ocean				
Costa Rica rift	Hole 504B	Sr isotope balance in rock	1.6	Kawahata and Shikazono, 1988
″	″	S isotope balance in rock	2–7	″
21° N EPR		Sr isotope ratio in solution	0.7 ± 0.2	Albarede *et al.*, 1981
Galapagos Spreading Center	Rose Garden	From ^{3}He content	0.34	Dymond *et al.*, 1983
″	″	From ^{226}Ra content	0.19–0.53	″
Juan de Fuca Ridge, southern segment	Monolith	From Li and B contents	0.56–0.94	Butterfield and Massoth, 1994
″	Pipe Organ	″	0.37	″
″	Diffuse	″	4.6	″
Ancient deposits				
Iberian Pyrite Belt	Huelva	O isotope balance in rock	0.3–0.7	Fouillac and Javoy, 1988
Troodos ophiolites, Cyprus	Agrokipia	Sr isotope balance in rock	12	Kawahata and Scott, 1990
Semail ophiolites, Oman		O isotope balance in rock	15–40	McCulloch *et al.*, 1980

Existence of a boiling zone within the system. Venting of heterogeneous water–vapor fluids was never observed during submersible dives at deep ocean hydrothermal sites. The existence of boiling zones in the interiors of some convective systems can be supposed on the basis of variations in solution chemistry correlated with the concentrations of dissolved gases. This question is considered in more detail in Chapter 6.

Subsurface mixing. Starting from the investigations of thermal springs in the Galapagos Spreading Center (GSC) (Edmond *et al.*, 1979), there is a growing body of evidence that some solutions from oceanic hydrothermal systems have interacted with rocks at temperatures higher than those directly measured. To explain this discrepancy, it was suggested that the high-temperature solutions were mixed during their ascent to the ocean floor with seawater that did not pass through the hot part of the system. This phenomenon was referred to as subsurface mixing. If it occurs, the decrease in temperature due to mixing must promote precipitation of metals from solutions in the crustal layers, and formation of disseminated and vein mineralization (stockwork). Such mineralization patterns were observed, for instance, in an ancient inactive system in the GSC (Embley *et al.*, 1988) and in drill cores from Hole 504B (Alt *et al.*, 1989). The investigation of the TAG system suggested that subsurface mixing was probably responsible for the formation of considerable amounts of anhydrite within this structure (Mills *et al.*, 1998).

The commonly used method of processing solution compositions includes extrapolation to Mg = 0 and does not allow one to discriminate between the addition of seawater to hydrothermal solution during subsurface mixing and seawater contamination during sampling. The compositions of solutions determined recently in several systems show very low Mg concentrations indicating a total contribution from both sources of 4–5%. This allows us to ignore the effect of subsurface mixing for the construction of thermodynamic models.

The questions on the role of magmatic fluids and internal zoning of ore bodies are considered below in more detail because of their fundamental importance to the thermodynamic model.

Influx of magmatic fluids. The assessment of the contribution of magmatic fluids to the hydrothermal process is one of the most important problems and has a long history of research. As to the hydrothermal systems of mid-ocean ridges, when the first data on the chemical and isotopic compositions of hydrothermal solutions were obtained, it became clear that their major (possibly, the only) source is seawater (Edmond *et al.*, 1982; Wehlan and Craig, 1983). Oxygen and hydrogen isotope systematics are the main indicators used in modern geochemistry for the identification of water sources. Figure 17 displays the available data on the compositions of oceanic hydrothermal solutions (Table 8) on the Taylor diagram. It indicates that the ocean is the main water source of the hydrothermal systems. According to the calculations of Bowers and Taylor (1985), the observed small isotopic deviations can be adequately explained by seawater–basalt interaction during convective circulation in fissures. The contribution of the magmatic component is smaller than the resolution of the isotopic method (<5%). As a result, the problem of the participation of magmatic fluids in oceanic hydrothermal systems received little attention in the international literature over the given time period. The views of Russian researchers on this problem were more contradictory (Butuzova, 1986a, 1986b; Grichuk and Krasnov, 1989; Krasnov, 1994), which was probably related to the long tradition of plutonism in Russian geology.

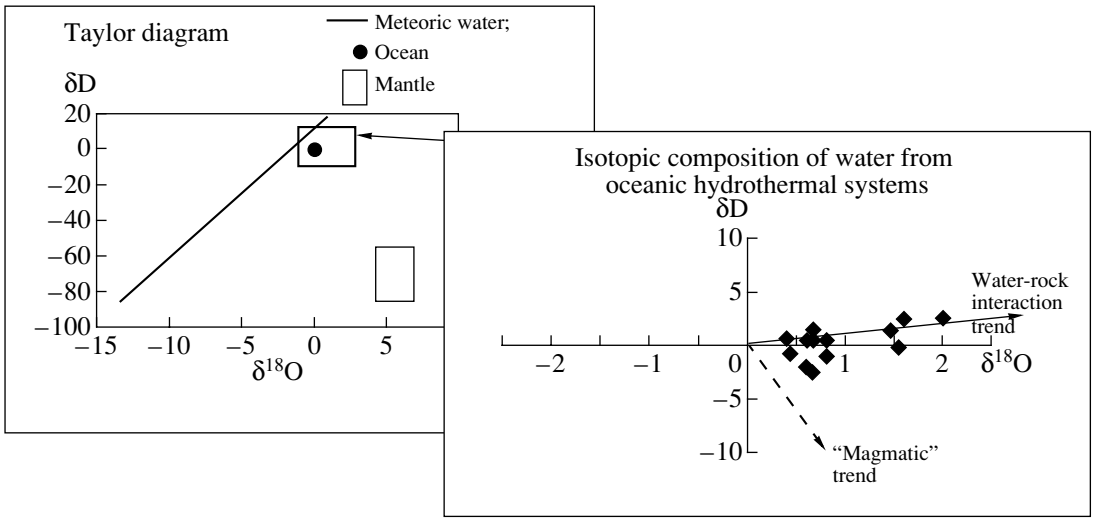

Fig. 17. Isotopic composition of water from oceanic hydrothermal systems in the Taylor diagram.

Since 1990s this problem has received renewed interest owing to the discovery of a strong influence of volcanic and seismic events on hydrothermal activity (Von Damm *et al.*, 1995; Von Damm, 2000; etc.). Various pieces of evidence suggested that magmatic fluids may be introduced into oceanic hydrothermal systems, which has a bearing on the behavior of metals in solution: (a) a high concentrations of gases (CO_2, H_2S, and H_2) in high-temperature hydrothermal springs (Ishibashi *et al.*, 1995; Charlou *et al.*, 2000; Seewald *et al.*, 2003), (b) indications for basalt degassing (see Rubin, 1997 for a review), and (c) discovery of ore element minerals in gas–liquid inclusions from the igneous rocks of oceanic basins (e.g., Kamenetsky *et al.*, 2002). It can be seen that these data have an indirect bearing on ore formation. However, they are indispensable for the solution of the fundamental question in model construction: whether magmatic fluids must be taken into account in the model.

A contribution from endogenous fluid to the hydrothermal systems of ore deposits is usually identified from Pb, S, Sr, and He isotopic parameters. However, attempts to use these indicators for oceanic hydrothermal systems were hampered by the following circumstances. The aforementioned elements can be introduced into a hydrothermal system in two ways: (a) directly with magma-derived fluid or (b) in two stages, through capturing during basalt crystallization (as minerals, admixtures, gas inclusions, etc.) and subsequent leaching with hot seawater. In both cases the components are transferred into solution without any changes in isotopic ratios, which thus cannot be used to discriminate between these two mechanisms. They also cannot be used for the identification of a direct influx of magmatic fluids into oceanic hydrothermal systems.

The problem can be approached by means of indirect methods. They are certainly less accurate but can be used to constrain natural values.

Estimation from heat and water fluxes. The fraction of magmatic fluid can be assessed from the amount of mantle-derived water relative to the water flux in the hydrothermal systems of mid-ocean ridges. The flux of mantle-derived water into the ocean was independently estimated by various authors. According to the theoretical model by O.G. Sorokhtin (*Geophysics of…*, 1979), it equals 10^{14} g/y. The calculation of water balance in the hydrosphere (Timofeev *et al.*, 1986) yielded a value of 5×10^{14} g/y. A value of $(1.1 \pm 0.3) \times 10^{14}$ g/y was obtained from the concentration of H_2O in magmatic melts of mid-ocean ridges (Ito *et al.*, 1983).

Water flux through the hydrothermal systems of mid-ocean ridges was estimated by a number of authors on the basis of heat transfer (Q) calculations for hydrothermal systems. This value was determined through either thermal models or measurements of the ^3He flux and the $^3He/Q$ ratio (e.g., Rona, 1984; Merlivat *et al.*, 1987). The estimates obtained show a considerable scatter related primarily to the imprecise determination of the world's average temperature of effluent hydrothermal solutions. Nonetheless, all the estimates are higher than 10^{17} g/y. These values suggest that the contribution of magmatic water to the total flow of hydrothermal solutions is no higher than 0.1–0.5%. This value is perhaps overestimated, because it is based on the assumption that all the water transported from the mantle by basaltic melts is released through the hydrothermal systems of mid-ocean ridges. However, this estimate has a global character and does not exclude local variations.

Estimation from the heat balance of a hydrothermal system. A local estimate can be obtained through the calculation of the amount of seawater necessary for the

Table 13. Concentrations of water and other volatile components in glasses from mid-ocean ridge basalts

Region	Object	Mg#	Concentration, %						Reference
			H_2O	CO_2	CO	CH_4	Cl	F	
MAR	basalts (average)	63	0.21	0.13	–	–	0.01	0.02	Byers *et al*., 1983
"	basalts (average)	62	0.22	0.015	–	0.002	–	–	Grichuk *et al*., 1988
21° N EPR	basalts (average)	63	0.12	0.163	0.023	0.002	0.005	0.005	Byers *et al*., 1986
Red Sea	basalt	–	0.36	0.047	–	–	0.057	0.02	Almuhamedov *et al*., 1985
Loihi Volcano	basalts	–	≈0.6	0.033–0.066	–	–	0.065–0.128	–	Garcia *et al*., 1989
86° W GSC	Fe-basalts (average)	51	0.32	0.10	0.03	0.02	0.12	0.01	Byers *et al*., 1983
"	Fe-andesites (average)	25	0.96	0.11	0.01	0.02	0.32	0.07	"

Note: Mg# = Mg/(Mg + Fe).

cooling of one mass unit of basaltic melt and its comparison with the quantity of volatile components dissolved in this melt. Heat production associated with the formation of igneous rocks includes the latent heat of crystallization and heat release due to basalt cooling. The former constituent is 0.4 kJ/kg (Cann *et al.*, 1985/1986; Brikovski and Norton, 1989), and the latter depends on the temperature drop. If the temperature decreases from 1150°C (approximate solidus temperature) to 370°C (temperature in the center of a hydrothermal system), heat release can be calculated using the average heat capacity of basalts (*Physical Properties…,* 1984; Brikovski and Norton, 1989). The resulting value is 0.69–0.82 kJ/g (0.75 on average).

The amount of water needed to cool one gram of basalt can be calculated from the amount of heat removed, the change in water temperature (from 0 to 350°C), and the average heat capacity of water in this temperature interval. This estimate gives $M_{H_2O} = \frac{0.4 + 0.75}{370 \times 0.0044} = 0.71$ g water per gram of basalt.

The concentrations of water in primary MORB melts were estimated by many authors (Table 13). According to their data, the average water content in the melt can be estimated as 0.2% or 0.002 g per one gram of basalt. If all this water were released during crystallization (which is certainly an overestimation), its fraction in the flow of cooling seawater would be only 0.28%.

This estimate is local (related to an individual chamber) but averaged over time. It must be taken into account that the release of volatiles may vary during the lifetime of a magma chamber. Volatiles with a low solubility in melt, primarily CO_2, escape during the initial stages of magma chamber evolution, which is indirectly suggested by the existence of popping rocks with a total CO_2 content of up to 0.85% (Sarda and Graham, 1990), whereas water behaves as an incompatible component and is accumulated in the residual melts up to 1–2% (Table 13). However, such strongly evolved melts can be formed only immediately before the complete solidification of small isolated reservoirs producing Fe–Ti basalts and Fe-andesites (for instance, in the Galapagos Spreading Center; Beyers *et al.*, 1983, 1984). These residual magma bodies have low heat resources, and large hydrothermal systems can hardly be generated by them.

Estimation from CO_2 flux. This method utilizes the main geochemical feature of magma-derived gases of mid-ocean ridges, a strong predominance of CO_2 over all other components (Kyser and O'Neil, 1984; Sommer and Gibson, 1985; Gerlach, 1986; Gurenko *et al.*, 1990). This topic was discussed in detail by Grichuk *et al.* (1988). Assuming that all the carbon dioxide dissolved in hydrothermal solution came directly from a magmatic source, its concentration can be used to estimate the fraction of the magmatic component in the mixture.

The data of Table 14 show that the maximum fraction of magma-derived fluid estimated by this method is only 0.02–0.3%. A higher CO_2 content was detected in some hydrothermal systems (Table 6). Solutions from the Guaymas Basin contain up to 1 g/kg, but this CO_2 was derived mainly from the metamorphism of a sedimentary sequence. A high CO_2 content was measured in the freshened fluids from the Juan de Fuca Ridge (Table 14 shows the maximum values for the Virgin Mound and Cantilever vents, 12.54 and 3.12 g/kg, respectively). The water of these vents is a condensate of the vapor that formed in the zone of phase separation. Such vents usually show low metal contents and unstable regimes.

Elevated CO_2 levels were reported in hydrothermal systems from other geodynamic settings including the JADE and CLAM sites in the Okinawa trough (island arc) and Loihi Seamount (hot spot): 4.0, 8.5, and 13 g/kg, respectively. The above-described method of estimation is not appropriate for such objects, because the proportions of H_2O and CO_2 may be different in their magmatic fluid.

When using the constraints presented in Table 14, one should keep in mind that some CO_2 comes into hydrothermal systems with seawater (decreasing the estimate by 0.013%) and is extracted from crystallized basalts (decreasing the estimate by approximately 0.01%). The magmatic addition consists mainly of CO_2, and the fraction of magmatic H_2O is several times lower (Grichuk *et al.*, 1988).

Thus, three independent methods indicate a very small contribution from magmatic fluids to the hydrothermal systems of mid-ocean ridges, no higher than 0.0*n*–0.*n*%.

On the other hand, the existence of a small influx of magmatic fluids is demonstrated by the data on CO_2 content in glasses and solidified basalts (Bottinga and Javoy, 1989; Gerlach, 1989) and U/^{4}He values (Zingler and Hart, 1986). These data are suggestive of a preeruptive loss of gases with low solubilities in melts from the magma chambers of mid-ocean ridges.

The second question related to the assessment of the role of magmatic fluids in the metal content of oceanic hydrothermal systems is the possible extent of ore metal transportation by these fluids.

The metal content of juvenile fluids can be estimated from the direct analyses of metalliferous volcanic exhalations. Within the available worldwide data set, the Great Tolbachik Fissure Eruption (GTFE) is petrochemically most similar to oceanic basalts. Condensates collected during the GFTE were negligibly altered by interactions with the country rocks and meteoric water and reflected the compositions of magmatic volatiles (Menyailov *et al.*, 1984). The raw data and results of calculations are given in Table 15.

It should be noted that the analogy between the fluids of mid-ocean ridges and GTFE is not quite adequate, because the solid products of the GTFE are petrologically more similar to ocean island basalts. The GTFE gases are strongly dominated by water (83.5% H_2O and 5.55% CO_2), whereas gases from mid-ocean ridge basalts display the opposite relation. The GTFE fluids are more efficient with respect to ore element transportation than the magmatic fluids of mid-ocean ridges. However, even assuming an analogy between them, Table 15 suggests that the observed metal contents in the oceanic hydrothermal systems require a few tens of percent of Tolbachik-type fluids.

Rubin (1997) analyzed a large body of diverse information and distinguished a series of elements that must be extensively removed from magma chambers with the fluid phase: As, Sb, Pb, Mo, Tl, and Po. A comparison with the data on the compositions of hydrothermal solutions and ores from mid-ocean ridges clearly shows that there is no enrichment in these elements. It should be noted that a strong enrichment was observed in the ores of the JADE island-arc hydrothermal system (see Glesby and Notsu, 2003 for a review).

The role of magmatic mass transfer can be qualitatively estimated from the Zn and Cd relationship. These

Table 14. Calculation of the fraction of magma-related fluids from the concentration of CO_2 in hydrothermal solutions

Object	Concentration of CO_2 in solution, mg/kg (calculated from the data of Table 6)	Maximum fraction of magmatic fluid, %*
EPR, 21° N	252	0.03
EPR, 13° N	475–735	0.06–0.09
EPR, 9°40′ N	502–682	0.06–0.09
EPR, 17° S	580	0.07
Juan de Fuca Ridge, Endeavour segment	127–970	0.015–0.12
Juan de Fuca Ridge, Axial Seamount, Inferno	2200	0.28
Juan de Fuca Ridge, Axial Seamount, Virgin Mound	12540	1.6
Juan de Fuca Ridge, Cleft segment	172–196	0.02–0.025
Juan de Fuca Ridge, Cleft segment, Cantilever (1999)**	3120	0.39
MAR, MARK, 23° N	230–295	0.03–0.04
MAR, TAG, 26° N	128–150	0.016–0.019
MAR, Lucky Strike	1250	0.016
Lau Basin, Vai Lili	334–686	0.04–0.08
Manus Basin	260	0.03
East Manus Basin, Pacmanus	1410	0.18
Seawater	101	–

* For a magmatic gas containing ≥80% CO_2.
** After Seewald *et al.* (2003).

Table 15. Estimation of the fraction of magmatic fluid from the composition of condensates from the Great Fissure Tolbachik Eruption

Element	Concentration, mg/kg		Necessary fraction of magmatic fluid, %
	in hydrothermal systems of 21° N EPR	in gases of GFTE (average values; Menyailov *et al.*, 1984)	
Cu	0.6–2.8	6.4	9–44
Zn	5.8–6.9	33	18–21
Ag	0.0028–0.0041	0.0034	>82
Cd	0.016–0.020	1.07	1–2
Pb	0.04–0.074	1.42	3–5
Co	0.004–0.013	0.018	20–72

Table 16. Zn/Cd values for various hydrothermal systems and related objects after Metz and Trefry (2000), with modifications

Object	Zn/Cd, molar
MORB	907–1100
Juan de Fuca Ridge, Cleft segment, hydrothermal solutions	800–906
Juan de Fuca Ridge, Cleft segment, Zn–Fe sulfides	1220
MAR, TAG, hydrothermal solutions	620
MAR, TAG, Zn–Fe sulfides	560–640
Zn–Fe sulfides of other fields	630
Condensate of volcanic gas, GFTE, Kamchatka*	40
Proportion in the magmatic degassing flux**	8

* Menyailov *et al.* (1984).
** Rubin *et al.* (1998).

elements are geochemically very similar and behave sympathetically in most natural systems. Therefore, the Zn/Cd value is rather stable in nature. However, it was found that Cd is much more mobile in magmatic gases than Zn (e.g., Symonds *et al.*, 1992). The emanation coefficient of Cd is two orders of magnitude higher than that of Zn (Rubin, 1997). (The reason for this difference is probably that Cd, in contrast to Zn, can occur as Cd^0 in magmatic fluid.) Table 16 shows Zn/Cd values in some objects, which suggest that there is no significant contribution from magmatic fluid to hydrothermal systems.

Considering all these data, it can be concluded that the transportation of metals by magmatic fluids is not a significant control on the composition and properties of hydrothermal ores of mid-ocean ridges. This allows us to ignore this factor in the construction of a thermodynamic model for the hydrothermal system.

It should be noted, however, that the relationships of element sources are probably different in island-arc hydrothermal systems (Chapter 7).

Internal zoning of ore bodies and its evolution in time. Given the diversity of mineral assemblages and chemical compositions observed in oceanic sulfide ores, there is a need to reproduce the spatial and/or temporal sequence of their formation.

Among the samples and observations obtained from the ocean floor, the most distinct zoning was revealed in smoker chimneys. Mechanisms of chimney development were proposed by Haymon (1983) and Graham *et al.* (1988). According to their models, edifice growth begins with the deposition of anhydrite, which is subsequently replaced by sulfides starting from the inner channel of the chimney. The scenario proposed by Graham *et al.* (1988) includes a successive change in the identity of predominant sulfides: marcasite + wurtzite–pyrite–bornite–chalcopyrite. A sulfide pipe formed by such concentric zones corresponds to the mature stage. The subsequent evolution of the pipe includes oxidation and destruction, and its inner channel is overgrown with the formation of the reverse zoning pyrite–marcasite–sphalerite–opal.

Such idealized patterns are not always observed, and other variants of vent development were reported (*Hydrothermal Sulfide…*, 1992). In particular, some elements of the ideal sequence may be missing, and different mineral assemblages may occur (e.g., pyrrhotite + isocubanite). In edifices with a solution discharge temperature of lower than 350°C, porous cavernous pyrite–marcasite–sphalerite ores are often deposited, whereas copper mineralization is absent. Low- and medium-temperature vents form small opal and barite edifices (such objects were found in back-arc spreading basins; Lisitsin *et al.*, 1991). The lack of copper mineralization associating with low-temperature solutions is unanimously explained by a decrease in the transport capacity of the solution. It is usually noted that Cu and Fe sulfides can be deposited in the channelway. The same logic is applied to barite edifices, because the reconstructions of temperature conditions within such systems often yield values identical to those of black smokers.

Compared with chimneys, the situation with smoker edifices as a whole is more complicated, primarily because of the paucity of data. The growth of edifices occurs largely through the formation and subsequent destruction of ore pipes (Lisitsin *et al.*, 1990; Bogdanov *et al.*, 1997b), and their ore material should consist of mixed chimney fragments of different compositions, but the available samples do not have such chaotic compositions. Moreover, large edifices contain ore types that are absent in small ones, including massive pyrite and pyrite–chalcopyrite ores confined to the central parts of the edifices (*Hydrothermal Sulfide…*, 1992). The outer parts of large structures are usually made up of pyrite–marcasite–sphalerite ores and covered by oxidation crusts (Lisitsin *et al.*, 1990).

The interior zoning of sulfide edifices was reconstructed by Hekinian and Fouquet (1985), who pointed out the difference in the character of hydrothermal discharge between small individual chimneys and large edifices: the latter are characterized by an increasing role of slow solution percolation through the ore body. As a result, processes of metasomatic replacement become more intense in the inner parts and a large-scale zoning develops within the edifice. Proceeding from the data obtained in the hydrothermal field of 13° N EPR, Hekinian and Fouquet proposed a scenario of ore body evolution.[8] A generalized

[8] It was shown that some elements of this scenario are of only local significance. Furthermore, the suggestion that the process begins with the appearance of low-temperature springs and is accompanied by an increase in temperature was not confirmed. Observations at 9° N on the EPR (Von Damm *et al.*, 1995) demonstrated that the beginning of hydrothermal activity is very vigorous and high-temperature. The deposition of anhydrite with a sulfide admixture from high-temperature solutions mixed with seawater was observed during an experiment lasting many days at the vents of the Endeavor hydrothermal field (Tivey *et al.*, 1990).

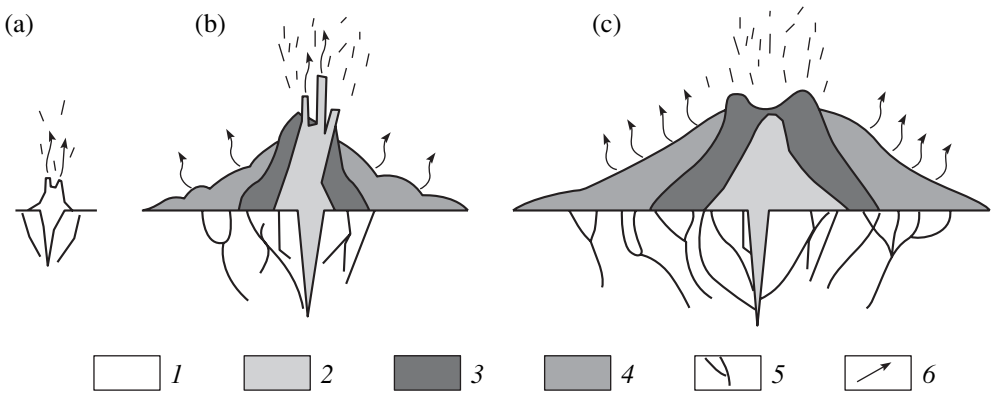

Fig. 18. Schematic evolution of a black smoker after Hekinian and Fouquet (1975) modified in *Hydrothermal Sulfide…* (1992). (a) Stage of formation of an anhydrite embryonic structure on the ocean floor. (b) Stage of high-temperature hydrothermal activity and formation of a sulfide edifice. (c) Stage of diffuse hydrothermal activity. (*1*) Anhydrite, (*2*) Cu and Fe sulfides, (*3*) Zn and Fe sulfides, (*4*) low-temperature Fe sulfides, (*5*) stringer and disseminated mineralization in basalt, and (*6*) direction of hydrothermal solution movement.

variant of the Hekinian–Fouquet scenario was developed by Krasnov (Krasnov *et al.*, 1990; *Hydrothermal Sulfide…*, 1992) (Fig. 18). It includes three stages: (a) an initial stage, when an embryonic anhydrite–sulfide body is formed, and the major deposition process is the mixing of the hydrothermal solution with seawater; (b) a stage of high-temperature hydrothermal activity, when a sulfide edifice is formed mainly at the expense of sulfide precipitation due to the abrupt cooling of hydrothermal solutions; and (c) a stage marked by a large hydrothermal edifice with predominantly diffuse venting and a leading role of metasomatic reworking in the inner parts of the ore body. Similar reconstructions were proposed for large bodies from the TAG field by Lisitsin *et al.* (1990) and Rona *et al.* (1993). They were confirmed by the data obtained by drilling on an active mound of this field (Herzig *et al.*, 1998) (except for the surprising abundance of anhydrite in the interior of the mound and in the upper parts of the feeder stockwork).

The change in the character of ore-forming processes is mirrored in the mineralogy of the ores: the large deposits contain abundant massive pyrite and pyrite–chalcopyrite ores, which form the central parts of edifices, whereas such ores either are absent or occur in minor amounts in the small bodies. This causes variations in the bulk chemistry of ore bodies: the size of ore bodies is correlated with the degree of copper enrichment (Krasnov, 1990).

Metasomatic alteration in the central parts of large edifices has important consequences for the behavior of minor elements of the ores. They give rise to zone refining phenomena, which produce massive ores strongly depleted in trace elements (except for Se, Mo, and Co) compared with the outer parts of the edifices (Hekinian and Fouquet, 1985; Fouquet *et al.*, 1988; *Hydrothermal Sulfide…*, 1992; Hannington *et al.*, 1998). Krasnov pointed out some delicate differences in trace-element (including Ag and Au) geochemistry between the sphalerite ores deposited during stage (b) from high-temperature solutions and the sphalerite ores forming the outer portions of large edifices during stage (c). The reason for these differences is probably related to the removal of these elements during metasomatic processes in the central parts of the bodies.

The zoning developing in sulfide edifices on the ocean floor resembles that of ancient massive sulfide ore deposits. In contrast to the ocean, the zoning of massive sulfide deposits has been extensively studied and described in a number of publications. Ore bodies from many massive sulfide deposits in the ophiolitic associations of Cyprus and the Mugodzhar Hills (Southern Urals), the contrasting and continuous associations of the Urals, and the andesite–dacite–rhyolite associations of Japan, Australia, and the Caucasus show distinct zoned structures, which are controlled by feeder axes. The zoning of ore bodies is expressed by a regular increase in the abundance of main rock-forming minerals in the sequence pyrite–chalcopyrite–sphalerite–galena–barite in the direction from the footwall to the hanging wall and laterally outward from the feeder axis. Siliceous (jasper) deposits with iron and manganese oxide phases usually occur above and at the flanks of the massive ores.

The following is a typical vertical zoning of the well known massive copper sulfide deposits of the Cyprus type (Zlotnik-Khotkevich and Adriyanova, 1987): (1) maghemite–magnetite ores at the base of the ore body, (2) massive and brecciated pyrite ores with magnetite relicts, (3) massive chalcopyrite–pyrite ores, (4) brecciated sphalerite–chalcopyrite–pyrite ores, and (5) massive and banded sphalerite–pyrite ores with minor chalcopyrite; banding is due to the presence of thin siliceous laminae at the roof of the body (Priorskoe deposit in the Mugodzhar Hills).

The nature of zoning in massive sulfide ore bodies was long a subject of debate (see Franklin *et al.*, 1981

for a review). Many researchers (Smirnov, 1982; Ohmoto *et al.*, 1983) explained the heterogeneity of ore bodies by the sequential formation of ores from solutions with different compositions, as a result of either the regular evolution of the feeding hydrothermal system or the repeated resumption of hydrothermal activity with changing characteristics. Another popular explanation for ore zoning postulates spatial variations in the conditions of ore deposition, which results in sequential changes in mineral assemblages (Large, 1977; Solomon and Walshe, 1979; Franklin *et al.*, 1981). Some authors emphasized the role of redeposition and metasomatic replacement of ore materials during formation and diagenetic alteration of the ore body (Skripchenko, 1972). The sequential influx of solutions with different geochemical characteristics is suggested by some features systematically observed in massive sulfide deposits, including intersection structures, corrosion and cementation phenomena, and replacement of minerals. On the other hand, the regular change in mineral assemblages on the scale of an ore deposit irrespective of the particular geologic environment may be indicative of ore deposition from a single solution, whose properties and occurrence conditions vary regularly in space. Many recent studies noted the coexistence of zoning patterns related to different factors (*Prospecting of…*, 1985).

A comparison of oceanic hydrothermal occurrences with ancient massive sulfide deposits reveals an obvious influence of deposition conditions (primarily temperature) on the zoning patterns of the ores. The Hekinian–Fouquet scenario for the evolution of ore edifices uses the concept of metasomatic replacements. The idea of the evolution of parent solutions cannot be evaluated, because the duration of observations in active hydrothermal systems is not yet sufficient. The role of this factor cannot be established by direct observation or comparative analysis of the structures of ore bodies, because the relevant drilling data are still scanty and the reconstructions of the interior structure of seafloor sulfide edifices are oversimplified.

The analogy between modern and ancient ore bodies appears to be far from complete. Massive sulfide deposits do not contain mineral associations corresponding to the early stages of oceanic system development (Fig. 18a). Strong zinc enrichment is typical of oceanic sulfide bodies but was never reported in massive sulfide deposits.

The considerations presented above were used as a basis for the logical scheme of oceanic hydrothermal ore formation, which was used for the construction of its physicochemical model.

3.3. Modeling of Modern Ore Formation in the Ocean: Previous Work

Numerical thermodynamic modeling of high-temperature seawater–basalt interaction was first performed by T. Wolery in 1978, but the results of that study were never published.

A thermodynamic model for the behavior of seawater during heating to a temperature of 300–350°C, which is characteristic of oceanic hydrothermal systems, was calculated by Reed (1982). The results of modeling were compared with the experimental data of Bischoff and Seyfried (1978), who studied the properties of seawater between 25–350°C. The goal of these calculations was to demonstrate the possibility of an adequate thermodynamic description of the behavior of seawater in the hydrothermal process. Good agreement with experimental data allowed the simulation of more complex models involving silicate rocks.

The calculations of isothermal seawater–rhyolite interactions were performed by Reed (1982), and seawater–basalt and seawater–peridotite interactions were calculated by Grichuk *et al.* (1982) and Reed (1983). These calculations showed adequate agreement with the available experimental data on the respective systems. The general trends of changes in solution chemistry were also consistent with natural observations. However, since the method of the degree of reaction progress was used in the aforementioned studies, they failed to adequately reproduce sulfur behavior (the reason for this discrepancy was discussed in Section 2.1). Correspondingly, ore elements were also not properly evaluated.

Further progress in the thermodynamic modeling of oceanic hydrothermal systems was made in two directions: (a) simulation of ore deposition during cooling of hydrothermal solutions on the basis of analytical data on the compositions of natural hydrothermal solutions and (b) simulation of the formation of hydrothermal solutions from seawater as a result of interaction with rocks. The former approach makes use of more specific information, but it is restricted to the zone of ore deposition and does not elucidate the general properties of the hydrothermal system. The latter approach encountered considerable difficulties, because it employs poorly constrained model parameters. However, it allows the construction of a comprehensive thermodynamic model for a hydrothermal system, from the area of hydrothermal solution generation to the zone of ore deposition, and the properties of this model can be explored. Such a formulation exploits most comprehensively and efficiently all the advantages of the method of thermodynamic modeling.

Ore deposition from smoker solutions was first simulated by Janecky and Seyfried (1984), who calculated the mixing of hydrothermal solutions from 21° N EPR with cold seawater. Their model took into account 15 elements including Fe, S, Cu, Zn, Pb, and Ba (the composition of the multisystem with respect to minerals and solution species was not specified). The calculations ignored aluminosilicates and silicates; the former, because Al was not present in the multisystem, and the latter, because preliminary calculations overes-

timated (in the authors' opinion) the amounts of precipitated quartz, talc, serpentine, and tremolite. The calculations were carried out within a temperature interval from 350 to 25°C and a pressure of 250 bar.

The results of these calculations proved to be strongly dependent on whether the equilibrium between oxidized and reduced sulfur species is attained. Calculations with metastable sulfate reduction reactions yielded the following temperature sequence of mineral precipitation: chalcopyrite–anhydrite–pyrite (pyrrhotite)–sphalerite–graphite–barite. A scenario assuming an equilibrium sulfur speciation suggested earlier pyrite deposition and formation of the following sequence of copper-bearing minerals: chalcopyrite–bornite–chalcocite–covellite. The assemblages of ore minerals obtained in these models were similar to those observed in nature, and the authors noted that the equilibrium sequence was closer to that observed on the inner walls of smoker chimneys. It is also similar to the mineral zoning of ancient massive sulfide ores.

The analysis of the simulation procedure used by Janecky and Seyfried shows that it is a modification of the method of the degree of reaction progress by Helgeson (see Chapter 2), which includes a peculiar titration of the hydrothermal solution with cold seawater without the removal of reaction products. The method of Janecky and Seyfried does not, in principle, reproduce the differentiation of ore components. In the simulation of the equilibrium scenario (Janecky and Seyfried, 1984, Fig. 12), the amounts of copper minerals (covellite and chalcocite) produced by the end of the process at temperatures below 100°C were identical to the amount of chalcopyrite at the beginning of the process. This is not consistent with the natural process, in which copper is removed from solution to form chalcopyrite and does not occur in the subsequent mineral assemblages. Nonetheless, the results of Janecky and Seyfried (1984) appeared to be similar in many respects to the natural prototypes. They demonstrated that the methods of thermodynamic modeling are promising for the analysis of even such relatively rapid processes as hydrothermal–sedimentary ore formation.

Bowers *et al.* (1985) used a similar simulation procedure and a more comprehensive data set on the composition of hydrothermal solutions from the 21° N EPR field and the Guaymas Basin. Their multisystem included some additional elements (Al, Mn, and Ag), and the raw analyses were corrected for a pH shift due to the cooling of samples. The studies of Tivey and McDuff (1990) and Tivey (1995) were of considerable importance for the simulation of oceanic hydrothermal mineralization. These authors explored heat and mass transfer and chemical interaction in the walls of smoker chimneys. The Tivey–McDuff model accounted for heat conduction, diffusion, solution flow through a porous wall, and local thermodynamic equilibrium between solution and solid phases. The problem considered was steady-state with respect to temperature and concentration profiles.

The calculations yielded several variants of zoning in the chimney wall depending on the parameter F, which is a function of chimney diameter. The typical zoning is as follows: (chalcopyrite)–(anhydrite + bornite)–(pyrite + bornite)–(silica + pyrite + sphalerite + chalcocite), which is similar to that observed in the natural prototypes. It was shown that, for the processes of the chimney-wall scale and low porosity, diffusion plays a significant role in the formation of zoning, whereas the kinetics of precipitation is not important, i.e., equilibrium in the systems was reached rather rapidly.

Thermodynamic modeling of hydrothermal solution formation and complete models for oceanic hydrothermal systems.

All the published models of the type considered use the concept of a step flow reactor in some form. The downwelling limb of a convection cell is usually simulated by a chain of steps with increasing temperatures maintaining local equilibrium, whereas the upwelling limb and the discharge zone are approximated by a single step or several steps with decreasing temperatures. The schemes of these models are in principle identical, but there are many particular differences. The most sophisticated models were constructed by the author at the Geochemistry Department of Moscow State University (these results are described in detail in the next chapter) and T.S. Bowers at Massachusetts Institute of Technology.

The problems that should be solved during the construction of models for convection hydrothermal systems can be divided into two groups: (1) those inherent in any thermodynamic model of hydrothermal processes and (2) those specific to the scenario of recycling with hydrothermal–sedimentary ore deposition (such a combination defines the specific features of models for oceanic hydrothermal systems).

One of the general problems is the creation of an internally consistent thermodynamic database. Grichuk *et al.* (1985), Grichuk (1988, 1996), and *Hydrothermal Sulfide…* (1982) used the UNITHERM data bank (Moscow State University). The thermodynamic properties of solid phases were taken mainly from Robie *et al.* (1978) and *Thermodynamic Properties…* (1978–1982) (see also Borisov and Shvarov, 1992). The data bank used the model of Helgeson *et al.* (1981) for simple ions before 1989, and the modified Helgeson–Kirkham–Flowers (HKF) model later on (Shock and Helgeson, 1988; Johnson *et al.*, 1992). The properties of complex ions were calculated by a semiempirical modification of the Ryzhenko equation (*Methods of…*, 1988; Borisov and Shvarov, 1992). The models by Reed (1983), Bowers and Taylor (1985), and Bowers (1989) were based on the thermodynamic constants taken mainly from Helgeson *et al.* (1978, 1981) and Robie *et al.* (1978). Silantyev *et al.* (1992) used the

thermodynamic properties of substances from the DIANIK database (Vernadsky Institute of Geochemistry and Analytical Chemistry, Russian Academy of Sciences), which employs the modified HKF model for simple ions and the Ryzhenko equation modified by Bryzgalin (1985) for complex species. It can be seen that, although there are differences between the thermodynamic databases used by various authors, they are not very significant, because all the databases rely mainly on the same fundamental compilations. The discrepancies between the results of simulation are related, to a greater extent, to different sets of minerals and dissolved species. Considerable changes in the results of simulation were only caused by the introduction of the modified HKF model, which significantly improved the accuracy of the thermodynamic properties of dissolved species at high temperatures and pressures.

With respect to the choice of the compositions of initial solutions and rocks, the models of oceanic hydrothermal systems have important advantages over the models of other hydrothermal objects, because the country rocks and initial seawater are fairly homogeneous. The range of conditions is also relatively narrow: temperatures between 100–150 and 350–400°C and a pressure of up to 500 bar. The aforementioned studies are practically identical with respect to these parameters (except for Silantyev *et al.*, 1992, which is discussed below).

There are several specific problems associated with the simulation of oceanic hydrothermal systems: (a) procedure for prescribing the rock/water ratio controlling the intensity of interaction in the steps of the downwelling flow and (b) scenarios of ore deposition.

A comprehensive model for the hydrothermal system was developed by Reed (1983). In this model, the recycling process was divided into three sequential stages: (1) heating of seawater up to 300°C at 500 bar; (2) isothermal water–basalt reaction at 300°C and 500 bar; and (3) solution cooling accompanied by ore deposition. Anhydrite precipitates from seawater during heating, which removes 1/3 of the initial SO_4. Reed calculated water–basalt interaction by the degree of reaction progress method. The model trends of Mg, Ca, SO_4, H_2S, Fe, Ag, Cu, and Zn concentrations were in adequate agreement with the available experimental and natural data. Two scenarios of ore deposition were explored by Reed: (a) conductive cooling and (b) mixing with seawater at 25°C. The simulation used solutions from the previous stage obtained at $R/W = 0.045$ with $H_2S >$ (Fe + Zn + Cu) and $R/W = 0.062$ with $H_2S <$ (Fe + Zn + Cu). The cooling of the former solution produces the quartz + pyrite + chalcopyrite + chalcocite + sphalerite + acanthite assemblage, and excess hydrogen sulfide is retained in the solution. During cooling of the latter solution, magnetite is added to the above assemblage and hydrogen sulfide is completely fixed. In the scenario with mixing, chalcopyrite does not form and magnetite is replaced by hematite.

A detailed analysis of Reed's study demonstrated that the use of a two-stage downwelling limb (heating of solution followed by reaction with basalt) and the method of the degree of reaction progress significantly distorted the results. Owing to the possible occurrence of a back-reaction, Reed's model exaggerated the stability field of sulfate sulfur, up to the largest R/W value considered, which resulted in the removal of calcium from the solution. The concentrations of hydrogen sulfide appeared to be high at the expense of marine sulfate reduction, which is in conflict with sulfur isotope data. As was demonstrated by subsequent studies, the relationships of hydrogen sulfide and ore metals obtained in Reed's model, with a hydrogen sulfide deficit at high R/W, were an artifact of the simulation procedure. This affected the behavior of all chalcophile elements. The mixing scenario of ore deposition did not account for heat balance: all the mixtures were equilibrated at 25°C, although their temperatures must depend on the mixing proportions (Janecky and Seyfried, 1984).

Despite these shortcomings, Reed's study played a significant role in the development of concepts of chemical processes in oceanic hydrothermal environments (Krivtsov, 1987).

A complete model based on the method of a step flow reactor was first developed for an oceanic hydrothermal system by Grichuk and Borisov (1983) and Grichuk *et al.* (1985). This model considered seawater interaction with fresh basalt (i.e., passage of the first portion of solution). It was assumed that the rock/water ratio is an exponential function of temperature, such that the weight ratio $\Sigma R/W$ is 0.173–1.143 (Fig. 9). Three scenarios were considered for the upwelling limb and the zone of ore deposition: (a) slow conductive cooling, which was also simulated by a step flow reactor; (b) rapid cooling during ejection on the seafloor but without a chemical reaction with seawater; and (c) cooling with concurrent mixing, which is similar to the model explored by Janecky and Seyfried (1984). Because of the paucity of thermodynamic data available at that time, the model was restricted to a temperature interval of 150–350°C at saturated vapor pressure and a 13-component multisystem including Fe, S, and Pb as ore elements. The multisystem included 36 minerals and 48 dissolved species.

The model mineral assemblages of metasomatic rocks and the compositions of model solutions formed in the downwelling limb were generally consistent with natural observations. The calculation of the rapid cooling of model solutions produced typical mineral assemblages of the suspended particulate matter of smokers. However, these calculations failed to reproduce the observed concentrations of some components in the solution. The results obtained for 350°C underestimated Ca concentrations and overestimated Fe, Al, and H_2 concentrations, and the pH_T values appeared to be

slightly alkalic. These discrepancies reflected errors in the thermodynamic properties of dissolved species of these elements (chloride complexes of Ca and Fe and hydroxide complexes of Fe^{III}).

Bowers and Taylor (1985) simulated the formation of oceanic hydrothermal solutions. Their model also presented the downwelling limb of a convection cell as a step flow reactor, and simulated the passage of the first portion of solution through it. The thermodynamic multisystem of this model included 11 elements with only Fe and S as ore elements, and its complete component composition was not specified by Bowers and Taylor (1985). The bulk model rock/water ratio was taken as 1.787, which corresponds to the estimates obtained for the hydrothermal systems of 21° N EPR (2 according to Von Damm *et al.*, 1985). In order to distribute this amount between the steps of the model, the authors used the maximum likelihood estimates based on some characteristics of mineral and chemical compositions (appearance of epidote in the mineral assemblage and an increase in solution pH), i.e., they solved the inverse problem. However, these criteria were not formalized in their study, and the choice of specific *R*/*W* values for each step was largely arbitrary. Bowers and Taylor (1985) calculated equilibria using the EQ3/6 program. This program utilizes the algorithm proposed by Helgeson, and its main parameter is the degree of reaction progress (ξ, see Chapter 2). It cannot therefore calculate equilibrium parameters for the given composition of the rock–water system but constructs the path of solution titration by the rock. Because of this, Bowers and Taylor calculated a closed system for each temperature step, with ξ changing from zero to the desired value, after which the resulting solution was transferred to the next step. This method was referred to as the complex open-system model, and Bowers and Taylor argued that it is the most realistic simulation method.[9] The path of such a process in the *R*/*W*–*T* coordinates is a broken line (Fig. 9b). Ore deposition in the upwelling limb of the system was not considered by Bowers and Taylor (1985). An important feature of their model is that it involved H and O isotope equilibria. The isotopic part of the model was based on the Ohmoto method and utilized the results of chemical equilibrium calculations as input information (see Chapter 5 for more detail). In order to realize isotopic calculations, a special module was implemented into the EQ3/6 code.

Bowers and Taylor (1985) reproduced rather realistically the mineral associations of oceanic metabasic rocks and obtained a generally adequate description of recycling-related changes in seawater composition. However, similar to the results of Grichuk *et al.* (1985), the calculated concentrations of Fe and Al in the solution appeared to be overestimated, whereas those of Ca were strongly underestimated compared with the natural prototypes, and the pH_T values were neutral rather than weakly acidic. A fundamentally important result was obtained in the isotopic part of this model. The calculated values $\delta D = +2.67‰$ and $\delta^{18}O = +2.0‰$ for hydrothermal solutions appeared to be consistent with those observed in natural hydrothermal systems (Table 8). This suggests that the isotopic shift of oceanic hydrothermal solutions relative to seawater can be fully explained by reactions with rocks, and does not require other hypothetic water sources (including magmatic fluids) in the hydrothermal systems.

Unfortunately, there are some doubts on the accuracy of the model's estimate of δD shift. The input information of the Bowers and Taylor model included extrapolated values for the fractionation coefficients of hydrogen isotopes between minerals and water. Their form of the extrapolation function was determined on the basis of kaolinite–water experiments. For this pair Taylor obtained a sinusoidal dependency with a maximum near 300°C using the data available at that time. He supposed that isotope fractionation with other hydrous minerals could be approximated by similar dependencies (except for epidote). It was later found (Gild and Sheppard, 1996) that the low-temperature data for kaolinite that were used by Taylor were erroneous, because isotopic equilibrium was not reached in these experiments. Correspondingly, the hydrogen isotope shifts obtained in the Bowers–Taylor model are probably overestimated by a factor of two. However, this error does not affect the aforementioned fundamental conclusion on the role of seawater.

The isotopic direction in the simulation of oceanic hydrothermal systems was further developed by Grichuk (1988), Grichuk and Lein (1991), and Bowers (1989), who analyzed the behavior of sulfur isotopes, one of the major ore elements, in the descending convection flow. These results are discussed in Chapter 5. The chemical compositions of these models were extended to include Cu and Zn with corresponding solid phases and dissolved species.

The MSFR method was used to simulate the evolution of an oceanic hydrothermal system by Krasnov *et al.* (1990), Grichuk and Lein (1991), and *Hydrothermal Sulfide…* (1992). These studies used the modified HKF model for the calculation of input thermodynamic data, which improved the agreement with natural prototypes with respect to the concentrations of dissolved Ca, Al, and H_2 and pH values.

A novel approach to the description of water–rock interaction was proposed by Silantyev *et al.* (1992), who also utilized the concept of a multiwave step flow reactor. In order to simulate metamorphic alterations in the oceanic crust, these authors considered a heterogeneous crustal section composed of basalts, gabbroids, and ultrabasic rocks. They did not employ the principle of partial equilibrium and assumed that the whole rock

[9] It can be easily seen that, at equal final R/W values in reactor steps, the result of calculations for such a model will be identical to those obtained by the step flow reactor method proposed by Grichuk and Borisov (1983) and Grichuk *et al.* (1985), but the latter is superior in terms of computational efficiency.

body took part in interactions. The computational procedure was designed accordingly: all water portions reacted in each step with considerable amounts of rock (10 kg of rock per one kilogram of solution, which approximately corresponds to the porosity of basalts) and was subsequently moved to the next step. The model was calculated between 150–500°C with a temperature increment of 50°C. All the steps up to 350°C, inclusively, contained basalts, and the following steps were either gabbroic or ultrabasic. The multisystem consisted of 14 elements (including Fe, S, and Pb) forming 45 solid phases and 39 dissolved species. The EQUILIBR computer program was used for calculations. The computation was terminated after the passage of 60 water portions, which resulted in an integrated rock/water ratio of 0.167 for the first step and 0.83 for the last "basaltic" step (350°C).

A comparison with the data presented in Section 2.1 shows that this method (step reactor with large rock masses in steps) adequately reproduces an infiltration metasomatic column, but the desired compositions of the back zones can be reproduced with a very large number of solution portions (R/W must become lower than 0.02). Because of this, tremolite and epidote were predominant in the calculated assemblage of the 150°C step, which was interpreted by Silantyev *et al.* (1992) as an example of the zeolite facies. It seems likely that the assumption on the effective interaction of the whole rock volume with water is not quite realistic for the upper part of the basaltoid section. On the other hand, for the hotter zones, the model showed good agreement with the typical natural assemblages of metabasic greenschist-facies rocks.

However, the compositions of model solutions reported by Silantyev *et al.* (1992) differ in many parameters from observations in oceanic hydrothermal systems. For instance, the compositions obtained for the 350 and 400°C steps, which most closely match the conditions of oceanic hydrothermal systems, are consistent with the natural data only with respect to Na, whereas the concentrations of K, Ca, SiO_2, and Pb are lower by 0.5–2.0 orders of magnitude. It is also noteworthy that oxidized sulfur species prevail over reduced ones, which is not observed in oceanic hydrothermal systems. This is indicative of flaws in the model related to the thermodynamic description of the behavior of dissolved species. It is also obvious that the procedure of model verification must include a comparison of solution compositions, and the use of data only on mineral assemblages is not sufficient.

It should be noted that the model of Silantiev *et al.* for the interaction of water with ultrabasic rocks has acquired special importance in connection with the discovery of hydrothermal systems related to ultrabasic rocks.

The results obtained during the past two decades demonstrated that quite comprehensive thermodynamic models can be created for the modern hydrothermal process in the ocean. On the other hand, the results obtained by the simulation of oceanic hydrothermal systems revealed the most important unresolved problems related to the method of model construction and verification of model results.

3.4. Model Description
3.4.1. Geological model

The geological model (logical scheme) of geochemical processes in a mid-ocean ridge hydrothermal system, which was discussed in detail in Section 3.2, can be summarized as follows.

The model consists of three parts with distinctly different characteristics of geochemical processes (Fig. 8): (a) the downwelling limb of the convection system, where a hydrothermal solution is generated by the interaction of seawater with hot rocks of the oceanic crust; (b) the upwelling limb corresponding to the feeder conduit of ancient deposits; and (c) the zone of ore deposition, the most important part of which is the sulfide body growing on the ocean floor.

Downwelling limb. The convection cells of hydrothermal systems have characteristic vertical dimensions of 1.5–3.0 km (extending to the roof of a magma chamber) and lateral dimensions of about 6 km. Seawater percolates downward through fractures and reacts with the country rocks under gradually increasing temperatures. The high-temperature zone (focus of the system) directly contacts the magma chamber, and its maximum temperature is 370–395°C. The maximum pressure in the cell can be estimated from hydrostatic conditions, as the sum of pressures imposed by the seawater column and the column of hydrothermal solution below the seafloor. Such estimates for hydrothermal systems yield 350–400 bar for the EPR and 500–650 bar for the MAR.

The residence time of a hydrothermal solution in the zone of the most intense interactions (focus) and in the upwelling limb was estimated as about ten years (Kadko and Moore, 1988; Kim and McMurtry, 1991). According to the data for hydrothermal systems at 13° N and 21° N on the EPR, the lifetime of an individual smoker is several decades, and the activity periods of systems was estimated as $n \times 100 - n \times 1000$ y (Lalou *et al.*, 1993). Hydrothermal processes were repeatedly reactivated in the TAG field over 140 ka (Lalou *et al.*, 1995).

The qualitative chemical structure of the model (i.e., the set of elements) is defined by the problems addressed. The results of simulation presented below were obtained for a 15-element multisystem (H–O–R–Na–Ca–Mg–Fe–Al–Si–C–S–Cl–Cu–Zn–Pb) including all the major elements and some key ore elements. The geochemically interesting Mn and Ba could not be included because of the lack of necessary thermodynamic data (Section 3.4.2).

Systems involving sedimentary rocks were not considered in this study, which allowed us to significantly simplify the model, and assume that the crust is composed of a homogeneous tholeiitic basalt sequence. The composition of basalts used in our model (Table 17) corresponds to the most abundant statistical group of the oceanic crust (Yaroshevsky and Tsekhonya, 1986). The initial rock was regarded in the model as a homogeneous reactant. The composition of the initial solution was identical to the standard mean ocean water. The model accounted for changes in the bulk composition of the model rock due to metasomatic phenomena.

The key parameter of equilibrium dynamic models is the ratio of the rates of solution–rock interaction and mass transfer. In the MSFR method for extended nonisothermal systems with fracture percolation (Section 2.2), the similarity criterion of the model is the ratio of the masses of fresh rock and solution effectively participating in reactions integrated over the flow line of solution, $\Sigma R/W$. This parameter was estimated by two methods for active systems: from the concentrations of mobile elements and from Sr isotope ratios (Tables 11, 12), which yielded similar values of 0.5–2.0.

The products of seawater–basalt interaction are metasomatic mineral assemblages of the chlorite and propylite facies. They include, respectively, (a) chlorite, mixed-layer chlorite/smectite, quartz, hematite, and anhydrite; and (b) epidote, chlorite, albite, actinolite, and minor quartz and sulfides. Chlorites from the metasomatic rocks of the downwelling limb are usually magnesian and ferromagnesian. The list of minerals that should be taken into account in the model was defined by the mineralogy of metasomatic rocks and ores (Table 3), the elemental composition of the model, and the availability of thermodynamic data.

The role of magmatic fluids in the hydrothermal systems of mid-ocean ridges was evaluated in Section 3.2, and it was demonstrated that it could not be significant in such systems. This factor was therefore ignored in our model.

The upwelling limb of a convection cell in oceanic hydrothermal systems is characterized by rapid solution movement and relatively weak interactions with the country rocks. The character of processes in the upwelling limb may probably be different between systems. At least three extreme variants can be distinguished:

(1) solution ascent with adiabatic cooling,

(2) solution ascent with significant conductive cooling, and

(3) subsurface mixing with cold seawater.

The high temperatures of black smoker solutions in many hydrothermal systems directly indicate the realization of the first variant. It is certainly the most efficient in terms of ore formation on the seafloor. The adiabatic ascent of solution (if it is not accompanied by boiling) provides only minor cooling by 20–30°C (Bischoff and Pitzer, 1985). Conductive cooling and mixing result in the removal of ore metals from the solution and development of dispersed and vein sulfide mineralization.

Table 17. Compositions of initial basalt and seawater used in the model

Element	Basalt, g-atom/kg (Yaroshevsky and Tsekhonya, 1986)	Seawater, g-atom/kg H_2O
H	–	111.022114
O	27.325426	55.630401
K	0.0382	0.0099
Na	0.7936	0.468
Ca	2.0837	0.0103
Mg	1.9606	0.0532
Fe	1.4364	–
Al	2.9756	–
Si	8.4231	–
C	0.0088	0.002327
S	0.0209	0.02823
Cl	–	0.5459
Cu	0.00116	–
Zn	0.0011	–
Pb	0.000012	–

Note: For the recalculation of basalt composition to element concentrations, P and Ti were eliminated as apatite and TiO_2, respectively; Mn was summed with Mg; and the $Fe^{III}/\Sigma Fe$ ratio was taken as 0.15. The composition of seawater included 0.0025 mol/kg of dissolved O_2.

It is concluded that the effects of solution interaction between the walls of the channelways and the ascending fluids can be ignored during the simulation of the hydrothermal system as a whole. Only the simulation of metasomatic zoning in the channel walls is of interest.

The zone of ore deposition is certainly the most interesting for geologists. This part of oceanic hydrothermal systems has been explored most extensively. The zone of ore deposition includes the ore body proper and the area of mixing with cold seawater on its surface.[10] Ore deposition in modern oceanic hydrothermal systems is controlled by two factors:

(a) mixing with seawater, which abruptly changes the temperature and, correspondingly, the migration ability of ore elements, but also, gives rise to chemical reactions between the mixed components; and

(b) considerable heat loss from the surface of the ore body, which leads to its conductive cooling and may cause metasomatic reactions within the body between the previously deposited material and the new portions of hydrothermal solution.

[10] Hydrothermal plumes are not considered in this paper.

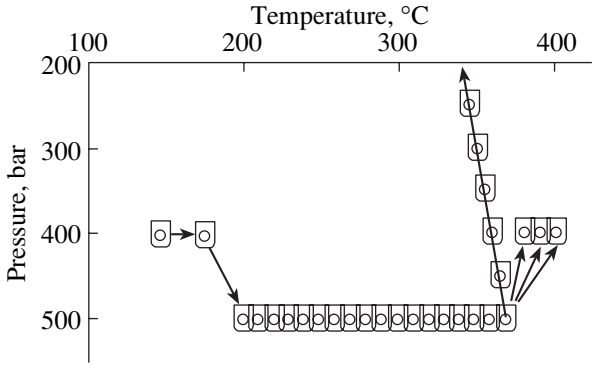

Fig. 19. Scheme of a chain of reactors in the *T–P* coordinates.

As was shown above, the relationships of these factors change with time owing to the growth of the edifice, which results in the zonal structure of the ore body evolving with time. The ore edifice is made up mainly of anhydrite, amorphous silica, and sulfides (the complete list of minerals is given in Table 3).

The temperature of ore deposition varies from 350 to 0°C, and most of the material is precipitated at temperatures above 200°C. Pressure corresponds to the hydrostatic value for the given ocean depth, 250–350 bar. According to available measurements, the discharge rates of individual black smokers are 0.*n*–*n*.0 kg/s (Table 5). The total discharge of large mounds comprising groups of active vents and significant diffuse venting may be an order of magnitude higher. The mixing proportions of hydrothermal solution and seawater vary from 0 to 100%, and the temperature of the mixture also depends on the mixing proportion. Mixing is a very fast process, which can result in the formation of metastable compounds (for instance, pyrrhotite instead of pyrite in smoke) and nonequilibrium states in some chemical reactions, especially redox reactions (Janecky and Seyfried, 1984).

There is an important aspect of the geological model that must be clarified: boiling in the focus and the ascending channel of the hydrothermal system, and its influence on ore formation. The thermodynamic modeling of boiling hydrothermal systems poses a special problem, which is examined in Chapter 6.

Thus, the input information for thermodynamic modeling includes the following characteristics of the geological model:

—distribution of temperature and pressure along the flow line of the solution;

—initial compositions of seawater and basalt;

—the general set of possible metasomatic and ore minerals; and

—bulk rock/water ratios, $\Sigma R/W$.

The following observations can be used for model verification:

—mineral assemblages of metasomatized rocks,

—compositions of hydrothermal solutions produced by the hydrothermal system and their dependence on the parameters of the system, and

—mineral assemblages of the newly formed ores.

The isotopic compositions of ore minerals and solutions can be used as an additional criterion, which is discussed in Chapter 5.

3.4.2. Physicochemical model

The physicochemical model that was utilized in this study to describe processes in oceanic hydrothermal systems belongs to the class of equilibrium dynamic models. It makes use of the MSFR method described in Section 2.2. According to this method, the hydrothermal system is represented by a series of reactors (steps), where an equilibrium thermodynamic state is achieved in local chemical systems in each step and in each stage computation. The bulk composition of the system is controlled by dynamic relations: transportation of solution between reactors in each stage of computation and interaction of solution with new portions of fresh rock. The mineral products formed during the previous stages of calculation remain in the reaction zone.[11] Thus, the passage of a solution portion (wave) through a step reactor simulates the process of water–rock interaction along the flow line of the solution. The sequential movement of many portions (waves) of solution through the downwelling and upwelling limbs of convection cells and the zone of ore deposition simulates the development of the hydrothermal process in time.

Calculations were carried out in the temperature range 150–400°C. Lower temperature conditions were not considered because of the weak influence on the ore potential of the system. The division of the convection system into isothermal steps is shown in Fig. 19. The temperature increment was taken as 25°C at 150–200°C and 10°C at 210–400°C. The temperature increment was reduced to 5°C in the upwelling limb and in the zone of ore deposition till 300°C in order to characterize ore deposition occurring in these zones in more detail. The reactor chain consisted of up to 50 sequential steps in some model variants. The correlation between temperature and pressure in each step (Fig. 19) approximated the conditions of solution flow through the contact zone of a magma chamber (Fig. 16). In some model variants, the solution composition obtained in the 350, 380, and 400°C steps were used as initial solutions for the upwelling limb of the system. This allowed us, in particular, to estimate the influence of temperature in the focus of the system on metal transportation by solutions.

In each stage of calculation, the solution was completely transferred from step to step. The rate of solu-

[11] A more complex dynamic system was used for the zone of ore deposition, see Section 4.3.2.

Table 18. Minerals and dissolved species used in the thermodynamic model

Minerals			Dissolved species			
Quartz (Qtz)	Zoisite (Zo)	Serpentine (Srp)	H_2O	Fe^{++}	$PbCl^+$	H_2^0
Calcite (Cal)	Prehnite (Prh)	Brucite (Brc)	H^+	$FeOH^+$	$PbCl_2^0$	CH_4^0
Dolomite (Dol)	Lawsonite (Lws)	Graphite (Gr)	OH^-	$FeCl^+$	$PbCl_3^-$	O_2^0
Magnesite (Mgs)	Wairacite (Wai)	Halite (Hl)	K^+	$FeCl_2^0$	$PbCl_4^{--}$	SO_4^{--}
Hematite (Hem)	Laumontite (Lmt)	Anhydrite (Anh)	KCl°	$FeOHCl^\circ$	Zn^{++}	HSO_4^-
Magnetite (Mag)	Heulandite (Hul)	Pyrite (Py)	Na^+	$FeOHCl_2^-$	$ZnOH^+$	$NaSO_4^-$
Albite (Ab)	Pumpellyite (Pmp)	Troilite (Po)	$NaCl^0$	$Fe(OH)_2^+$	$ZnCl^+$	$CaSO_4^0$
Microcline (Mc)	Muscovite (Ms)	Galena (Gn)	$NaHCO_3^0$	$Fe(OH)_3^0$	$ZnCl_2^0$	$MgSO_4^0$
Clinochlore (Cch)	Paragonite (Pg)	Sphalerite (Sph)	Ca^{++}	$Al(OH)_2^+$	$ZnCl_3^-$	H_2S^0
Daphnite (Dph)	Diaspore (Dsp)	Chalcocite (Cc)	$CaCl^+$	$Al(OH)_3^0$	$ZnCl_4^{--}$	HS^-
Tremolite (Tr)	Kaolinite (Kln)	Chalcopyrite (Ccp)	$CaCl_2^0$	$Al(OH)_4^-$	$CuCl^0$	Cl^-
Fe-tremolite (Fe-Tr)	Pyrophyllite (Prl)	Bornite (Bn)	Mg^{++}	$H_2CO_3^0$	$CuCl_2^-$	HCl^0
Epidote (Ep)	Talc (Tlc)	Sulfur (Su)	$H_2SiO_4^0$	HCO_3^-	$CuCl_3^-$	

Intermediate minerals
Chlorite–50 (Cch : Dph 1 : 1) (Chl50)
Chlorite–75 (Cch : Dph 1 : 3) (Chl75)
Actinolite–80 (Tr : Fe-Tr 4 : 1) (Act80)
Epidote–75 (Ep : Zo 3 : 1) (Ep75)
Epidote–60 (Ep : Zo 3 : 2) (Ep60)
Sericite (Ms : Pg 1 : 1) (Ser)

Note: Symbols of minerals used in this paper are given in parentheses. Quartz was changed to amorphous silica (ASi) during the simulation of solution cooling.

tion–rock interaction was defined in the model in the same manner as described in Section 2.2 [Eq. (9)] using the similarity criterion $(\Sigma R/W)_1$. This parameter varied over a wide range from 0.03 to 10, which overlaps its natural dispersion (Table 12). The propagation of the zone of metasomatized rocks with time was governed by the diffusion model of Korzhinskii [Eq. (11)]. The limiting proportion for the complete basalt alteration [right-hand side of inequality (12)] was taken as 80 kg of rock per one kilogram of solution, which corresponds to basalt and hot water densities of 2.9 and ≈0.7 g/cm^3, respectively, and a fracture porosity of ≈5% (Hyndman and Drury, 1976).

Thermodynamic data. Thermodynamic equilibria in the system were described within the 15-component multisystem H–O–K–Na–Ca–Mg–Fe–Al–Si–C–S–Cl–Cu–Zn–Pb. The model did not include Mn and Ba, because they do not form their own phases in the downwelling limb but occur as isomorphous components in metasomatic minerals. There are no reliable thermodynamic data for such compounds, which prevents a reliable calculation of the behavior of Mn and Ba during hydrothermal solution formation. The concentration of Mn in the initial chemical analysis of fresh basalt (Table 17) was added to Mg, and that of Ba, to Ca.

The multisystem included 45 fixed-composition minerals and aqueous solution, which was described by 50 dissolved species. The minerals and the solution species are listed in Table 18. Since some rock-forming minerals of metasomatic rocks (actinolite, epidote, and chlorite) are solid solutions, the model included both end-members and intermediate compositions from the typical ranges of the objects modeled (Gillis and Robinson, 1990). The energies of formation of intermediate

chlorites, actinolite, and sericite were calculated assuming ideal multisite mixing, and the model of Bird and Helgeson (1980) was used for epidote. The model accounted for the most important dissolved species of the elements: free ions and chloride and hydroxo complexes. Sulfate and hydrocarbonate complexes of the major components were also calculated. Preliminary calculations (Grichuk *et al.*, 1985) showed that under the model conditions, sulfate, hydrosulfide, and hydroxo–carbonate complexes of ore elements are never predominant, which allowed us to omit these species from the model. The set of complex compounds used in our model is rather typical of such modeling exercises with hydrothermal processes (Rafal'sky, 1993).

The set of minerals considered (Table 18) provides some simplifications to the physicochemical model in comparison to the geological model, which must be taken into account during interpretation. The most important among them are the following.

(a) The multisystem does not include smectites because of the lack of reliable thermodynamic data. Hence, the mobility of Al can be overestimated and the pH may be too alkalic in the low-temperature part of the system (150–200°C).

(b) Isomorphic substitution of Zn and Pb in aluminosilicates is ignored. This results in the overestimated mobilization of ore elements from metasomatic rocks in the absence of Zn and Pb sulfide minerals.

Thermodynamic data (g_T) for equilibrium calculations in the multisystem were taken from the UNITHERM data bank (Geochemistry Department, Moscow State University). The g_T values of simple (base) ions were calculated in the data bank using the modified Helgeson–Kirkham–Flowers model (Johnson *et al.*, 1992), and those of complex ions were extrapolated by the Ryzhenko equation. The extrapolation of the properties of complex ions of ore elements was based on the following reference experimental data: Plyasunov and Ivanov (1990) for Zn, Var'yash (1991) for Cu, and Seward (1984) for Pb. The thermodynamic characteristics of H_2S and complex Fe species were additionally refined. The data used to derive the thermodynamic properties of substances compiled in the UNITHERM data bank were described by Borisov (2003).

The activity coefficients of dissolved species were calculated by the third approximation of the Debye–Hückel equation. The values of *å* were taken after Garrels and Christ (1965), and those for complex ions absent in this compilation were taken as 4.5 (Rafal'sky, 1993). The temperature dependence of the coefficient of the linear term was taken from Helgeson and Kirkham (1974).

Quality control of thermodynamic calculations. The errors of thermodynamic calculations related to the accepted characteristics of substances must be discussed. The determination of these errors is one of the most difficult problems in the modern thermodynamics of geochemical processes, and it is not yet rigorously solved. Various approaches were discussed by Karpov *et al.* (1976) and Dorogokupetz and Karpov (1984).

The UNITHERM data bank does not include global procedures for the derivation of internally consistent data, which are implemented in the DIANIK and THERMINEOS data banks (e.g., Dorogokupetz and Karpov, 1984). Thermodynamic parameters from UNITHERM must be preliminary refined using some particular systems. It is known that experimental data and, correspondingly, thermodynamic constants derived from them involve random and systematic errors. The confidence limits provided in publications usually characterize only random experimental errors. A combined processing of many experimental investigations may reveal systematic errors in particular data series. If the experimental information is limited, systematic deviations are possible. Their influence on the results of calculations in multicomponent systems cannot be determined from the confidence intervals.

The overall quality of calculations can be assessed for particular (with certain sets of elements and conditions) types of systems by the simulation of experiments in complex systems. A number of reliable experimental studies have been reported for multicomponent systems approaching complex geologically relevant systems. The results of these experiments cannot commonly be used to derive fundamental thermodynamic constants (formation constants of complexes and free energies of compounds). However, they can be applied for the integrated assessment of thermodynamic data sets obtained in simpler systems. This method was used in a number of studies (e.g., Rafal'sky, 1993).

For the problems related to hydrothermal ore formation, the experimental study by Hemley *et al.* (1992) is of special significance in this respect. These authors studied the combined solubility of the most important sulfides of Cu, Zn, and Pb in chloride solutions in equilibrium with the microcline–muscovite–quartz and pyrite–pyrrhotite–magnetite buffer associations. An important point is that the experiments of Hemley *et al.* (1992) reached equilibrium. Experiments in the basalt–seawater system are chemically closer to the subject of our study. Unfortunately, they are not suitable for the assessment of the quality of equilibrium calculations, because equilibrium states are not reached in such systems even in very long experiments (up to two years).

Using the UNITHERM database, we calculated a model reproducing Hemley *et al.*'s (1992) experiments. Figure 20 compares the results of these experiments and calculations for ore metal concentrations at 300–400°C and a pressure of 500 bar. It can be seen that there is general agreement between the calculated and experimental parameters, although there is a small systematic error for all metals, positive for Fe and Zn and negative for Cu and Pb. In this case the mean square deviation for the total concentrations of ore metals is ±0.26 logarithmic units. This value can be regarded as

a general approximate estimate of the error of equilibrium calculations for the minor components of the system. The concentrations of major components are defined by mass balance equations, and the quality of calculation depends on the accuracy of the bulk compositions of initial solutions and rocks. The relative errors in these values are no higher than 20%.

The uncertainty of this estimate of the accuracy of thermodynamic calculations is related primarily to the fact that the calculated model assemblages of aluminosilicate minerals are more complex than those in Hemley *et al.*'s (1992) experiments. Unfortunately, there are no reliable experimental data on the composition of equilibrium solutions in systems containing coexisting epidote, actinolite, chlorite, albite, sulfides, and other aluminosilicates present in the model multisystem (Table 18). However, the experiments that were used for testing were carried out under temperature, pressure, pH (pH_T = 4.5), and chloride contents similar to those of oceanic hydrothermal solutions. Hence, the solubilities of ore metal sulfides in the experimental solutions are also close to those observed in the ocean.

The test performed here does not guarantee the reliability of calculations for individual species, because owing to the competitive character of complexation, the corresponding errors can be mutually compensated in the total solubility of elements. This compensation suggests that any extreme extrapolation of the estimation of accuracy is dangerous, especially with respect to temperature. However, Hemley *et al.*'s experiments were performed in the same range of conditions as our calculations (300–400°C and 500 bar as compared with 150–400°C and $P_{sat.\ vap}$ = 500 bar in model calculations). The estimated accuracy of total concentrations will be little changed if proper allowance for compensated errors is made.

Thus, the total errors of the equilibrium calculation are estimated as ±0.1 logarithmic units for the concentrations of major components and ±0.5 logarithmic units for trace components.

3.4.3. Software for thermodynamic modeling

Thermodynamic calculations relevant to the problem addressed in this study were performed from 1980–1990s using the GIBBS program developed by Yu.V. Shvarov at the Geochemistry Department of Moscow State University. The results were reported by Grichuk and Borisov (1983), Grichuk *et al.* (1985), Grichuk (1988), and *Hydrothermal Sulfide…* (1992). The GIBBS program was designed for equilibrium calculations in chemical systems of an arbitrary phase complexity (*Methods of…*, 1988) and was implemented in high-performance computers of the Minsk and ES series. The GIBBS program was not intended for model calculations with dynamic scenarios.

In 1991–1992, together with M.Yu. Korotaev, the author developed the GBFLOW program for the calculation of equilibrium dynamic models by the method of a step flow reactor on IBM-compatible personal computers. All the model calculations presented henceforth were performed by the author using this program. The GBFLOW program includes a block for the minimization of the Gibbs free energy of the system, which was previously created by Shvarov as part of a simplified version of the GIBBS program for small computers.[12] Subsequently, GBFLOW was optimized by the author for the calculation of models using the MSFR method, which increased its performance rate in such problems by approximately one order of magnitude. The GBFLOW v.3.1 (1995) used for calculations in this study includes a block for isotopic chemical modeling (Chapter 5), and the format of its output files is oriented for the subsequent graphical processing using the MS Excel package. On the basis of the GBFLOW program, the author developed the following versions for the calculation of models with special dynamic scenarios:

—GRDEP, for the simulation of a growing ore body (Section 4.3.2); since such models require considerable computation time, GRDEP is also compatible with the UNIX platform; and

—PENG, for the calculation of boiling systems (Chapter 6).

The precision of computational programs can be estimated by comparing the results obtained by several programs for the same problem. Such a test for GBFLOW was performed by Borisov and colleagues using the GIBBS program, which, in turn, was compared with the SELECTOR program developed at the Siberian Institute of Geochemistry (e.g., Borisov and Khodakovsky, 1989). The programs yielded identical results for thermodynamic equilibria within the declared calculation accuracies (GBFLOW: 0.001% for

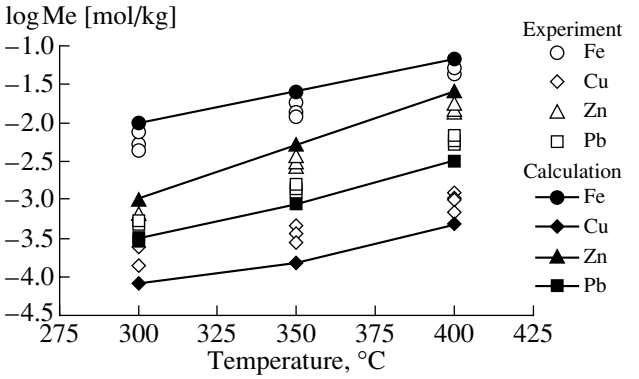

Fig. 20. Comparison of model results with experiments on the dissolution of buffer associations (Hemley *et al.*, 1992). Experimental conditions: T = 300–400°C, P = 500 bar, 1 mol NaCl, and excess Py + Po + Mag + Kfs + Ms + Qtz + Ccp + Sp + Gn.

[12] This block allows the calculation of systems with partially determined phase compositions, where the presence of an aqueous solution is mandatory.

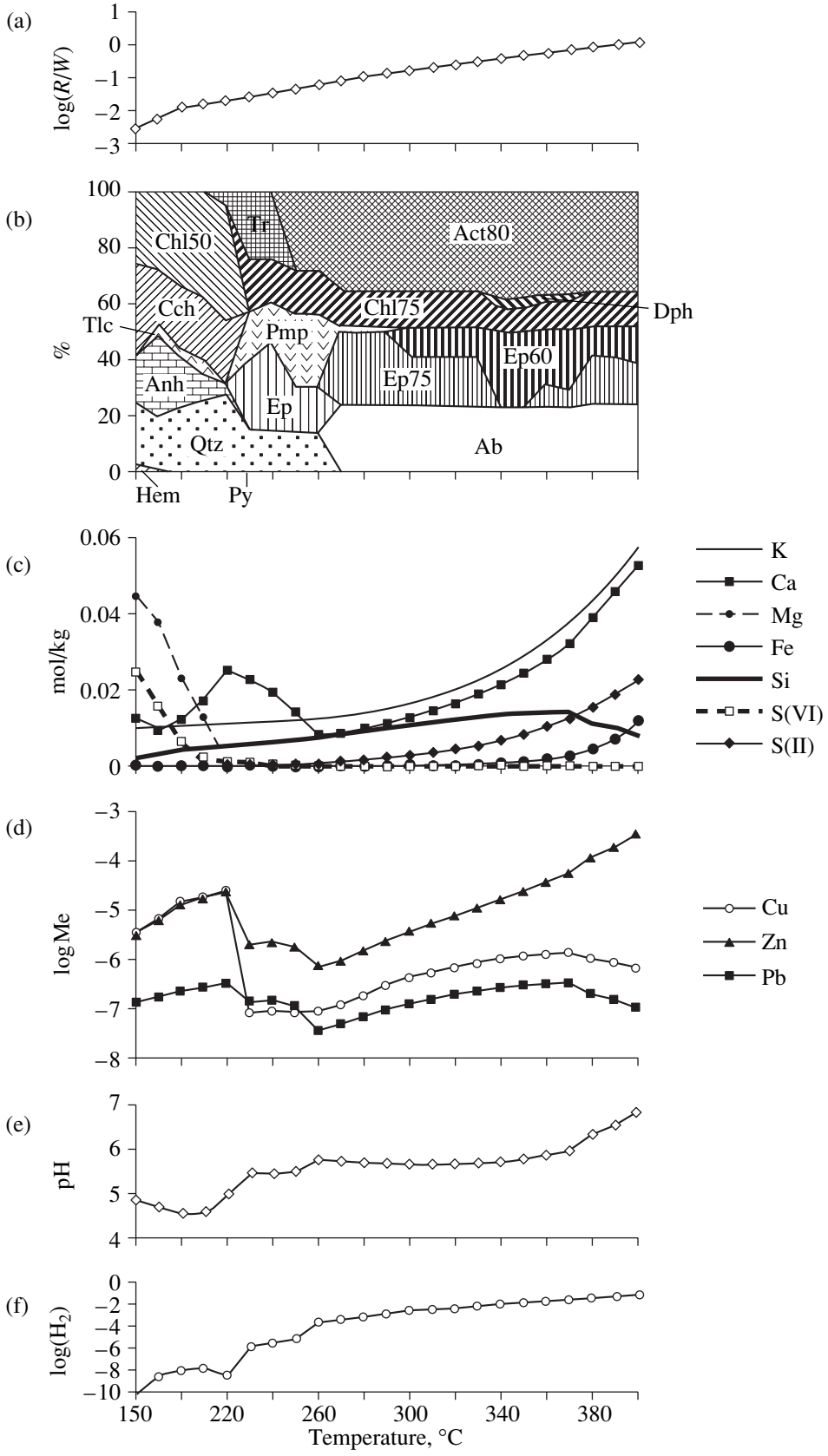

Fig. 21. Results of the simulation of seawater–basalt interaction in the downwelling limb of a hydrothermal system for the model case with total $R/W(400°C) = 1.26$ and wave no. 1. (a) Cumulative R/W, (b) mineral assemblages, (c) major components of solution, (d) heavy metals in the solution, (e) pH, and (f) equilibrium hydrogen activity.

the concentration of a substance, if the abundances of its elements are higher than 10^{-7} mol/kg H_2O).

The thermodynamic data bank UNITHERM was used in this study. It was created at the Geochemistry Department, Moscow State University by Shvarov with the participation of Borisov and Grichuk. The processing of experimental data and derivation of the thermodynamic characteristics of dissolved species were carried out by the author using the UT-HEL and UT-RYZ programs designed by Shvarov.

CHAPTER 4. SIMULATION OF GEOCHEMICAL PROCESSES IN THE HYDROTHERMAL SYSTEM OF A MID-OCEAN RIDGE

4.1. Results of Simulation for the Downwelling Limb of a Convection System

4.1.1. Model of a short-lived hydrothermal system

Let us consider first the results of calculation for seawater interaction with fresh basalt, i.e., a model variant (first wave) corresponding to the initial stages of hydrothermal activity or short-lived systems. This calculation is illustrated by Fig. 21.

Metasomatic mineral assemblages are controlled in the model by temperature and the amount of rock reacting with solution. At low *R*/*W* and low *T*, basalts are altered to metasomatic mineral assemblage I: quartz + chlorite + hematite + anhydrite ± kaolinite ± talc. Mg is removed from the solution to form chlorite, and iron and sulfur are oxidized in the basalts by seawater-dissolved oxygen. Most of the basaltic components (except for Al, Fe, Si, and Mg) are extracted by the solution. The migration of Ca from the rock to water causes anhydrite precipitation.

An increase in *T* and related intensification of solution–rock interaction (i.e., an increase in *R*/*W*, Fig. 21a) change the metasomatic association. In the case with $T > 230$°C and $R/W > 0.027$ (Fig. 21b), the basalt is altered to assemblage II: chlorite + epidote + actinolite ± quartz ± sulfides. Albite is added to the assemblage at $R/W > 0.06$. Pumpellyite is also stable in this association up to temperatures of 260–290°C. In the assemblage II field, the solution is reduced and contains significant amounts of H_2S and H_2. The development of assemblages I and II is a persistent feature of the model and, as will be shown below, a change from one assemblage to the other affects the composition of solution and the behavior of ore elements.

Since the transition from association I to association II is of particular importance, it should be determined whether temperature or *R*/*W* value is the major controlling factor. To this end, we performed a series of calculations, in which varying Σ*R*/*W* values were reached (from 0.02 to 12 at a temperature of 400°C). In the Σ*R*/*W*–*T* coordinates, the calculated trends are subparallel (Fig. 22a) and the points of reactor steps with identical mineral assemblages form separate areas. It can be clearly seen that the boundary between the fields of

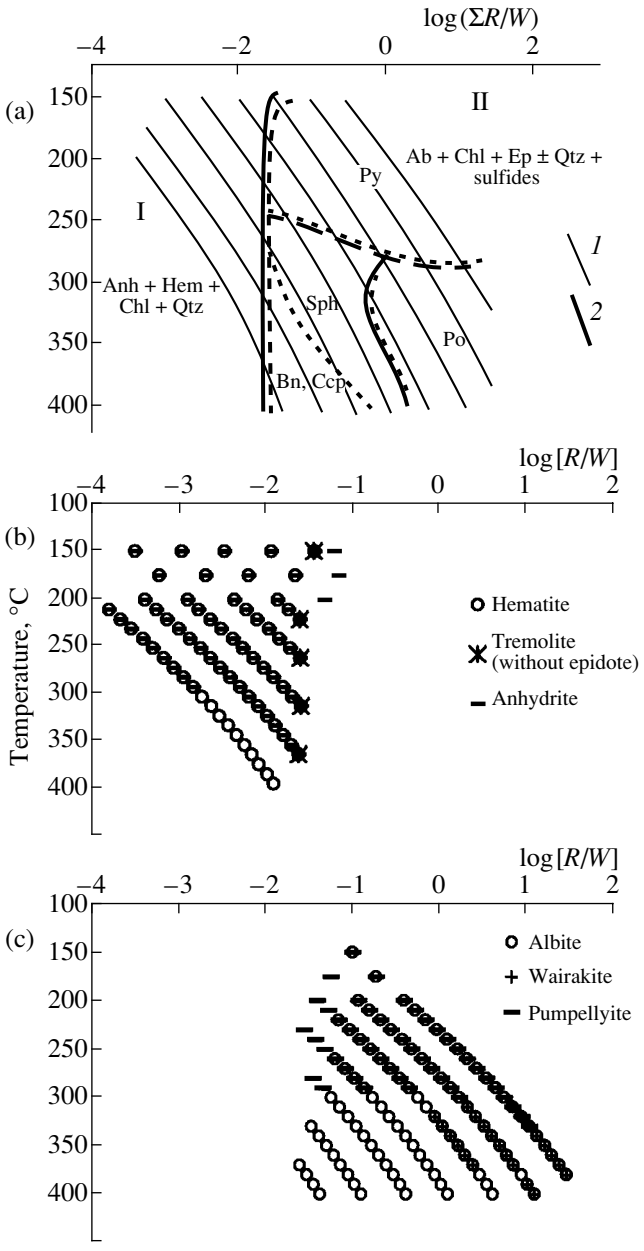

Fig. 22. Stability fields of mineral assemblages and some indicator minerals in the downwelling limb of a hydrothermal system (wave no. 1). (a) Stability fields of assemblages I (Anh + Hem + Chl + Qtz) and II (Ab + Chl + Ep ± Qtz ± sulfides) and sulfide minerals with (*1*) solution flow lines and (*2*) the boundary between associations I and II. (b) Stability fields of hematite, anhydrite, and tremolite (without epidote). (c) Stability fields of albite, wairakite, and pumpellyite.

assemblages I and II, which is marked by the appearance of epidote, is controlled primarily by *R*/*W* and lies within the interval 0.02–0.03. The position of this boundary shows only a very weak dependence on temperature. It is caused by two reasons: (a) changes in the thermodynamic properties of the reactants (pumpelly-

ite and quartz occur in association II at low temperature, whereas pumpellyite is absent at high temperatures; Fig. 22c); (b) the previous history of the solution: solutions attaining $\Sigma R/W \approx 0.03$ at high temperatures lose a significant amount of anhydrite during heating.

A detailed analysis of the results of the simulation showed that assemblage I changes to assemblage II not directly but through transitional mineral associations (Fig. 22b), which consist of various combinations of tremolite, chlorite, quartz, hematite, and some aluminosilicates observed only in this transitional zone (sericite and pyrophyllite). The real existence of these transitional assemblages is not quite clear. The fractions of these aluminosilicates are not large, and their appearance could be related to the fact that the model ignored aluminous end-members of rock-forming actinolite and chlorite. When albite and pumpellyite appear in association II, these phases disappear and the *R*/*W* range where the transitional assemblages are stable is only from 0.025 to 0.04 (Figs. 22b, 22c). These transitional associations have no particular effect on the calculated solution composition.

Within the downwelling limb, sulfide minerals are stable only in the assemblage II zone (Fig. 22a). Sulfides are dissolved and partly oxidized at low *R*/*W*. The stability conditions of sulfide minerals are different in the zone of assemblage II. The smallest field is characteristic of iron sulfides: pyrite is stable only up to a temperature of 250–270°C, and pyrrhotite is present in the mineral association at higher temperature and $R/W > 0.3$. At low temperatures sphalerite and galena are stable at $R/W > 0.03$, but when temperatures increases above 300°C, their fields are reduced and shift to higher *R*/*W*. The zone of assemblage II closely corresponds to the stability field of copper sulfides. At high *R*/*W* disseminated chalcopyrite forms in the rock, and bornite occurs near the boundary. In the transitional assemblages, copper is usually incorporated into chalcocite. These features suggest that sulfide minerals can occur in metasomatized basalts only in reduced environments. The differences between their stability fields are related primarily to the different temperature dependencies of sulfide solubilities. The small stability field of pyrrhotite, which is the main repository of sulfur in fresh basalts, indicates rapid mobilization of magmatic sulfur under the influence of hydrothermal solutions, which was in fact observed in ocean floor basalts (Gitlin, 1985).

Major components of hydrothermal solutions. The compositions of hydrothermal solutions equilibrated with mineral assemblage I bear some resemblance to their source, seawater. They show near neutral acid–base and redox characteristics, the concentration of Mg in them is higher than those of Ca and K, and SO_4^{2-} is the second most abundant anion after Cl^-. In the stability zone of assemblage II, the chemical compositions of hydrothermal solutions change dramatically. In the high-temperature part of the system, they are essentially free of Mg and SO_4^{2-} and enriched in Ca, K, Si, Fe, and H_2S (Fig. 21c). Some representative compositions of hydrothermal solutions obtained in various model variants are shown in Table 19. These results are, in general, consistent with the previously published versions of the model (Grichuk *et al.*, 1985; *Hydrothermal Sulfide…*, 1992).

The components of a solution can be divided into four groups on the basis of their behavior in the system: (1) those occurring mainly in the liquid phase: Cl, Na, K, and H_2O; (2) components occurring mainly in the solid phase and whose behavior is controlled by the solubility of rock-forming metasomatic minerals: Mg, Ca, Fe, Al, Si, H^+, and OH^-; (3) components whose behavior is controlled by redox reactions: C, S, and H_2; and (4) chalcophile trace elements, which are controlled by the sulfur regime: Cu, Zn, and Pb.

Chlorine behaves conservatively in the solutions, and its concentration only slightly rises at high *R*/*W* owing to water fixation in the rock. The main chlorine species is Cl^-; of lesser importance are the complex species $NaCl^0$, $CaCl_2^0$, and, at high temperatures, HCl^0.

During water–basalt interaction under the stability conditions of assemblage I, sodium is completely extracted into solution. In the moderate-temperature transitional region, the concentration of Na ceases to increase when sericite appears in the system and albite crystallizes after $R/W \approx 0.6$ is reached (at any *T*). At higher *R*/*W* values, it gradually decreases, mainly at the expense of Ca–Na exchange (Table 19, solution nos. 5–7). The main dissolved Na species are Na^+, $NaSO_4^-$, and $NaCl^0$.

Almost within the whole range of conditions, potassium is extracted from the solid phase and is rapidly accumulated in solution. Its concentration is limited at high *T* and $R/W > 2$ by the formation of microcline (Table 19, solution nos. 6 and 7). Potassium is also partly retained in the transitional zone in sericite. Its predominant dissolved species is K^+ at low temperature, and KCl^0 occurs in similar concentrations at high temperatures.

Water is captured by the secondary mineral products of solution–basalt interactions. During the formation of metasomatic assemblage I, the water content is up to 8–12% of the mass of metasomatic rock. The formation of metasomatic assemblage II is accompanied by much less extensive hydration, about 2.5–3.0 wt %, because epidote and actinolite occurring in this assemblage are relatively poor in hydroxyl groups. However, during interaction with a large amount of rock (about 34 kg per one kilogram of solution), the solution can be completely exhausted.[13] The binding of water is about 3% in oceanic hydrothermal systems with ordinary *R*/*W* values of 0.5–2.0.

[13] This variant is not realized in actively discharging hydrothermal systems.

Table 19. Composition of ore-forming solutions calculated in different model cases

Solution component	Unit	Conditions and results of model calculations						
		$T = 300°C$, $P = 500$ bar, $R/W = 0.0169$, first wave	$T = 370°C$, $P = 500$ bar, $R/W = 0.0244$, first wave	$T = 370°C$, $P = 500$ bar, $R/W = 0.244$, first wave	$T = 370°C$, $P = 500$ bar, $R/W = 0.0335$, wave no. 53	$T = 370°C$, $P = 500$ bar, $R/W = 0.732$, first wave	$T = 370°C$, $P = 500$ bar, $R/W = 2.439$, first wave	$T = 400°C$, $P = 400$ bar, $R/W = 2.967$, second wave
Solution no.		1	2	3	4	5	6	7
Na	mmol/kg	481.4	482.5	478.4	470.5	441.7	363.2	267.8
K	″	10.6	10.8	19.22	7.03	37.9	82.6	72.5
Ca	″	18.7	26.5	23.22	33.29	32.1	48.8	84.9
Mg		7.19	0.0005	0	0.0004	0	0	0
Fe	″	3.53	2.06	1.88	1.71	2.53	2.69	15.7
Zn	μmol/kg	18.6	26.8	115.9	18.5	57.3	58.4	470.0
Cu	″	19.6	28.3	4.77	35.1	1.41	1.06	0.76
Pb	″	0.30	0.39	0.69	0.30	0.35	0.37	0.185
SiO_2	mmol/kg	10.9	15.2	12.76	14.4	14.2	15.1	10.51
Cl	″	545.9	545.9	545.9	545.9	545.9	545.9	545.9
H_2S	″	0	0.298	4.73	0.688	12.4	19.2	22.16
SO_4	″	1.73	1.82	0	0	0	0	0
pH_T		4.02	5.63	6.02	5.69	5.94	5.79	6.67
$pH_{25°C}$		6.09	5.60	4.05	4.20	3.51	3.63	3.63
Phase assemblage		Qtz Hem Cch Chl50 Tlc Anh	Ab Ep Chl50 Chl75 Act80	Ab Chl50 Act80 Ep75 Ep60 Sp Bn	Ab Chl50 Chl75 Act80 Ep Ep75 Bn	Ab Chl75 Dph Act80 Ep75 Ep60 Gn Sp Ccp	Ab Mc Chl75 Dph Act80 Ep60 Wai Po Gn Sp Ccp	Ab Mc Chl75 Act80 Ep75 Ep60 Po Gn Sp Ccp

Magnesium is intensely removed from solution within the whole range of model conditions. In the stability field of assemblage I, Mg is incorporated in chlorite (clinochlore) and talc; and into the fields of assemblage II and transitional assemblages, it is incorporated into actinolite. Its residual concentrations established in equilibrium with mineral assemblage II are 10^{-5}–10^{-7} mol/kg (in contrast to 53.2 mmol/kg in seawater). The decrease in magnesium content in the solution is approximately proportional to an increase in *R*/*W*. The main dissolved magnesium species is Mg^{2+}, and $MgSO_4^0$ also occurs at low *R*/*W*.

Calcium behavior in the hydrothermal system is more complicated, and its concentration forms a rather complex pattern in the $\Sigma R/W$–*T* coordinates (Fig. 23a). At low *R*/*W* values, calcium is extracted from basalts and magnesium substituted for it in metasomatic minerals. The extracted calcium immediately precipitates from the solution as anhydrite, which results in a slight decrease in the residual concentration of calcium in the solution (Fig. 21c). This decrease is more pronounced at high temperatures, because the solubility of anhydrite is negatively correlated with temperature. Since the amount of sulfates in hydrothermal solution is limited (seawater contains about 28.2 mmol/kg of sulfates), the concentrations of Ca and SO_4^{2-} become equal at $R/W > 0.01$, and then the concentration of Ca begins to increase. It reaches a local maximum in equilibrium with transitional assemblages (marked by the point of anhydrite disappearance), after which it decreases until the appearance of albite in the mineral assemblage. From that moment the concentration of calcium increases gradually again, owing mainly to its complexation and formation of $CaCl_2^0$ at high temperatures. This species is predominant in the high-temperature part of the system, whereas the low-temperature speciation includes major Ca^{2+} and minor $CaSO_4^0$ and $CaCl^+$. At temperatures of 370–400°C, the concentration of Ca in the hydrothermal solution is 3–8 times higher than that of the initial seawater.[14]

Almost within the whole range of concentrations, silica is gradually extracted from the basalts and accumulated in the solution. Its concentration increases monotonously with temperature reaching 10–

[14] These calculations are in agreement with the analyses of natural solutions and are strongly different from the results obtained in the early versions of the model (Grichuk *et al*., 1985) and the data of Bowers and Taylor (1985), where such a resemblance was not attained (see Section 3.3).

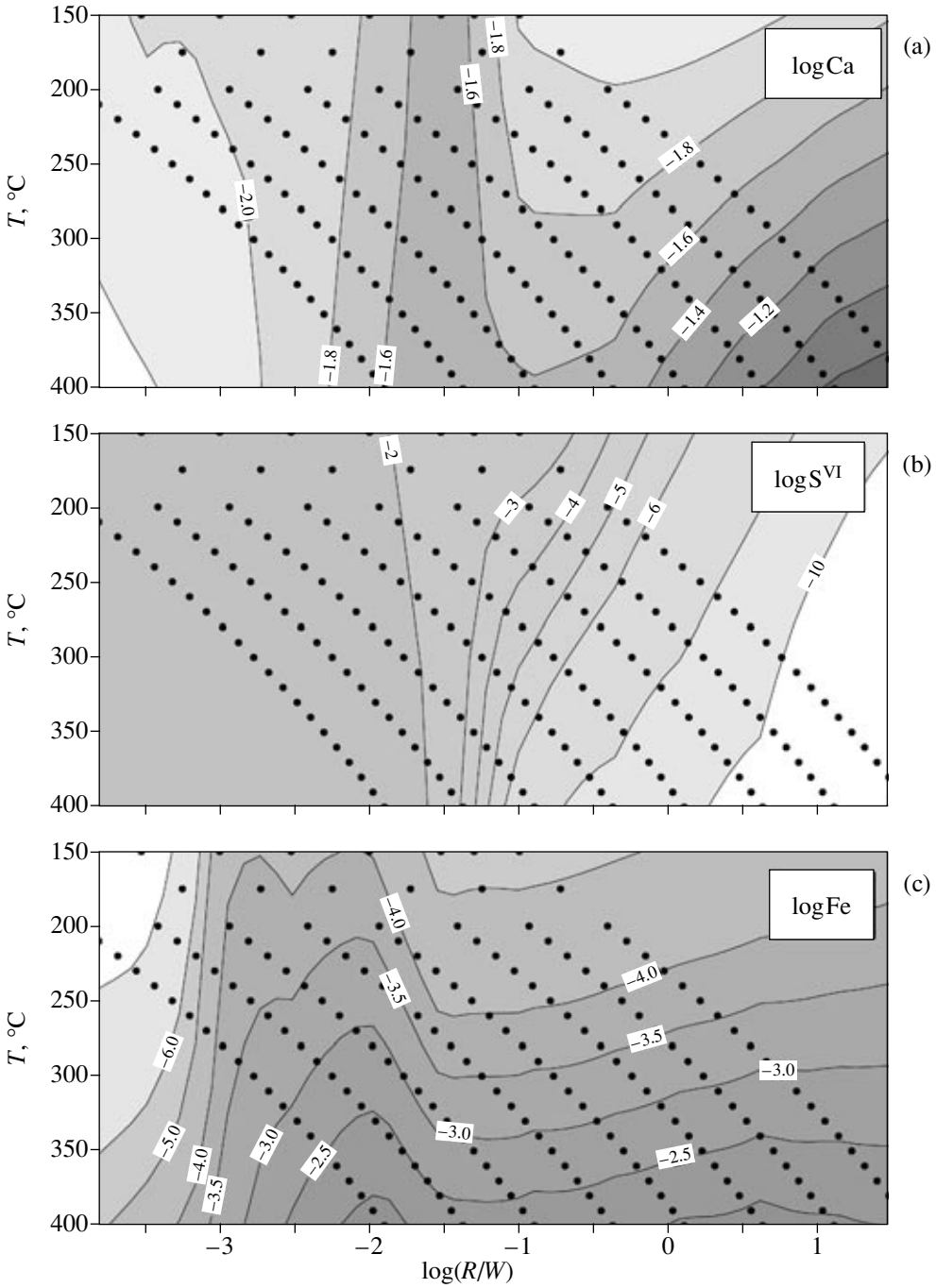

Fig. 23. Concentrations of components in solution as a function of temperature and rock/water ratio. (a) Ca, (b) S^{VI}, (c) Fe, (d) S^{II}, and (e) Fe/S^{II}.

15 mmol/kg in the hot part of the system. Note that at high *R*/*W*, quartz is absent in the mineral assemblage, and the hydrothermal solutions are not quartz-saturated. Similar conclusions were derived by Wells and Ghiorso (1991) on the basis of experimental data and investigation of natural prototypes.

Aluminum shows inert behavior in hydrothermal systems: it is tightly bound in aluminosilicates (chlorite, epidote, and albite) and is not extracted by solution. Its concentration in the low-temperature part of the system is $n \times 10^{-6}$ mol/kg, and $Al(OH)_3^0$ is the most abundant species. In the high-temperature part of the system, the concentration increases up to $n \times 10^{-5}$, and $Al(OH)_4^-$ is prevalent in the solution.

Considering the basalt–seawater system as a whole, iron is characterized by a relatively low mobility, which increases with increasing temperature owing to more

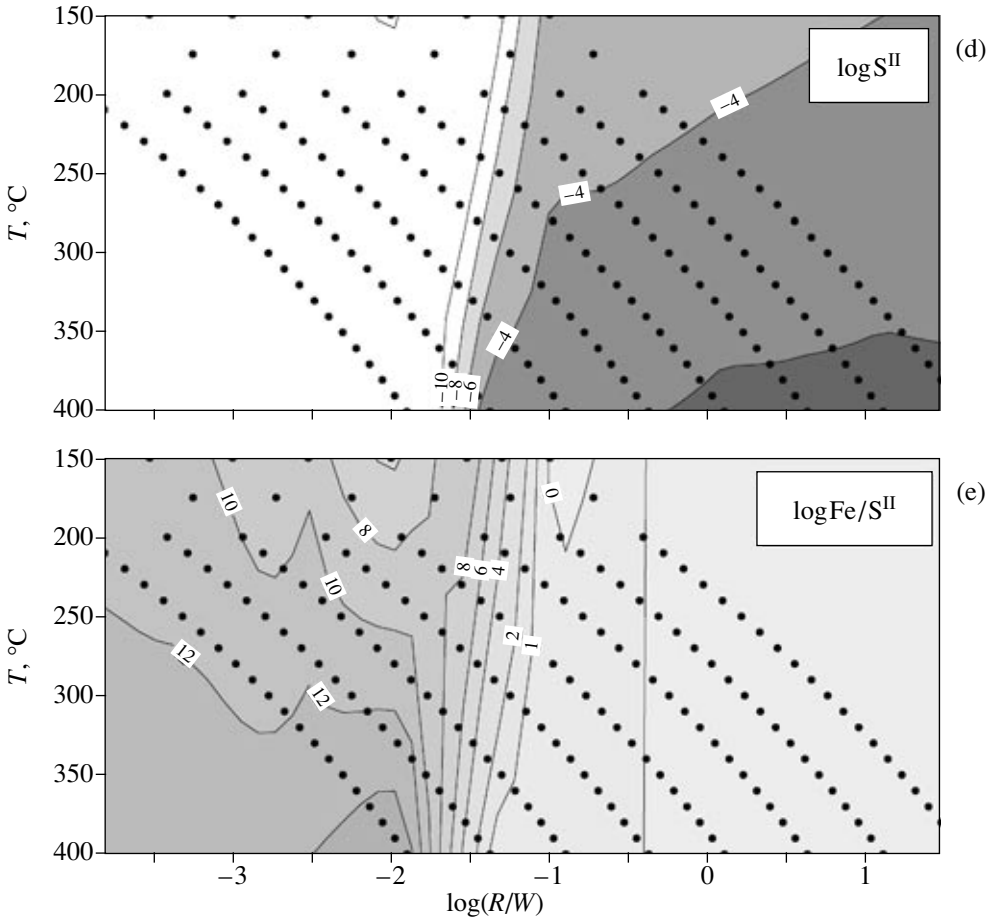

Fig. 23. (Contd.)

extensive complexation, primarily with the chloride ion. On the other hand, iron behaves differently in equilibrium with mineral assemblages I and II (Fig. 23b). At low R/W, when the main iron repositories are hematite (Fe^{III}) and ferromagnesian chlorite (Fe^{II}) (Figs. 21b, 22a), the solution is gradually enriched in iron (up to 0.3 mmol/kg at 200°C and $\Sigma R/W$ = 0.015 and 3.5 mmol/kg at 300°C and $\Sigma R/W = 0.017$; Table 19, no. 1). In the stability field of assemblage II, in equilibrium with iron-rich chlorite, epidote, and actinolite, iron content in the solution decreases abruptly and iron remains practically immobile at temperatures up to 280°C. The concentration of Fe in the solution increases only at temperatures higher than 350°C in response to more extensive complexation and reaches 3–12 mmol/kg under near critical conditions (Table 19, nos. 5–7; Figs. 21c, 23b). Within the whole range of model conditions, Fe^{II} prevails in solution; the major species are Fe^{2+} and $FeOHCl_2^-$ at low temperatures, and $FeOHCl_2^-$ and $FeOHCl^0$ at high temperatures (Fig. 24a). The concentrations of Fe^{III} complexes are negligible within the whole range of model conditions.

The behavior of sulfur in the solution is complicated by the existence of two valence states with high mobilities and strongly different properties, sulfate and hydrogen sulfide. The initial seawater is free of H_2S and contains 28 mmol/kg SO_4^{2-}. The fate of the sulfate ion is controlled in the low-temperature part of the system by two factors: (a) with increasing temperature, seawater reaches saturation with respect to anhydrite, whose solubility shows a negative temperature dependency (up to ≈300°C), and (b) Ca extraction from the basalt during its interaction with the solution enhances anhydrite deposition. The combined effect of these two factors scavenges sulfate species from the solution: in the case shown in Fig. 23c for T = 220°C and R/W = 0.02, only 1.07 mmol/kg of sulfate is retained in the solution, which is 4% of its initial concentration. In the cases that reach $R/W = 0.02$ at higher temperatures, the concentrations of SO_4^{2-} are even lower (Fig. 23c). The S^{II} of the initial basalt is completely extracted into solution and oxidized to SO_4^{2-} in this part of the downwelling limb. The equilibrium concentration of H_2S in the solution is no higher than 10^{-5} mmol/kg.

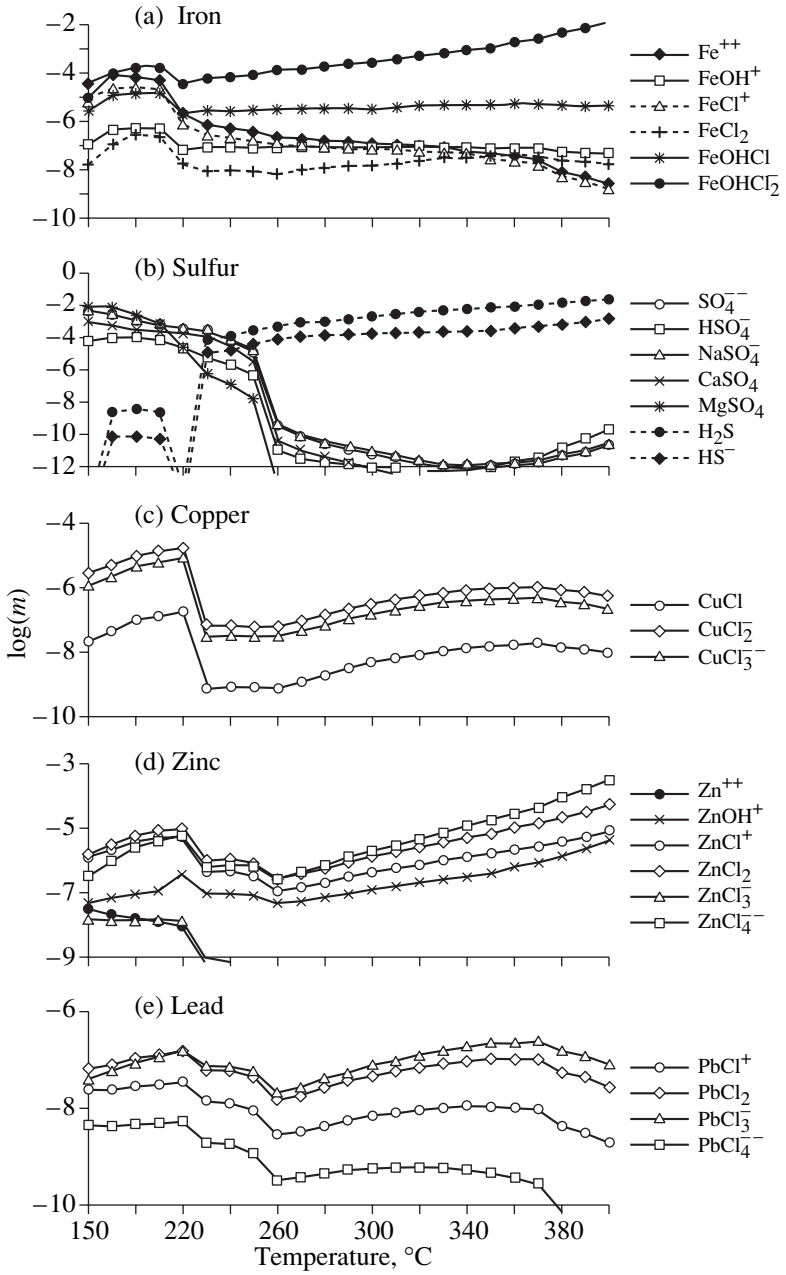

Fig. 24. Speciation of ore elements in solution for the model of the downwelling limb with the cumulative $R/W = 1.26$ (wave no. 1) corresponding to Fig. 21.

A sharp change in the behavior of sulfur occurs at the transition to assemblage II. When the buffer association epidote–iron-rich chlorite is produced from basaltic material, SO_4^{2-} is reduced, anhydrite disappears from the solid phase assemblage (Fig. 22b), and the concentration of SO_4^{2-} in the solution falls to almost zero. The concentration of H_2S increases (Fig. 23d) at the expense of both sulfate reduction and enhanced S^{II} mobilization from the basalt with increasing *R*/*W*. The solution becomes saturated with respect to initial magmatic sulfides at $T > 270$°C and $R/W > 1$, when FeS (model analog of pyrrhotite) appears in the mineral association (Fig. 22a). The concentration of H_2S in the solution increases up to 10–20 mmol/kg (Table 19), mainly at the expense of rock sulfur, which is suggested by the isotopic model (Chapter 5). As a result, in contrast to Fe, whose concentration in the solution depends on temperature only within the stability field of assemblage II, the concentration of S^{II} also varies with $\Sigma R/W$ (Fig. 23d). The relative amounts of sulfide sulfur and iron in the solution change depending on *T* and $\Sigma R/W$

(Fig. 23e): iron prevails over sulfur at low *R*/*W* and high *T* (>370°C). As will be shown below, these features of sulfur behavior are reflected in the histories of other ore elements.

Within the whole range of model conditions, S^{II} migrates mainly as $H_2S^0_{aq}$. S^{IV} occurs mainly as $MgSO_4^0$ in the beginning of the downwelling limb of the convection cell, when the solution is similar to seawater. With increasing Mg bonding in the rock, the fractions of SO_4^{2-} and $NaSO_4^-$ rise (Fig. 24), and HSO_4^- becomes the major species at high temperatures.

Carbon barely forms mineral phases within the range of model conditions. Only at very high *R*/*W* (>1) and low *T* was calcite obtained in the model mineral assemblage. Within the stability fields of mineral assemblage I and transitional assemblages, the main carbon species is $H_2CO_3^0$. Its content is 2 ± 1 mmol/kg within the whole range of conditions. The reduction of the system results in the appearance of methane in the solution. Its concentration reaches *n* mmol/kg at high *R*/*W*. The initial model basalt composition included a small amount of carbon (0.0088 mol/kg, Table 17), and the bulk C content of the solution increases during its interaction with rock. Although carbon was taken as CO_2 for the calculation of the redox state of the basalts, its concentration increases mainly at the expense of methane. This is not fully consistent with the data on oceanic hydrothermal systems, where CO_2 is more abundant than CH_4 (Tables 6, 9).

Acid–base conditions (pH). The downwelling limb of the system generally has near neutral pH_T values, within 2 units of the neutral value for the given temperature. There is a distinct tendency for pH_T to increase with increasing *R*/*W*. Solutions in contact with mineral assemblage I have pH_T 4–5, whereas those equilibrated with assemblage II show higher values from 5 to 7 (Table 19). There is an abrupt pH increase by approximately 1.0 when one assemblage changes to the other (Fig. 21e). In the stability region of assemblage I, the pH of the solution is defined by the precipitation of Mg minerals (talc and chlorite) and is therefore controlled mainly by the solution composition, primarily by its Mg content.

At high *R*/*W* the acidity of the solution is buffered by the reactions of mineral assemblage II (epidote + albite + chlorite + actinolite) with Na and Ca in the solution. A numerical experiment with the addition of a strong acid (HCl) into the 370°C reactor step (Table 20a) showed that the metasomatized rock is an efficient pH buffer. The addition of 20 mmol of acid to the system changed the pH by only 0.1 (addition of the same amount of acid to seawater shifts pH from 8 to about 2 at 25°C). Simultaneously, a significant amount of Ca is withdrawn into the solution, Na is removed from the solution, the concentration of the clinozoisite end-member in epidote increases (Ep60), epidote is partly dissolved, and the amounts of iron-rich chlorite and albite increase (Table 20a). This reaction can be simplified as

$$12\text{Ep} + 35\text{H}^+ + 6\text{H}_2 + 9\text{Na}^+ \longrightarrow \text{Zo} + 4\text{Dph} + 9\text{Ab} + 22\text{Ca}^{2+} + 17\text{H}_2\text{O}. \quad (17)$$

This equation is similar to the reaction derived by Seyfried *et al.* (1988) from the results of experiments in the water–basalt system.

In order to compare these results with observations in the natural analogs, the pH_T values need to be recalculated to pH_{25}. To this end, the following numerical experiment was performed: the solutions obtained for the downwelling limb were recalculated to equilibrium at 25°C without the formation of solid phases (except for sulfide and amorphous silica) and carbon dioxide reduction to methane. This experiment closely simulates quenching of natural hydrothermal solutions during sampling.[15] The recalculated pH_{25} values are systematically lower than pH_T, and the difference increases with increasing temperature and decreasing pressure of the hydrothermal solution, reaching 2–3 pH units. As a result, the pH_{25} values of solutions obtained at $\Sigma R/W > 0.2$ vary from 3.5 to 4.05 (Table 19), which is in agreement with natural observations (2.7–4.5, Table 6). The lowest pH_{25} values of about 2 were calculated for the solutions in equilibrium with assemblage II at a temperature of 425°C and a pressure of 400 bar; their pH_T values were about 6.

The change in pH during cooling is related, first, to the balance of hydrolytic reactions between solution components: the hydroxo complexes of Al and Fe, on one hand, and the undissociated acid species $H_2CO_3^0$ and H_2S^0, on the other hand; and, second, sulfide precipitation associating with an increase in solution acidity (this effect was discussed in detail by Rafal'sky, 1993):

$$FeCl_2^0 + H_2S \longrightarrow FeS + 2H^+ + 2Cl^-.$$

If *R*/*W* is low and *T* is high, the dissociation of HSO_4^-, whose concentration may be as high as *n* mmol/kg under such conditions, also contributes significantly to the pH change. At high *T* and *R*/*W* and low *P*, the aforementioned strong pH changes are due to HCl^0 dissociation.

Redox conditions and dissolved hydrogen. The redox conditions of the downwelling limb are defined by the proportion of valence forms of iron, sulfur, carbon, and hydrogen. In the multisystem modeled, copper can also occur in several valence states, but its content

[15] During sampling of high-temperature smoker solutions for pH measurement, it is not possible to prevent the generation of sulfide suspension (Trefry *et al.,* 1994).

Table 20. Results of a numerical experiment on the estimation of the buffer capacity of mineral assemblage II for the initial composition of the system corresponding to the case shown in Table 19 (no. 5): 370°C step, P = 500 bar, $\Sigma R/W$ = 0.732, and the first wave

(a) Influence of strong acid addition

Parameter	Initial composition	HCl addition, mmol			
		1	3	10	20
Solution components					
pH	5.936	5.931	5.921	5.884	5.834
Na, mmol	441.7	441.6	441.4	440.0	436.7
Ca, mmol	32.1	32.6	33.7	37.8	44.3
$-\log(H_2)$	1.750	1.754	1.761	1.778	1.787
Minerals, mmol					
Ab	115.2	115.3	115.4	116.9	120.2
Chl75	19.4	19.2	18.6	18.3	20.3
Dph	5.12	5.46	6.11	6.94	5.93
Act80	56.4	56.5	56.7	56.8	56.1
Ep75	17.2	14.5	9.3	–	–
Ep60	57.1	59.4	63.9	71.1	68.5

Addition of acid results in the simultaneous occurrence of several reactions: ion exchange of Ca^{2+} for H^+ and Na^+, partial dissolution of epidote, and reduction of Fe^{III}. Dissolved hydrogen and methane served as reducers. The integral reaction is

$$101.4H^+ + 9Na^+ + 28Chl75 + 262Ep75 + 15.5H_2 + 3.8CH_4 \longrightarrow 53Ca^{2+} + 9Ab + 33Dph$$
$$+ 8.6Act80 + 182Ep60 + 2.2Fe^{2+} + 5.1H_4SiO_4^0 + 3.8H_2CO_3^0 + 45.2H_2O.$$

The coefficients of this equation are noninteger, because it is a sum of several individual reactions (exchange, dissolution, and oxidation) and the contributions of these reactions depend on the composition of the system (for instance, on the ratio of methane and hydrogen concentrations). In general, if acid is added to the system, it is almost completely neutralized and Ca is extracted into solution. Epidote is enriched in the zoisite end-member, and chlorite is enriched in the iron-rich (daphnite) end-member;

(b) Influence of reducer addition

Parameter	Initial composition	H_2 addition, mmol					
		0.5	1	3	5	10	20
Solution components							
pH	5.936	5.938	5.94	5.946	5.948	5.954	5.965
Na, mmol	441.7	442.1	442.5	443.2	443.2	443.2	443.1
Ca, mmol	32.1	31.9	31.7	31.3	31.4	31.4	31.5
H_2, mmol	17.8	17.9	17.9	18.6	19.9	23.5	32.4
H_2CO_3, mmol	1.19	1.18	1.16	1.01	0.81	0.43	0.12
$\Delta(H_2)$	0	0.073	0.15	0.84	2.06	5.66	14.6
$-\log(H_2)$	1.75	1.75	1.75	1.73	1.70	1.63	1.49
Minerals, mmol							
Ab	115.2	114.8	114.4	113.7	113.7	113.7	113.8
Chl75	19.4	18.7	17.9	16.3	16.3	16.2	16.2
Dph	5.12	5.82	6.52	7.98	8.00	8.03	8.10
Act80	56.4	56.7	56.9	57.4	57.4	57.4	57.4
Ep75	17.2	13.0	8.7	–	–	–	–
Ep60	57.1	61.2	65.2	73.7	73.7	73.6	73.6

Table 20. (Contd.)
(c) Influence of oxidizer addition

Parameter	Initial composition	O_2 addition, mmol					
		1	3	10	30	60	100
Solution components							
pH	5.936	5.927	5.917	5.898	5.631	5.448	5.318
Na, mmol	441.7	440.2	439.0	438.9	431.6	421.6	420.0
Ca, mmol	32.1	32.8	33.4	33.5	37.5	42.9	56.2
H_2, mmol	17.8	17.5	16.2	11.6	0.15	0.01	5×10^{-15}
O_2, mmol	1.3×10^{-33}	1.4×10^{-33}	1.6×10^{-33}	3.1×10^{-33}	1.9×10^{-29}	2.7×10^{-27}	0.016413
S(VI), mmol	8×10^{-9}	8×10^{-9}	1×10^{-8}	4×10^{-8}	0.41	1.52	1.38
S(II), mmol	12.7	12.7	12.7	12.7	9.22	0.003	0
Minerals, mmol							
Qtz	–	–	–	–	–	21.3	1.14
Hem	–	–	–	–	–	5.88	61.0
Ab	115.2	116.7	117.9	118.0	125.3	135.3	113.6
Chl50	–	–	–	–	13.4	29.7	–
Chl75	19.4	22.5	25.1	25.1	13.0	–	–
Dph	5.12	2.31	–	–	–	–	–
Tr	–	–	–	–	–	7.57	50.0
Act80	56.4	55.5	54.7	54.6	50.0	34.5	–
Ep	–	–	–	–	28.5	77.6	62.9
Ep75	17.2	34.1	48.1	48.7	49.4	–	–
Ep60	57.1	40.8	27.3	26.7	–	–	–
Ser	–	–	–	–	–	–	46.7
Anh	–	–	–	–	–	11.3	11.5
Sulfides	0.27	0.27	0.27	0.26	1.70	–	–

is too low to exert a significant influence on the character of the processes.

Iron is the main variable valence element in the metasomatic rocks after basalts. In assemblage I, iron is incorporated into hematite (Fe^{III}) and ferromagnesian chlorite (Fe^{II}) (Figs. 21b, 22a). In association II iron is distributed among epidote (Fe^{III}) and iron-rich chlorite (Fe^{II}), as well as sulfides and actinolite at high *R*/*W*. The $Fe^{III}/\Sigma Fe$ ratio is higher than that of the initial basalt (0.15) in all model steps. This is indicative of the reaction of iron oxidation by oxidants supplied by seawater, O^2 and SO_4^{2-} and H_2O at high temperature. Since the solution contains a limited inventory of O_2 and SO_4^{2-}, the formation of epidote results in a gradual accumulation of hydrogen (Fig. 21f), whose concentration in the solution reaches $n \times 10^{-2}$ mol/kg in some calculated variants. Methane is also accumulated in the solution; however, since the amount of carbon in the system is low, methane is the third most important reduced component of solution, after H_2S and H_2.

For the interpretation of model data, it is important to determine the factors that control the redox state of the system. A numerical experiment with the addition of a reducer into the system (Table 20b) showed that accompanying changes can be described by the reaction

$$30\text{Ep} + 8\text{Cch} + 16\text{Ab} + 8\text{Ca}^{2+} + 15\text{H}_2 \longrightarrow 24\text{Zo} + 5\text{Dph} + 10\text{Act80} + 16\text{Na}^{+}. \quad (18)$$

Similar to the addition of acid (Eq. 17), this reaction results in Fe reduction and migration from epidote to iron-rich chlorite, but its influence on the composition of solution is the opposite: Ca is fixed and Na is released. The reducer has practically no effect on the pH of the system (Table 20b). Since reaction (18)

involves dissolved Ca and Na, the redox state of the system depends on their proportion:

$$f_{H_2} \approx K_{18}\frac{a_{Na^+}}{(a_{Ca^{2+}})^{1/2}}. \quad (19)$$

Therefore, mineral assemblage II is not a classic redox buffer (like NNO or QFM). Exchange reaction (18) only imposes some relations but does not control f_{H_2}. The capacity of the system with respect to reducers is very low. If only 3 mmol H_2 is added, the phase association is changed, $H_2CO_3^0$ reduction to methane begins, and the gain of H_2 concentration in the solution [$\Delta(H_2)$ in Table 20b] becomes practically equal to the amount of hydrogen introduced into the system (i.e., there is no buffering effect with respect to reduction).

The buffering capacity of the system with respect to the addition of an oxidant is significantly higher. The addition of oxygen to assemblage II shifts reaction (18) to the left. The solution is enriched in Ca^{2+} substituting for Na^+, and the iron of the rock is oxidized and transferred from chlorite and actinolite to epidote. However, these changes become significant only with a substantial addition of oxygen, more than 30 mmol per one kilogram of solution (Table 20c). A further oxygen input results in the disappearance of sulfides from the system and the appearance of anhydrite, dissolved sulfates, and hematite. The oxidation of the system is accompanied by a decrease in pH.

In the assemblage II field, the redox state of the environment is controlled by the balance of cations produced in the irreversible solution–basalt reaction. In the model case shown in Fig. 21 for a reactor step with a temperature of 300°C and $\Sigma R/W = 0.169$, this balance is expressed as (in moles per one kilogram of initial rock):

$$\begin{aligned}&\text{Basalt} + 1.62H_2O + 0.123Na^+\\ &\longrightarrow 0.917Ab + 0.198Chl + 0.593Ep + 0.428Act\\ &+ 0.023H_4SiO_4 + 0.038K^+ + 0.042Ca^{2+}\\ &+ 0.0017Fe^{2+} + 0.0016OH^- + 0.015H_2\\ &+ 0.018CH_4 + 0.0175H_2S.\end{aligned} \quad (20)$$

The same balance for a temperature of 370°C and $\Sigma R/W = 0.732$ is

$$\begin{aligned}&\text{Basalt} + 1.58H_2O + 0.110Na^+\\ &\longrightarrow 0.903Ab + 0.192Chl + 0.582Ep + 0.443Act\\ &+ 0.0016H_4SiO_4 + 0.038K^+ + 0.033Ca^{2+}\\ &+ 0.0051Fe^{2+} + 0.00015Zn^{2+} + 0.0055OH^-\\ &+ 0.035H_2 + 0.0081CH_4 + 0.0183H_2S.\end{aligned} \quad (21)$$

With an increase in R/W, the newly formed epidote is enriched in the clinozoisite end-member, and chlorite gains the daphnite end-member (this is reflected in the change of calculated transitional phases of variable composition: Ep ⟶ Ep75 ⟶ Ep60 and Cch ⟶ Chl50 ⟶ Chl75; Fig. 21b). Because of this, $Fe^{III}/\Sigma Fe$ gradually decreases along the flow line approaching 0.30–0.32. In such a way, a balance between the reducing substances of the rock and the accumulation of reduced products is established in the moving solution.

Trace ore metals. The behavior of ore elements is closely related to changes of metasomatic assemblages.

In the stability region of assemblage I, copper is mainly removed from the basalt at the expense of chalcopyrite oxidation and dissolution in seawater. In the stability region of assemblage II, solution is in equilibrium with chalcopyrite and bornite (at high T and low R/W) or chalcocite (along association boundaries) (Fig. 22a). Owing to the high content of H_2S, the equilibrium solubility of copper in the assemblage II region decreases abruptly, and its migration ability vanishes. A redox barrier at the boundary between assemblages I and II separates the segments of the downwelling limb with high and low copper mobility (Fig. 21d), and, consequently, is a boundary of copper precipitation. The main mobile copper species is $CuCl_2^-$ within the whole range of conditions (Fig. 24c).

The behavior of zinc in the system is simpler: it is removed from the assemblage I region and shows a low mobility in the assemblage II region, where it precipitates as sphalerite owing to high a H_2S content (Fig. 22a). It should be noted that the sphalerite-in line in Fig 22a does not exactly coincide with the boundary between the assemblages. It is displaced toward higher R/W at high temperatures. The concentration of Zn in sphalerite-saturated solution depends on temperature: it increases gradually with increasing T owing to enhanced complexation reaching $n \times 10^{-4}$ mol/kg at 400°C (Fig. 21d).

The same tendencies are exhibited by the behavior of lead. Similar to Zn and Cu, it is highly mobile in the stability region of assemblage I and of low mobility at high R/W in the presence of H_2S. Similar to sphalerite, the boundary of galena stability is shifted to high R/W, and both Zn and Pb are mobile within the stability region of assemblage II. The main mobile Zn species are $ZnCl^+$ and $ZnCl_2^0$ at low temperatures and $ZnCl_4^{2-}$ at high temperature; and those of lead are $PbCl_2^0$ and $PbCl_3^-$, respectively (Figs. 24d, 24e).

A comparison of the behavior of Cu, Zn, and Pb in the downwelling limb of the model is of special interest. Almost within the whole stability region of assemblage I, they are completely removed from the rock, and the proportions of their concentrations in the solution correspond therefore to those of the initial basalt ($Zn \approx Cu > Pb$). This relationship holds with an increase in the concentration of the elements in the solution related to increases in R/W and temperature. Within the

stability region of assemblage II, the concentrations of the elements decrease abruptly when the solution becomes saturated with respect to the corresponding sulfides. This change occurs in the sequence Cu → Zn, Pb. In the high-temperature part of the system, the model of the first wave (Fig. 21d) yields Zn > Cu ≈ Pb in the solution. Thus, according to the model, solutions are significantly enriched in zinc relative to copper and lead during the initial stage of high-temperature hydrothermal activity.

The results of calculations imply that the relative mobility (i.e., fraction of dissolved metal in its total content in reactor steps) of these elements decreases in the sequence Pb (23%) > Zn (12%) > Cu (0.9%).[16] This array differs from the sequence of sulfide solubilities, which is Zn > Cu ≈ Pb under the model conditions (Fig. 21d). The relative mobility is affected by the fact that the abundance of Pb in the initial rock is two orders of magnitude lower than those of Zn and Cu. Because of this, despite its relatively low solubility, Pb can be completely mobilized from the rock by solution, whereas the more soluble Zn is partly retained in the metasomatic rock as sphalerite.

4.1.2. Chemical evolution of the system during the development of the hydrothermal process (model of a long-lived hydrothermal system)

Long-lived hydrothermal systems differ from short-lived ones in two aspects important for the model considered: (1) the amount of metasomatized rocks gradually increases, and correspondingly, the fraction of unaltered basalts in the interior of the system and the rate of metasomatic zone propagation decrease; and (2) the composition of metasomatic rocks changes, because some elements are introduced with seawater and others are removed by hydrothermal solution. These phenomena are reproduced in our model by the passage of many sequential solution portions (waves) through a step flow reactor (Section 2.2). The amount of added fresh basalt decreases gradually in each step according to Eq. (13).

The results of calculations for such a model (corresponding to the first wave in Fig. 21) are shown in Figs. 25 and 26. The main result of the development of the process in the downwelling limb of the hydrothermal system is a gradual expansion of the stability region of assemblage I under the influence of the addition of oxidants (O_2 and SO_4^{2-}) and Mg and the removal of reducers (H_2, H_2S, and CH_4) by hydrothermal solution. The boundary between assemblages I and II travels along the flow line inside the system to higher temperature steps. This can be clearly seen from the expansion of the stability fields of hematite and anhydrite (Fig. 25) and the diminishing of the stability fields of epidote, actinolite, albite, and sulfides. The evolution is imprinted in the solution composition as an increase in the mobility of Mg and SO_4^{2-} introduced by seawater (Fig. 26).

The system evolves mainly owing to a gradual decrease in the rate of metasomatic zone propagation perpendicular to fracture walls. Correspondingly, the involvement of new portions of fresh basalt slows down, and *R*/*W* values decrease in the reactor steps. This influences the dissolution of easily mobilized components, such as S^{II}, K, and Pb. A decrease in *R*/*W* with each new solution portion (wave) reduces the concentrations of these components in the hydrothermal solutions (Fig. 27).[17] It is remarkable that iron, whose concentration in the solution is controlled by the solubility of aluminosilicates, shows a different behavior: in the beginning of the process, S^{II} > Fe in the solution (Fig. 21c), but this relation later reverses (Fig. 27a). An interesting feature of the late stage of development, when the boundary between the assemblages moves into the high-temperature region, is that the equilibrium concentration of sulfates increases within the assemblage II region. As can be seen in Fig. 26b, the residual concentration of SO_4^{2-} is 2 mmol/kg for wave no. 800. Under the corresponding temperature conditions, comparable amounts of sulfate and hydrogen sulfide (0.*n* mmol/kg) can coexist.

The extensive S^{II} removal results in the dissolution of sulfides that were formed during the early stages of simulation and the reduction of their stability fields (Fig. 25). The fates of the trace ore elements (Zn, Pb, and Cu) are different, and variations in their concentrations in the solution are not in tandem. This peculiarity of ore element behavior can be clearly seen from the composition of solution in the 370°C reactor step corresponding to the hottest part of the hydrothermal system (its focus) (Fig. 27b). Two regimes are possible for these elements, depending on whether or not sulfide saturation is reached in the given step.

(1) If the sulfide of an element is not formed at the local equilibrium between solution and metasomatic rocks, the element concentration in the solution decreases with each successive wave proportionally to *R*/*W*, which is exemplified by the behavior of Zn and Pb at large wave numbers (Fig. 27b).

[16] These estimates depend on *T* and *R*/*W*; the values presented here are mean squared values for the zone of assemblage II and the case shown in Fig. 21. The observed differences between the relative mobilities of Zn and Pb are within the uncertainties of the thermodynamic model.

[17] Periodic variations in hydrogen sulfide content were obtained in the model within the assemblage II region (Fig. 27a). They are artifacts of the computational procedure related to the discrete structure of a step flow reactor (Section 2.1). In particular, this is manifested in that within a temperature interval of up to 270°C, when the boundary between assemblages I and II jumps to the next reactor step, anhydrite and pyrite appear together in the set of minerals and the concentration of S^{II} increases simultaneously in solution. The subsequent water portions dissolve pyrite, and the equilibrium solution is depleted in hydrogen sulfide.

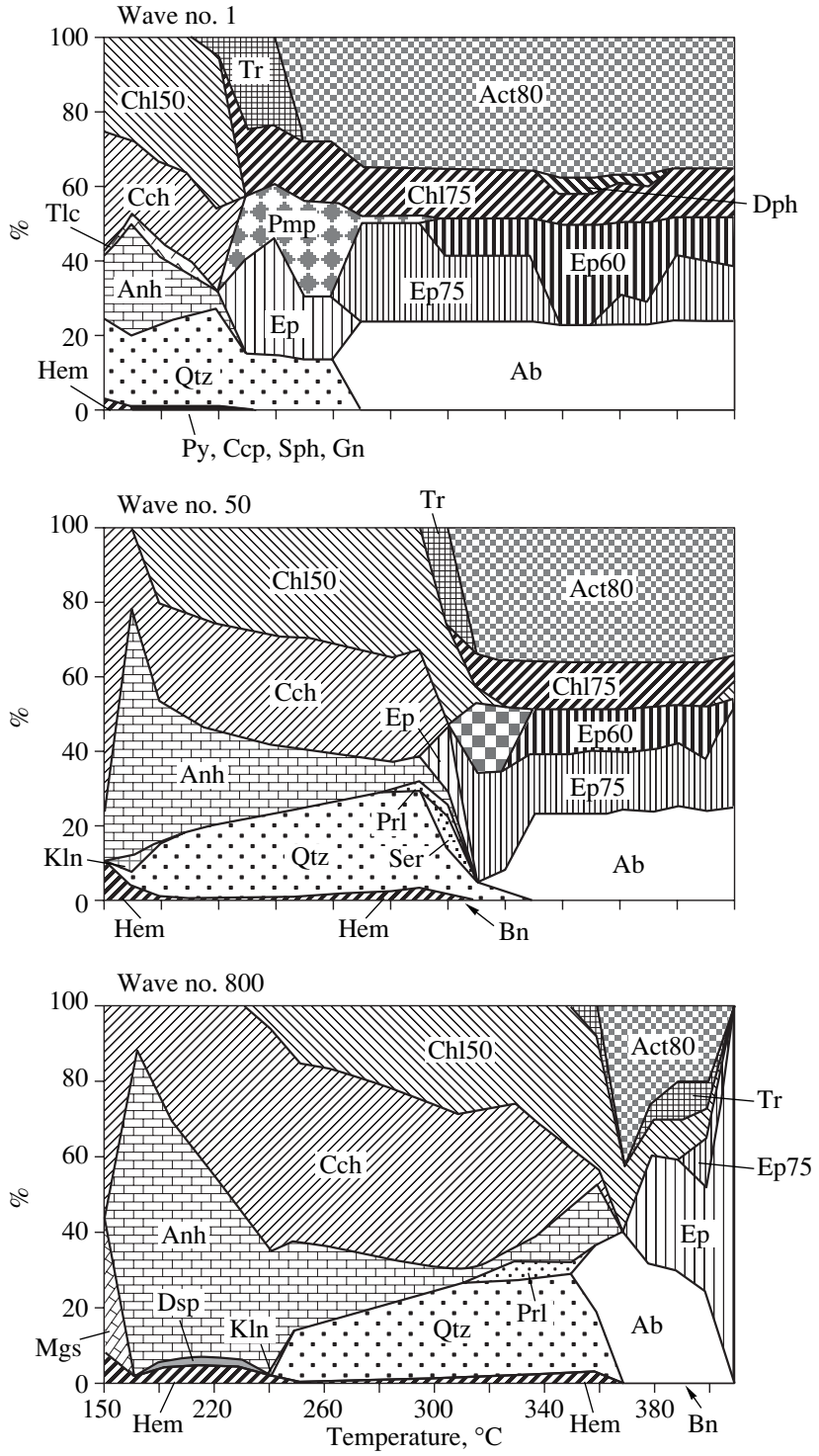

Fig. 25. Variations in the position of stability fields of metasomatic associations during the development of a long-lived hydrothermal system. The case corresponds to the initial $\Sigma R/W$ (400°C) = 1.26. Arrows show the position of the sulfide appearance boundary.

(2) If the sulfide phase is stable, the concentration of the trace ore element depends via the solubility product on the concentration of sulfur, which is a major element. Since the concentration of H_2S decreases during the system evolution, the concentration of the ore element increases, which is exemplified by Cu (Fig. 27b).[18]

[18] In addition to a gradual increase, Cu concentration shows oscillations opposite to those of the precipitant (S^{II}); the reason for such oscillation was discussed above.

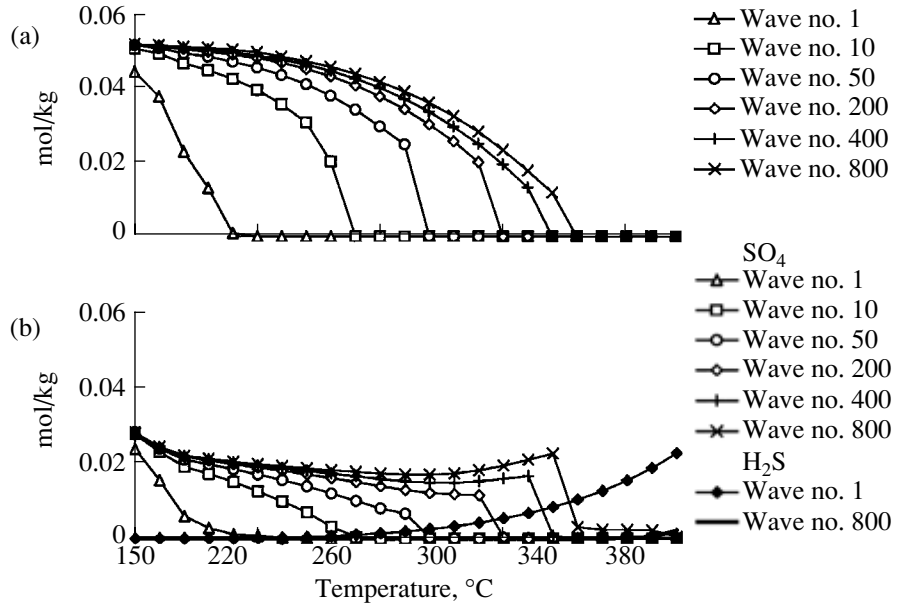

Fig. 26. Movement of magnesium sulfate metasomatic solutions (heated seawater) during the development of a long-lived hydrothermal system. The case corresponds to the initial (wave no. 1) $\Sigma R/W(400°C) = 1.26$ (Fig. 21c). (a) Mg in solution and (b) sulfate ion and hydrogen sulfide in solution.

In the case shown in Fig. 27b, zinc and lead show a dual behavior. In the initial waves, they have regime (2) (sphalerite and galena are stable), which changes later to regime (1). As a result, their concentrations in the solution pass through a maximum at the boundary between these regimes (wave no. 17 for Zn and wave no. 27 for Pb). It is obvious that a change from regime (2) to (1) must be a common feature of all the elements forming their own sulfides in the stability region of assemblage II. The sequence of ore elements showing the change of regimes depends on their relative mobility in equilibrium with mineral assemblage II. According to the calculation of the first-wave model, the sequence of relative mobility is Pb ≈ Zn > Cu, which is in agreement with the results of calculations for the multiwave model (Fig. 27b).

The differences in the behavior of Zn and Cu during the evolution of the downwelling limb have important consequences. The model hydrothermal solution generated in the early waves shows Zn > Cu, the concentrations of these elements become equal during further evolution, and the relation eventually reverses to Cu > Zn. In the simulation case shown in Fig. 27b, initial Zn concentrations in the solution of 0.1–0.2 mmol/kg H_2O decrease to 0.014. In contrast, the concentration of Cu increases initially from 0.00*n* to 0.09 mmol/kg and decreases abruptly to the Zn level after wave no. 667, when copper sulfides disappear from the mineral assemblage. Similar inversions were obtained for models similar to those shown in Fig. 27b but calculated at different temperatures and *R*/*W* values (see also Krasnov *et al.*, 1990; Abramova and Grichuk, 1994; Grichuk, 1996). Thus, an important conclusion derived from the simulation is that the relationships of ore metal concentrations must change from Zn > Cu ≈ Pb to Cu > Zn > Pb during the activity period of a hydrothermal system.

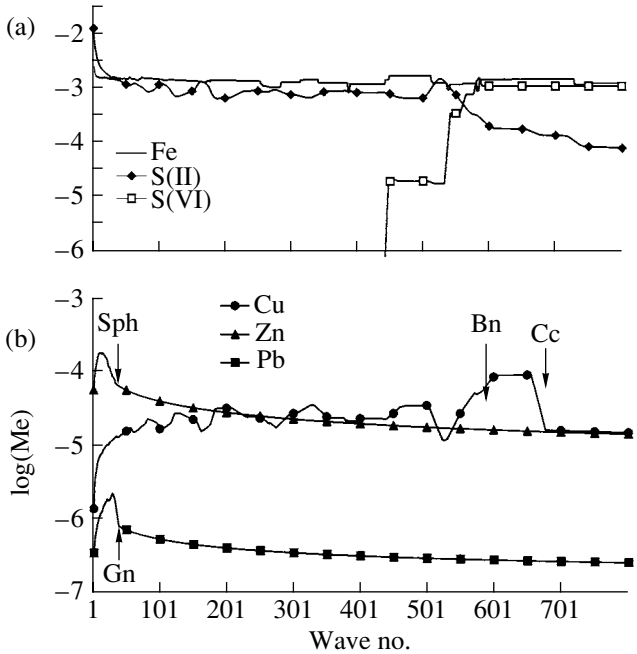

Fig. 27. Variations in the concentrations of ore elements in hydrothermal solutions during the development of a long-lived hydrothermal system. A reactor step with $T = 370°C$, $P = 500$ bar, and $\Sigma R/W$ (first wave) = 0.732. The case corresponds to that shown in Figs. 21, 25, and 26. Arrows mark the disappearance of sulfide minerals. (a) Iron, sulfate sulfur, sulfide sulfur, and (b) heavy metals.

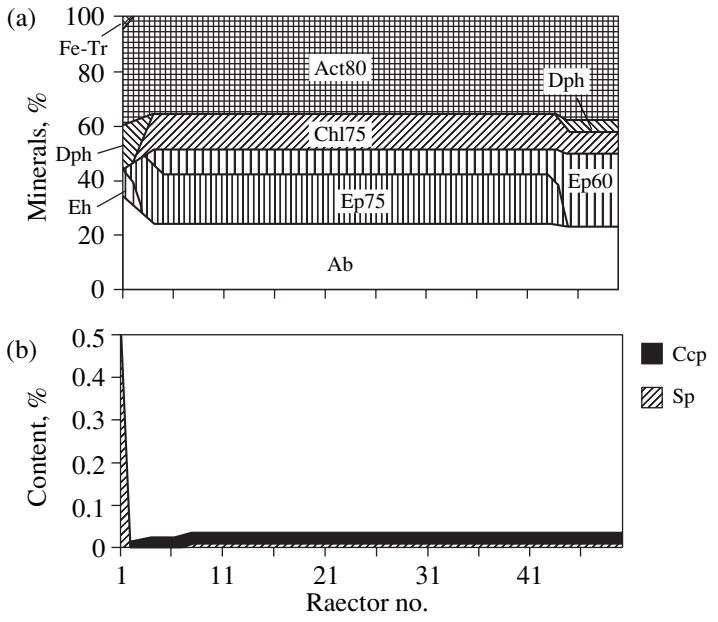

Fig. 28. Simulation of infiltration metasomatic columns around a feeder channel: (a) rock-forming minerals and (b) sulfides. T = 350°C, P = 300 bar, and wave no. 1.

4.2. Metasomatic Alteration of the Feeder Conduit

As was noted in Chapter 3, the oceanic hydrothermal systems under investigation show a limited development of metasomatic haloes around feeder conduits. They are different in this respect from ancient massive sulfide deposits on continents, where footwall hydrothermal alterations are pronounced. The secondary mineral assemblages in the oceanic crust that could be unequivocally interpreted as alteration haloes around feeders are also different from terrestrial ones: the altered basalts show the development of iron-rich chlorite and are free of sericite, which is a typomorphic mineral in the footwall haloes of massive sulfide deposits.

These data suggest that metasomatic processes in the upwelling limb of the oceanic hydrothermal system are different from those of ancient deposits. The reason for this difference is obscure. It could be related to solution chemistry (ancient massive sulfide-forming systems could contain magmatic fluids), the character of initial material (tholeiitic basalts versus island-arc basalts and rhyolites), different T–P conditions, or other factors. This topic is discussed in more detail in Chapter 7.

The goal of this section is to characterize the metasomatic alterations developing in the convection–recycling model considered.

Model parameters. Metasomatic changes in spreading-center basalts, which are fractured and porous rocks, have an inherently coupled infiltration–diffusion character. The infiltration mechanism of metasomatic column formation was utilized in our model. The column was regarded as an isothermal step flow reactor similar to that described in Section 2.1.4. The initial solution was represented by the calculated composition of downwelling fluid in a convection cell with T_{max} = 370°C, P = 500 bar, and $\Sigma R/W$ = 0.732 for wave no. 1 (Table 19). This composition is probably typical of short-lived hydrothermal systems. The conditions in the reactor (metasomatic column) are T = 350°C and P = 300 bar. Thus, a solution entering the column was not in equilibrium under the given conditions. The model reactor consisted of 50 steps, each of which initially contained 10 g of tholeiitic basalt.

The results of simulation after the passage of ten solution portions (waves) are shown in Fig. 28. It can be seen that the basalts are altered under the influence of hydrothermal solutions to the typical propylite assemblage albite + epidote + chlorite + actinolite. The chlorite shows an iron-rich composition (Chl75 and Dph total at ≈80% of iron end-members). There are no potassium-bearing minerals in the column, because K is removed by the first solution portion. The compositions of mafic minerals in the back zone of the column (reactors 1–3) are even richer in iron, up to the appearance of ferroactinolite. This reflects an Fe (also Si and Na) addition with the introduced hydrothermal solutions. However, this part of the column is very thin. The major elements Al, Ca, and Mg are not moved.

The column displays some redistribution of ore minerals (Fig. 28b). The accumulation of sphalerite (up to 0.45%), galena, and chalcopyrite was observed in the first step of the reactor. This process is due to the problem formulation, which implies that the input solution is generated in the downwelling limb at a temperature of 370°C and becomes undercooled in the reactor with 350°C. Several subsequent steps show a removal of ore

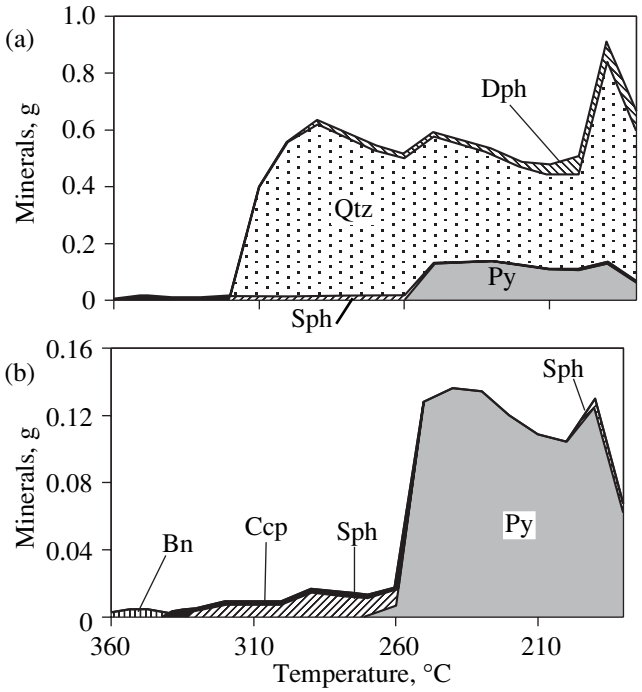

Fig. 29. Fractionation of metals during the slow cooling of solution. The composition of an ore-forming solution was obtained in the downwelling limb at $T = 370°C$, $P = 500$ bar, and $R/W = 0.244$ (wave no. 10). The amount of precipitate is given for 1 kg of ore-forming solution. (a) The net result of mineral formation and (b) the deposition of ore minerals.

metals, after which their concentrations are stabilized at a level corresponding to the prescribed concentration of base metals in the initial basalts.

Thus, the results of simulation are consistent with the observed weak development of metasomatic alterations around the channelway of upwelling fluid. They are not accompanied by sericitization, which is typical of continental massive sulfide deposits (*Metasomatism and…,* 1998). The main metasomatic effect is the enrichment of iron in the altered rock. Ore minerals are deposited in the feeder area only at the expense of cooling, and the metasomatic alteration of rocks is accompanied by a minor removal of base metals from the back part of the column.

4.3. Models of Ore Deposition

As was shown in Chapter 2, depending on the character of the hydrothermal solution discharge on the ocean floor, the processes of ore deposition can be described by different models: slow cooling, rapid cooling, or cooling with mixing. The main factor of ore deposition is always a decrease in solution temperature, and the models correspond to various dynamic scenarios of the process. The simulation results for these ore deposition scenarios are given in Section 4.3.1. The investigation of oceanic hydrothermal systems demonstrated that the style of ore formation varies during the growth of a large edifice (Section 3.2). A combined scenario describing this evolution and numerical results for the corresponding thermodynamic models are presented in Section 4.3.2.

4.3.1. Scenarios of ore deposition during cooling

The model of slow cooling is a step flow reactor in which temperature and pressure decline gradually from step to step (Fig. 10c). This scenario ignores solution interactions with the wallrocks in the feeder conduit.

Figures 29a and 29b show some representative results obtained for such a model: simulation of the slow cooling of the hydrothermal solution formed in the downwelling limb at 370°C, 500 bar, and $\Sigma R/W$ (370°C) = 0.244 (wave no. 10). The deposited minerals are dominated by quartz and pyrite (Fig. 29a) with an admixture of base metal sulfides. It can be clearly seen from Fig. 29b that the temperature maxima of sulfide deposition are different for different metals: bornite (350°C); chalcopyrite (310°C); sphalerite (290°C); galena (260°C); pyrite (240°C). Under other model parameters, the temperature ranges of sulfide precipitation may be different, but the deposition sequence Cu $\longrightarrow$ Zn $\longrightarrow$ Pb is rather stable. The maxima of iron sulfide deposition are more variable, and the model cases with high R/W produced pyrrhotite at 300–320°C (usually above the temperature of sphalerite formation). Consequently, the model of slow cooling allows the fractionation of ore metals at the expense of their precipitation at different temperatures.

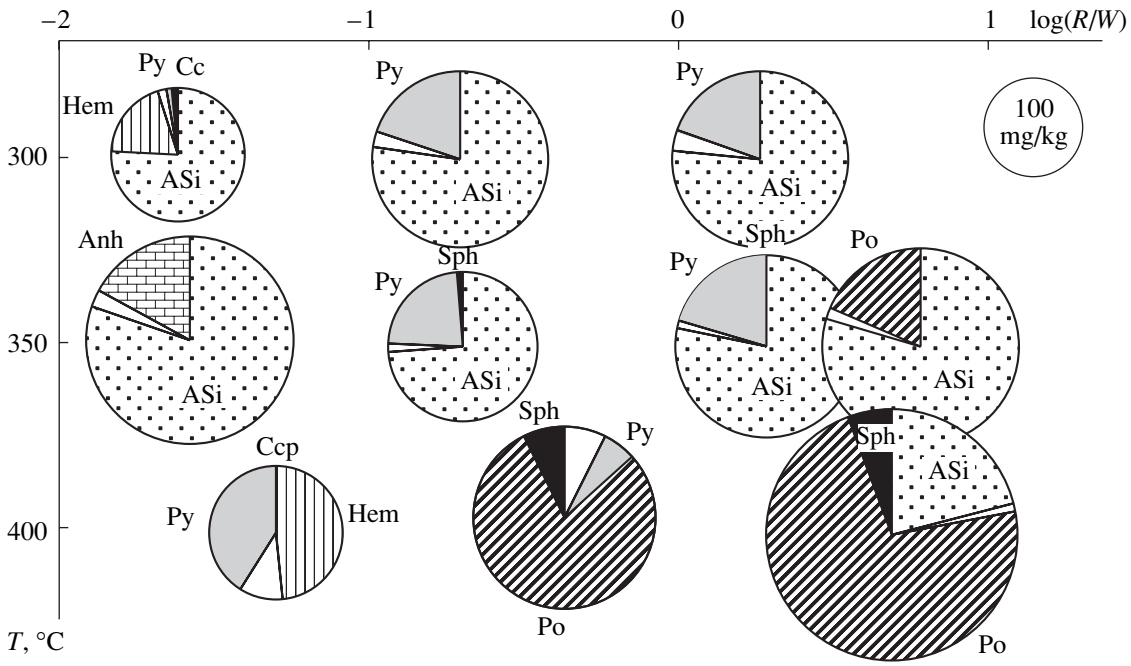

Fig. 30. Mineralogy of the products of the rapid cooling of solutions as a function of temperature and *R*/*W* in the focus of the system. Cooling was calculated to a temperature of 150°C (P = 250 bar); the pie area is proportional to the amount of precipitate; the empty sectors correspond to aluminosilicates (chlorite, actinolite, kaolinite, and pyrophyllite); and ASi is amorphous silica.

This model is probably valid for hydrothermal systems with low discharge temperatures. As was first noted by Rona (1984) and reemphasized in later studies, such systems are characterized by the prevalence of Zn over Pb and other ore components in the deposited products. Many authors explained this phenomenon by the loss of metals (primarily, Cu) in subseafloor environments. The model of slow cooling confirms the possibility of such a process resulting in the formation of veins and disseminated mineralization (stockwork). Its efficiency with respect to the formation of massive sulfide bodies is probably very low, because the ore mineralization is strongly diluted by quartz, which is deposited within a wide temperature range below 330°C.

The model of rapid cooling corresponds to the ejection of high-temperature solution into bottom ocean water, when the chemical reactions between the components of the resulting mixture do not have enough time to occur. This is realized in the model by the transportation of solutions from the high-temperature part of the reactor directly into one of the low-temperature steps, where ore deposition is calculated (Fig. 10b). In such a manner, the quenching of ore precipitates is simulated. The main variables of this dynamic process are (a) the parameters controlling the composition of discharged solutions (T_{max} and $\Sigma R/W$ for the downwelling limb and wave number) and (b) the P–T conditions of the reactor step where the solution is conveyed. Variations in these parameters produce different model compositions of ore deposits.

A significant problem with the realization of such a thermodynamic model arises because of the possible nonequilibrium character of reactions and formation of metastable compounds in the natural prototype of the rapid discharge scenario. The metastable character of the natural process is evident for silica: amorphous silica instead of quartz is often observed in sulfide precipitates. There is no unambiguous evidence for the metastable deposition of other identified phases. In order to take this factor into account in our model of rapid cooling, $g_T(SiO_2$, quartz) was changed by $g_T(SiO_2$, amorphous silica) in the reactor steps corresponding to the zone of ore deposition.

Figure 30 shows the results of calculation for ore deposition during the rapid cooling of hydrothermal solutions (first wave) to ΣT = 150°C. It can be seen that, at varying T_{max} and $\Sigma R/W$ of the downwelling limb of the convection cell, the masses of precipitates and proportions of minerals in the zone of ore deposition are strongly variable. The obvious reason for these distinctions is the derivation of hydrothermal solutions in the stability fields of different mineral assemblages. Indeed, solutions formed at low $\Sigma R/W$ (<0.02) in contact with mineral assemblage I yield hematite-bearing precipitates, whereas those in equilibrium with transitional assemblages ($\Sigma R/W$ = 0.020–0.050) produce precipitates with hematite and pyrite. The solutions that have reacted with a considerable amount of rock produce sediments dominated by silica and iron sulfide and free of hematite.

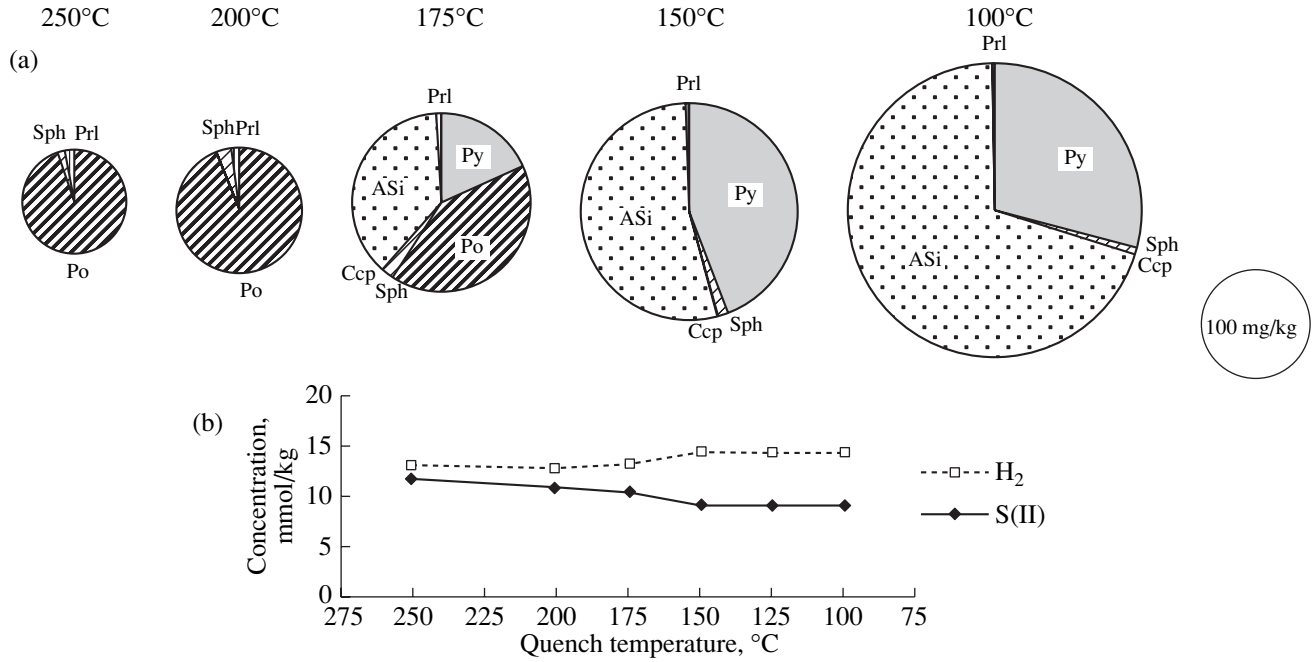

Fig. 31. Simulation of the effect of quench temperature on the composition of ore precipitates in the model of rapid cooling. The composition of the ore-forming solution was obtained in the downwelling limb at T = 370°C, P = 500 bar, and $\Sigma R/W$ (370°C) = 0.712 (wave no. 1). (a) Mineral proportions in the precipitates and (b) concentrations of selected components in the solution.

The proportions of iron sulfides and silica in the precipitate are strongly dependent on the maximum temperature reached in the downwelling limb: the higher T_{max}, the higher is the fraction of iron in the sediment. Pyrrhotite is predominant in the ore material at a temperature of 400°C in the focus of the downwelling limb (Fig. 30). This is evidently related to the significant temperature dependence of iron accumulation in the downwelling limb of the system (Fig. 23b). On the other hand, the concentration of silica in the descending fluid is not particularly temperature-sensitive, and may even decrease with increasing T in quartz-free assemblages. Pyrrhotite-bearing precipitates were obtained from the hottest solutions, whereas the iron sulfides are dominated by pyrite at focus temperatures of 370–300°C. The main reason for this difference lies in the Fe and H_2S relationships in the mineralizing solutions: pyrite is precipitated from solutions whose sulfur contents are much higher than those of iron (Figs. 23b, 23d), whereas pyrrhotite forms at approximately equal Fe and S concentrations, which is typical of solutions in the highest temperature steps of the downwelling limb.

For the solutions formed at 370°C, the identity of iron sulfide depends also on "quench" temperature. Figure 31 shows the dependence of the mineralogy of the precipitate on deposition temperature. According to Fig. 31a, pyrrhotite precipitates at an ore deposition temperature of ≥200°C, and pyrite forms at lower temperatures. The change of phase is accompanied by a change in solution composition: the transition from the monosulfide to disulfide leads to a decrease in S^{II} content and an increase in dissolved hydrogen content (Fig. 31b). Thus, the precipitation of FeS_2 at the expense of H_2S involves water as an oxidizer, and the change of mineral forms depends, in such a case, only on the temperature dependencies of the thermodynamic properties of the reactants. Figure 31a shows that the relationships of sulfides and opal are also dependent on quench temperature: opal does not form at $T > 200$°C, but the relative amount of opal increases progressively below this temperature.

The silica–sulfide assemblages produced at high R/W always contain several percent sphalerite (Fig. 30) and an admixture of chalcopyrite and galena. The fraction of sphalerite in the precipitate reflects the accumulation of Zn in the mineral-forming solutions, which is controlled mainly by temperature. Almost complete and simultaneous deposition of the chalcophile metals during the rapid cooling of solutions with excess H_2S prevents fractionation of these elements (in contrast to the model of slow cooling). Therefore, their proportions in the ore material are inherited from the compositions of mineralizing solutions in the hottest steps of the downwelling limb of the system. This simple correlation is disturbed only in the solutions produced in the stability region of transitional assemblages ($\Sigma R/W$ = 0.02–0.05, Fig. 30), where pyrite and chalcopyrite are selectively deposited owing to the deficiency of sulfide sulfur in the solution.

Anhydrite occurs in the products of rapid cooling only within a narrow field at low R/W and T = 350°C. The reason for its dependency on R/W is undoubtedly

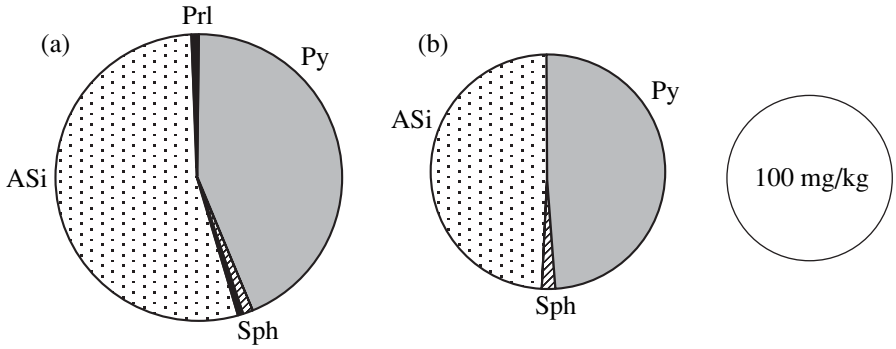

Fig. 32. Comparison of the results of rapid and stepwise cooling of hydrothermal solutions. The initial ore-forming solution was obtained in the downwelling limb at T = 370°C, P = 500 bar, $\Sigma R/W$ (370°C) = 0.712 (wave no. 1). (a) Rapid cooling to 150°C and (b) slow cooling to 300°C followed by rapid cooling to 150°C.

that solutions in equilibrium with mineral assemblage II are free of sulfates and contain excess reducers. The temperature dependency is more ambiguous: it is well known that anhydrite solubility in pure water decreases with increasing temperature (Ryzhenko, 1981), and correspondingly, it is not expected to precipitate in response to a T decrease. However, anhydrite solubility in seawater and seawater-derived solutions is strongly affected by complexation, which results in that HSO_4^- and $CaCl_2^0$ become the major calcium and sulfate species. Because of this, the temperature dependency of anhydrite solubility in such solutions appeared to be more complicated, which was reflected in the results of simulation: anhydrite precipitated from solutions with an initial temperature of 350°C and was absent in other cases.

The suspended matter exiting from smokers is a natural ore material whose deposition must correspond to this scenario. The calculated precipitates of silica, pyrrhotite, pyrite, and sphalerite are the main constituents of smoke produced by high-temperature black smokers (Feeley *et al.*, 1990). It is interesting to note that pyrrhotite occurs in natural analogs only in smoke and is absent in chimney walls.[19] This was usually interpreted as an outcome of metastable precipitation, because the formation of monosulfides is kinetically preferable to that of disulfides. Our simulation demonstrated that the rapid quenching of hydrothermal solution may give rise to the formation of stable pyrrhotite (Figs. 30, 31).

Grichuk *et al.* (1985) supposed that the formation of hematite-bearing siliceous precipitates from the solutions of the downwelling limb at low R/W in the model of rapid cooling could be correlated with white smokers. However, this analogy may not be quite adequate. White and black smokers often coexist within single edifices (Lisitsin *et al.*, 1990). It is difficult to understand how hydrothermal solutions with significantly different histories of interaction with rocks could be ejected through closely spaced channels without mixing en route to the surface. The major-component compositions of solutions from black and white smokers of a single system are not very different (Table 6 shows the data on the TAG hydrothermal field). It is highly probable therefore that the solutions of the two smoker types have a common source. Hekinian *et al.* (1983) documented conversion of a white smoker to the state of a black smoker when an almost closed chimney was destroyed during sampling.

It could be suggested that the formation of white smokers is related to the partial loss of ore load from hydrothermal solutions due to a minor cooling either below the surface of the ocean floor or within the chimney. Indeed, the temperatures of white smokers are systematically lower than those of black smokers (Chapter 3). This suggestion can be tested by simulation using a combination of the models of slow and rapid cooling. Figure 32 shows the results of calculations for deposition from a solution formed by wave no. 1 at T_{max} = 370°C, P = 500 bar, $\Sigma R/W$ = 1.26 and experiencing (a) rapid cooling or (b) preliminary slow cooling (with an increment of 10°C) to 300°C. These results clearly show that preliminary cooling reduces the mass of precipitate without changing the proportions of iron sulfides, silica, or the general character of the solid material. The typical sulfate phases of white smokers are missing in the combined scenario. A characteristic feature of the combined discharge scenario is the slight increase in the relative amount of sphalerite. It is known from natural observations that the precipitates of medium-temperature hydrothermal springs are relatively rich in Zn.

Thus, the model of rapid cooling corresponds to the active discharge of hydrothermal solutions of the black smoker type into cold seawater. The correspondence between the equilibrium thermodynamic model of rapid discharge and the natural process can certainly be approximate, because the process is very rapid, such that metastable phases may be formed and crystallization of some other minerals may be kinetically inhib-

[19] Except for systems in the sediment cover, such as the Guaymas Basin, Escanaba Trough, and Middle Valley fields.

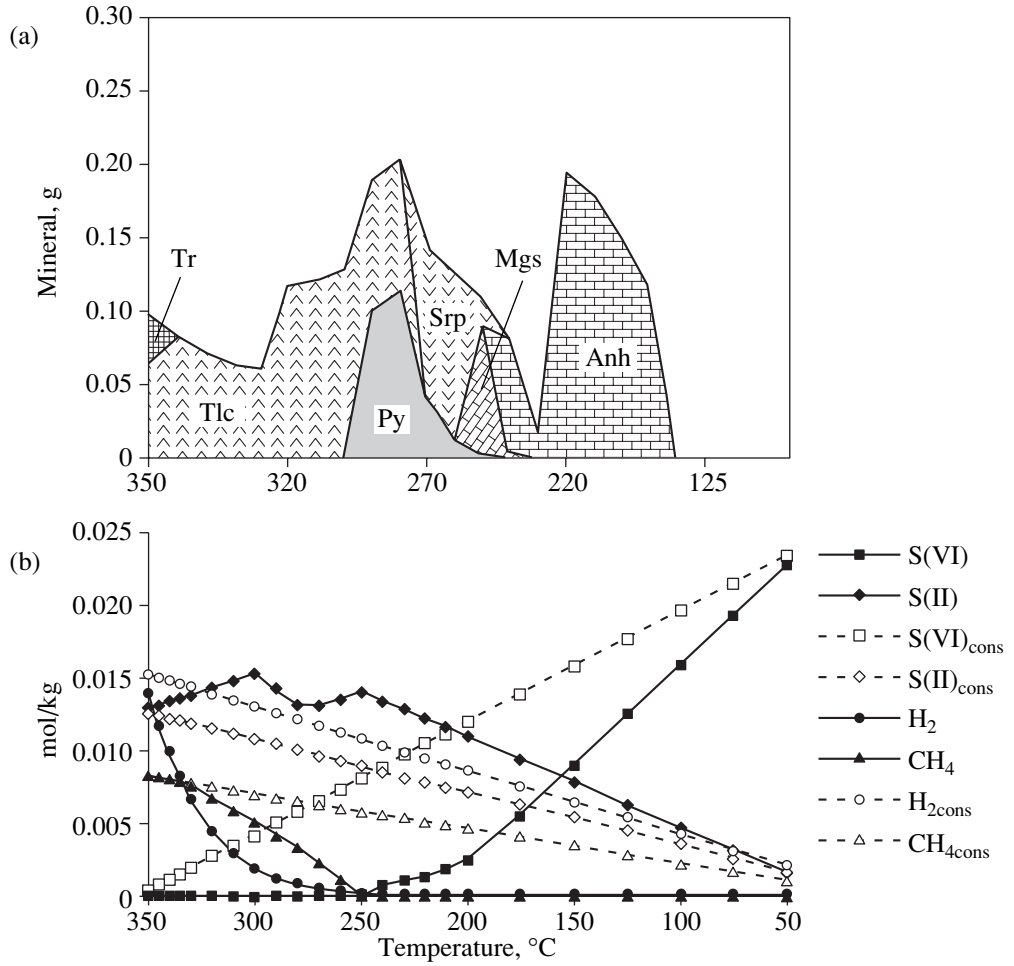

Fig. 33. Sequence of mineral deposition during the mixing of hydrothermal solutions with seawater. The composition of ore-forming solution was obtained in the downwelling limb at $T = 370°C$, $P = 500$ bar, and $\Sigma R/W = 0.732$ (wave no. 1). The amount of precipitate is given for 1 kg of ore-forming solution. (a) The mineralogy of the precipitate and (b) the concentrations of sulfur species and reducers in the solution. The subscript *cons* denotes the hypothetical conservative behavior of components during mixing.

ited. The results of calculations (Figs. 30–32) should probably be regarded as a general sketch rather than a tool for detailed interpretations of natural observations. However, the main conclusion that chalcophile metals do not significantly fractionate during the rapid discharge of hydrothermal solutions seems to be adequately substantiated.

The model of cooling coupled with mixing was considered in detail by Janecky and Seyfried (1984) and Bowers and Taylor (1985), but their simulation procedures allowed the occurrence of back-reactions with previously precipitated products. In order to describe the sequence of deposition of mixing products, one has to construct a model based on the scenario of successive mixing (Fig. 10d).

Figure 33 presents the results of calculation for one variant of such a model. Mixing of hydrothermal solution with cold seawater precipitates the following mineral sequence: tremolite (350°C)–talc (350–270°C)–pyrite (300–250°C)–serpentine (270–250°C)–magnesite (250–240°C)–anhydrite (230–175°C) (Fig. 33a). Minor amounts of copper sulfides (bornite and chalcopyrite, 340–280°C), sphalerite (270–230°C), and galena (250°C) are formed simultaneously. Variations in $\Sigma R/W$ and T_{max} in the downwelling limb do not change the general sequence of mineral precipitation. At $T_{max} = 400°C$, pyrrhotite crystallizes before pyrite; and at high R/W, magnesite and dolomite are deposited before anhydrite.

This model shows a decrease in the extent of anhydrite deposition with increasing R/W. This feature suggests the nonconservative behavior of the seawater sulfate ions during mixing with hydrothermal solution. Figure 33b compares S^{VI} and S^{II} concentrations in the solution with their hypothetical conservative concentrations calculated under the assumption that there are no reactions. It is clearly seen that the equilibrium concentrations of sulfate sulfur are much lower and those

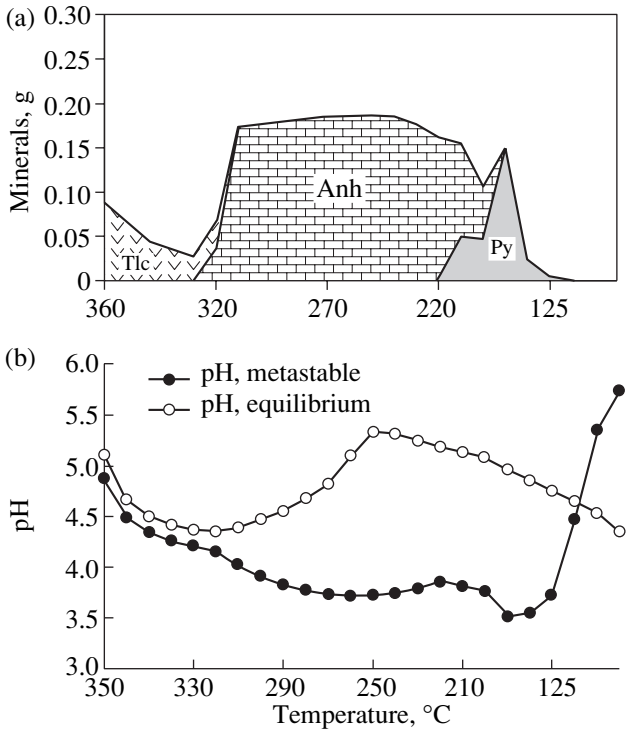

Fig. 34. Metastable sequence of mineral deposition during the mixing of a hydrothermal solution with seawater with inhibited reduction of the sulfate species. The ore-forming solution is identical to that shown in Fig. 33. It was obtained in the downwelling limb at $T = 370$°C, $P = 500$ bar, and $\Sigma R/W = 0.732$ (wave no. 1). The amount of precipitate is given for 1 kg of ore-forming solution. (a) The mineralogy of the precipitate and (b) the acidity of the solution during mixing.

of sulfide sulfur are much higher than the conservative values. This indicates that a sulfate reduction occurs in the model up to a temperature of 210°C. As H_2 and CH_4 serve as reducers in the system, their concentrations are much lower than the conservative values.

With increasing *R*/*W*, when the solutions generated in the downwelling limb become more reduced, this process is more pronounced and continues to temperatures of 200–175°C. The reality of sulfate reduction in the course of mixing is disputable. Experiments suggest that the sulfate ion can be reduced to hydrogen sulfide under hydrothermal conditions (Ohmoto and Lasaga, 1982), but this reaction is rather sluggish at temperatures below 300°C and can be slower than mixing.

In order to account for this factor, we calculated a metastable model for cooling with mixing. In this model sulfur was represented by two quasi-elements (*Methods of…*, 1988), S^{VI} and S^{II}, which prevented the reduction reaction. The results of calculation for such a metastable model are shown in Fig. 34. They indicate that the metastable and equilibrium models diverge not only in sulfur behavior but also with respect to other components. The deposition of magnesium silicates (except for talc) is depressed in the metastable model, and the main newly formed phase is anhydrite (Fig. 34a). The deposition of all sulfides is shifted to lower temperatures: pyrite, 220–100°C; sphalerite, 210–75°C; chalcopyrite, 230–220°C; and galena, 150–125°C.[20] In cases with low *R*/*W*, considerable amounts of opal appear starting from 290°C. The reason for the decrease of the role of magnesium silicates in the metastable model is the significantly more acidic solution pH (< 4) as compared with the equilibrium model (Fig. 34b). In the equilibrium model, the pH of solution increases at the expense of the reactions

$$SO_4^{2-} + CH_4 \longrightarrow H_2S + H_2CO_3 + 2OH^-$$

$$\text{and } SO_4^{2-} + H_2 \longrightarrow H_2S + 2H_2O + 2OH^-.$$

The metastable model is much more realistic than the equilibrium one and the composition of its mineral products corresponds to those of white smokers.

Thus, the difference between white and black smokers is probably related not to the compositions of mineral-forming solutions or temperature parameters but rather to different styles of the discharge process. In the case of a vigorous discharge, smoke generation approaches the quenching scenario during rapid cooling and black smokers are formed. In the case of a calmer discharge, the role of mixing processes (which

[20] Graphite crystallization was observed in the metastable model below 100°C at the expense of methane oxidation by oxygen dissolved in seawater. The attainment of equilibrium in this reaction is improbable at such temperatures for kinetic reasons. However, small amounts of graphite were found in the smoke (Jedwab and Boulegue, 1984). Graphite formation was excluded in the calculations shown in Fig. 34.

probably begin already within the edifice) and related chemical reactions increases. The temperature decreases inevitably, and white smokers are developed.

It should be noted that neither of the cases considered produces ore occurrences significantly enriched in base metal sulfides. The fraction of sphalerite is no higher than 4% in the model of rapid cooling (Fig. 31), and 1% in the model of slow cooling with mixing. The formation of massive sulfide bodies with high Zn and Cu concentrations, which are often observed in nature, is not reproduced in such models.

4.3.2. Scenarios of growing edifices

As was mentioned above, the style of ore-forming processes in large sulfide mounds is significantly different from that in small individual smokers. In particular, they are characterized by the predominance of diffuse discharge over the whole surface of the body. Such a character of solution discharge is favorable for efficient ore matter deposition (Krasnov, 1993). Short-lived systems with rapid discharge lose more than 90% ore metals with smoke, whereas large bodies retain much more of the ore material. Large edifices show zonal internal structures. The simulation of the formation of such ore objects is a special challenge. The model of this process was developed by the author together with E.E. Abramova and A.V. Tutubalin (Grichuk *et al.*, 1998).

The available data on the internal structure of edifices and their development in time are summarized in Chapter 3. The most general conclusion from these data is that the large edifices have zonal structures (Fig. 18) and the duration of their formation is $n \times 10^2$–$n \times 10^4$ y. During the initial stages, ejection of high-temperature solutions on the ocean floor produces a rapidly growing embryonic anhydrite–sulfide edifice, mainly owing to mixing with cold seawater. It grows further at the expense of both the deposition of ore minerals from new solution portions percolating through the body, and the mixing of these partially altered solutions with the surrounding seawater on the surface of the body. The development of internal zoning in an ore body is controlled by two factors (Krasnov, 1993): (a) variations with time in the composition of mineralizing fluid and (b) metasomatic redeposition of material within the edifice during the percolation of hydrothermal fluid through it. Such a mechanism for the formation of zonal ore edifices is not specific to spreading zones and may operate in all submarine hydrothermal systems.

The development of an adequate model for the formation and evolution of a zonal ore body requires special modeling methods. The changes of ore-forming solutions over time are reproduced by the model of a long-lived hydrothermal system (Section 4.1.2). This model must be supplemented by a block describing processes in the zone of ore deposition (within and on the surface of the ore body).

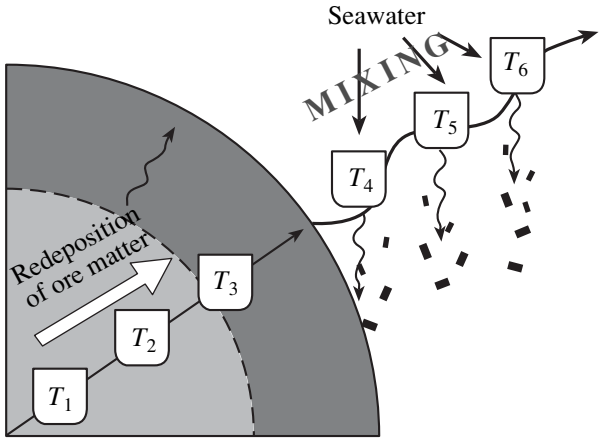

Fig. 35. Cartoon illustrating the model of a growing ore body.

All the parts of the hydrothermal system, including the convection cell and the zone of ore deposition, can be simulated by step flow reactors. A model for the zone of ore deposition must include two constituents. One of them describes deposition and replacement processes during solution filtration within the ore body, and the other describes deposition on the surface of the body during mixing of the emanating solution with ambient seawater (Fig. 35). A characteristic feature of the reactor simulating the zone of ore deposition is that the boundaries of temperature steps move with time in response to the growth of the ore body. As a result, materials deposited at some temperature appear later in a higher temperature region, which is one of the main factors of metasomatic replacements.

The thermodynamic modeling of a growing ore body requires the knowledge of temperature distribution within the body, its surface temperature, and growth rate. The distribution of temperature within the body controls zoning patterns of ore deposition, and the surface temperature defines the relative amount and composition of matter deposited during mixing with seawater. These characteristics vary along with the growth of the body. There is almost no information on the distribution of temperatures within modern sulfide edifices on the ocean floor. The temperatures of the formation of most ancient ore bodies are known only qualitatively: hot central parts (300–350°C) and cooler outer zones (150–200°C) were reconstructed in such bodies (Franklin *et al.*, 1981). We therefore used a theoretical estimate for the distribution of temperature in a growing ore body obtained through the calculation of its thermal model.

Thermal model of a sulfide edifice model conditions. The ore body is approximated in the thermal model by a hemisphere with radius R, whose center is situated in the point of ore-forming solution influx (Fig. 36). The ore-forming solution percolates through the ore body toward its surface (tangential component of the perco-

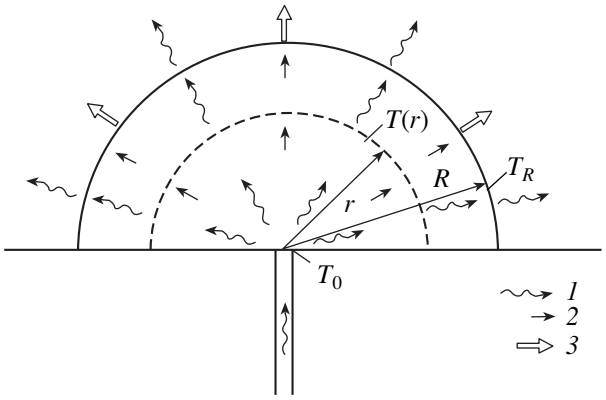

Fig. 36. Thermal model of the formation of an ore body. (*1*) Solution flow and convective heat transfer, (*2*) heat transfer by conduction, and (*3*) heat loss at the surface.

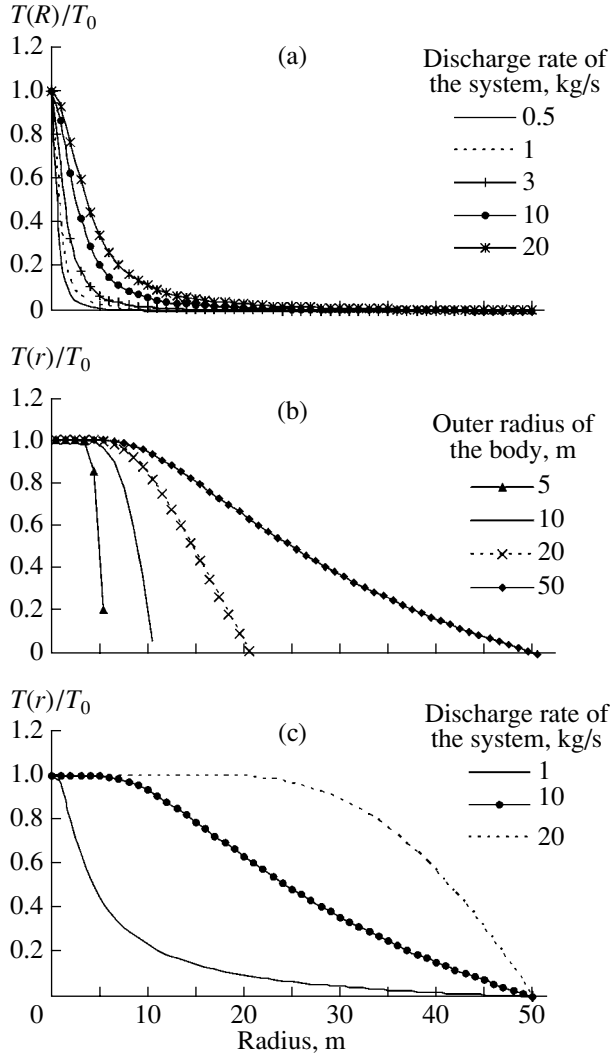

Fig. 37. Results of the calculation of the thermal model of an ore body. (a) The surface temperature of the ore body as a function of its radius and the discharge rate of the vent; (b) distribution of temperature within bodies of various sizes at a fixed discharge rate of 10 kg/s; and (c) distribution of temperature within a body with a radius of 50 m and a varying discharge rate.

lation velocity is zero) and emanates into bottom water. Heat is transferred within the ore body by convective fluid flow and thermal conduction through the solid phase. Heat loss into the environment occurs via the ejection of solution filtered through the body and heat removal from the body surface. The thermal regime of the body can be regarded as steady-state, because its growth is much slower than heat transfer.

In order to simplify the model, the thermal conductivity and filtration properties of the body were assumed to be uniform throughout the whole volume. The heat capacity (C) and density of the solution were taken to be temperature-invariant, and correspondingly, the density component of solution convection within the ore body was ignored. Heat transfer across the lower boundary of the body was also ignored.

The spherical symmetry of the ore body allows us to obtain an analytical solution to this problem (it was derived by Tutubalin).

Calculation of the surface temperature of the body. For the model considered, heat removal from the surface into the environment can be described by the Newton equation

$$\left(\frac{\partial Q}{\partial t}\right)^{-}_{cond} = \alpha S(T_R - T_{ext}), \quad (22)$$

where α is the heat transfer coefficient, S is the surface area of the body (area of a hemisphere with radius R is $S = 2\pi R^2$), T_R is the surface temperature, and T_{ext} is the temperature of bottom water (it can be taken as 0°C without sacrificing the model quality).

Heat input from the source is

$$\left(\frac{\partial Q}{\partial t}\right)^{+} = qCT_0, \quad (23)$$

where q is the discharge rate of the hydrothermal system, and T_0 is the source temperature. Owing to the mass balance condition for the solution entering from the source and exiting into seawater, the convective heat loss into the environment is

$$\left(\frac{\partial Q}{\partial t}\right)^{-}_{conv} = qCT_R. \quad (24)$$

For a thermal steady-state of the ore body, heat balance must be satisfied. Taking into account Eqs. (22)–(24), it can be expressed as

$$qCT_0 = 2\pi R^2 \alpha T_R + qCT_R. \quad (25)$$

The surface temperature of the ore body can be readily obtained from Eq. (25):

$$T_R = T_0 \frac{qC}{2\pi R^2 \alpha + qC}. \quad (26)$$

The coefficient of the T_0 term reflects the contribution of convective heat transfer in the heat balance on the body surface.

Figure 37a shows the dependency of surface temperature on the radius of the body and the discharge rate of the source. This diagram suggests that the surface temperature can be very high only for a very small body, whereas the surface of large ore bodies is efficiently cooled under any realistic discharge rate.

Temperature distribution within the body. Let us consider heat transfer across an arbitrary spherical surface of radius r within the body (Fig. 36). It consists of convective transfer due to solution circulation and conductive transfer. The latter component can be written as

$$\left(\frac{\partial Q}{\partial \mathrm{t}}\right)_{r\,\mathrm{cond}} = -\lambda S_r \frac{\partial T}{\partial r}, \quad (27)$$

where λ is the heat conductivity of the solid. Since the problem is steady-state, heat transfer through any spherical surface is the same and equal to heat supply from the source, it follows from Eqs. (23), (24), and (27):

$$-2\pi r^2 \lambda \frac{\partial T}{\partial r} + qCT(r) = qCT_0. \quad (28)$$

The solution to this equation is

$$T(r) = T_0 + \gamma \exp\left(-\frac{qC}{2\pi\lambda r}\right), \quad (29)$$

where γ is the constant of integration. It can be determined by setting $r = R$ and equating the $T(r)$ value from Eq. (29) with $T(R)$ from Eq. (26):

$$\gamma = -T_0 \frac{2\pi\alpha R^2}{2\pi\alpha R^2 + qC} \exp\left(\frac{qC}{2\pi\lambda R}\right). \quad (30)$$

After substituting this value into Eq. (29) and simplifying, we obtain

$$T(r) = T_0 \left\{1 - \frac{2\pi\alpha R^2}{2\pi\alpha R^2 + qC} \exp\left[\frac{qC}{2\pi\lambda}\left(\frac{1}{R} - \frac{1}{r}\right)\right]\right\}. \quad (31)$$

Figure 37b displays the calculated temperature distribution within bodies of various sizes at a certain discharge rate of the source, and Fig. 37c shows the distribution of temperature at a certain size of the body and varying discharge rates of the source. These diagrams indicate that small-sized ore bodies (10–20 m) with discharge rates similar to those observed in modern hydrothermal systems (0.5–5.0 kg/s) (Little *et al.*, 1987) are characterized by extensive high-temperature zones and narrow peripheral zones with high temperature gradients. The hot zone of large bodies with a radius of more than 50 m occupies a smaller volume fraction and may propagate into the outer part of the body only at high source discharge rates. The temperature gradients in the outer parts of large edifices are significantly smaller.

The growth of an ore body can be described by the equation

$$M_n = \sum_{i=1}^{n} (\Delta S_i q \tau), \quad (32)$$

where M_n is the mass of the ore body after the passage of the nth solution portion from the downwelling limb of the system, ΔS_i is the mass of ore precipitate produced from one kilogram of hydrothermal solution for the ith wave (calculated in the thermodynamic model of the ore deposition zone and dependent on the parameters of the downwelling limb), and τ is the time of discharge of a single solution portion.

In contrast to the downwelling limb of the system, where the time parameter τ is in fact a scaling factor and is not used in the calculation of R/W by Eq. (11), Eq. (32) requires the numerical value of τ. This parameter connects the rate of evolution of the downwelling limb of the convection system with the evolution of the ore body.

The observation periods of modern oceanic system are not long enough for the determination of τ from the chemical analyses of solutions. It can be estimated from indirect evidence as 10^8–10^9 s (3–30 y). Given such values, the solutions in young hydrothermal systems from the East Pacific Rise must not significantly change their composition during the observation period (≈10 y), whereas the long-lived TAG system in the Mid-Atlantic Ridge has evolved significantly, which was recorded in the relationship Cu > Zn in the solution (Edmond *et al.*, 1995).

Equation (32) implies that the solid phases formed in the ore deposition zone join the ore body. It is known from natural observations that this is not the case. In young systems the major portion of ore components (up to 98%) is removed with the smoke (Hekinian *et al.*, 1983), and this situation changes only with the growth of bodies. The parameter q of Eq. (32) therefore has the meaning of effective discharge, accounting for part of the measured total discharge. The discharge rates of individual smokers were estimated between 0.5 and 5.0 kg/s (Little *et al.*, 1987). Some other pieces of evidence for this parameter are shown in Table 5.

Since the objective of this section does not include the simulation of a particular object, the following estimates can be accepted for the reference model: $\tau = 10^8$ s, $q = 10$ kg/s; $\lambda = 20$ J/s cm^2 (corresponding to the mixture of 75% quartz and 25% pyrite), $\alpha = 100$ J/s cm^2 °C (*Handbook of…*, 1987), and the heat capacity of water is taken to be temperature independent (4184 J/g °C).

Thermodynamic model of a sulfide edifice. The thermal model allows the parameterization of the flow reactor simulating the process of submarine ore deposition. This reactor consists of two sequential parts. The first of them is correlated with the inner part of the body, where ore components are deposited owing to a decrease in temperature and replacement of previously formed pre-

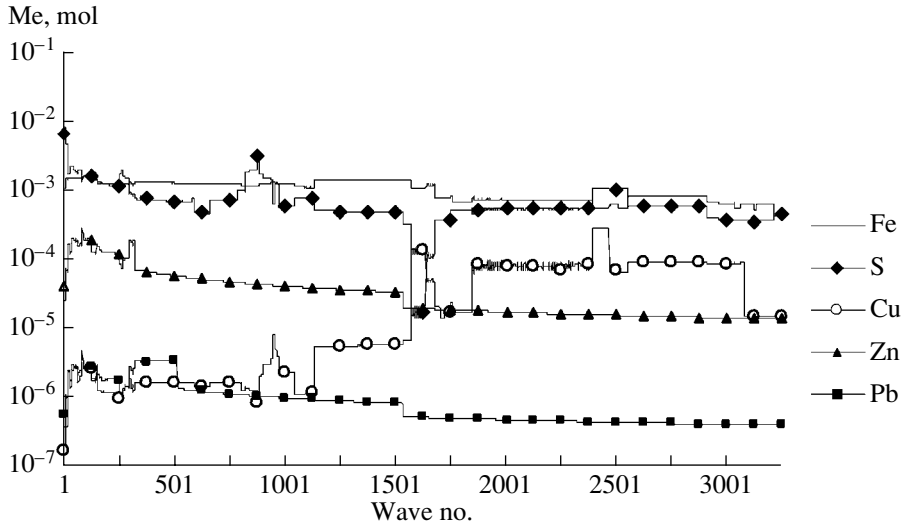

Fig. 38. Ore elements in the parent hydrothermal solution for the reference variant with T = 325°C at the vent mouth and $\Sigma R/W$ = 1.22.

cipitates. The second part describes reactions accompanying the mixing of solution exiting from the edifice with the ambient seawater. The boundary between these parts of the reactor is defined by the surface temperature of the ore body calculated by Eq. (26). Since the steps of the flow reactor are fixed in our model to boundary temperatures, the number of steps corresponding to the interior part of the body will increase at the expense of steps related to the mixing zone with the growth of the ore body and cooling of its surface. These temperature steps gradually expand and move away from the mouth of the feeder during the growth of the ore body at the expense of continuous ore deposition on its surface. As a result, the previously deposited material appears under conditions of progressively increasing temperature and can be partially removed and redeposited by solution closer to the surface of the ore body. Since the temperature distribution in the interior part of the ore body is uniform (Figs. 37b, 37c), in order to better reproduce its structure the increment of reactor steps was reduced to 5°C within the range 350–330°C. The pressure in the ore deposition zone was taken to be 250 bar, which corresponds to a sea depth of about 2.5 km. In accordance with mineralogical data on the modern hydrothermal ores of the ocean, quartz was changed in the model of ore deposition by more soluble metastable amorphous silica.

The software realization of this model required the addition of thermal and dynamic blocks to the standard computational procedure of a multiwave flow reactor implemented in the GBFLOW program. After the passage of a portion of hydrothermal solution through the reactor (ore deposition zone), the mass of the ore body, the temperature of its surface, the distribution of temperature, and the radii of temperature zones (reactor steps) were recalculated. Then, the composition of the matter in the reactor steps was matched to the new positions of temperature boundaries within the body. For the outer zone of ore deposition where mixing takes place, the amount of seawater participating in the mixing was calculated from heat balance using the method described in the previous section, Eq. (14). A new portion of seawater was then passed through the downwelling limb of the convection cell, the feeder channel, and the zone of ore deposition, after which the calculation cycle was repeated. These computations were carried out using the GRDEP program, which was developed for this purpose.

Results of modeling. Several calculations were performed for different T_{max} and $\Sigma R/W$ in the downwelling limb of the system. The results of calculations for a case with T_{max} = 350°C and $(\Sigma R/W)_1$ = 1.22 are described below in some detail. This case is presumably most similar to the widespread natural prototypes (reference variant). The major differences related to variations in $\Sigma R/W$ are characterized. The composition of the parent solution from the sulfide edifice is shown in Fig. 38. Its variations with time are identical to those discussed in Section 4.1.2 (Fig. 27), but the compositional evolution of solution is slower because of the higher rock/water ratio. In Fig. 23e the initial point of the reference variant is situated in the field of sulfur predominance over iron in the parent solution. The solution becomes relatively richer in iron during the evolution of the system (Fig. 38).

The history of the model ore body is distinctly separated into several stages. The first stage corresponds to the earliest solution portions passing through the downwelling limb, when the main factor of deposition is the mixing of hydrothermal solution with cold seawater. This stage produces precipitates consisting mainly of anhydrite and pyrite, which form an incipient (embryonic) edifice (Fig. 39a). The percolation of hydrother-

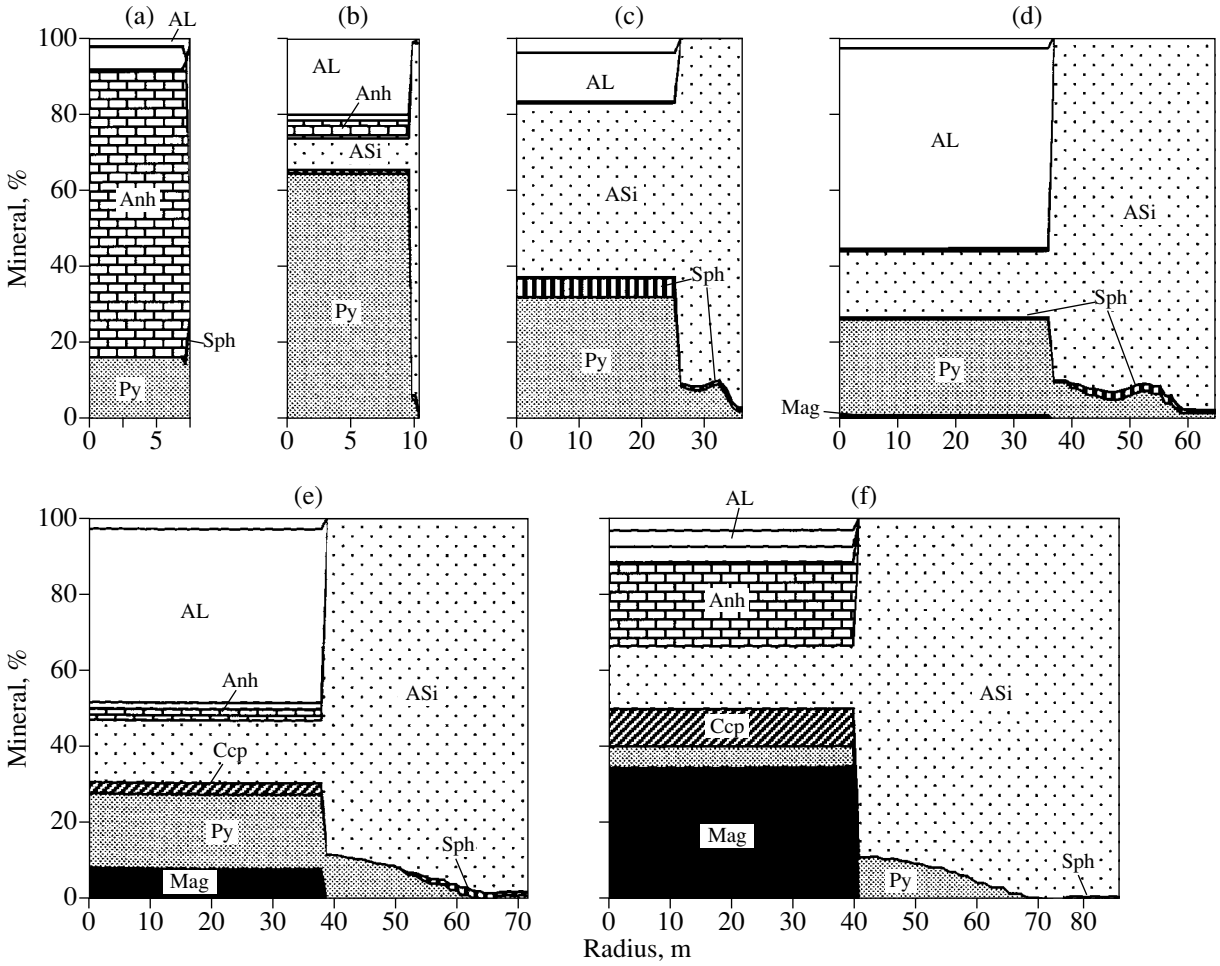

Fig. 39. Mineral proportions in the radial cross-section of a growing ore body. (a) Wave no. 3, (b) wave no. 20, (c) wave no. 500, (d) wave no. 3000, (e) wave no. 4000, and (f) wave no. 6500. AL is aluminosilicate and ASi is amorphous silica.

mal solution through it causes a rapid replacement of anhydrite by a silica–sulfide material in the inner part of the edifice (Fig. 39b). The mixing-related deposition of anhydrite in the outer zone ceases when the temperature of solution emanating from the surface of the body falls below 150°C (anhydrite solubility is characterized by a negative temperature dependency). Extensive silica deposition begins simultaneously in the peripheral zone. Zinc sulfide (sphalerite) is concurrently deposited in the zones with temperatures of 300–200°C, and its fraction in some temperature steps is higher than 50%. This stage is completed by the disappearance of anhydrite from the ore body (solution wave no. 28 in the reference variant, which corresponds to a growth time of approximately 100 y).

The second stage is characterized by the deposition of silica and pyrite, and the maximum of pyrite deposition moves from the hot zone to temperature steps of 280–230°C during the growth of the ore body. Simultaneously, sphalerite is gradually redeposited in the outer zones of the body (200–150°C), and its content may be as high as several weight percent in some steps. In the reference variant, this stage continues up to solution wave no. 2600 (≈8 ky) (Fig. 39c).

During the third stage, the progressive removal of sulfur from the rock and the decrease in its content in the parent solution give rise to partial pyrite replacement by magnetite in the hottest part of the body (Fig. 39d). Sphalerite disappears from the hottest central zones of the body, and minor amounts of copper sulfides (chalcopyrite and bornite) are deposited (0.1–0.2%) (up to wave no. 3200 in the reference variant, corresponding to ≈10 ky).

The maximum contents of copper incorporated in chalcopyrite and, later, bornite and chalcocite are reached at the late stage of development, when anhydrite appears in the hot zone, which indicates a penetration of seawater sulfate through the whole downwelling limb of the system (Figs. 39e, 39f). Because of the deficiency of sulfide sulfur in the solution, sphalerite and galena are rapidly dissolved in the outer zone during that period, and lead and zinc are removed outside the ore body. This is the longest stage, which was tracked in the reference variant to solution wave no. 6500 (≈20 ky).

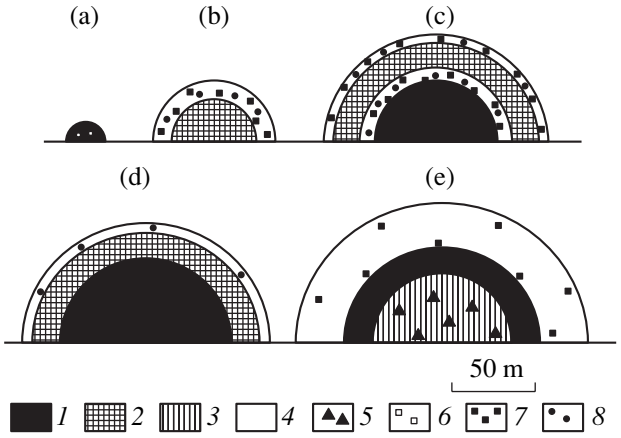

Fig. 40. Relationships of the size and structure of a model ore body for various growth stages. (a) Wave no. 20, (b) wave no. 500, (c) wave no. 3000, (d) wave no 4000, and (e) wave no. 6500. (*1*)–(*3*) Massive sulfide ores: (*1*) iron, (*2*) zinc, and (*3*) copper; (*4*) quartzite and disseminated ore; (*5*) magnetite; (*6*) anhydrite; (*7*) pyrite, and (*8*) sphalerite.

During the final stage of simulation, extensive hematite development begins in the central part of the body under the influence of the oxidized components of seawater, pyrite and copper sulfides are gradually oxidized, and the hydrothermal structure loses its similarity to massive sulfide ores.

During the whole history of the ore body, minor amounts of galena (0.*n*–0.0*n*%) are formed in the outer cold zones of the body ($T < 175$°C) and also in its center at wave nos. 100–300. Throughout the whole evolution of the ore body, its central part is made up of massive ores (pyrite ± magnetite ± sphalerite ± chalcopyrite). Silica is the most abundant component in the peripheral part of the body.

The relationships of the size of the body and its internal zoning for various growth stages are presented in Fig. 40. This diagram clearly shows that distinct zoning patterns are developed in the ore body under the influence of temperature gradients, and this zoning evolves in time owing to changes in the composition of the parent solution, i.e., owing to the metasomatic evolution of the interiors of the hydrothermal system.

The maximum Zn concentrations (up to 1.8% in the calculated case) are attained in the model ore body during the initial stage of its growth (Fig. 41c). Sphalerite is very unevenly distributed in the volume of the body, and there are temperature zones strongly enriched in Zn. Although the influx of zinc from the interiors of the system continues during subsequent stages and its total amount in the body increases (Fig. 41e), the average concentration declines owing to dilution with pyrite and silica. Lead shows the same behavior. The concentration of Fe in the ore body changes relatively weakly and is about 10% in the reference variant (Fig. 41b). The Fe/S ratio decreases regularly in accordance with the changing proportions of these elements in the parent solution and the gradual replacement of pyrite by magnetite in the hottest part of the ore body. In contrast to these elements, the abundance of Cu in the ore body is very low during the early growth stages. Copper con-

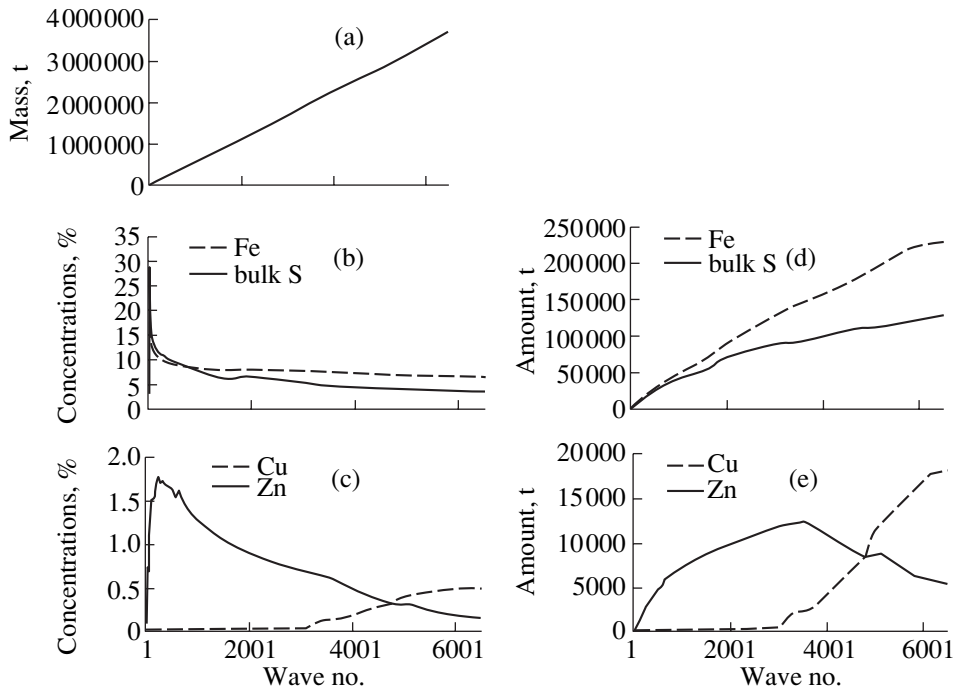

Fig. 41. Reference model for the growth of an ore body. (a) The mass of the ore body, (b) the concentrations of major ore components, (c) the concentrations of base metals, (d) the amounts of major ore components, and (e) the amounts of base metals.

centration begins to increase only after the intensification of copper removal from the interior parts of the system (Fig. 38) and becomes equal to that of Zn at the final growth stage, when anhydrite appears within the body. In contrast to the concentrations of the ore elements, their total amounts in the model body increase in accordance with the growing mass of the body (Figs. 41b, 41c). Only the final stage of development is marked by zinc and lead removal from the body.

An increase in the total mass of the ore body is shown in Fig. 41a for the reference model variant. It increased from 12 kt at the stage of an embryonic anhydrite edifice (Figs. 39a, 39b, 40a), 2 Mt at the stage of a pyrite–sphalerite body (Figs. 39c, 39d, 40b, 40c), to 3.5 Mt by the beginning of hematitization (Figs. 39f, 40e).

For other values of the R/W parameter, the evolution of zoning patterns and the dynamics of accumulation of ore elements may be somewhat different. At low R/W values ($\Sigma R/W_1 = 0.40$), the complete cycle of development of the model body corresponds to a smaller number of waves, 100–600. Because of this, the masses of resulting edifices are proportionally smaller than those of the reference variant for the same discharge rate values. The evolution of the ore body in these variants of simulation differs from that described above because of the lower contents of S, Zn, and Pb in the parent solutions and different Fe and S relationships (Fe > S, Fig. 23e). This gives rise to the rapid appearance of sulfide sulfur deficiency in the ore-forming solution owing to its precipitation by excess Fe. Therefore, the removal of Zn and Pb outside the ore body begins already at the stage of a silica–pyrite edifice with a zoning shown in Fig. 39d. As a result, by the final stage of development (replacement of sulfides by hematite), the edifice has an iron sulfide composition with a small (≈0.2%) copper admixture.

The simulation with an initial $\Sigma R/W$ of 8 is, in general, identical to that described above except for rather slow variations in the downwelling convective flow: the penetration of sulfate species through the hydrothermal system is only detected at a wave number of more than 10 000, which is equivalent to a time period of $n \times 10^4$ y if τ is about 10^8 s. According to the observations in relatively long-lived hydrothermal systems of the Mid-Atlantic Ridge, such total lifetimes may be attained in the case of repeated reactivation of hydrothermal systems within a single crustal block (Lalou *et al.*, 1995). Such nonsteady-state systems are not described by our model. In the case of long-lived systems, it is also possible that the sulfide body will be overlain by extrusive rocks, which will give rise to a multilevel deposit. Therefore, the case with $\Sigma R/W = 8$ can be regarded as a boundary case for our model.

Discussion. The simulated evolution of the model ore body at the early stages of ore formation is consistent with the well-known significant zinc enrichment in modern oceanic sulfide edifices and with the reconstructions of their formation sequences (Fig. 24). The initial anhydrite body on the seafloor is also replaced by silica and sulfides with the formation of characteristic zoning patterns: Cu in the middle and Zn in the periphery. The zoning patterns obtained by the simulation of medium and late stages are, for the most part, similar to those observed in massive sulfide deposits of the Cyprus and Ural types. The model reproduces the spatial and temporal sequence magnetite → pyrite + copper sulfides → pyrite + zinc and lead sulfides. The evolution of the ore body in time with a late stage of copper enrichment and the replacement of sulfides by magnetite near the mouth of the channel (and later by hematite + anhydrite) are in agreement with the available data on natural analogs. This suggests that the mechanism of ore formation is controlled by two factors, the metasomatic evolution of the feeding hydrothermal system and temperature gradients in the ore deposition zone, and corresponds in major aspects to the physicochemical processes accompanying the formation of both modern sulfide bodies on the oceanic floor and massive sulfide ores of the Cyprus and Ural types.

It is obvious that there are other important factors influencing ore deposition during the formation of massive sulfide deposits. A detailed analysis of the results of simulation reveals a number of discrepancies between the model and its natural prototypes, which suggests that some factors of the natural process were not accounted for in the model.

(1) The simulation of a large ore body showed that considerable amounts of matter are deposited in temperature steps occurring within the body, i.e., in its pore space. Our model ignores changes in the filtration properties of the ore body and implies that they provide conditions for the percolation of hydrothermal solution with the given discharge rate. Clogging of pores (mainly by silica) must lead to the cessation of solution flow. According to the calculation of hydrostatic equilibrium in a hydrothermal system, the clogging of the mouth of the feeder channel can generate an excess pressure of about 30–60 bar, which is sufficient for the formation of hydrofractures in the ore body. In recent publications on the structure of large sulfide mounds in the Mid-Atlantic Ridge (Bogdanov *et al.*, 1997b), this phenomenon was referred to as the hydrothermal explosion. The appearance of fissure channels for discharge will result in the penetration of high-temperature solutions into the outer parts and distortion of zoning patterns predicted by the model. Indeed, many large sulfide structures on the ocean floor comprise localized groups of vents (smokers) (e.g., Lisitsin *et al.*, 1990), which account for 10–20% of the total discharge of the feeding system (Rona *et al.*, 1993). The collapse of these chimneys results in the input of relatively high-temperature products of ore deposition into the outer parts of the sulfide edifice. The occurrence of hydrofracturing phenomena in nature is also suggested by widespread ore breccias in ancient massive sulfide deposits. These breccias show a persistent correlation

with a certain domain of zoning at the transition from pyrite–chalcopyrite to pyrite –sphalerite ores (Zlotnik-Khotkevich, 1992).

(2) The simulated cases revealed a significant deficit of sulfide sulfur in the ore body in the stage of copper transfer activation (Fig. 39f). Under model conditions, combined copper and sulfur transport is thermodynamically limited because of the low solubility of copper sulfides. The deficit of solubility is far greater than the possible uncertainties of thermodynamic calculations. The probable explanation for this discrepancy is that the model ignores possible phase separation (boiling) in the interior parts of the system and in the ascending channel (see Chapter 6).

(3) The penetration of seawater sulfates through the whole convective system that was obtained in the model of the final stages of ore body development is probably not realized in modern high-temperature oceanic hydrothermal systems. Anhydrite found in the interior parts of a sulfide body from the TAG field probably has a different origin (subsurface mixing; Mills *et al.*, 1998). However, late hypogenous anhydrite is common in the footwall levels of some ancient massive sulfide deposits of the Central and Southern Urals and other regions (see Stolyarov, 1972 for a review). The origin of this anhydrite was traditionally explained by the influence of an endogenous source, and the change from sulfides to sulfates was attributed to the hypothetical redox evolution of a magma chamber. The model presented above readily explains this fact by the penetration of seawater sulfates through the whole hydrothermal system in the case of its prolonged activity. This explanation is consistent with the sulfur isotope systematics of anhydrite from the footwall of massive sulfide deposits (Vinogradov *et al.*, 1968; Grinenko *et al.*, 1969), which appeared to be similar to that of seawater of the corresponding age.[21]

Thus, the combined mechanism of submarine ore deposition includes ore matter deposition due to the mixing of hydrothermal solutions with bottom seawater and cooling and takes into account the evolution of the feeding hydrothermal system and metasomatic replacements within the ore body. The results of our simulation show that this mechanism can produce a zonal ore body with time-varying chemical and metallogenic characteristics. The early stages of this evolution are correlated with the well known sulfide edifices on the ocean floor. The mature stages give rise to massive sulfide ore bodies, whose compositions and zoning patterns are similar to those of known ancient continental ore bodies. The advanced evolution of the feeding system results in the hematitization of the sulfide edifice, which loses its similarity to massive sulfide ores. This situation is more probable in small near-surface systems, which provide conditions for the extensive alteration of rocks by hydrothermal solutions.

4.4. Verification of Simulation Results

The first question arising during the analysis of results derived from a complex model is the correctness of this model, i.e., its consistency with the natural object. The verification of the model of an oceanic hydrothermal system was based on the comparison of secondary mineral assemblages developing after basalts in the downwelling and upwelling limbs of the convection system, the mineral and chemical compositions of ore precipitates, and the chemical compositions of solutions produced by the hydrothermal system.[22]

(1) The model described in the previous sections reproduces the discrimination of metasomatic rocks into two large groups, chlorite and epidote ones. Such a discrimination was first established in natural oceanic metabasalts by Humphris and Thompson (1978) and repeatedly confirmed by subsequent studies (Mottl, 1983; Kurnosov, 1986). The model sets of minerals obtained for these two associations (quartz + chlorite + hematite + talc and albite + epidote + actinolite + chlorite + sulfides, respectively) are typical of the greenschist and propylite metasomatic facies. The same sequence of mineral assemblages is characteristic of metasomatic haloes around massive sulfide deposits of the Ural type (Surin, 1993). The simulation implied a narrow stability field of carbonates (150°C, dolomite at low *R*/*W* and calcite at extremely high *R*/*W*). The low content of carbonates in the secondary associations of the oceanic crust distinguishes them from the metasomatic rocks of ophiolitic complexes, where carbonates are widespread (Coleman, 1979). The presence of anhydrite in mineral assemblage I and its highest abundance within 200–250°C are in line with evidence from the sections of the young oceanic crust (data for ODP Hole 504B; Alt *et al.*, 1983, 1989).

When rock-forming metasomatic minerals were simulated as phases of intermediate composition (epidote, chlorite, and actinolite), their compositions appeared to be consistent with their natural prototypes. For instance, according to Gillis and Robinson (1990), epidote with 20–25% pistacite end-member is typical of the Troodos ophiolites. Such intermediate phases (epidote-60 with 20% and epidote-75 with 25% pistacite end-member, respectively) were obtained in assemblage II of the downwelling limb (Fig. 21b). Among other characteristic features reproduced by the model are the increase in the iron content of chlorite with the intensification of metasomatic alteration (Mottl, 1983; Surin, 1993) and the higher Fe/(Fe + Mg) ratio of chlorite compared with actinolite, which is typical of metabasic rocks (Plyusnina, 1983).

[21] A marine sulfur source for hypogenous anhydrite was proposed by Stolyarov (1965), but his explanation was not supported by subsequent studies.

[22] Data on sulfur isotopes are discussed in Chapter 5.

Table 21. Comparison of model results with the data obtained from some natural objects

Solution component	Unit	Object	Model calculation		Object	Model calculation
		EPR, 21° N, HG, T = 351°C	T = 370°C, P = 500 bar, wave no. 1, R/W = 0.732	T = 370°C, P = 500 bar, wave no. 2, R/W = 0.517	MAR, 26° N, TAG, T = 366°C	T = 360°C, P = 500 bar, wave no. 53, R/W = 0.027
No. in Table 6		4	–	–	35	–
Cl	mmol/kg	496	545.9	545.9	636	545.9
Na	″	443	441.7	468.0	557	472.6
K	″	23.9	37.8	21.5	17.1	6.92
Ca	″	11.7	32.1	27.1	30.8	32.85
Mg	″	0	0	0	0	0.001
Fe	″	2.429	2.527	2.249	5.59	1.16
Zn	μmol/kg	104	57.3	89.2	46	15.3
Cu	″	44	1.41	3.82	120–150	74.5
Pb	″	0.359	0.349	0.535	0.11	0.267
SiO_2	mmol/kg	15.6	14.17	13.46	20.75	15.0
H_2S	″	8.4	12.39	6.58	3.5	0.661
pH(25°C)		3.3	3.51	3.45	3.35	3.82

However, some results of our simulation cannot be unambiguously correlated with natural observations. The mineral assemblages of the downwelling limb often contain minor amounts of aluminous minerals: kaolinite and pyrophyllite in assemblage I and wairakite and sericite in transitional assemblages. These minerals were identified in deep-sea drill core samples (Kurnosov, 1986), and there is no apparent conflict between their presence in the simulated assemblages and natural observations. However, their appearance could be related to a flaw in the model, the lack of aluminous end-members in the compositions of chlorite and tremolite. It is conceivable that, if the multisystem involved mixed-layer smectite/chlorites and actinolite contained several percent of alumina, these phases would not appear in the simulated products. The accuracy of our thermodynamic model is insufficient to resolve these details.

(2) The minerals obtained by the simulation of ore deposition (Section 4.3.1) correspond to those observed in ore bodies (Table 3). The mineralogy of solid phases from the quenching scenario of rapid mixing (Fig. 30) is identical to that observed in the smoke of submarine vents (Feeley *et al.*, 1990). The model reproduces even such an indicator feature as the presence of pyrrhotite in the smoke, although it is absent in sulfide edifices. The model of disequilibrium mixing shows a predominance of anhydrite in the precipitate (Fig. 34), which is in good agreement with the results of natural experiments reported by Tivey *et al.* (1990).

The simulation of the growing edifice scenario (Section 4.3.2) reproduces the development of oceanic sulfide edifices (Fig. 24), with respect to both the zoning patterns of sulfide bodies and stages of their development. This model yielded zinc enrichment during the initial stage of sulfide edifice development, which is characteristic of oceanic hydrothermal ores, and Zn and Pb redeposition in the peripheral part of ore structures during their prolonged evolution. The formation of massive pyrite ores with relatively high copper contents in the central part of edifices is consistent with the conclusions derived by Krasnov (1993) from the data on the mineral and chemical compositions of oceanic sulfide ores.

(3) The composition of the hydrothermal solution is the most sensitive and complex indicator of the correctness of the model. The data presented in Section 4.1.1 show that the model adequately reproduces all the main changes in the composition of natural hydrothermal solutions relative to the initial seawater: enrichment in K, Ca, Si, S^{II}, Fe, chalcophile elements, dissolved hydrogen, and methane; depletion in Mg; and a decrease in pH (recalculated to 25°C). A comparison of data presented in Table 19 with the chemical characteristics of oceanic hydrothermal solutions (Table 6) indicates a qualitative and quantitative correspondence between the model and natural solutions.

A detailed inspection (Table 21) reveals that the chemical compositions of solutions from 21° N EPR (and similar solutions from other sites) correspond to the model solutions obtained in cases with low wave numbers, i.e., with excesses of fresh basalts. It is interesting to note that a number of components (K, Ca, Zn, and S) showed a closer match with wave no. 2 rather

than with wave no. 1 (Table 21). The smoker solutions of the TAG field are similar with respect to Zn and Cu relationships to those from a long-lived system model (Table 21, simulation for wave no. 53). Thus, the results of simulation are in reasonable agreement with natural observations with respect to a number of indicators.[23]

(4) The inversion of Zn and Cu proportions in the model ore-forming solutions is of special importance for the interpretation of geochemical and metallogenic data on oceanic ores. It is therefore important to estimate whether this result is of general or local significance. According to the model, the inversion is related to two phenomena: (1) faster Zn removal from a young hydrothermal system compared with Cu and (2) an increase in Cu concentration in the solution during the evolution of the system. The former phenomenon is controlled by the relative solubilities of Zn and Cu sulfides. The experiments by Seyfried and Janecky (1985) conducted under similar temperature and chemical conditions yielded a Zn enrichment relative to Cu (Table 10). In our model Zn is incorporated in sulfides only, whereas part of the Zn in natural metasomatic rocks may occur as an isomorphous admixture in aluminosilicates. Nonetheless, the investigation of a modern hydrothermal system at 21° N on the EPR suggested that the removal of Zn is 3–4 times more efficient than that of Cu (Von Damm *et al.*, 1985).

According to the simulation results, the increase in Cu concentration during the evolution of the system is controlled by the rapid removal of S^{II} from basalts, which increases the solubility of Cu sulfides. The main mineral repository of sulfur in basalts is pyrrhotite, which is much more soluble than chalcopyrite under hydrothermal conditions (Fig. 22a). Rapid disappearance of magmatic sulfides during basalt alteration was repeatedly documented (Gitlin, 1985). The efficiency of S^{II} removal from the hydrothermal systems of 21° N EPR is 30–60 times that of Cu removal (Von Damm *et al.*, 1985). On the other hand, data on the composition of epidosite from the Troodos ophiolites suggest that up to 90% Cu may be removed from a strongly altered rock (Richardson *et al.*, 1987). The apparent discrepancy between these data on modern and ancient systems is easily explained by the simulation results: the removal of Cu is intensified in long-lived systems.

[23] A better agreement between the calculated solution composition and a particular natural object can probably be achieved by the refinement of model parameters (primarily, sulfur content in the basalts under investigation) and accounting for the influence of phase separation due to boiling (Chapter 6). Therefore, the data presented here have no direct implications for the inverse problem, i.e., the determination of characteristics of natural objects.

The above considerations suggest that the change from Zn > Cu to Cu > Zn is not an accidental effect or a specific feature of the model but is caused by the physicochemical properties of compounds of these elements. Consequently, it must be systematically observed in evolving hydrothermal systems fed by seawater. The analysis of the available data on oceanic deposits shows that solutions from most of them have Zn > Cu (Table 6). However, the investigations of an ore-forming solution from a long-lived hydrothermal system in the TAG field (Edmond *et al.*, 1995) revealed Cu concentrations higher than those of Zn (Table 6, analysis 35; Table 21) and higher than in any other system studied. The calculated enrichment of copper in the central part and zinc in the peripheral part of a mature ore body is in agreement with the results of drilling in a sulfide mound at the TAG field (Hannington, 1998).

4.5. Conclusions

The agreement between the results of the thermodynamic modeling of oceanic hydrothermal systems and natural data with respect to many mineralogical and geochemical indicators indicates that the model developed in this paper is realistic. This offers the possibility of using the model for the interpretation and prediction of some properties of natural hydrothermal systems.

The simulation of oceanic hydrothermal systems demonstrated that an increase in the lifetime of a hydrothermal system is favorable for a relative copper enrichment in the resulting ore body. On the other hand, long-lived systems form large ore bodies. Consequently, a correlation is expected between the size of sulfide edifices and their copper enrichment. Such a correlation was observed in nature (*Hydrothermal Sulfide…*, 1992; Krasnov, 1993): copper enrichment was documented in large sulfide mounds from the TAG field and the Galapagos Spreading Center. The ore bodies of these areas have very long lifetimes (repeated reactivation is also possible) compared with the hydrothermal edifices of the East Pacific Rise. Thus, the reason (or one of the main reasons) for copper enrichment in large long-lived sulfide structures on the ocean floor is the extensive metasomatic alteration of rocks within the system.

What are the geologic factors favorable for this process? One of the obvious factors is the prolonged circulation of hydrothermal solutions within a single block of oceanic crust, which is possible in a slow-spreading ridge near a periodically replenished magma chamber. Such a situation occurs in the TAG region. Another favorable setting is probably an off-axis volcanic center, which also possesses a magma chamber fixed within the oceanic crust. Copper enrichment was reported from the sulfide bodies of off-axis volcanic centers (Alt *et al.*, 1987; Krasnov, 1990; Fouquet *et al.*, 1996).

Steady-state magma chambers probably exist beneath fast-spreading mid-ocean ridges. Prolonged

hydrothermal circulation (continuous or intermittent) therefore occurs in these structures, and the hydrothermal systems of fast-spreading ridges are formally also long-lived. The obvious differences of such systems from those described above are the rapid withdrawal of crustal rocks from the zone of convective circulation and the continuous supply of fresh basalts owing to dike emplacement and crystallization at the roof of magma chambers. Hence, the hydrothermal activity in any given crustal block appears to be shorter and metasomatic alterations are less extensive than in slow-spreading ridges. There is a persistent excess of fresh basalts within the hydrothermal systems. In particular, this is suggested by the calculation of oxygen isotope balance (Merlivat *et al.*, 1984) and the isotopically light composition of sulfide sulfur (Chapter 5).

Investigations of ancient objects in the well-known Semail ophiolitic complex (Oman) showed that large massive copper sulfide bodies are related to off-axis volcanic centers (Haymon *et al.*, 1989), and the ore bodies are associated with abundant epidosites (Nehlig *et al.*, 1994).

The results of our simulation indicate fundamental changes in the behavior of many components depending on the R/W value. This property of our model implies that it does in fact reproduce the distinction between the fluid-dominated and rock-dominated regimes of water–rock interaction (Fyfe *et al.*, 1981). The transition between these regimes probably occurs close to the boundary between model assemblages I and II (Fig. 22). Its calculated position at $R/W \approx 0.03$ is consistent with available experimental estimates for the basalt–seawater system (Seyfried and Mottl, 1982). Up to $R/W \approx 0.03$, the geochemical characteristics of the steps of the model reactor are controlled mainly by the input of Mg, SO_4, and O_2 with seawater; and the removal of components from basalts becomes of prime importance at higher R/W values.

The change in the behavior of ore elements near the boundary of the stability fields of metasomatic assemblages I and II implies that this boundary (and the adjacent region) is a geochemical barrier. According to the calculations, the concentrations of many components are affected by this barrier, but the most pronounced changes are observed for variable-valence elements, H, C, S, Fe, and Cu (Figs. 21c, 21d, 23). The main driving force of this barrier is a solution–basalt redox reaction, which reduces SO_4 to H_2S, H_2CO_3 to CH_4, and H_2O to H_2. Fe^{II} of the basalt is simultaneously oxidized to occur as Fe^{III} in epidote. Among the ore metals considered, Cu is most sensitive to this geochemical barrier. The movement of this barrier during the development of the hydrothermal system results in the redeposition of copper sulfides, which are oxidized near the front and deposited in the back part. The high Cu concentration in the solution before the barrier (Fig. 21d) promotes a gradual copper accumulation on the barrier. The maximum Cu content in the ore-forming solutions of the upwelling limb is attained when this barrier approaches the focus of the hydrothermal system (Figs. 27b, 38).

CHAPTER 5. THERMODYNAMIC MODELS OF ISOTOPIC CHEMICAL SYSTEMS

5.1. Method of H. Ohmoto and Its Application in Thermodynamic Models for the Hydrothermal Process

Isotopic geochemistry provides one of the most powerful tools for geochemical investigations. Unique results were obtained using isotopic methods, including the identification of sources of hydrothermal solutions and ores. However, when isotopic indicators are used without nonisotopic ones, the interpretation of results may often be ambiguous. Therefore, modern stable isotope geochemistry relies on a combined use of isotopic and geochemical information.

The idea that physicochemical factors in a reaction environment can influence the distribution of isotopes between reactants and, consequently, that isotopic ratios are not universal signatures of sources in geologic processes was first advanced by Sakai (1968). Ohmoto (1972) developed this idea and proposed a method for the calculation of isotopic variations in systems with chemically reacting substances. Although Ohmoto (1972) and Ohmoto and Rye (1979) applied this method to systems with sulfur and carbon, it is a versatile tool, which has subsequently been used to tackle a variety of geochemical problems (Bannikova and Ryzhenko, 1984; Bowers and Taylor, 1985; Janecky and Shanks, 1988; etc.).

Ohmoto proposed calculation of isotopic compositions in a closed system with chemical reactions in two stages. The first stage deals with the chemical composition of the system; its aim is to calculate the concentrations of substances participating in isotope exchange reactions. In simple situations (Ohmoto, 1972), these concentrations are defined by the occurrence of a simple chemical reaction or change in external parameters. The concentrations of substances in complex systems are calculated by the methods of thermodynamic modeling using appropriate computer programs (Bannikova and Ryzhenko, 1984; Bowers and Taylor, 1985). During the second stage, the calculated concentrations of chemical compounds are used to evaluate the equilibrium distribution of isotopes among them. This second stage was developed by Ohmoto.

In the general form, the Ohmoto method is reduced to the solution of the following system of equations:

(a) isotope balance equation

$$\sum_{i}^{n} m_i \nu_i (\delta_i - \delta_\Sigma) = 0, \quad (33)$$

where m_i are the molar amounts of substances involved in the isotopic exchange, ν_i are the stoichiometric coef-

ficients of the element whose isotopic exchange is considered, δ_i are the isotopic compositions of these compounds (shifts relative to an isotope standard), δ_Σ is the bulk isotopic composition of the system, and n is the number of compounds involved in the isotopic exchange;

(b) $(n - 1)$ equations for isotopic exchange equilibrium:

$$\delta_i - \delta_a = 1000 \ln \alpha_{i-a}, \quad (i \neq a), \tag{34}$$

where δ_a is an arbitrarily chosen substance from those present in the system, and α_{i-a} is the isotope fractionation coefficient between the substances i and a.[24]

The system is linear with respect to the unknown δ_i parameters, and its solution is straightforward. Ohmoto (1972) solved the problem explicitly by substituting δ_i expressed from the exchange equation through δ_a and $\ln\alpha$ into the balance equation. Bowers and Taylor (1985) and Janecky and Shanks (1988) designed special computer subroutines for the solution of isotopic problems, which were implemented in the EQ3/6 program for the calculation of chemical equilibria. A similar isotopic subroutine was designed by the author as a module in the GBFLOW (v.3.1) program.

In his pioneering study, which has been extensively cited in the geochemical literature (e.g., Faure, 1986), Ohmoto calculated variations in the isotopic compositions of sulfur and carbon depending on the intensive parameters of the hydrothermal process, and quantitatively evaluated the influence of chemical reactions on the isotopic compositions of components in hydrothermal solutions (Ohmoto, 1972).

Various geochemical problems were approached using the Ohmoto method. Bannikova and Ryzhenko (1984) studied the carbon and sulfur isotope compositions of compounds of the C–H–O–S system. They revealed significantly nonlinear dependencies of the isotopic compositions on the initial bulk composition of the system. These authors constructed alignment charts on the basis of simulations and correlated the isotopic compositions of fluids with their chemical characteristics, in particular, with the degree of oxidation. These results were used by Bannikova (1990) for the geochemical reconstruction of hydrothermal ore formation.

The most sophisticated combined isotopic and geochemical model was constructed by Bowers and Taylor (1985) for the convective hydrothermal system of a mid-ocean ridge (see Section 3.3). They calculated the oxygen and hydrogen isotopic evolution of a hydrothermal solution in a ten-component chemical multisystem including more than 30 minerals. They showed that the isotopic shifts δD_{H_2O} and $\delta^{18}O_{H_2O}$ are not large in a convective system, reaching +2.6‰ and +2.0‰, respectively, which was in agreement with the direct measurements by Wehlan and Craig (1983) for hydrothermal systems at 21° N on the EPR. The model bulk isotopic compositions of secondary minerals developing after basalts are also reasonably consistent with the isotopic systematics of altered ocean-floor basalts and ophiolitic rocks.

Janecky and Shanks (1988) derived an isotopic geochemical model based on sulfur isotopes for the process of ore deposition in oceanic hydrothermal systems. Its chemical part is identical to the model of ore deposition with mixing developed by Janecky and Seyfried (1984) on the basis of the titration concept (Section 3.3). These authors assumed that the hydrothermal solution entering from the convective system has a constant $\delta^{34}S_{H_2S}$ of +1‰ and demonstrated by calculation that no process which accompanies mixing with seawater and reactions with the country rocks is capable of increasing $\delta^{34}S_{H_2S}$ above +4.5‰ (observed in some oceanic hydrothermal systems, see Section 5.3). In order to explain the heavy sulfur isotopic composition, they invoked additional reduction of marine sulfate species by interaction with basalts within the feeder channel (i.e., the subsurface mixing of solutions with different histories).

The use of the Ohmoto method in the aforementioned and other studies allowed a comprehensive interpretation of isotopic data and in some cases provided isotopic geochemical criteria for the reconstruction of hydrothermal processes. The development and application of this method contributed significantly to the general geochemical theory of hydrothermal processes.

5.2. Method of an Isotopic Chemical System

Ryzhenko proposed an alternative approach to the calculation of isotopic equilibria in systems with chemical reactions. The basic idea underlying his method is that both chemical reactions and isotopic exchange are governed by the fundamental principle of chemical thermodynamics—a tendency toward the minimum free energy of the system. If isotopes rather than elements are used as independent components, thermodynamic equilibrium can be simultaneously calculated for chemical reactions and isotope exchange reactions.

Based on this approach, Bannikova *et al.* (1987) and Grichuk (1987, 1988) developed a method for the thermodynamic calculation of isotopic and chemical reactions, which is referred to as the method of isotopic chemical systems. In contrast to the two-stage calculation procedure by Ohmoto (chemical equilibrium followed by isotopic equilibrium), the method of isotopic chemical systems achieves the desired goal in a single calculation step. Such equilibria can be calculated using standard programs designed for the solution of nonisotopic thermodynamic problems.

[24] Bowers and Taylor (1985) used a more rigorous equilibrium condition, $\delta_j = (1000 + \delta_i)\alpha_{ij} - 1000$.

It should be noted that the method of isotopic chemical systems is theoretically more rigorous than the Ohmoto method. The validity of the two-stage computational procedure relies on the negligible influence of isotope redistribution on equilibrium in chemical reactions. The advantages and disadvantages of the Ohmoto method and the method of isotopic chemical systems are analyzed below.

The implementation of the method of isotopic chemical systems requires knowledge of the thermodynamic characteristics of the components of the system, the Gibbs free energies of the isotopic forms of compounds, $\Delta_f G^{0I}$. The existing fundamental handbooks on the thermodynamic properties of substances (*Thermal Constants…*, 1965–1979; *Thermodynamic Properties…*, 1978–1982; IVTANTERMO, 1983–1985) provide systematic data only for the compounds of hydrogen isotopes, ^{1}H, ^{2}D, and ^{3}T. For other elements, there are only practical thermodynamic functions for the compounds of natural isotopic mixtures. They do not account for nuclear constituents, including those related to the mixing of various isotope forms. The method of isotopic chemical systems must include a means for calculating the free energies of formation of isotopic forms of compounds from the available experimental data.

This problem was addressed by Grichuk (1987), who derived a general equation for the calculation of $\Delta_f G^{0I}$ from the known practical function, free energy of formation of compounds, $\Delta_f G^{0E}$, and isotope fractionation coefficients between the given compound and the element in a standard state, α. For the arbitrary compound Z composed of y chemical elements, the free energies of fully substituted forms, under the conditions of independent isotopic exchange between elements in a Z molecule, can be expressed as

$$\Delta_f G^{0I}_{Zyj} = \Delta_f G^{0E}_Z + RT\sum_y \left[n_y \sum_j^{l_y} (N_{yj\text{st}} \ln^{yij} \alpha_Z) \right] - RT\left(\varphi_Z + \sum_y n_y n_{y\text{st}} \psi \right), \quad (35)$$

where n_y is the number of atoms of y in Z, l_y is the number of isotopes of element y, $N_{yj\text{st}}$ is the average abundance of the isotope in nature, and φ_Z and ψ are corrections for possible variations in the isotopic composition of the compound.

For the relevant case of two isotopes of the element considered (^{1}H–^{2}D, ^{12}C–^{13}C, ^{14}N–^{15}N, ^{16}O–^{18}O, and ^{32}S–^{34}S), Eq. (35) can be significantly simplified. For the element X of the compound AX, consisting of light (X^0) and heavy (X^*) isotopes:

$$\Delta_f G^{0I}_{AX^0} = \Delta_f G^{0E}_{AX} + N_{X^*} RT \ln \alpha_{AX} \quad (36a)$$

and

$$\Delta_f G^{0I}_{AX^*} = \Delta_f G^{0E}_{AX} + N_{X^0} RT \ln \alpha_{AX}, \quad (36b)$$

where N_{X^0} and N_{X^*} are the average relative abundances of the isotopes, and α_{AX} is the isotope fractionation coefficient for AX relative to the standard state of X.

The equations derived above are valid for both the Gibbs free energies of the isotopic forms of compounds, $\Delta_f G^{0I}$, and the reduced free energies, g^{0I}_T.

Isotopic exchange between geologically important compounds has been studied for only a few elements (H, C, O, and S). Data on the isotopic fractionation of most major elements are scanty. Therefore, most of the problems addressed in geochemical studies concern isotopic fractionation with respect to one or a few elements occurring in the system. Such problems can be referred to as semi-isotopic to discriminate them from full isotopic problems accounting for all isotopes of the chemical elements occurring in the system. The calculation of the thermodynamic properties of isotopic forms of compounds for such semi-isotopic systems presents no considerable difficulties, because isotopic exchanges of various elements (except for hydrogen) occur practically independently. The coupling of isotopic exchanges of hydrogen and other elements is a second-order effect, and its magnitude is comparable with the errors of the experimental and theoretical determination of α. Such problems can be resolved using Eqs. (36a) and (36b) (e.g., Bannikova *et al.*, 1987). The results of thermodynamic calculations for the semi-isotopic (sulfur) model of a convective hydrothermal system in the oceanic crust are discussed in Section 5.4.

Comparison of the methods of Ohmoto and isotopic chemical systems. The method of isotopic chemical systems considers isotopes as independent components of the system. The basic principles of chemical thermodynamics are therefore applicable, and, correspondingly, standard programs can be used for the simulation of such systems. As was mentioned above, the Ohmoto method involves two stages: chemical equilibrium is calculated in the first stage, and isotopic equilibrium is calculated in the second stage. The first stage can be performed using standard programs for thermodynamic modeling, whereas special program modules are needed for the second stage (e.g., Bowers and Taylor, 1985; Janecky and Shanks, 1989). Each of the two methods has its own advantages and limitations.

Method of isotopic chemical systems. Any program of thermodynamic modeling can be used for the simulation of isotopic chemical models of homogeneous systems (liquid or gas). However, geochemically important problems usually involve isotopic exchange in heterogeneous systems (gas–solid or aqueous solution–solid phases). In such a case, each solid phase participating in the isotopic exchange must be considered as a solid solution of isotopic forms (isotopic end-members). The simulation of such systems requires pro-

grams for the calculation of equilibria in systems with several phases of variable composition. Such programs belong to the highest complexity class according to the nomenclature by Shvarov (*Methods of…*, 1988) and are few in number (GIBBS, SELECTOR, and HCh). This imposes technical limitations for use of the isotopic chemical systems method.

The input information for the method is the isotopic ratios of the initial system and the thermodynamic properties of isotopic forms of compounds. The initial isotopic ratios are defined by geological models and their quality is not discussed here. The thermodynamic properties of isotopic compounds can be calculated from ordinary (elemental) thermodynamic parameters and the fractionation coefficients of isotopes using the equations derived in the previous section. This can be done without any principal difficulties using thermodynamic data banks similar to UNITHERM, because only $\Delta_f G^0$ (298 K) values and two or three coefficients of heat capacity equations (depending on the form of the temperature function of $\ln\alpha$) have to be changed. The shortcoming of this approach is that the calculation of isotopic exchange for several elements (e.g., H, O, and C) involves a considerable number of isotopic forms that must be accounted for. The thermodynamic data banks will be expanded correspondingly. In this respect, the potential of the method of isotopic chemical systems appears to be somewhat excessive for the present-day status of the thermodynamic modeling of geologic processes.

The accuracy of calculations by this method is controlled by the errors of the input thermodynamic data and uncertainties imposed by the computational program. The errors of thermodynamic data are propagated from (a) errors in elemental thermodynamic properties and (b) errors in isotope fractionation coefficients (obtained experimentally or calculated), which are usually between $n \times 10^{-4}$ and $(1–2) \times 10^{-3}$ ($\ln\alpha$). It should be noted that the assumption used for the derivation of Eqs. (35) and (36) do not affect the quality of the calculation of isotope fractionation. The computational error for the simulation of equilibria in the GIBBS, HCh, and GBFLOW programs is no higher than 10^{-5} in the molar fractions of components, which corresponds to 0.01‰ for the equilibrium isotopic composition of compounds.

It can be seen that the main source of error in the method under question is ordinary thermodynamic data. The internal sources of error are several orders of magnitude smaller. Correspondingly, the computational errors are smaller than the experimental uncertainties of $\ln\alpha$.

The Ohmoto method involves the development of special isotopic blocks (subroutines) extending any program for the calculation of chemical equilibria. The program realization of these blocks is straightforward. The input isotopic data are not connected with the thermodynamic properties of substances in the Ohmoto method, and there is no need to include them in basic thermodynamic data banks. This facilitates the use of this method for the solution of particular geochemical problems. The Ohmoto method utilizes the same g_T^0 (or equilibrium constants) and $\ln\alpha$ values as the method of isotopic chemical systems. Consequently, the errors of these parameters contribute similarly to the results of calculations by the both methods.

The Ohmoto method is theoretically less rigorous than the method of isotopic chemical systems because of a number of inherent simplifications.

(1) The two-stage calculation procedure in the Ohmoto method is based on the implicit assumption that isotopic exchange does not influence chemical equilibria, i.e., there are no coupled isotopic–chemical effects. In general, this is in agreement with empirical data.

(2) In the system of Eqs. (33) and (34), the mass conservation equations for each isotope (which are exactly satisfied in the method of isotopic chemical systems) are replaced by the balance equation of isotopic shift (Eq. (33)).

(3) The derivation of Eq. (34) in the Ohmoto method is based on the approximation of natural logarithms $\ln(1 + \delta) \approx \delta$.

The inspection of errors related to these assumptions suggests that they are usually negligible. The errors in the equilibrium constants of chemical reactions related to assumption (1) (ignoring coupled isotopic–chemical effects) are described for each atom participating in isotopic exchange by the following equation (Grichuk, 1998):

$$\delta(\mathrm{p}K_r) \approx \frac{1}{2303} X^* \ln\alpha \ln\left(\frac{X^*}{X^0}\right), \qquad (37)$$

where X^* is the fraction of the less abundant isotope, and X^0 is the fraction of the more abundant isotope. For geochemically important reactions, this effect is no larger than $n \times 10$ J/g-atom and usually much smaller. It is much smaller than the typical errors of elemental thermodynamic parameters.

The maximum systematic error in the results of calculation of isotope fractionation due to assumption (2) is given by the following equation for the isotopic exchange between two compounds:

$$(-\varepsilon_\delta)_{\max} = \frac{10^3}{4}\left(\frac{X^*}{X^0}\right)(\ln\alpha)^2(‰). \qquad (38)$$

The magnitude of this systematic shift is no higher than $0.0n$‰ for all light elements (except for Li and B), and it can be ignored in geochemical applications.

Assumption (3) introduces an error in the calculation of isotopic compositions specified by the equation

$$\xi_\delta \approx \delta_{\mathrm{av}} \ln\alpha_{ij}, \qquad (39)$$

where $\delta_{\mathrm{av}} = (\delta_i - \delta_j)/2$. If δ_{av} is strongly different from the isotopic standard, this assumption may lead to con-

siderable errors, which are higher than the confidence limits of empirical constants used in the models (up to 3–9‰). It is desirable, therefore, to use the Ohmoto method with the exact equation of isotopic exchange (instead of Eq. (34)) in the form

$$\alpha_{ij} = \frac{X_i^* X_j^0}{X_i^0 X_j^*}$$

in combination with the mass conservation condition for each isotope, or in another form:

$$\alpha_{ij} = \frac{\delta_i + 1000}{\delta_j + 1000},$$

as was proposed by Bowers and Taylor (1985).

Taking into account these refinements, it can be concluded that the Ohmoto method and the method of isotopic chemical systems give practically identical results for geochemical problems, and the choice of a particular procedure depends on practical circumstances, including the availability of software complexes and convenience of their application. For instance, the two methods were successfully used by Bannikova (1990).

5.3. Sulfur Isotopic Systematics of Oceanic Sulfide Ores

Sulfur isotopic systematics are among the most sensitive indicators in the geochemistry of hydrothermal processes, because sulfur is a major ore element undergoing complex chemical transformations which are recorded in the distribution of its isotopes. There are more than 30 publications on the investigation of the sulfur isotopic compositions of modern oceanic sulfides.

Early studies (Styrt *et al.*, 1981; Arnold and Sheppard, 1981) reported $\delta^{34}S$ values for oceanic sulfides between +1 and +4‰, and it was argued that their sulfur had a mixed origin: most sulfur is derived by the leaching of sulfides from basalts ($\delta^{34}S \approx 0$‰), and a smaller portion is produced by the reduction of seawater sulfate species within the convective system ($\delta^{34}S \approx +20$‰). This interpretation was in agreement with the most popular concept of the source of sulfur in massive sulfide deposits (Ohmoto and Rye, 1979) and was based on the experimental data in the seawater–basalt system then available.

An alternative hypothesis for the genesis of sulfur in massive sulfide deposits is sulfur isotope fractionation during the reduction of marine sulfate sulfur (Sasaki, 1970; Kajiwara, 1971). It appeared to be completely at odds with the data obtained for smokers. This hypothesis was based on an isotopic fractionation of between –21 and –17‰ for the SO_4–FeS_2 pair at 300–350°C. In such a case, the reduction of marine sulfate would have produced sulfides with near zero isotopic signatures, corresponding to those observed in massive sulfide ores. However, such $\delta^{34}S$ values of sulfides could be obtained only if there is an excess of sulfate sulfur. If the inventory of sulfates is limited, a Rayleigh distillation must occur and the resulting sulfur isotope composition of the sulfides must become heavier, approaching that of initial sulfate at complete reduction. The question on the content of SO_4 in the zone of ore formation of ancient massive sulfide deposits has not yet been clarified. The complete reduction of sulfates was established for smokers from the chemical compositions of emanating solutions. Consequently, the Sasaki–Kajiwara hypothesis cannot explain the isotopically light composition of sulfides.

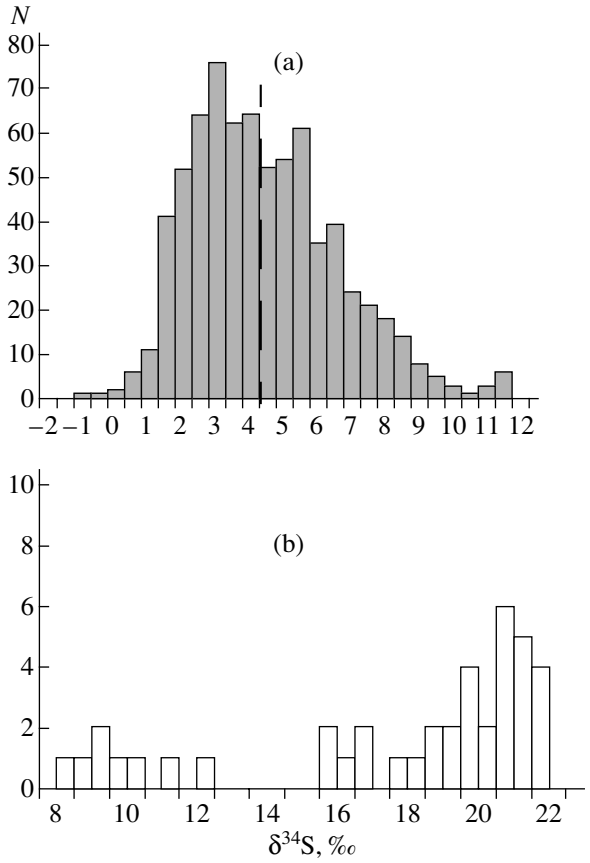

Fig. 42. Isotopic compositions of sulfide and sulfate sulfur from oceanic sulfide edifices (excluding the Guaymas Basin). The sources of data are given in Fig. 43. (a) Sulfides, the dashed line shows the average $\delta^{34}S$ value for the data set; and (b) sulfates (barite and anhydrite).

Figure 42 shows a generalized distribution of isotopic compositions in all oceanic hydrothermal objects. Although the extent of sampling varies considerably between the sites, the data set is still representative owing to the great number of objects studied (845 determinations were processed). The diagram shows that the average $\delta^{34}S$ of modern marine sulfide deposits is +4.41‰ (Fig. 42a). The distribution of isotopic compositions is distinctly asymmetric with a mode of $\delta^{34}S = +3.0$‰.

The $\delta^{34}S$ of anhydrite and barite from modern hydrothermal systems ranges between +8 and +22‰

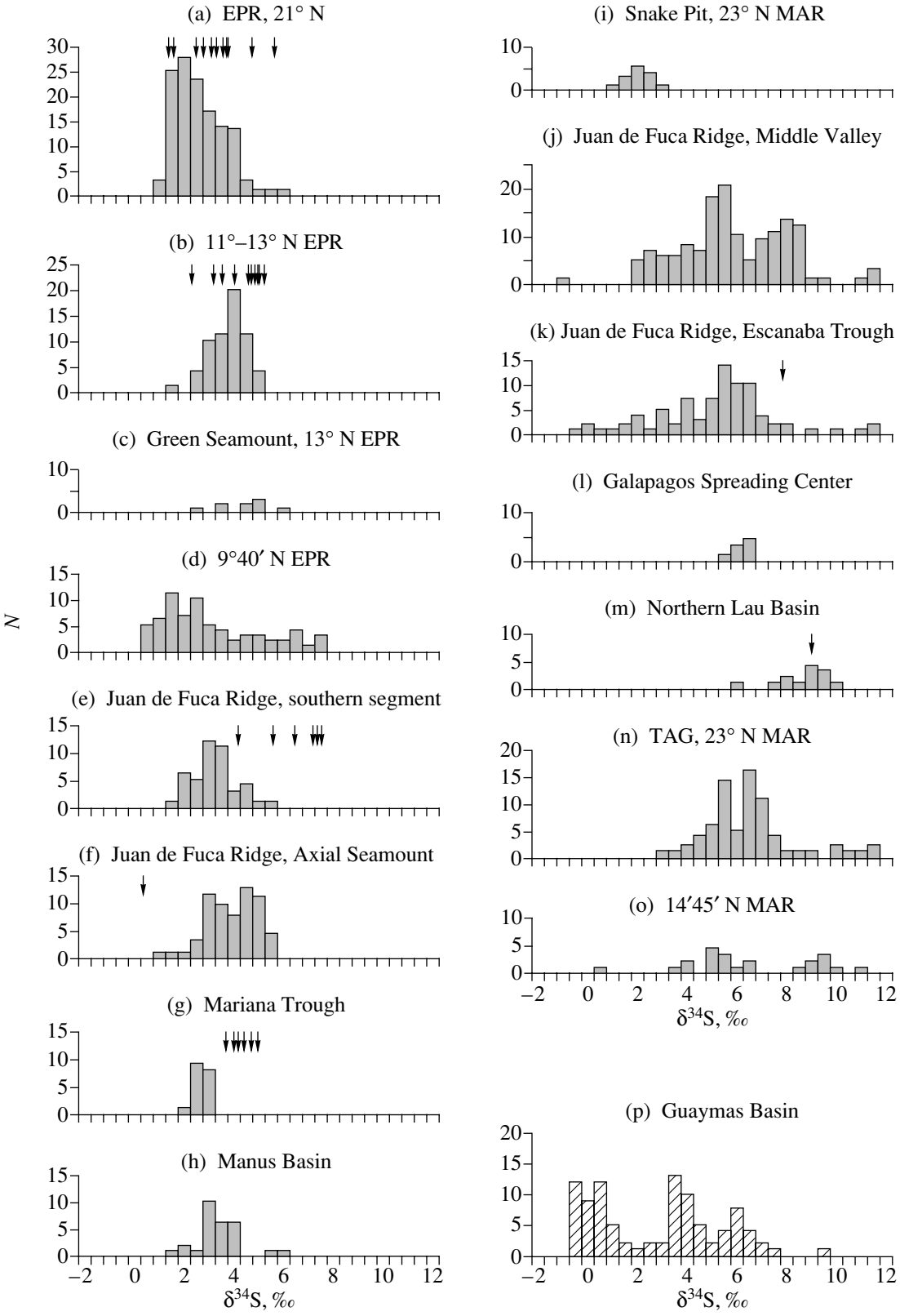
(a) EPR, 21° N
(b) 11°–13° N EPR
(c) Green Seamount, 13° N EPR
(d) 9°40′ N EPR
(e) Juan de Fuca Ridge, southern segment
(f) Juan de Fuca Ridge, Axial Seamount
(g) Mariana Trough
(h) Manus Basin
(i) Snake Pit, 23° N MAR
(j) Juan de Fuca Ridge, Middle Valley
(k) Juan de Fuca Ridge, Escanaba Trough
(l) Galapagos Spreading Center
(m) Northern Lau Basin
(n) TAG, 23° N MAR
(o) 14′45′ N MAR
(p) Guaymas Basin
N
δ34S, ‰
δ34S, ‰

Fig. 43. Histograms of sulfur isotope compositions of oceanic sulfides. Arrows show the isotopic compositions of hydrogen sulfide from smoker solutions. Data sources: (a) 21° N EPR (Styrt *et al.*, 1981; Arnold and Sheppard, 1981; Kerridge *et al.*, 1983; Zierenberg *et al.,* 1984; Woodruff and Shanks, 1988); (b) 11°–13° N EPR (Bluth and Ohmoto, 1988; *Hydrothermal Sulfide…,* 1992); (c) 13° N EPR, Green Seamount (Alt, 1988); (d) 9°40′ N (*Hydrothermal Sulfide…*, 1992); (e) Juan de Fuca Ridge, southern segment (Shanks and Seyfried, 1987); (f) Juan de Fuca Ridge, Axial Seamount (Hunnington and Scott, 1988); (g) Mariana Trough (Kusakabe *et al.*, 1990); (h) Manus Basin (Lein *et al.*, 1993); (i) Snake Pit, 23° N MAR (Kase *et al.*, 1990); (j) Juan de Fuca Ridge, Middle Valley (Goodfellow and Blaise, 1988; Goodfellow and Franklin, 1993); (k) Juan de Fuca Ridge, Escanaba Trough (Koski *et al.*, 1988; Zierenberg *et al.*, 1993); (l) Galapagos Spreading Center (Skirrow and Coleman, 1982); (m) northern Lau Basin (Bortnikov *et al.*, 1993); (n) TAG field, 23° N MAR (Lein *et al.*, 1991; *Hydrothermal Sulfide…,* 1992; Herzig *et al*., 1998b); (o) 14°45′ N MAR (Bogdanov *et al.*, 1997a); and (p) Guaymas Basin (Koski *et al.*, 1985; Lein *et al.*, 1988; Peter and Shanks, 1992).

with a mode of 21‰ (Fig. 42b). This is interpreted as the result of formation of the main mass of sulfate minerals by mixing of hydrothermal solutions with seawater.

A comparison of the sulfur isotope data for individual hydrothermal fields (Fig. 43a–43p) reveals some general relationships.

(1) In the majority of sampled edifices, sulfide minerals are isotopically disequilibrated (Styrt *et al.*, 1981; Zierenberg *et al.*, 1984). Attempts to calculate isotopic temperatures yielded unrealistically high values (450–700°C), and some data could not be interpreted at all.[25]

(2) In some edifices later sulfides appeared to have higher $\delta^{34}S$ (e.g., at 21° N on the EPR, data by Woodruff and Shanks, 1988).

(3) Intriguing results were obtained from a comparison of the $\delta^{34}S$ values of sulfide minerals and H_2S of hydrothermal solution (Figs. 43a, 43b, 43e, 43f, 43g, 43k, 43m). In the majority of hydrothermal vents, hydrogen sulfide is isotopically heavier than sulfides from the edifice (Bluth and Ohmoto, 1988). The opposite relationship was reported only from three of 27 sampled hydrothermal vents.

(4) The isotopic compositions of sulfides from the vents of the Guaymas Basin, whose hydrothermal system develops mainly in a sedimentary sequence, appeared to be systematically lighter than in other systems, and even lighter than magma-derived sulfur (Peter and Shanks, 1992) (Fig. 43p). The histogram of isotopic compositions illustrates their distinct polymodal distribution. This is interpreted as resulting from the contribution of bacterial sulfides mobilized from sediments to the formation of the isotopic compositions. However, this effect has not been observed in other similar systems (Escanaba and Middle Valley) where solution circulation entrains sediments (Figs. 43j, 43k).

(5) A comparison of data on various hydrothermal sites showed that sulfides from large hydrothermal structures are isotopically heavy (compare Figs. 43a–43i and 43j–43o). This phenomenon was pointed out by Lein *et al.* (1991), Grichuk and Lein (1991), and by the authors of *Hydrothermal Sulfide…* (1992).[26] When all the available data are grouped into two sets, small edifices and large structures (the latter includes sulfide bodies from the TAG, Middle Valley, Escanaba, and Galapagos Spreading Center with masses of $n \times 10^5$–$n \times 10^6$ t), their average $\delta^{34}S$ values are +3.19 and +5.75‰, respectively. The distributions appear to be almost normal (Figs. 44a, 44b).

The isotopic heterogeneity of modern oceanic hydrothermal deposits has long intrigued researchers, and a number of hypotheses have been proposed to explain this phenomenon (see Bluth and Ohmoto, 1988 for a review). They invoked different origins of the isotopic signatures of hydrothermal solutions and different places of the generation of variations in sulfide composition.

The sulfur isotope compositions of sulfides from oceanic deposits were first reported by Styrt *et al.* (1981), who supposed that the observed isotopic variations reflect different proportions of sulfur leached from basalts and marine sulfur reduced to hydrogen sulfide during water–basalt interaction. This hypothesis was further developed by Bluth and Ohmoto (1988), who argued that the proportion of sulfur sources changes with time: the fraction of S^{II} reduced from sulfate increases and, as a result, the isotopic composition of dissolved hydrogen sulfide is systematically heavier compared with that of the sulfide body. These authors explained local variations in the composition of sulfides by the isotopically disequilibrium processes of sulfide replacement in the chimney walls of smokers. Thus, at any given time, each hydrothermal system shows its own $\delta^{34}S$ value of hydrothermal solution depending on the water–rock interaction within it. Grichuk (1988) and Grichuk and Lein (1991) developed an isotopic chemical thermodynamic model corresponding to this hypothesis. The structure and outcomes of this model are discussed in detail in Section 5.4.

An alternative hypothesis was proposed by Shanks and Seyfried (1987). They supposed that SO_4^{2-} is reduced during seawater circulation in basalts through

[25] The minerals that must be isotopically lighter than pyrite in equilibrium, for instance, bornite, pyrrhotite, and sphalerite, appeared to be isotopically heavier, which can be exemplified by the data from 21° N EPR (Woodruff and Shanks, 1988) and Axial Seamount and Middle Value of the Juan de Fuca Ridge (Hannington and Scott, 1988; Goodfellow and Franklin, 1993).

[26] Sulfides with very high $\delta^{34}S$ were recently reported from a small sulfide edifice in the northern Lau back-arc basin (Fig. 43m).

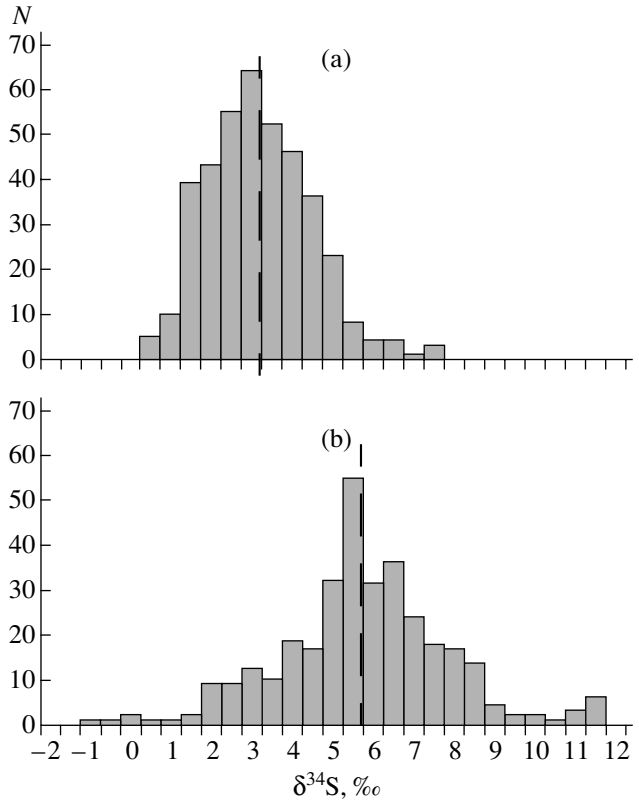

Fig. 44. Histograms of the isotopic compositions of sulfides from ore structures of (a) small and (b) large sizes. The dashed lines show average values for the data sets.

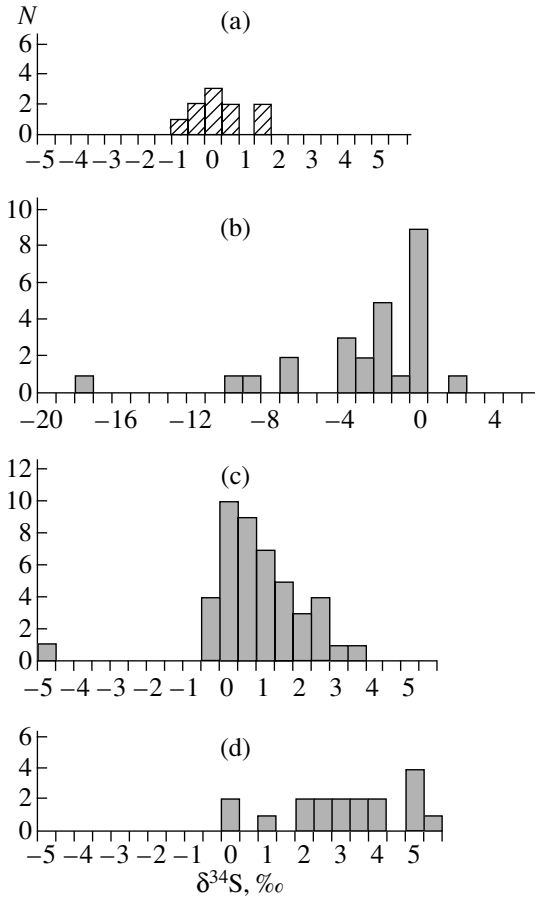

Fig. 45. Selected results of the investigation of oceanic basalts recovered from ODP Hole 504B in the Costa Rica rift. (a) Monosulfides from the basalts of the dike complex (Alt *et al.*, 1989); (b) disseminated pyrite from the transitional zone (Belyi *et al.*, 1984); (c) disseminated pyrite from the rocks of the dike complex (Alt *et al.*, 1989); and (d) vein pyrite (Kawahata and Shikazono, 1988; Alt *et al.*, 1989).

the conversion of magmatic pyrrhotite to pyrite via the reaction

$$7FeS + 8H^+ + SO_4^{2-} \longrightarrow 4FeS_2 + 4H_2O + 3Fe^{2+}.$$

They supposed also that the newly formed pyrite has a mixed isotopic composition, which was estimated as +2.9‰ by isotope balance calculations in accordance with the stoichiometry of this reaction. It was also suggested that the hydrothermal solution has to be in isotopic equilibrium with this pyrite, which constrains its $\delta^{34}S$ = +2.1‰ at 370°C. This value must characterize hydrothermal solutions produced within any oceanic hydrothermal system. The logic of this hypothesis implies that the only factor affecting the $\delta^{34}S$ value of solution within the system is temperature: the lower the temperature, the higher the fractionation coefficient α for the pyrite–hydrogen sulfide pair, and the lighter the isotopic composition of hydrogen sulfide (however, the degree of fractionation is rather low: at 300°C the $\delta^{34}S$ of solution in the interior part of the system is +1.7‰).

It can be easily seen that this scenario is based on several arbitrary assumptions. The pyrrhotite–pyrite conversion is not the only possible mechanism of sulfate reduction during solution–basalt interaction. Both experimental data and calculations suggest that the reduction occurs with concurrent transformations of iron-bearing aluminosilicates (Fe^{II} of pyroxenes and olivine to Fe^{III} of epidote). Shanks and Seyfried (1987) mentioned a $\delta^{34}S$ value of between +2.9 and +5.0‰ for vein pyrite from DSDP Hole 504B (Honnorez *et al.*, 1985). However, this vein pyrite was precipitated from solutions ascending in a stockwork zone at a relatively low temperature (about 200°C). The subsequent analyses of disseminated pyrite from the rocks of the dike complex (Alt *et al.*, 1989) yielded much lower $\delta^{34}S$ values (+0.69‰ on average) (Fig. 45c), which are only slightly higher than that of the initial monosulfides (+0.2‰ on average, Fig. 45a). Many analyses of oceanic sulfides (more than 15% of the data set, Fig. 42a) have $\delta^{34}S$ values below a critical value of +2.1‰.

In a later study, Janecky and Shanks (1988) dismissed the idea of the pyrrhotite–pyrite conversion and postulated that the isotopic composition of an ascending hydrothermal solution is close to that of magmatic sulfides, $\delta^{34}S$ = +1.0‰. The negligible contribution from marine sulfate into the isotopic composition of

Table 22. Estimation of the fraction of seawater in mixtures according to the Shanks hypothesis

Hydrothermal system	Sampled object	Reference	c_{H_2S}, mmol/kg	δ_{H_2S}, ‰	X, %
Juan de Fuca Ridge, Cleft segment, 45° N	Plume	[Shanks and Seyfried, 1987]	0.72	5.6	0.66
	"		2.617	4.2	1.66
	"		0.2	7.3	0.25
	vent 1		0.544	6.4	0.58
Juan de Fuca Ridge, Escanaba Trough, 41° N	–	[Zierenberg *et al.*, 1993]	1.1	7.8	1.48
EPR, 21° N	NBS	[Woodruff and Shanks, 1988]	3.8	3.4	1.80
	OBS		7.4	1.5	0.73
	OBS		6.9	1.3	0.41
	SW		4.0	3.5	1.98
	HG		3.9	2.3	1.00
	HG		3.0	3.2	1.31
EPR, 13° N	vent 6	[Bluth and Ohmoto, 1988]	8.2	4.7	6.00
	vent 8		4.5	3.3	2.05
	vent 10		8.0	4.6	5.70

solutions generated within the hydrothermal system was explained by the removal of sulfate from the solution by anhydrite precipitation at the beginning of the downwelling convective flow. According to the modified hypothesis, isotopic variations are already generated in the ascending channel beneath ore bodies and within ore bodies at the expense of mixing with seawater and/or anhydrite reduction. The different magnitudes of $\delta^{34}S$ increase in sulfides from various hydrothermal systems are explained by variable mixing proportions.

As was mentioned in Section 3.1, the scales of subsurface mixing cannot be reliably constrained from the data on solution chemistry, because the currently accepted method of analysis recalculation involves extrapolation to Mg = 0. The fraction of seawater (X) required, according to the Shanks hypothesis, for such a mixing can be estimated by chemical and isotopic balances calculated using equations similar to Eq. (33):

$$C_o = C_d(1 - X) + C_wX$$

and

$$C_o\delta_o = C_d\delta_d(1 - X) + C_w\delta_wX,$$

where the subscripts d, w, and o refer to the deep hydrothermal solution, seawater, and the values observed in smokers, respectively; C is the concentration of sulfur in the solution (hydrogen sulfide in hydrothermal solutions and sulfate in seawater). This system can be readily transformed to

$$X = \frac{C_o}{C_w}\frac{\delta_o - \delta_d}{\delta_w - \delta_d}.$$

Following the model of Shanks, let us accept δ_d = +1.0‰, δ_w = +20‰, and C_w = 28.23 mmol/kg. Then, X can be calculated for any given δ_o and C_o. Such calculations for some sampled vents are shown in Table 22. It can be seen from these results that the observed variations in the isotopic composition of hydrogen sulfide imply a relatively small fraction of seawater in the mixture, only 0.25–6.0%. However, even such small additions of seawater should have resulted in the precipitation of considerable amounts of magnesium silicates (talc and serpentine, Section 4.3.1) comparable with the amounts of newly formed sulfides, which is not the case in the objects studied.

The isotopic chemical simulation carried out by Janecky and Shanks (1988) showed that the disequilibrium reduction of sulfates during mixing provides $\delta^{34}S$ values of solutions no higher than +2.5‰, and sulfides deposited from them have $\delta^{34}S$ values no higher than +4.5‰. A comparison of these results with natural data (Figs. 42a, 43) shows that the mixing model does not explain the observed diversity of isotopic compositions. Janecky and Shanks proposed that a more extensive process of sulfate reduction must occur in the feeder zone with the participation of hydrothermal solutions, fresh basalts, and anhydrite. The supposed reduction of isotopically heavy sulfate can provide any increase in the $\delta^{34}S$ of solution discharging on the ocean floor. Thus, the Shanks hypothesis implies that the isotopic variations are related to factors that are accidental with respect to processes in the interior of hydrothermal systems (subsurface mixing and anhydrite occurrence in the channel). Therefore, the existence of the aforementioned persistent relationships in

the isotopic composition of sulfides cannot be explained by this hypothesis.

As possible indirect indicators, the Janecky–Shanks model predicted a decrease in copper content in the system with increasing $\delta^{34}S$ and a decrease in $\delta^{34}S$ with decreasing temperature, which must result in an expansion of the $\delta^{34}S$ range toward isotopically light compositions in large hydrothermal structures. These authors noted that the modern ore-forming systems of mid-ocean ridges are too small, too young, and too poorly sampled to display such effects (Janecky and Shanks, 1988, p. 820). The data of subsequent studies were not compatible with these predictions. Large hydrothermal systems are relatively enriched in copper (Section 3.1) and show the heaviest isotopic compositions of sulfides (Figs. 43i–43l). The Shanks hypothesis does not explain the systematic increase in $\delta^{34}S$ of dissolved hydrogen sulfide relative to the sulfides of hydrothermal edifices.

Bowers (1989) presented isotopic chemical models for the downwelling limb of a hydrothermal convection system. She considered four types of models. Types *1* and *2* reproduced isothermal seawater–basalt interaction by the method of the degree of reaction progress, i.e., in a closed system. Types *3* and *4* simulated polythermal step flow reactors with different *R*/*W* distributions between temperature steps. Owing to the closed character of the systems (Section 2.1), marine sulfur was not removed from the system in isothermal models type *1* and *2*, and $\delta^{34}S$ of hydrogen sulfide increased accordingly to +15–17‰ at $R/W \approx 0.2$. $\delta^{34}S$ decreased to +5.2 and +8.8‰ at higher $R/W = 2$ owing to the dilution by sulfur from basalts. Since it is clear that such a model (closed system with back-reactions) is not appropriate for convective systems, Bowers carefully interpreted these results. The mineral assemblages and compositions of solutions obtained in type *3* and *4* models are very similar to those of the model of Bowers and Taylor (1985). These calculations suggest that sulfate is exhausted at a step of 250°C with concurrent anhydrite precipitation and, to a smaller extent (15–40% of initial content), is reduced to H_2S. The $\delta^{34}S$ of hydrogen sulfide and sulfide minerals increases in this step up to +(7–10)‰. The dissolved sulfur is diluted by magmatic sulfur during the following steps, and $\delta^{34}S$ declines rapidly in the solution to +0.5‰.

Proceeding from the results of these calculations, Bowers concluded that the reduction of marine sulfate within hydrothermal systems does not exert a strong influence on the isotopic composition of solutions and $\delta^{34}S < +1$‰ at $R/W > 1$. Thus, she supported the conclusions of Janecky and Shanks (1988) on the near-zero sulfur isotopic composition of solutions produced in the interior parts of hydrothermal systems. As to the reasons for the systematically higher $\delta^{34}S$ values of the sulfides and solutions of smokers, Bowers also accepted the explanation of Janecky and Shanks and rejected the idea of Bluth and Ohmoto (1988). Similar conclusions were derived by Kusakabe *et al.* (1990) from a study of hydrothermal systems in the Mariana Trough and, with some variations, by Herzig *et al.* (1998) for the Valu Fa Ridge.

The entrainment of isotopically heavy sulfate into the ore process through subsurface mixing was actively debated in connection with the results of drilling in the TAG hydrothermal field. The participants of this project accepted the Shanks model (e.g., Herzig *et al.*, 1998b). A detailed evaluation of their data is beyond the scope of our study. Note only that the main difference between the Shanks and Bluth–Ohmoto hypotheses is related to the place where the sulfur isotopic composition of fluid becomes heavier. According to the Bluth–Ohmoto hypothesis, this occurs in the downwelling limb of the system, and the feeder channel contains isotopically heavy hydrogen sulfide. According to Shanks, hydrogen sulfide entering the channel is isotopically light and its $\delta^{34}S$ increases through a reaction with anhydrite or subsurface mixing. In the TAG field, the isotopically heaviest pyrite ($\delta^{34}S_{av} = +8.0 \pm 0.7$‰) was found in the lowest parts of boreholes, below the zone of anhydrite occurrence (Knott *et al.*, 1998; Gemmell and Sharpe, 1998). Pyrite associating with anhydrite is lighter ($\delta^{34}S_{av} = +5.6 \pm 0.7$‰). In an attempt to reconcile these facts with the Shanks hypothesis, the aforementioned authors suggested a mixing of two fluids: a fluid of deep circulation with $\delta^{34}S \approx 5.5$‰ (this is merely the minimum value for sulfides from pyrite–anhydrite veins and is higher by 1‰ than the maximum value admitted by the model of Janecky and Shanks, 1988) and a hypothetical fluid of subsurficial circulation with isotopically heavy hydrogen sulfide ($\delta^{34}S \approx 9.0$‰). How can this mixing be correlated with the high temperature of the fluid emanating from edifices? How can the shallow convection cell, which is supplied by cold seawater, be heated up to the temperature of deep circulating fluid? The fact is that isotopically heavy pyrite was found in the same zones where the highest temperatures were recorded (Petersen *et al.*, 1998).

It can be easily seen that all these complex scenarios proposed by the authors cited stemmed from their conviction that a fluid with $\delta^{34}S$ higher than +4.5‰ cannot theoretically be derived in the downwelling limb of a convection cell.

Summarizing the current state of the problem of interpretation of oceanic sulfur isotope data, we conclude that a relatively simple and clear-cut qualitative model was proposed by Bluth and Ohmoto (1988). According to this model, sulfur from oceanic sulfide ores has a mixed (magmatic + marine) origin and the mixing proportion changes in time toward increasing contribution from the marine source. The local variations in isotopic compositions within edifices are related to the isotopic disequilibrium processes of mineral replacement. In principle, this scheme provides an explanation for all the observed relationships. However, the published quantitative models for the genera-

Table 23. Reference values of $10^3 \ln\alpha_{AX-BX}$ used for calculations; $10^3 \ln\alpha_{i\text{-}H_2S_{(g)}} = \frac{A}{T^2} \times 10^6 + C$ (after Ohmoto and Rye, 1979)

Substance	*A*	*C*	Estimated error, *	Note
S (g)	–0.16	0	±0.5	Consistent with Grinenko and Thode (1970)
$CaSO_4$	5.26	6	4–2	Similar to estimates by Friedman and O'Neil (1977) and Golyshev *et al.* (1983)
FeS_2	0.4	0	0.4–0.1	
FeS	0.1	0	0.3–0.1	
PbS	–0.63	0	0.3–0.1	
ZnS	0.1	0	0.3–0.1	Consistent with compilation by Friedman and O'Neil (1977)
Cu_2S	–0.75	0	0.5–0.15	Approximate estimate
$CuFeS_2$	–0.05	0	0.4–0.15	
Cu_5FeS_4	–0.25	0	0.5–0.15	Approximate estimate
SO_4^{2-}	5.26	6	4–2	=α for $CaSO_4$, anhydrite
$CaSO_4^0$				
$MgSO_4^0$				
$NaSO_4^-$				
HSO_4^-	6.3	1.9	4–2	After Igumnov *et al.* (1977)
H_2S	–	–	–	
HS^-	–0.06	–0.6	0.4–0.2	

* The uncertainty of α decreases with increasing *T*.

tion of sulfur isotopic compositions in oceanic hydrothermal systems are based on an alternative scenario, which cannot explain all the persistent relationships in the isotopic compositions of oceanic sulfides.

5.4. Isotopic Chemical Model for a Convective Hydrothermal System

Using the method of isotopic chemical systems described in Section 5.2, the author developed a quantitative model for the behavior of sulfur isotopes in the downwelling limb of an oceanic convective system (Grichuk, 1988; Grichuk and Lein, 1991; *Hydrothermal Sulfide…*, 1992). The chemical and dynamic aspects of this model are identical to those described in chapters 3 and 4. The processes of sulfur isotope redistribution occurring within the ore body are not considered in this model, because the available data suggest that they are strongly disequilibrated.

The main process reproduced by the isotopic chemical model is the mixing of marine sulfur ($\delta^{34}S$ = +20.0‰) with sulfur extracted from basalts by solutions ($\delta^{34}S$ = + 0.3‰; Sakai *et al.*, 1984). The mixing is complicated by isotope fractionation between dissolved sulfur species and sulfur-bearing minerals and a portion of the sulfur being expelled from minerals not in contact with solution, due to the transfer of solution portions (waves) to the next step of the flow reactor.

In order to simulate this model, the dimensionality of the chemical multisystem described in Section 3.4.2 was increased to 16 components through the separate consideration of ^{32}S and ^{34}S. The expanded set of species included seven ^{34}S isotope forms, and the sulfur-bearing minerals of the multisystem were regarded as ideal solid solutions of isotopic end-members forming eight series: anhydrite, pyrite, pyrrhotite (troilite), galena, sphalerite, chalcocite, bornite, and chalcopyrite. The thermodynamic properties of the isotopic forms were calculated from Eqs. (36a) and (36b) using elemental g_T^0 values from the UNITHERM database and α_T values taken from Table 23. Equilibria in isotopic chemical systems were calculated by the GIBBS program designed by Shvarov.[27]

Figures 46a and 46b show the calculated chemical and isotopic compositions of sulfur compounds in the downwelling limb of the convection cell for a case with $\Sigma R/W(400°C) = 1.26$ (wave no. 1). These results sug-

[27] These calculations were repeated using the GBFLOW v.3.1 program based on the Ohmoto method.

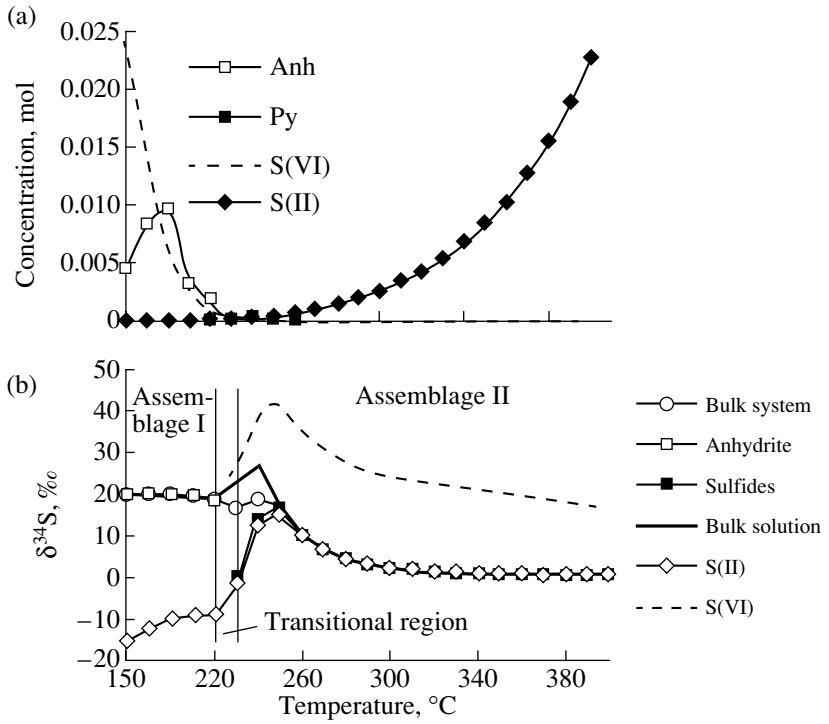

Fig. 46. Calculation of an isotopic chemical model for sulfur in the downwelling limb of a hydrothermal system at $\Sigma R/W(400°C) = 1.26$ (first wave). (a) The concentrations of major sulfur species and (b) the isotopic compositions of sulfur compounds.

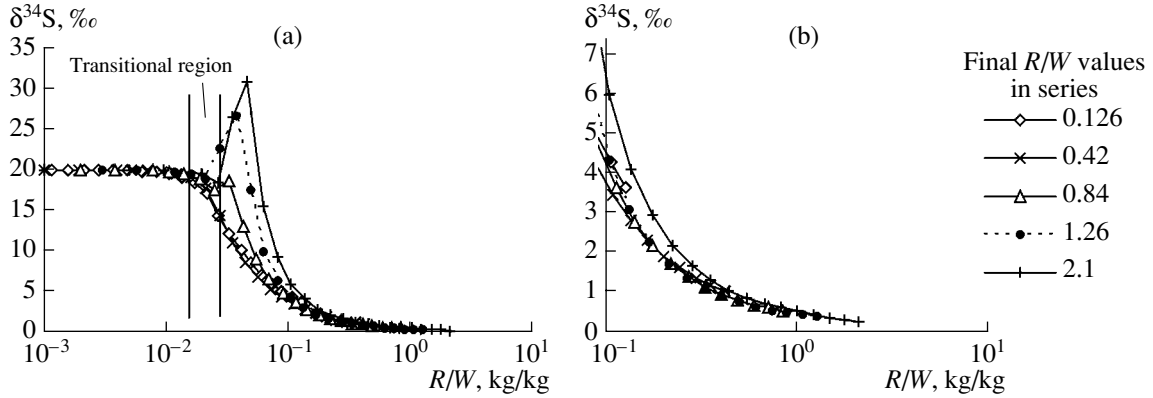

Fig. 47. Variations in the sulfur isotope composition of solution as a function of the cumulative R/W ratio calculated for variable intensity of interaction. (a) The dependency of isotopic composition on R/W and (b) the same for large R/W.

gest that within the stability field of assemblage I, the isotopic signature of sulfate sulfur remains almost constant. Hydrogen sulfide in equilibrium with the sulfate shows very low $\delta^{34}S$ values (but its concentration is very low). The concentration of sulfur in the solution decreases owing to anhydrite precipitation. In the region of transitional assemblages, the sulfate ion remaining in solution is reduced. During this process the $\delta^{34}S$ of hydrogen sulfide increases up to positive values, and that of residual sulfate may be as high as +40.7‰ owing to isotope fractionation. The isotopic compositions of sulfides are similar to that of H_2S, and the difference between them is in accordance with the fractionation coefficients in the mineral–hydrogen sulfide system. An increase in R/W in the stability field of assemblage II results in the entrainment of sulfur from igneous rocks, which lowers the $\delta^{34}S$ of solutions to ≈+0.5‰. These results were obtained by Grichuk (1988) and supported by the independent calculations of Bowers (1989) for a similar model. The bulk isotopic composition of solution ($\delta^{34}S_\Sigma$) is summed over various chemical forms and appears in the diagram (Fig. 46b) as a characteristic curve with a logistoid-like shape.

A comparison of the results corresponding to various R/W values (Figs. 47a, 47b) suggests that the tem-

perature of the system and R/W distribution in the model steps exert a noticeable influence on the form of the dependency of $\delta^{34}S_\Sigma$ on $\Sigma R/W$ in a hydrothermal solution. During a weak water–rock interaction ($\Sigma R/W(400°C) < 0.8$), the curves of the isotopic compositions of solutions practically coincide, whereas a stronger interaction significantly increases the bulk $\delta^{34}S$ of solution in the zone of transitional assemblages (Fig. 47a). The analysis of the simulation shows that this effect is related to the appearance of pyrite in the solid phase. In the presence of pyrite, the amounts of reduced and oxidized sulfur species become comparable, and isotopic fractionation between pyrite and dissolved sulfates results in a sharp increase in the $\delta^{34}S$ of solution. This increase is also evident in Fig. 46b. The stability field of pyrite in the downwelling limb is shown in Fig. 22a. It can be seen that the pyrite field is intersected by flow lines calculated for extensive water–rock interactions. The larger the pyrite stability field in the flow reactor, the more pronounced the results of fractionation. The scale of $\delta^{34}S$ increase in the bulk isotopic composition of solution depends on dynamic relationships rather than on the temperature dependencies of fractionation constants: in the cases with $\Sigma R/W$ (400°C) of 0.84, 1.26, and 2.1 (Fig. 47a), the maximum $\delta^{34}S_\Sigma$ values are attained at almost equal temperatures of 250, 240, and 230°C, respectively. The maximum $\delta^{34}S_\Sigma$ values are significantly different in these cases, whereas the fractionation coefficient is almost constant within such a narrow temperature interval: $\ln\alpha$(pyrite–sulfate) is –0.02376 at 250°C and –0.0252 at 230°C.

The influx of magmatic sulfur from the rock into the reaction volume increases at high R/W. As a result, $\delta^{34}S_\Sigma$ decreases gradually, and the transitional zone effects are strongly mitigated. Figure 47b presents a magnified portion of this diagram for $R/W > 0.1$. In the stability field of mineral assemblage II, the curves of the sulfur isotope composition of solution form a narrow band. The weak dependence of $\delta^{34}S_\Sigma$ on R/W distribution in the temperature steps is a favorable property of the curve, because this distribution cannot now be reliably determined in natural systems and is estimated in the model considered by theoretical methods (Section 2.2).

A surprising feature of the model is the pressure dependency of $\delta^{34}S_\Sigma$ in the interior part of the system (Grichuk, 1988) (Fig. 48). This effect is also related to the chemistry of the process rather than to the thermodynamics of isotope exchange (our model uses pressure-independent fractionation coefficients). The reason resides in the strong pressure sensitivity of anhydrite solubility (Blownt and Dickson, 1969). The solubility of this mineral controls the concentration of residual marine sulfate affected by reduction. The higher the solubility, the larger the contribution of isotopically heavy marine sulfur, and the gentler the slope of the $\delta^{34}S_\Sigma$ dependency.[28]

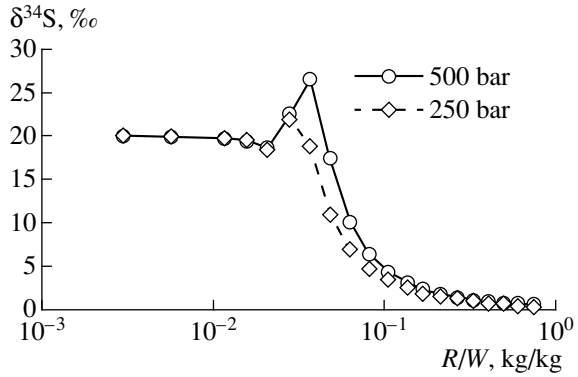

Fig. 48. Sulfur isotopic composition of solution as a function of pressure in the downwelling limb of the convective system.

The correlation of the $\delta^{34}S_\Sigma$ value of solution with $\Sigma R/W$ (Fig. 47b) makes it possible to independently determine $\Sigma R/W$ from data on the isotopic composition of oceanic hydrothermal solutions. The analysis of the errors of the model (Grichuk, 1988) yielded an estimated accuracy of $\Sigma R/W$ of ±0.2 logarithmic units. However, the $\Sigma R/W$ value obtained from Fig. 47b for the best studied hydrothermal system at 21° N on the EPR (average $\delta^{34}S$ = +2.59 for 129 determinations, Fig. 43a) gives $\Sigma R/W$ = 0.15–0.20. This is significantly different from the $\Sigma R/W$ values obtained by other methods (0.90–0.55, Tables 11, 12). The reason for this discrepancy is that the curve in Fig. 47b was constructed for the model of the first wave, i.e., for a very young hydrothermal system.

In order to assess the influence of time, we simulated a multiwave scenario corresponding to the evolution of a long-lived hydrothermal system. Figure 49 shows variations in the isotopic composition of sequential solution portions (waves) for a model with initial $\Sigma R/W$ = 1.26. This diagram shows a distinct progressive increase in $\delta^{34}S_\Sigma$ during the lifetime of the system. The reason for the increase in $\delta^{34}S$ of the model solution is obvious. The influx of isotopically heavy marine sulfur into the convective system is constant, whereas that of isotopically light magmatic sulfur declines in accordance with the accepted model dependency of R/W on $1/\sqrt{\tau}$ (Eqs. 2.10, 2.11). Thus, the isotopic composition of the solution becomes heavier in response to the deceleration of the diffusion metasomatic process controlling water–rock interaction and sulfur extraction from the basalts. This is fully consistent with the conclusion of Bluth and Ohmoto (1988) that the increase in the $\delta^{34}S$ of smoker solutions is related to the formation of altered layers (armoring) on the walls of fractures, through which seawater circulates.

[28] Pressure estimates for the interiors of convective systems were discussed in Section 3.2.

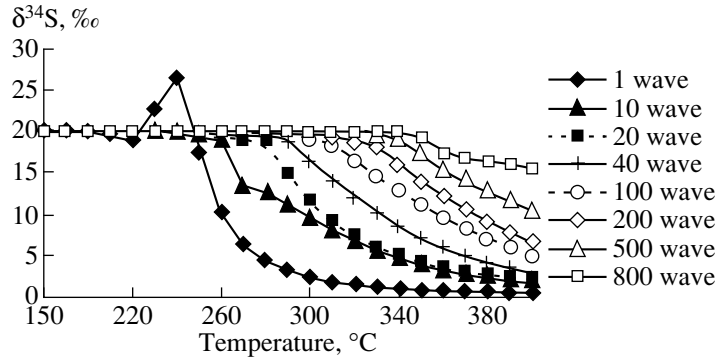

Fig. 49. Variations in the $\delta^{34}S$ of solution for the model of a long-lived hydrothermal system with initial $\Sigma R/W$ (400°C) = 1.26.

The chemical evolution of the system in the zone of assemblage I is additionally marked by a decrease in the rate of Ca extraction from the basalts. Correspondingly, less marine sulfate species are deposited in the initial steps of the reactor, and the sulfate ion can penetrate deeper into the system (Section 4.1.2). In contrast, the extraction of isotopically light S^{II} is depressed with decreasing current R/W values in the reactor steps. The combined action of these two factors results in the near parallel displacement of $\delta^{34}S_\Sigma$ curves in Fig. 49.

In isothermal sections of the system (reactor steps), $\delta^{34}S_\Sigma$ increases gradually with time, i.e., with increasing number of waves (Fig. 50a). The simulation of this process revealed the flaw of the method of a step flow reactor that was discussed in sections 2.1.4 and 4.1.2: a jump of a boundary between mineral assemblages from one step to another is accompanied by oscillations in the sulfur content of the solution, which is reflected in the calculated isotopic compositions. This is illustrated by small variations in both the isotopic compositions of sulfur species and the bulk composition of solution in Fig. 50a. Nonetheless, it can be clearly seen in this diagram that the isotopic variations are separated into two stages:

(a) $\delta^{34}S$ of hydrogen sulfide increases systematically with time from +0.61‰ in the first wave to +16‰ in wave no. 530, $\delta^{34}S$ of sulfate increases from +20‰ to +34‰, and the bulk isotopic composition of solution is identical to that of hydrogen sulfide; and

(b) after wave no. 531, the $\delta^{34}S$ of solution decreases abruptly to almost zero, and that of sulfate decreases to +18‰, and the bulk composition of the solution continues to change gradually and approach the composition of sulfate.

A comparison of this diagram with Fig. 27a suggests that the isotopic composition changes abruptly when the oxidizing sulfate solution reaches the given reactor step. It is characteristic that the isotopic composition of sulfates does not become identical to that of the initial seawater: the sulfates are isotopically lighter owing to an admixture of sulfur extracted from basalts in previous steps.

After passing through the high-temperature reactor steps, the solutions are introduced through the ascending channel into the ore deposition zone, where a sulfide edifice gradually forms. Its average isotopic composition will correspond to the bulk composition of hydrogen sulfide of all sequential solution portions.[29] Figure 50b illustrates the calculation of the cumulative isotopic composition of S^{II} emitted from the 370°C reaction step (focus of the system). It can be seen that, at a small number of waves, the bulk sulfur isotopic

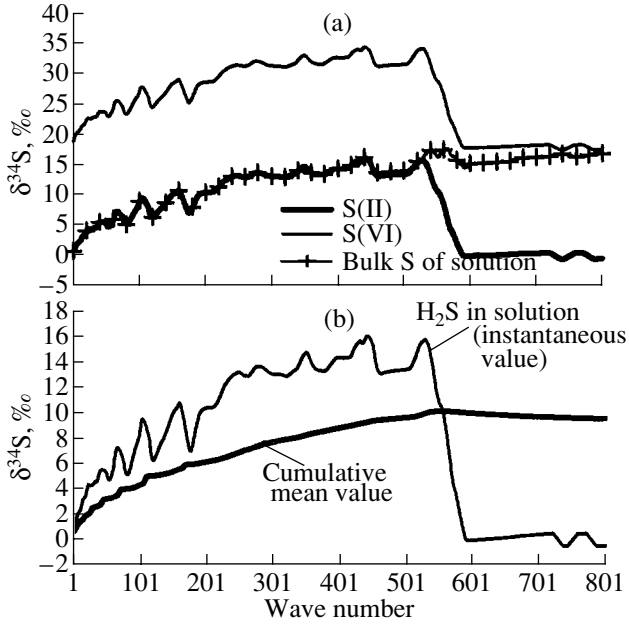

Fig. 50. Variations in the isotopic composition of solution in the 370°C isothermal section obtained by the simulation of a long-lived hydrothermal system with the initial $\Sigma R/W$ = 0.732. (a) The isotopic compositions of sulfur species and (b) the cumulative curve of the isotopic composition of hydrogen sulfide removed from the downwelling limb of the system.

[29] Ignoring the loss of hydrogen sulfide during the early stages of black smoker development and anhydrite reduction in the sulfide body.

composition of the sulfide edifice ranges between +1 and +4‰. With the increasing lifetime of the system, the $\delta^{34}S$ of the edifice will increase (in the case considered, up to +10‰). The quantitative parameters of isotopic evolution of the sulfide body will depend on the $\Sigma R/W$ value reached in the system, because it affects the compositions of parent solutions. The general tendency of a $\delta^{34}S$ increase with time will be retained.

In addition to the cumulative curve, Fig. 50b shows the isotopic composition of hydrogen sulfide in a current solution portion, i.e., the instantaneous $\delta^{34}S$ value. A comparison of these curves suggests that, owing to the regular evolution of the system, the composition of the sulfide edifice, which is a time-integrated characteristic, will inevitably be delayed relative to the variations in solution composition, which has the latest and, correspondingly, the highest $\delta^{34}S$ value. Such relationships are observed in most hydrothermal systems (Figs. 43a, 43b, 43e, 43g, 43k).

It should be noted that some hydrothermal edifices show evidence for a reverse evolution trend: a decrease in $\delta^{34}S$ with time (Woodruff and Shanks, 1988; Bluth and Ohmoto, 1988). Taking into account the results of simulation, such a trend can be interpreted as a consequence of the rejuvenation of the hydrothermal system by some tectonic events, when considerable amounts of fresh basalt come into contact with the solution (for instance, owing to rock fracturing).

Verification of the model. A comparison of the results of simulation with the data obtained for natural complexes shows an overall consistency between the model and natural processes.

The data on the secondary alteration of oceanic basalts show that magmatic sulfur is rapidly mobilized by hot seawater. This is indicated by the absence of pyrrhotite in the model, except for the region of very high R/W. The upper part of the crustal section penetrated by Hole 504B contains pyrite with a strongly variable isotopic composition, from –18.3 to +0.5‰ (average –3.1‰, Fig. 45b) (Belyi *et al.*, 1984). Sulfides from the underlying dike complex are isotopically heavier (Figs. 45c, 45d): pyrite from stringers shows an average $\delta^{34}S$ of +3.15‰ (from 0 to +5.8‰), and disseminated pyrite, +0.7‰. This is correlated with the abrupt increase in $\delta^{34}S$ of hydrogen sulfide and sulfides from negative to positive values obtained in the model for the transitional zone (Fig. 46b).

Anhydrite from stringers in basalts shows a $\delta^{34}S$ value similar to that of seawater, from +20 to +22‰, which is in good agreement with the calculations for the stability field of assemblage I (left part of Fig. 46b). The model predicts a heavier isotopic composition of sulfates in the transitional zone. It is difficult to assess the adequacy of this model effect to natural processes, because an increase in the $\delta^{34}S$ value of sulfates occurs directly before their complete disappearance. Nonetheless, sulfates with $\delta^{34}S$ of up to +36.7‰ were found in drill cores from Hole 504B in the Costa Rica Rift (Alt *et al.*, 1983), which is in agreement with the model values for the beginning of the assemblage II zone (Fig. 46b).

In general, the isotopic composition of edifices approximately corresponds to the composition of their parent solutions. The calculations imply that oceanic hydrothermal systems must produce solutions with a small positive $\delta^{34}S$ value (Figs. 46–50). This result is in agreement with observations in natural solutions (Figs. 42, 44a).

The magnitude of an increase in $\delta^{34}S$ depends mainly on $\Sigma R/W$ and rises over the lifetime of the system (Fig. 50). In the context of the model considered, the observed diversity of $\delta^{34}S$ values in sulfides from oceanic hydrothermal systems can be explained by varying degrees of maturity of the hydrothermal systems, i.e., different extents of transformation of the crustal materials by hydrothermal processes. According to this criterion, the hydrothermal systems of 21° N, 11°–13° N, and 9° N on the EPR; Cleft segment and Axial Seamount on the Juan de Fuca Ridge; and Snake Pit on the MAR, having an average $\delta^{34}S$ of sulfide bodies from +2 to +4‰ (Figs. 43a–43g), are classified as young or short-lived hydrothermal systems containing excess fresh basalts in their interior parts. The hydrothermal vents of the TAG field, Galapagos Spreading Center, and, presumably, Middle Valley and Escanaba troughs with average $\delta^{34}S$ values higher than +6‰ (Figs. 43j–43l, 43n) are classified as long-lived systems, whose deep parts were extensively altered by hydrothermal processes. This result provides a simple explanation for the correlation mentioned in Section 5.3 between the isotopic compositions of sulfide sulfur and the size of sulfide edifices (Figs. 44a, 44b). It is also in agreement with the results of simulation of the chemical composition of solutions and ores (Chapter 4) and geological evidence for these hydrothermal sites.

The isotopic compositions of sulfides from the off-axis sulfide occurrences of the EPR correspond in general to the range obtained by our simulation: their average $\delta^{34}S$ values are +4.3‰ for Green Seamount (21° N EPR) (Alt, 1988) and +1.8‰ for the marginal high and SE Seamount (13° N EPR) (Fouquet *et al.*, 1996). In the latter case, there is no correlation between the isotopic composition and size of edifices, but the data for such objects are still very limited.

Sulfides from the hydrothermal ores of the Logatchev and Rainbow fields, which sit on ultrabasic blocks, are characterized by heavy isotopic compositions (Bogdanov *et al.*, 1997a; Lein *et al.*, 2003). A model similar to that described above can probably be used for the interpretation of these data, taking into account the specific features of seawater–peridotite interactions (cf. Alt and Shanks, 2003).

The available limited data on the isotopic compositions of sulfides from hydrothermal occurrences in island arcs do not contradict the model described above. Samples of massive sulfides from the JADE field

in the Okinawa Trough yielded $\delta^{34}S$ values between +3.2 and +6.1‰ (Marumo and Hattori, 1999) and between +5.2 and +7.2‰ (Glasby and Notsu, 2003).

Sulfides from the hydrothermal fields of back-arc spreading centers yielded the following average $\delta^{34}S$ values: +2.65 at 18° N in the Mariana Trough (Kusakabe *et al.*, 1990), +3.35 in the Manus Basin (Lein *et al.*, 1993), and +4.2‰ in the Lau Basin in the northern Valu Fa Ridge (Herzig *et al.*, 1998a). In the context of the model considered, these values are in agreement with the small sizes of hydrothermal edifices observed in these localities. Sulfides from the Vai Lili field in the central part of the Valu Fa Ridge show a heavier isotopic composition, $\delta^{34}S_{av}$ = +8.6‰ (n = 27) (Bortnikov *et al.*, 1993; Herzig *et al.*, 1998). This could be due to the high intensity of hydrothermal processes in this field, which lowered the $\Sigma R/W$ values in the interior part of the system and accelerated the evolution of isotopic ratios compared with other systems.

It should be noted that not all the available data are consistent with the above-described model. Isotopically light sulfides with $\delta^{34}S_{av}$ = –5.06‰ (n = 13) were found in the Hine Hine hydrothermal field (Lau back-arc basin) (Herzig *et al.*, 1998). Negative values cannot be obtained by mixing of marine and magmatic sulfur. In our model negative $\delta^{34}S(H_2S)$ values are generated in the transitional region (Fig. 46) owing to fractionation with SO_4^{2-}; however, sulfate must be isotopically heavier than seawater. Barite from this field shows $\delta^{34}S_{av}$ = +16.4‰ (n = 5). Such relationships cannot be elucidated by the model developed.

Herzig *et al.* (1998) explained their data by the influx of SO_2-bearing magmatic gas into the Hine Hine hydrothermal system, which is situated in the caldera of a submarine volcano. The disproportionation reaction

$$4SO_2 + 4H_2O \longrightarrow H_2S + 3H_2SO_4$$

is accompanied by the fractionation of sulfur isotopes and produces sulfides with peculiar isotopic characteristics. This explanation is supported by the unusual mineral composition of the edifice, where sulfides and barite associate with pyrophyllite, kaolinite, alunite, and native sulfur. The numerical model makes no provision for a contribution from magmatic gas, and it must be modified to be applicable to such objects.

CHAPTER 6. SIMULATION OF BOILING IN OCEANIC HYDROTHERMAL SYSTEMS

6.1. Role of Boiling in Ore Formation: Overview of the Problem

Boiling (more generally, phase separation in fluid) in hydrothermal systems is traditionally regarded as one of the main factors controlling their ore potential.[30] Boiling can influence ore deposition via several mechanisms.

Loss of complex-forming species. In the geochemical literature, the most popular mechanism of the influence of boiling on ore metal deposition is the removal of complex-forming ligands into the gas phase. The decomposition of complex species results in reactions of the type

$$Zn(HS)_2^0 \longrightarrow ZnS\downarrow + H_2S\uparrow. \quad (40)$$

This mechanism can be exemplified by uranium precipitation from carbonate complexes in response to solution degassing and CO_2 loss.

Loss of a precipitant. Some anion-forming ore components (primarily H_2S and CO_2) are highly volatile and rapidly escape into the gas phase during boiling. The loss of precipitants may result in the dissolution of ore minerals occurring in contact with a heterogeneous fluid via reactions of the type

$$ZnS + 2H^+ \longrightarrow Zn^{2+} + H_2S\uparrow. \quad (41)$$

It is evident that the loss of precipitants due to boiling prevents ore deposition. Such a mechanism is important for chalcophile elements, whose precipitant, S^{II}, readily escapes into the vapor phase as H_2S. It is essential that if this mechanism operates, ore deposition is associated with vapor condensation, which is the opposite of boiling. This process was addressed by Bychkov and Grichuk (1991) by the example of As and Sb deposition in the hydrothermal system of the Uzon caldera (Kamchatka).

Change in pH and Eh. The migration into the gas phase of substances containing variable-valence elements and substances showing electrolytic dissociation in the aqueous phase may change the redox and acid–base states of the system, which, in turn, will affect the behavior of ore components. This point can be illustrated by the reaction

$$2Au_{(cr)} + 2H^+ \longrightarrow 2Au^+ + H_2\uparrow. \quad (42)$$

A shift in pH and Eh has repeatedly been invoked as a possible reason for gold precipitation (Cunningham, 1985; Cline *et al.*, 1992). However, in contrast to the loss of complex-forming ligands, this mechanism may exert different influences on the behavior of ore components: ore minerals may either precipitate or dissolve.

Among the compounds of variable-valence elements occurring in hydrothermal solutions, those of low valence states show higher affinities to the gas phase (H_2S, CH_4, and H_2). Therefore, boiling usually shifts the redox state of hydrothermal solutions toward

[30] Boiling and degassing can be regarded as particular cases of heterogenization, the separation of a liquid into liquid and gas phases. Boiling refers to the situations when the main component of the gas phase is H_2O, and degassing implies that another volatile component is predominant in the gas phase. There is no fundamental physical difference between the terms boiling, degassing, and phase separation.

more oxidized states. This is favorable for the dissolution of the most common minerals of some ore elements (Au, Ag, and U), whereas minerals of other elements (Fe and Mn) can be precipitated.

Some important components of hydrothermal solutions, including H_2S and H_2CO_3, are characterized by acid-type dissociation. The partitioning of their dissociated forms into the gas phase will increase the pH of the residual solution:

$$HCO_3^- \longrightarrow CO_2\uparrow + OH^-. \quad (43)$$

This effect is favorable for the precipitation of sulfide, carbonate, and oxide ore minerals.

Loss of a solvent. The boiling off of liquid and an accompanying increase in the mineralization of the liquid phases leads to mineral deposition. This is probably one of the most important deposition mechanisms for some components of hydrothermal solutions, for instance, SiO_2. Correspondingly, the opposite process, vapor condensation, produces a low-mineralized solution, which may be aggressive with respect to the country rock. In contrast, an increase in solution concentration may enhance complexation and result in dissolution of solid phases of those ore components that form complex dissolved species with a large number of ligands (primarily Fe, Zn, Cu, and Pb chloride complexes).

Temperature and pressure effects. In addition to purely chemical interactions, boiling is related to strong thermal effects. During the discharge of a two-phase hydrothermal fluid, its temperature is constrained by the *T–P* boiling curve. The ascent of such fluid toward the surface will be accompanied by decompression and, consequently, strong cooling. The majority of ore components precipitate during cooling. Such *P–T* constraints were used, in particular, as an important indicator of sea depth during the formation of massive sulfide deposits (Ridge, 1973; Finlow-Bates and Large, 1978; Krasnov, 1987).

In addition to the above-described mechanisms, boiling can probably affect the behavior of ore minerals in other ways. For instance, the influence of the major-component composition of hydrothermal solutions on ore components via changes in the dielectric constant of solution has recently been discussed in the geochemical literature (Kolonin *et al.*, 1994; Akinfiev, 1994). The escape of CO_2 into the gas phase is probably accompanied by such effects, but it is currently difficult to assess their scales in natural environments.

Competitive mechanisms. The complexity of the problem of boiling is largely related to the diversity of mechanisms through which important components of hydrothermal solutions, such as H_2S and CO_2, can affect the behavior of ore metals during boiling. For instance, H_2S may be simultaneously a precipitant and a complex-forming substance. Since these mechanisms operate in opposite directions, they compete for influence, and the resulting effect cannot be determined *a priori.* It will depend on the conditions of boiling and the composition of the system.

In some cases, theoretical analysis of such a competition is instructive. For instance, if the prevailing zinc species in a solution are free ions or chloride complexes, the boiling of the solution intensifies reactions (41) and (44):

$$ZnS + 2H^+ + 2Cl^- \longrightarrow ZnCl_2^0 + H_2S\uparrow. \quad (44)$$

There is no ore deposition, and moreover, the ore mineral will be dissolved. The process proceeds similarly in the case of the predominance of $ZnHS^+$:

$$ZnHS^+ + H^+ \longrightarrow Zn^{2+} + H_2S\uparrow. \quad (45)$$

When $Zn(HS)_2^0$ is the major dissolved species, reaction (40) occurs and the ore phase will be deposited during boiling.

A more complex problem was encountered in the analysis of gold behavior during boiling (Drummond and Ohmoto, 1985). If there are no complex-forming substances, boiling promotes reaction (42), which results in gold dissolution. However, within a wide range of conditions, $Au(HS)_2^-$ is the predominant species of hydrothermal solutions, and the loss of complex-forming components causes the reaction

$$2Au(HS)_2^- + H_2\uparrow + 2H_2O \longrightarrow 2Au_{(cr)} + 4H_2S\uparrow + 2OH^-. \quad (46)$$

Assuming that liquid pH and the composition of the released gas phase are constant, the equilibrium constant of reaction (46) can be written as

$$K = \frac{P_{H_2S}^4 a_{OH^-}^2}{P_{H_2}} = \frac{x_{H_2S}^4 a_{OH^-}^2}{x_{H_2}} P_{tot}^3 = \text{const} \times P_{tot}^3, \quad (47)$$

where P_i is the partial pressure, P_{tot} is the total pressure, and x_i is the molar fraction of the ith component in the gas phase.

Thus, a pressure drop (enhancement of boiling) shifts the reaction to the right, toward gold precipitation. The loss of complex-forming components appears to be more important than the change of redox state of the system. However, the assumption of constant pH and gas composition (especially the latter) degrades the importance of this conclusion. Note also that a decrease in the pH value of the system promotes gold dissolution in reaction (42) and deposition in reaction (46).

The influence of three of the aforementioned mechanisms on ore matter is unambiguous: the loss of complex-forming components and adiabatic cooling promote ore mineral deposition, whereas the loss of a precipitant results in dissolution. The action of other mechanisms may be different depending on the identity of ore components.

Drummond and Ohmoto (1985) showed that pH buffering by dissolved substances and/or solid phases can also influence the behavior of ore components during boiling. In addition, these authors demonstrated

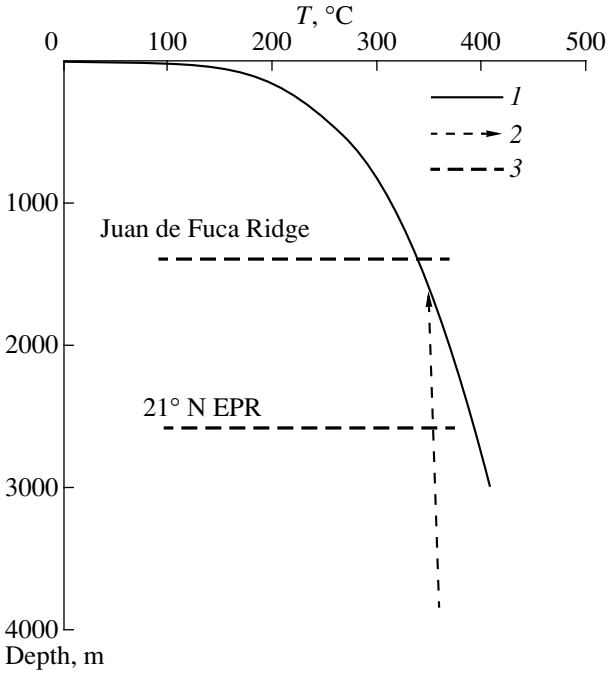

Fig. 51. Analysis of the possibility of boiling in oceanic hydrothermal systems on the basis of the phase diagram of seawater (Delaney and Cosens, 1982). (*1*) Boiling curve for seawater, (*2*) adiabat for ascending hydrothermal solutions, and (*3*) minimum ocean depths for the EPR and the Juan de Fuca Ridge.

that, if the system is open to the vapor phase (which is removed), the loss of highly volatile components is most extensive during the initial stage of boiling. Correspondingly, the relative contributions of different mechanisms may vary during boiling.

To take into account this diversity, one has to consider simultaneously a number of components, and this exercise cannot be done "manually" at the level of theoretical constructions. The investigation of such systems is only possible by means of computer thermodynamic modeling.

Thermodynamic modeling of boiling of hydrothermal solutions. The pioneering study of Drummond and Ohmoto (1985) played a crucial role in the development of modern concepts on the connection between boiling and ore formation. These authors performed thermodynamic calculations of equilibria in a heterophase system using a method based on the coefficients of interphase partitioning (Henry constants) of the components. They demonstrated that open-system boiling (with vapor phase removal) is more efficient with respect to ore generation than the closed-system process. They proposed geochemical indicators for the identification of the products of ore deposition during boiling.

A thermodynamic model with adiabatic boiling was constructed by Spycher and Reed (1989) using the Broadlands hydrothermal system as an example. They demonstrated that the separation of volatile components changes the pH value of solution and, in combination with temperature variations, results in the deposition of sulfides, sulfosalts, carbonates, and native gold.

Bowers (1991) evaluated the influence of phase separation in CO_2-rich systems on the deposition of gold and base-metal sulfides. Her model was restricted to a three-component gas phase (H_2O, CO_2, and H_2S), but the liquid and solid phases were described by a complex 17-element multisystem. It was found that the effect of boiling on the behavior of ore elements is different in the presence and absence of a rock because of the buffering action of aluminosilicate minerals.

The aforementioned studies focused on the problem of ore deposition. The mobilization of ore matter during solution boiling was not addressed by these authors. Models of hydrothermal systems with ore dissolution during boiling were considered by Bychkov and Grichuk (1991) and Grichuk and Shvarov (1992). Some results of the investigation of these models are discussed below.

6.2. Boiling in Oceanic Hydrothermal Systems

The possibility of subsurface boiling in oceanic hydrothermal systems was first evaluated by Delaney and Cosens (1982), who used the phase diagram of seawater (Fig. 51) to predict the formation of boiling zones in the hydrothermal systems of seamounts and volcanoes at shallow depths (<1.6 km). The first natural observations for the existence of boiling zones (variations in the total salinity of hydrothermal solutions) were reported from a hydrothermal system at 13° N on the EPR (Michard *et al.*, 1984).[31] However, the ocean depth is more than 2.5 km in that site. According to the phase diagram of the H_2O–NaCl system, boiling of a solution with a salinity of 3.5 wt % requires temperatures higher than 390°C at this depth. The observed values were no higher than 350°C and prevented the interpretation of salinity variations resulting from phase separation. Various alternative explanations have been proposed (e.g., Seyfried *et al.*, 1986). The subsequent studies of hydrothermal systems in the Juan de Fuca Ridge (Von Damm and Bischoff, 1987), especially in the system of Axial Seamount (Massoth *et al.*, 1989; Butterfield *et al.*, 1990) clarified this problem. A number of indirect lines of evidence for subsurface boiling were found, including hydrothermal vents emitting solutions less mineralized than seawater and enriched in volatile components (CO_2, H_2S, etc.), which were produced by vapor condensation (Butterfield *et al.*,

[31] There is an extensive literature on the problem of fluid boiling in the deep levels of the oceanic crust, which involves the investigations of gas–liquid inclusions (Vanko, 1988; Kelley and Delaney, 1988; etc.). Since the correlation of these data with the structure of convective hydrothermal systems is not quite clear, they are not considered in this study.

Table 24. Compositions of hydrothermal solutions from ASHES hydrothermal field, Axial Seamount, Juan de Fuca Ridge (Butterfield *et al.*, 1990)

Hydrothermal vent		Inferno	Hell	Crack	Virgin Mound
Component, parameter	Unit				
T	°C	328	301	217	299
pH(25°C)		3.5	3.5	–	4.4
Cl	mmol/kg	624	550	258	176
SiO_2	″	15.1	–	–	13.5
CO_2	″	50	90	179	285
H_2S	″	7.1	–	–	18
He	μmol/kg	2.45	–	8.44	11.2
Fe	mmol/kg	1.065	0.868	0.0133	0.012
Mn	″	1.150	1.136	0.287	0.142
Zn	μmol/kg	111	134	2.6	2.2
Cu	″	9.9	1.2	0.1	0.4
Pb	″	0.302	–	–	0.101
Br	″	956	856	401	250
B	″	590	–	–	450
Br/Cl	$n \times 10^{-3}$	1.532	1.556	1.554	1.420
He/CO_2	$n \times 10^{-5}$	4.9	–	4.72	3.93

1990; Von Damm *et al.*, 1997). Note, however, that emanations of heterogeneous vapor–water jets were directly observed to date only in the shallow-water (400 m) hydrothermal system of Grimsey near the northern coast of Iceland (Hannington *et al.*, 2001).

Table 24 shows solution compositions for a group of closely spaced vents at the ASHES hydrothermal field (Butterfield *et al.*, 1990). The concentration of Cl^- in the Hell vent is almost identical to that of seawater, and there was probably no phase separation within it. The Inferno vent is enriched in chlorides by 14% relative to seawater, which is indicative of the partial boiling off of solution. This vent is also significantly enriched in Fe and Cu. The Crack and Virgin Mound vents are, in contrast, depleted in chlorides, and their Cl^- contents are only 47 and 32% of the seawater value. This suggests a contribution from condensed water vapor to the solutions of these vents. These observations suggest that the decrease in salinity is associated with an increase in the concentrations of volatile components, CO_2, H_2S, and He. The He/CO_2 ratio is almost constant, which suggests a simultaneous separation of these components into the gas phase. Similarly, the constant Br/Cl value (1.553 in seawater) reflects the conservative behavior of theses halogens during phase separation. The freshened vents are strongly depleted in chalcophile elements, especially Zn, probably owing to the high content of hydrogen sulfide. Given this variability, of special interest is the lack of difference between the vents with respect to B and SiO_2 contents. Boron is rather volatile under hydrothermal conditions (Ellis, 1979), and its relative enrichment (compared with more conservative Cl) in the Virgin Mound vent is geochemically understandable. Similar boron contents in water vapor were obtained in the experiments by Berndt *et al.* (1990). The relatively high content of silica in the freshened vent suggests that the condensed water vapor probably had enough time to react with the fracture walls and extract SiO_2 from them. Taking this fact into account, the similarity of pH values in high- and low-concentration vents can be interpreted in different ways: either phase separation under the *P–T* conditions of the ASHES hydrothermal system did not significantly affect the pH of solutions (in the experiments of Bischoff *et al.*, 1996, the pH of the vapor phase decreased at the expense of hydrolytic reactions), or wall-rock reactions depressed the excess acidity of the condensates.

Von Damm and Bischoff (1987) proposed a three-component mixing scenario for the interpretation of observed variations in the chemical composition of hydrothermal solutions from the southern segment of the Juan de Fuca Ridge. This scenario included the following components: (1) boiled-off hydrothermal solution, which is a brine with a salinity of about 3 mol/kg depleted in volatile components; (2) vapor condensate with a low mineralization and high content of volatiles; and (3) seawater introduced during sampling and by subsurface mixing. The concentration of the brine was estimated by these authors from the deficit of dissolved

Table 25. Experimental data of Bischoff and Rosenbauer (1987) on the simulation of seawater boiling in contact with a rock

T, °C	406	392	
P, bar	330	251	
Phase state of the system	Homogeneous	Heterogeneous	
Phase analyzed	Water	Water	Vapor
Cl, g/kg	18.97	55.13	1.173
Fe, mg/kg	973	1791	37
Mn, mg/kg	97	280	2.4
Zn, mg/kg	0.1	4.9	0.04
Cu, mg/kg	0.01	1.9	0.01
H_2S, mmol/kg	3.3	1.0	6.0
CO_2, mmol/kg	5.8	1.9	8.6
H_2, mmol/kg	0.6	0.1	1.1

Note: Rock/water = 1, the duration of the experiment is 20 days.

gases in the hydrothermal solutions studied. This value may be different in other hydrothermal systems, but the principal mixing scheme is probably of general significance (Edmonds and Edmond, 1995).

Phase separation within hydrothermal systems affects the fate of ore elements. As can be seen in Table 24, the residual brines are enriched in ore metals, whereas the condensed vapor is strongly depleted in them but enriched in hydrogen sulfide. Hence, the mechanism of precipitant loss is in this case operative for chalcophile elements. This is in good agreement with the experiments by Bischoff and Rosenbauer (1987) simulating seawater boiling in contact with a rock at *P–T* conditions approaching those of oceanic hydrothermal systems. Table 25 shows the results of one of their experiments. It can be easily seen that a three-fold increase in bulk mineralization due to boiling is accompanied by an enrichment in Fe by a factor of two; Mn, by a factor of three; and Cu and Zn, by approximately two orders of magnitude. This is indicative of extensive mobilization of chalcophile ore elements from the rock in response to H_2S partitioning into the vapor phase.

Using the concentration of Cl^- as an indicator of the degree of phase separation, the whole set of available data on the compositions of oceanic hydrothermal solutions (Table 6) was found to exhibit a distinct positive correlation of this parameter with the concentration of ore elements and a negative correlation with H_2S (Figs. 52a, 52b).[32] The observed exponential dependency indicates that, in addition to metal concentration due to evaporation, there is also an additional input into the solution.

[32] The analyses of Cu in hydrothermal solutions do not show a clear relationship, probably because Cu is prone to losses during cooling before and in the course of sampling.

Thus, the combined natural data set for all oceanic hydrothermal systems indicates the leading role of the mechanism of precipitant loss during subsurface boiling. Subsurface boiling serves in these systems as a factor to increase the metal-bearing potential of hydrothermal solutions.

The available data indicate the existence of phase separation (boiling) zones in the interiors of many oceanic hydrothermal systems, including 9° N, 11° N, 13° N, 17° S, 18° S, and 21° S on the EPR; the Cleft and Endeavor segments and Axial Seamount in the Juan de Fuca Ridge; the Logatchev, TAG, Broken Spur, Rainbow, Lucky Strike, and Menez Gwen fields on the MAR; the Kairei field in the Indian Ocean; the Lau, North Fiji, Manus, and Woodlark back-arc basins; and hydrothermal sites in the Okinawa Trough (Table 6). This raises the problem of assessing the factor of boiling for the geochemistry and metallogeny of oceanic hydrothermal systems.

Treatment of this problem by the thermodynamic modeling method leads to a number of specific issues, which are not typical of the classic problems of water–rock interaction considered in the previous chapters. Among them are

—a method for the calculation of thermodynamic equilibria in heterophase systems gas + aqueous solution + solid phases (accounting for nonideality of the gas phase, thermodynamic properties of solution components for the *P–T* conditions of the existence of multicomponent two-phase fluids, and programs for the simulation of systems with several nonideal solutions);

—methods for the construction of geological and physicochemical models of systems with boiling.

These issues are discussed in Sections 6.3 and 6.4, respectively.

6.3. Calculation of Thermodynamic Equilibria in Systems with the Gas Phase

6.3.1. Accounting for nonideal mixing in the gas phase

Gas phase as an ideal mixture. The simplest approach to the description of gas properties is obviously an ideal gas approximation. There are no chemical interactions between molecules in ideal gas (activity coefficients are equal to 1), and the following expressions hold for a pure gas component

$$g^0_{T,P,i} = g_{T,1\ \mathrm{bar},i} + RT\ln P \qquad (48)$$

and for the component of a gas mixture

$$g_{T,P,i} = g^0_{T,P,i} + RT\ln X_i, \qquad (49)$$

where X_i is the molar fraction of the component in the mixture.

The ideal gas approximation is adequate for the calculation of the properties of low-density gases, but it is not always plausible for hydrothermal conditions. At

pressures of tens to hundreds of bars or higher, the fugacity of a pure gas component (f_i) is significantly different from P, and this factor must be taken into account in calculations. Then, Eq. (48) must be changed to

$$g^0_{T,P,i} = g^0_{T,1\text{ bar},i} + RT\ln f_i. \quad (50)$$

The combined use of Eqs. (50) and (49) gives the approximation of an ideal solution of real gases (Lewis–Randall rule). It is usually believed that this approximation can be applied within a wide range of conditions, because the effects of nonideal mixing of gas components are small.[33]

Computer programs and models for ideal gas–mineral systems appeared even earlier than those for systems with an aqueous phase (Volkov and Ruzaikin, 1969). However, their application in geochemistry appeared to be limited and involved cosmochemical problems (e.g., Khodakovsky *et al.*, 1978) and calculation of the state of volcanic gases (Symonds *et al.*, 1992; Symonds and Reed, 1993). A mixed model is sometimes used: the deviation of fugacity from pressure is taken into account for major components (H_2O and CO_2) but ignored for minor components (Bowers, 1991).

Gas phase as a real solution. A provision for nonideal mixing must be made for a more accurate description of the properties of gas mixtures. Three main approaches are used to this end in the modern thermodynamics of gases. (1) The properties of gases and their mixtures (in a general case, equations of state) are expressed as polynomials of independent parameters of the system (T, P or V, and X_i). (2) Equations of state are constructed using physical model approximations connecting the T, P, and V of gases and their mixtures (the van der Waals equation and its modifications). (3) The molecular dynamics method employs calculations based on the model potentials of intermolecular interaction.

The molecular dynamics method probably has superior prognostic properties, but its application is restricted mainly to the calculation of gas properties under high parameters of state because of computational difficulties. To our knowledge, there have been no attempts to use this method for the thermodynamic modeling of hydrothermal ore formation.

The method of polynomial functions was used for the thermodynamic modeling of geochemical processes in the CHILLER program (Spycher and Reed, 1988, 1989). This method has the highest accuracy for the interpolation of experimental data sets. However, more important for the multicomponent systems of geological interest are extrapolation of properties both with respect to intensive parameters (T and P) and the component composition of the system. Holloway (1986) argued that the empirical parameters of polynomials obtained by the least squares method are usually strongly correlated. Therefore, the quality of data approximation decreases near the boundaries of the experimentally studied domain and extrapolation beyond it requires considerable care. As to the number of system components, the CHILLER program considers a gas phase consisting of five components, and nonideal mixing effects are taken into account only for H_2O, CO_2, and CH_4. Even such a simple gas mixture required the use of two-dimensional and three-dimensional arrays of cross-coefficients, each of which is a polynomial in T and P. This approach evidently requires a tremendous amount of experimental infor-

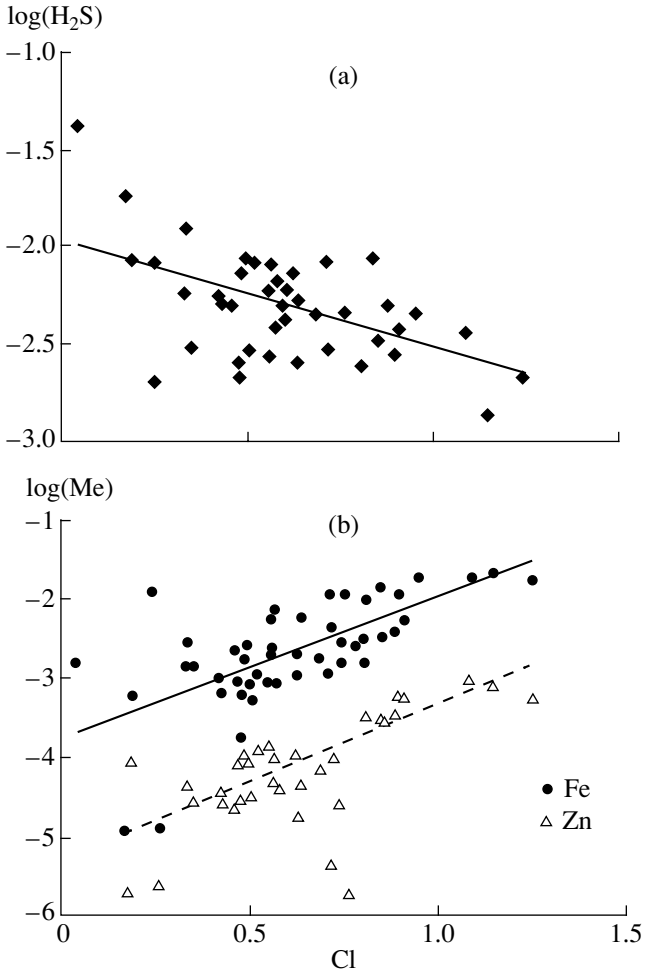

Fig. 52. Correlation of the concentrations of ore elements with the chlorinity of oceanic hydrothermal solutions. (a) Hydrogen sulfide and (b) iron and zinc. Concentrations are given in mol/kg.

[33] Fernandez-Prini and Crovetto (1985) showed that Henry's constants for water–nonpolar gas systems calculated in the Lewis–Randall approximation deviate from experimental values more strongly than those obtained in the ideal gas approximation. This phenomenon is related to the opposite signs of corrections for the fugacity of real gases and for real gas mixing. Thus, the resulting errors are cancelled in the ideal gas approximation. Similar relationships of errors were reported for some other instances by Spycher and Reed (1988).

Table 26. Critical parameters and acentric factors of geochemically important gas compounds

Compound	T_{cr}, K	P_{cr}, bar	V_{cr}, cm^3/mol	Z_{cr}	ω
H_2O	647.3	220.5	56.0	0.229	0.344
CO_2	304.2	73.8	94.0	0.274	0.225
CO	132.9	35.0	93.1	0.295	0.049
CH_4	190.6	46.0	99.0	0.288	0.008
H_2S	373.2	89.4	98.5	0.284	0.100
SO_2	430.8	77.8	122.0	0.268	0.251
HCl	324.6	83.1	81.0	0.249	0.120
HF	461.0	64.8	69.0	0.120	0.372
H_2	33.2	13.0	65.0	0.305	–0.220
N_2	126.2	33.9	89.5	0.290	0.040
NH_3	405.6	112.8	72.5	0.242	0.250
O_2	154.6	50.5	73.4	0.288	0.021
Ar	150.8	48.1	74.9	0.291	–0.004

mation, and its complexity increases as a power function of the number of components in the system. Thus, the price for the accuracy of the method is difficult application for complex systems.

The method of equations of state is based on the van der Waals equation, which extends the Clapeyron–Mendeleev equation of ideal gases ($PV = RT$, where R is the gas constant) by accounting for the nonzero volume of gas molecules:

$$P = \frac{RT}{V-b} - \frac{a}{V^2}. \quad (51)$$

This equation was modified in 1948 by O. Redlich and J. Kwong:

$$P = \frac{RT}{V-b} - \frac{a}{\sqrt{T}(V+b)V}. \quad (52)$$

The coefficients a and b of this equation can be readily determined on the basis of the corresponding state principle from the critical point parameters of pure substances.

The very popular Redlich–Kwong equation has repeatedly been modified by many authors, both with respect to the form of the second term and the method of a and b derivation. For instance, in the Soave equation, $a/\sqrt{T}$ is changed to

$$a(T) = a_{cr}\alpha(T),$$

$$\alpha(T) = 1 + m\left(1 - \sqrt{\frac{T}{T_{cr}}}\right),$$

$$m = 0.480 + 1.574\omega - 0.176\omega^2,$$

where ω is the Pitzer acentric factor, which is specific to each gas. A modified Redlich–Kwong equation was incorporated into a version of the EQ3/6 program designed for the calculation of heterogeneous systems with the gas phase (Bowers, 1991).

Peng and Robinson (1976) developed a modified equation of state, which showed important properties for the description of gas mixtures,

$$P = \frac{RT}{V-b} - \frac{a(T)}{V(V+b)+b(V-b)}, \quad (53)$$

where

$$b = 0.086640350\frac{RT_{cr}}{P_{cr}},$$

$$a(T) = 0.42748002327\frac{R^2T_{cr}^2}{P_{cr}}\left[1 + m\left(1 - \sqrt{\frac{T}{T_{cr}}}\right)\right]^2,$$

and

$$m = 0.37464 + 1.54226\omega - 0.26992\omega^2.$$

The Peng–Robinson equation describes the properties of a pure gas using only three individual properties: T and P of the critical point of the gas and the Pitzer acentric factor ω. These properties have been determined for a wide spectrum of substances, including many compounds of geochemical interest. The values of critical parameters and ω for some gases are listed in Table 26.

For the calculation of gas mixtures, Peng and Robinson made the following assumptions: (1) the properties of a gas mixture are identical to those of a hypothetical gas having the same critical T and P as the mixture; (2) the $\bar{a}$ and $\bar{b}$ parameters of a mixture are functions of mixture composition and the parameters of the mixed components, b_i and $a(T)_i$:

$$\bar{b} = \sum_i x_i b_i, \quad (54)$$

$$\bar{a} = \sum_i \sum_j x_i x_j a_{ij}, \quad (55)$$

and

$$a_{ij} = \sqrt{a_i a_j}(1 - \delta_{ij}), \quad (56)$$

where δ_{ij} is the cross-coefficient, $\delta_{ij} = \delta_{ji}$ and $\delta_{ii} = 0$.

Thus, only one two-dimensional array of coefficients is used for gas mixtures (δ_{ij}). Peng and Robinson (1976) argued that the δ_{ij} parameters can be regarded as temperature-invariant. Therefore, the Peng–Robinson equation must be very robust with respect to temperature extrapolation. In order to improve the accuracy of calculations, subsequent studies approximated the cross-coefficients by polynomial functions of temperature for some systems. The values of δ_{ij} have been determined for many pairs of geochemically important compounds (Table 27).

Equation (53) cannot be directly used in programs calculating equilibria under isobaric–isothermal conditions, because its arguments are T and V. Therefore, the Peng–Robinson equation, as well as other equations of the Redlich–Kwong type, must be recast by changing variables into a cubic polynomial in compressibility, Z:

$$Z^3 - (1 - B)Z^2 + (A - 3B^2 - 2B)Z - (AB - B^2 - B^3) = 0, \quad (57)$$

where

$$A = \bar{a}\frac{P}{R^2T^2},$$

$$B = \bar{b}\frac{P}{RT},$$

and

$$Z = \frac{PV}{RT}.$$

The Peng–Robinson equation allows calculation of the partial parameters of mixed components, among which the most important are the fugacity coefficients of individual components in the mixture, $\varphi_i = f_i/x_iP_{tot}$. Peng and Robinson (1976) transformed Eqs. (54)–(57) to obtain

$$\ln\varphi_i = \frac{b_i}{\bar{b}}(Z-1) - \ln(Z-B) - \frac{A}{B2\sqrt{2}} \times \left(\frac{2\sum_j x_i a_{ij}}{\bar{a}} - \frac{b_i}{\bar{b}}\right)\ln\left(\frac{Z+(\sqrt{2}+1)B}{Z-(\sqrt{2}-1)B}\right), \quad (58)$$

where Z, A, B, $\bar{b}$, $\bar{a}$, and a_{ij} are given by Eqs. (57) and (54)–(56), respectively. Thus, the fugacity coefficient of an individual component is defined by the composition and compressibility of the gas mixture (Z), the additive functions ($\bar{a}$ and $\bar{b}$) of the properties of pure components of the mixture ($T_{cr,i}$, $P_{cr,i}$, and ω_i), and the cross-coefficients (δ_{ij}).

Owing to its simplicity and the low number of empirical parameters, the Peng–Robinson equation is very attractive for the thermodynamic modeling of multicomponent systems. Mironenko and Kosorukov (1990) implemented the Peng–Robinson equation in their computer program for geochemical modeling.

The downside of the simplicity of the equation of state is its lower accuracy compared with polynomial equations. Therefore, the accuracy of the description of the properties of gas phase must be specially evaluated.

Estimation of errors related to the use of the Peng–Robinson equation. Similar to other model equations, the Peng–Robinson equation does not account for all physical properties of molecules. According to the corresponding states principle, it includes temperature and pressure normalized to the critical parameters (T/T_{cr} and P/P_{cr}, respectively) and the acentric parameter ω, which accounts for the deviation of the geometry of gas molecules from spherical symmetry. However, there is no explicit provision for possible dipole–dipole interactions. Correspondingly, the Peng–Robinson equation (as well as other Redlich–Kwong type equations) adequately describes nonpolar gases but is not so good for polar gases. The geochemically most important polar gas is water vapor.

Table 27. Cross-coefficients, δ_{ij}, for geochemically important gas compounds

Mixture components	δ_{ij}	Reference	T interval, °C
H_2O–CO_2	$-0.5572 + 0.001879T - 1.274\times10^{-6}T^2$	(a)	>100
	0.49852–0.0008T	(b)	
	0.057	(e)	
H_2O–H_2S	$-0.3897 + 1.565\times10^{-3}T - 1.142\times10^{-6}T^2$	(a)	0–220
	$-0.4860 + 2.092\times10^{-3}T - 1.87\times10^{-6}T^2$	(d)	
	0.157	(e)	
H_2O–H_2	0.30	(c)	<363
H_2O–N_2	0.53	(c)	<350
	0.45	(f)	
H_2O–NH_3	–0.260	(a)	
H_2O–He	0.80	(f)	
CO_2–H_2S	0.096	(a)	
	0.093	(e)	
CO_2–CH_4	0.65	(b)	
CO_2–NH_3	0.096	(a)	
H_2S–NH_3	0.324	(a)	

Note: (a) Roberts and Tremaine (1985), (b) Mironenko and Kosorukov (1990), (c) Alvarez *et al.* (1988), (d) Carroll and Mather (1989), (e) Shvedenkov and Savinov (1994), and (f) Fernandes-Prini and Crovetto (1989).

The properties of water vapor are well known. There are rather precise models allowing calculation of its properties, among which is the Haar–Gallagher–Kell model used in the modified HKF model and in the UNITHERM data bank. This provides an opportunity to check the accuracy of the Peng–Robinson equation for gaseous H_2O. Table 28 shows H_2O fugacity calculated along the boiling curve of pure water by means of the Haar–Gallagher–Kell model and the Peng–Robinson equation. According to these results, the error in water vapor fugacity calculated by the Peng–Robinson equation goes up to 2% relative and is highest at 250°C. The energy equivalent to this error ($g_T(H_2O)_{gas}$) is 30–

Table 28. Comparison of the calculated H_2O fugacities along the line of pure water boiling with the Haar–Gallaher–Kell model and the Peng–Robinson equation

Temperature, °C	Pressure, bar	Fugacity, bar		Deviation		
		Haar–Gallaher–Kell method*	Peng–Robinson equation	Δf, %	ΔG_{H_2O}, J/mol	ΔP, bar
150	4.758	4.604	4.54	–1.39	49.3	–0.07
200	15.537	14.321	14.48	1.11	–43.4	0.17
250	39.728	34.178	34.84	1.94	–83.4	0.77
300	85.805	67.442	68.33	1.32	–62.3	1.13
350	165.125	115.632	115.0	–0.55	28.4	–0.90

* Calculated using the UNITHERM data bank.

80 J/mol, which seems to be rather small compared with other error sources in multicomponent models. However, it should be kept in mind that models with boiling consider gas to be in equilibrium with liquid water. The uncertainty obtained in Table 28 corresponds to a displacement of the boiling curve by approximately one bar. This may be rather embarrassing in the calculations of isobaric–isothermal equilibria. An obvious way to circumvent this difficulty is the use of a combined method, involving the more accurate model of Haar–Gallagher–Kell for the fugacity of pure water vapor and the Peng–Robinson equation for other components and nonideal mixing effects (Japas and Levelt-Sengers, 1989).

A very important circumstance for the assessment of the plausibility of the Peng–Robinson equation is that H_2O shows a very strong dipole interaction. This interaction is characterized by the dipole moment of the molecule (μ). Table 29 presents dipole moments for the molecules of geochemically important gases. The dipole moment of the H_2O molecule is the highest. Correspondingly, the effects related to dipole interaction in water vapor are much higher than those for other substances. Therefore, the errors of the Peng–Robinson equation for H_2O are the maximum possible values in natural systems.

Table 29. Dipole moments of geochemically important gas molecules (Holloway, 1986)

Substance	Dipole moment, Debye
H_2O	1.86
CO	0.11
HCl	1.07
H_2S	0.9
SO_2	1.59
NH_3	1.47

Note: Nonpolar gases (CO_2, CH_4, H_2, N_2, O_2, etc.) show a dipole moment of zero owing to the symmetry of their molecules.

The substitution of a gas mixture by a hypothetical gas with the same critical parameters that is made in the Peng–Robinson equation (as well as in other Redlich–Kwong type equations) is theoretically not strictly correct (this issue was discussed by Namiot, 1991). The result of this substitution is that the equation better describes the homogeneous region than the liquid–gas phase boundaries.

The accuracy of various equations of state was assessed by Seitz *et al.* (1994) by the example of the CO_2–CH_4–N_2 system (200°C and 1000 bar), for which comprehensive experimental data are available. They showed that the accuracies of the Redlich–Kwong and Peng–Robinson equations are inferior to those of polynomial equations. One important conclusion by these authors is that the main contribution to the errors of the Redlich–Kwong and Peng–Robinson equations is related to the uncertainties in the properties of pure boundary components, which were discussed above in the example of H_2O. The mixing volume effect in the ternary system considered was very small (<3% of the volume of mixture), and the Peng–Robinson equation reproduced it with an error of ±45% relative, which is comparable to the error for pure components. The Peng–Robinson equation appeared to be more accurate than the Redlich–Kwong equation. Japas and Levelt-Sengers (1989) used the precise Haar–Gallagher–Kell equation for water and calculated the compositions of equilibrium gases in binary systems with water by means of the Peng–Robinson equation. Their results for the molar fractions of gas components were accurate to within about 1%.

Peng and Robinson (1976) assumed that the δ_{ij} values are temperature independent. A detailed study of the H_2O–H_2S system (Roberts and Tremaine, 1985; Carroll and Mather, 1989) showed that the properties of this system can be better described using temperature-dependent $\delta_{H_2O-H_2S}$ values. The polynomials obtained by these authors are given in Table 27. According to the results of Carroll and Mather, δ_{ij} varies from –0.06 at 0°C to +0.08 at 220°C. These variations in δ_{ij} for the H_2O–H_2S system result in variations in the activity

coefficient of H_2S within ±30% in the water-rich region, which is no higher than other errors in the thermodynamic models of multicomponent systems.

Several attempts have been made to improve the Peng–Robinson equation, for instance, the PRSV model by Stryjec and Vera (1986). However, all these attempts introduced new empirical parameters. The improvement of accuracy always reduced the possibility of practical application of the method.

Thus, the Peng–Robinson equation can be used in the thermodynamic models of multicomponent systems as a not very accurate but universal tool for the calculation of gas equilibria.

6.3.2. Specific features of the thermodynamic description of phase properties in the model of boiling hydrothermal systems

Phase diagram of the H_2O–NaCl system and its applications to seawater boiling. The H_2O–NaCl system has been extensively studied in the range of hydrothermal conditions. Early studies were surveyed by Holland and Malinin (1979). In the 1980s, detailed experimental investigations of the H_2O–NaCl system were performed by Bischoff *et al.* (1986), Bischoff and Rosenbauer (1988), and other authors. The results of this work were summarized by Bischoff and Pitzer (1989). Bischoff and colleagues paid considerable attention in their studies to the position of the critical line in this system, because the critical parameters of solutions play an important role in the corresponding states theory and their experimental determination is a significant challenge. The H_2O–NaCl system has been studied to such an extent that an equation of state was proposed for it (Tanger and Pitzer, 1989), which is unique for water–salt systems. The projection of the boiling surface on the *P–T* plane is constructed in Fig. 53a using the data of Bischoff and Pitzer (1989). Its isothermal sections, boiling curves for temperatures of 350, 370, 380, and 400°C, are shown in Fig. 53b. These diagrams exhibit the main property of water–salt solutions: the addition of electrolyte decreases the pressure (increases the temperature) of boiling. For the region of interest, the depression of boiling pressure is an almost linear function of solution salinity.

Since sodium chloride is the predominant salt component of seawater, the H_2O–NaCl system has traditionally been regarded as a reference system for the physicochemical analysis of geochemical processes involving seawater. The compositions of hydrothermal solutions only approximately correspond to the H_2O–NaCl binary and contain admixtures of K and Ca chlorides. However, these admixtures probably have a minor influence on the position of the boiling surface (Holland and Malinin, 1979).

The presence of dissolved gases will increase boiling pressure (decrease boiling temperature). The fundamental thermodynamic reason for this effect is the following: dissolved gases are extensively partitioned into the gas phase, which reduces the molar fraction of H_2O in the vapor and, correspondingly, the chemical potential of gaseous water. This stabilizes the gas phase.

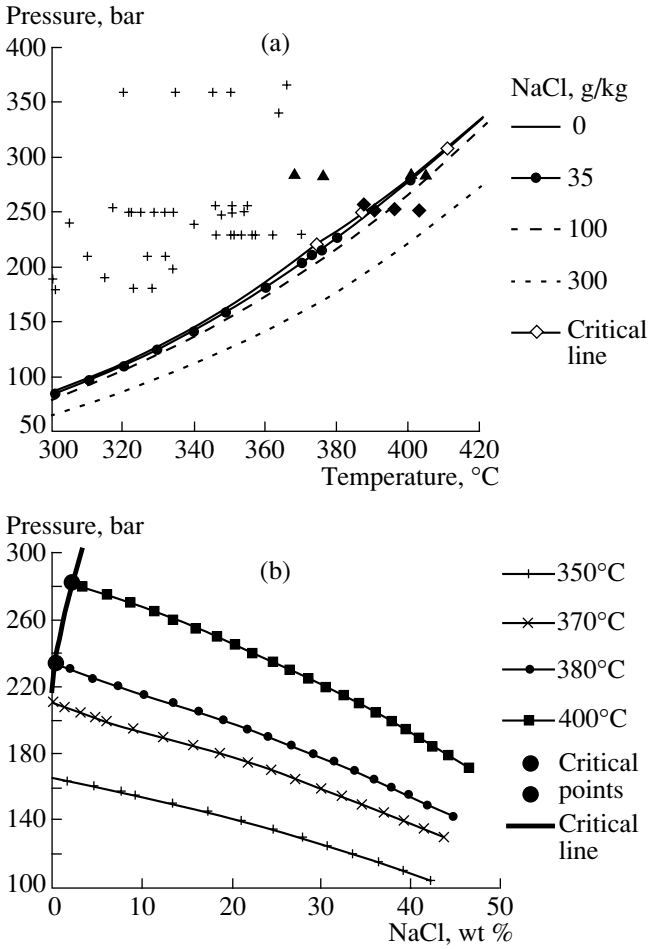

Fig. 53. Phase diagram of the H_2O–NaCl system with the boiling surface after Bischoff and Pitzer (1989). (a) Concentration isolines in the *T–P* coordinates and (b) isotherms in the *P–X* coordinates. Crosses show the *T–P* parameters of oceanic hydrothermal solutions, rhombs are the data for vents at 9°17′–9°46′ N on the EPR, April 1991 (Von Damm, 2000), and triangles are the data for the Brendon vent (21°34′ S EPR, November, 1998) (Von Damm *et al.*, 2003).

Figure 53a shows the points of temperature measurements in oceanic hydrothermal systems. According to these data, almost all solutions (except for two cases) occurred in the single-phase field at the moment of ejection. Extremely high for oceanic hydrothermal systems temperatures were recorded in smokers at the hydrothermal system of 9° N EPR in 1991 immediately after a submarine eruption, 388–403°C at 253–258 bar (Von Damm *et al.*, 1995). The samples of these solutions showed a low salinity (up to 10–15% of the normal seawater value, Table 6) and high gas contents, which indicates their relation to phase separation (boiling) phenomena (Von Damm, 2000). Even a higher

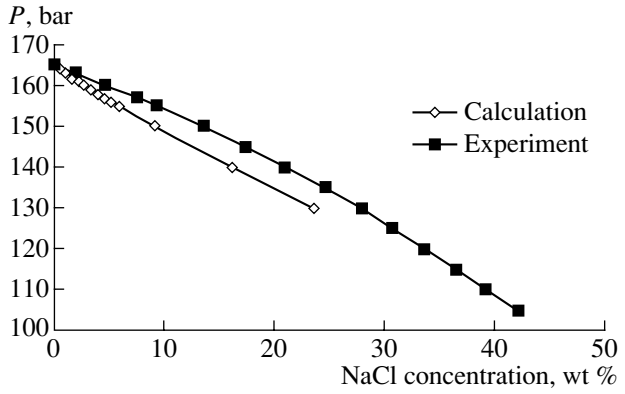

Fig. 54. Comparison of the thermodynamic calculation of boiling in the H_2O–NaCl system at 350°C with the experimental data of Bischoff and Pitzer (1989).

temperature of 405°C (287 bar) was documented in 1998 in the Rapa Nui vent field (21°34′ S EPR) (Von Damm *et al.*, 2003). These parameters almost exactly match the critical point of seawater (407°C and 298 bar). Fluid from three chimneys of the hydrothermal edifice was less saline than seawater, whereas two other chimneys discharged a more saline fluid, which is indicative of phase separation within the edifice.

Thermodynamic description of the properties of the liquid phase in a two-phase field. As was mentioned in Section 3.3, the current methods of derivation of the thermodynamic properties of dissolved substances are based on the modified Helgeson–Kirkham–Flowers model, which relies on the thermodynamic properties of pure water (density, dielectric constant, and their derivatives with respect to temperature and pressure). The simulation of boiling processes in water–salt systems encounters the problem of the existence of a liquid phase in the presence of salts under the *P–T* conditions where pure water exists in the vapor state. Standard programs for the calculation of thermodynamic properties (including SUPCRT 92 by Johnson *et al.*, 1992) are not appropriate for such conditions.

A pragmatic way to overcome this difficulty is to use the extrapolated thermodynamic properties of dissolved substances. The extrapolation of properties in pressure is evidently advantageous, because the pressure dependency of g_T is less steep than the temperature dependency. A check by the properties of substances used in our model of an oceanic hydrothermal system (Table 18) showed that the data obtained immediately near the boiling curve of pure water (from $P_{boiling}$ to $P_{boiling} + 20$ bar) are adequately described by a quadratic function of pressure. The error of such an approximation is no higher than ±100 J/mol. This allows extrapolation of g_T of dissolved substances within a limited range below $P_{boiling}$. It should be taken into account that the error of extrapolation definitely increases away from the boiling curve. Note, however, that the ordinary uncertainties of thermodynamic data, which are involved in the extrapolated values as systematic errors, are significantly higher. In general, the variations in g_T with pressure are rather small: at 350°C the g_T value of dissolved species changes by a few kilojoules as pressure decreases from 166 to 140 bar. The maximum effects were obtained for the OH^- ion and related hydroxo complexes (about –3.5 kJ/mol per one hydroxyl ion). Unfortunately, there are still no data that would allow the assessment of the accuracy of extrapolated values.

Thermodynamic properties of water vapor in the stability field of liquid water. As was mentioned above, the description of vapor phase properties in boiling systems is based on the thermodynamic properties of gaseous water calculated by an accurate model (for instance, by the Haar–Gallagher–Kell equation). Standard programs for the calculation of the thermodynamic properties of substances provide these parameters only for the stability field of the pure water vapor phase. If boiling is calculated in multicomponent systems at pressures above the boiling curve of the single-component system (which is very probable in systems with high gas content), the properties of H_2O_{gas} have to be extrapolated into the metastable field. It was shown that extrapolation of g_T in pressure using a third degree polynomial yields satisfactory results for the subcritical region.

Quality control of thermodynamic data for boiling systems. Currently, such a control can be performed only through the simulation of boiling in the H_2O–NaCl system. The simulation was carried out for the 350°C isotherm using the experimental data of Bischoff and Pitzer (1989) (Fig. 54). The diagram indicates that the calculated values are in general consistent with the experimental points. The model and experimental pressures of the beginning of boiling are identical, 165.2 bar. The calculated curve for salt solutions implies somewhat lower degrees of boiling compared with the experiments. The discrepancy increases with increasing salinity, and the maximum value of 5% NaCl was obtained at 150–140 bar.

Thus, the simulation of boiling is in general consistent with experimental data, and the model somewhat underestimates the fraction of water vapor in the system. The discrepancy may be as high as 5 bar in pressure or 5% in electrolyte concentration.

6.3.3. Software

The calculation of thermodynamic equilibria in boiling systems requires computer programs designed for systems with several phases of variable composition. To the author's knowledge, such programs are GIBBS (for large computers), SELECTOR, and HCh (for personal computers).

Boiling simulation was performed by the author using the PENG program, which is a modification of the GBFLOW software. PENG allows calculation of

equilibria in systems with two phases of variable composition, liquid and gas. According to Shvarov's nomenclature (*Methods of…*, 1988), PENG is a program for equilibrium calculations of the second class, i.e., a program for equilibrium calculation in systems with a partially constrained phase composition, because the liquid water phase must always be present in equilibrium. The PENG program utilized a modified algorithm of Gibbs free energy minimization, which included improved procedures for the calculation of activity coefficients (they are computed for the gas phase by a special subroutine based on the Peng–Robinson equation) and chemical potentials of components (transition from the molar amount of a component in the system to molar fractions requires separate summation for each phase of variable composition).

6.4. Thermodynamic Model of Boiling in Oceanic Hydrothermal Systems

The main obstacle to the simulation of boiling in oceanic hydrothermal systems is related to the almost complete lack of information on the situation in boiling zones. Neither the *T–P* conditions, the character of phase separation, nor the residence time of fluid in boiling zones are reliably known. Although the consequences of boiling and phase separation were tracked in the compositions of hydrothermal solutions, the real mechanism remains obscure. There were attempts to create conceptual scenarios of phase separation (two-layer convection cell by Bischoff and Rosenbauer, 1989 and separation in an oblique fault by Fox, 1990), but a quantitative dynamic model of the process has not yet been developed. Therefore, our study of the problems of the thermodynamic modeling of boiling in hydrothermal systems was restricted to the determination of such characteristic that are independent of the particular structure of boiling zones, i.e., invariants of the boiling process.

Some observed properties of oceanic hydrothermal solutions, an analogy with terrestrial hydrothermal systems, and general theoretical considerations constrain the diversity of possible scenarios of the boiling process. Among such constraints are the following.

(a) Two-phase fluids have a low bulk density. Therefore, the appearance of a boiling zone in a convection cell sharply increases the expelling force of convection and, correspondingly, the velocity of fluid movement. The boiling zone can be preserved only near the heater (magma chamber).

(b) The process can be regarded as adiabatic in the upwelling limb because of the rapid fluid movement (Bischoff and Pitzer, 1985).

(c) Since the vapor component of the two-phase fluid has a low viscosity, the boiling zone can propagate far upward along the channel of the convective system. However, as was mentioned above, the discharge of two-phase fluids in deep oceanic hydrothermal systems has never been observed. The reason for this peculiarity of oceanic hydrothermal systems is probably related to the rapid condensation of the vapor phase due to subsurface mixing (vapor bubbles are collapsed by the addition of only a small percent of cold seawater).

(d) The observed variations in the salinity of oceanic hydrothermal solutions suggest a possible phase separation (at least partial) of vapor and residual liquid.

(e) According to the calculations of Bowers *et al.* (1988), hydrothermal solutions with salinities higher than that of seawater are in equilibrium with the major minerals of metasomatic rocks. This suggests that the residual brines of many hydrothermal systems have been in contact with rocks for a fairly long time.

Taking into accounts these constraints, we considered the following boiling scenarios:

(1) isothermal boiling in contact with a rock without vapor phase elimination, which is an analog of boiling in the high-temperature focus of the system;

(2) phase separation in contact with a rock;

(3) adiabatic cooling of a two-phase fluid, which is an analog of upward movement along an extended conduit; and

(4) condensation of a two-phase fluid during mixing with seawater.

The principal schemes of these scenarios are shown in Fig. 55.

6.4.1. Isothermal boiling of solution in contact with a rock: a model for the focus of a hydrothermal system

In this scenario (Fig. 55a), the equilibrium compositions of the system tholeiitic basalt–hydrothermal solution–vapor were calculated as functions of confining pressure. The calculations were performed for a temperature of 350°C, which is sufficiently high to simulate the focus of a hydrothermal system but still allows for the acquisition of reliable thermodynamic data for dissolved species. The initial solution composition corresponded to that calculated by the simulation of the downwelling limb of a convection cell (Chapter 4) for the following conditions: T = 350°C, P = 500 bar, $\Sigma R/W$ = 0.496, and wave no. 1 (Table 30). Pressure in the boiling model varied between 190 and 130 bar ($P_{boiling}$ = 165.2 bar for pure water at 350°C), which allowed us to explore a wide range of the degree of boiling off. The amount of rock in contact with the boiling solution was taken as 0.1 kg per one kilogram of solution; the same value was accepted for this temperature in the model of the downwelling limb. The obtained set of equilibrium states of the system can be interpreted as a stepwise decrease in pressure in a closed system (autoclave with a pressure drop).

The results of simulation are shown in Fig. 56. Boiling in the model system begins when pressure falls to

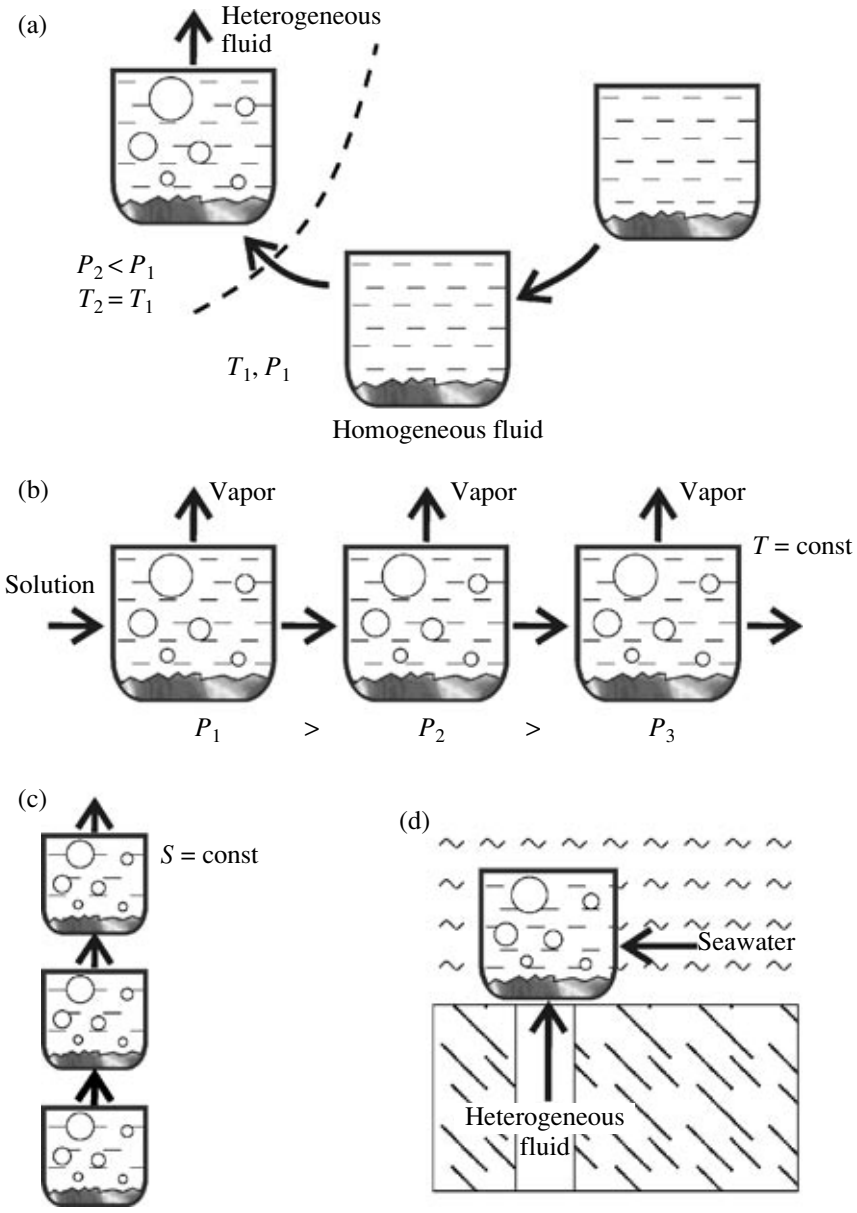

Fig. 55. Principal schemes of models for boiling scenarios. (a) Isothermal boiling, (b) phase separation, (c) adiabatic boiling, and (d) rapid discharge with vapor condensation.

165 bar. This pressure is close to the boiling point of pure water (165.2 bar), which results from the superposition of two opposite effects, a salinity-related increase in boiling pressure (by approximately 5 bar) and a decrease in pressure due to the presence of gases. A subsequent pressure decrease results in a rapid increase in the fraction of the vapor phase in the system (Fig. 56a), which reaches 50% of the mass of fluid at 155 bar and 88% at 130 bar. Boiling is accompanied by an increase in the salinity of the liquid phase: from an initial mineralization of 33 g/kg, it becomes twice as high at 155 bar and reaches 260 g/kg at 130 bar (Fig. 56b).

For the sake of comparison, Fig. 56b also presents the calculated mineralization of solution during boiling in the NaCl–H_2O system (at an initial NaCl concentration of 0.587 mol/kg H_2O, corresponding to the mineralization of the model hydrothermal solution) and the experimental data for boiling in the NaCl–H_2O system obtained by Bischoff and Pitzer (1989). The calculations for the binary system place the beginning of boiling (established by an inflection in the diagram) at a pressure of 159 bar, which is in good agreement with the experiments (161 bar for a salinity of 35 g/kg). Boiling in the multicomponent model system begins earlier, at a total pressure of 165 bar, because the partitioning of dissolved gases into the vapor phase reduces the frac-

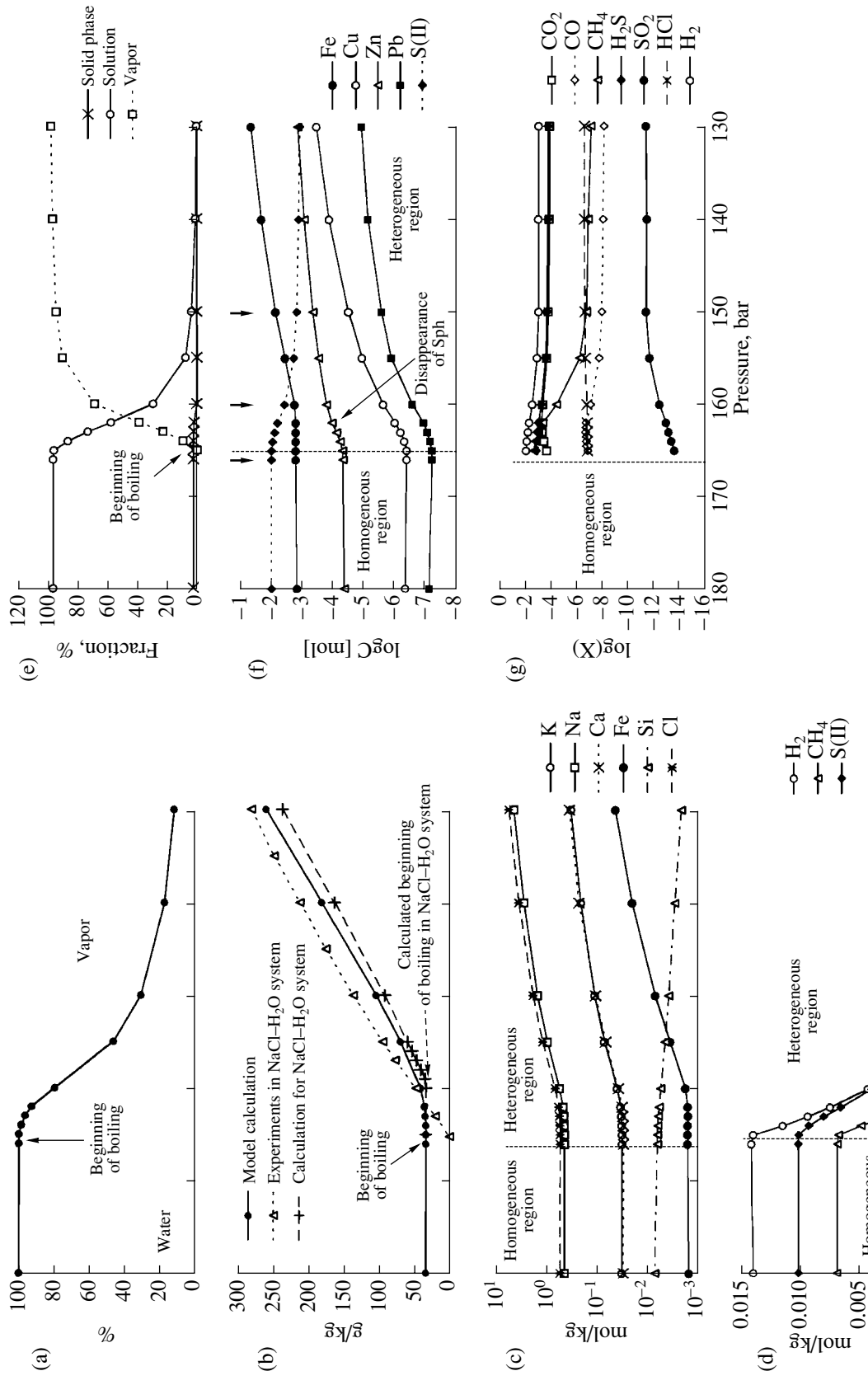

Fig. 56. Composition of hydrothermal solutions during boiling in contact with a rock calculated at $T = 350°C$ and $R/W = 0.1$. (a) The fraction of liquid water, wt %; (b) mineralization of residual solution after boiling off, g/kg; (c) concentrations of major components in solution, mol/kg; (d) concentrations of volatile components in solution, mol/kg; (e) partition of S^{II} between the phases of the system; (f) concentrations of ore elements in solution; and (g) mole fractions of gases in the vapor phase. The dashed line in Fig. 56b shows experimental data for the 350°C boiling isotherm in the NaCl–H_2O system (Bischoff and Pitzer, 1989). The arrows in Fig. 56f show the initial compositions in the model of adiabatic cooling.

Table 30. Composition of the model hydrothermal solution that was used as the initial state in models with boiling; this composition was obtained by the simulation of the downwelling limb of the convective system at T = 350°C, P = 500 bar, and $\Sigma R/W$ = 0.496 for the first wave

Component	Amount, moles
H	0.117304
O	0.060189
K	0.028856
Na	0.467914
Ca	0.024079
Mg	1.04×10^{-7}
Fe	0.001177
Al	8.12×10^{-6}
Si	0.013993
C	0.006694
S	0.008247
Cl	0.5459
Cu	1.26×10^{-6}
Zn	2.47×10^{-5}
Pb	3.27×10^{-7}
H_2O	54.59448
pH_T	5.73
Equilibrium mineral association	Gn, Sph, Ccp, Ab, Ep60, Chl75, Dph, Act80

tion of water in it to 98.6% in the boiling point of the model system. As pressure decreases to 160–155 bar, the model multicomponent system becomes similar to the binary system, because with increasing mass of the vapor phase, its composition approaches 100 mol % H_2O. When the pressure of the solution decreases below 150 bar, the simulated multicomponent solution deviates significantly from the binary system toward higher mineralization, perhaps owing to the accumulation of Ca and K chlorides in the solution (their content rises above 20% of the sum of salts). In general, the concentrations of solutions in the model of hydrothermal fluid boiling fall between the calculated and experimental curves of the binary NaCl–H_2O system. Taking into account the complex composition of the model solution and the model assumptions, such an agreement can be regarded as satisfactory.

This calculation revealed a characteristic feature of multicomponent systems with volatile components: boiling begins in them at higher pressure than in the binary system (by 5 bar), but the mass fraction of vapor increases rather slowly as pressure decreases within 165–160 bar (Fig. 56a). This is the net result of two opposite effects: the presence of admixture gases in vapor promotes boiling, whereas the enhancement of boiling dilutes the gas phase with water vapor and rapidly diminishes the role of the admixtures (Fig. 56g).

The concentrations of major components (Cl, Na, Ca, and K) in the solution increase proportionally during boiling. The concentration of Fe grows faster: while Cl concentration increases by a factor of 10, Fe shows a 30-fold increase and reaches 47 mmol/kg at 130 bar. This effect is a consequence of complexation: the main Fe species, $FeCl_2^0$ and $FeOHCl_2^-$, depend on the square of the chloride ion concentration. In contrast to the major cations, the concentration of Si in the solution decreases. The reason for such a behavior is that the activity of silica in solution is connected with Na activity through the activity product of albite, which is one of the major mineral phases in the system. Since the concentration of Na increases during solution evaporation, the equilibrium concentration of silica declines.

According to the results of simulation, the pH_T value of the solution is practically constant during boiling and only slightly increases (from 6.46 to 6.87) with considerable evaporation. In contrast, the redox state of the solution changes significantly during boiling: $\log(a_{H_2})$ declines from –1.85 at 166 bar (before boiling) to –2.73 at 50% evaporation (155 bar). This effect is related to the partitioning of volatile components between the liquid and vapor phases. Figure 56d shows the concentrations of reduced volatile components (H_2, CH_4, and H_2S) in the liquid phase. It can be seen that these components are already removed from the aqueous solution during incipient boiling, when the mass of the vapor phase is still low. As a result, the concentrations of hydrogen and hydrogen sulfide decrease in the liquid phase by an order of magnitude, and that of methane, by three orders of magnitude. The distribution of hydrogen sulfide between phases is shown in Fig. 56e, which suggests that half of the initial H_2S inventory has already migrated from the liquid phase into vapor when the degree of solution evaporation is 10%. The depletion of H_2S in the aqueous solution is much more pronounced in this diagram than in the previous one: Fig. 56e shows the partition of S^{II} between the phases of the system, whereas Fig. 56d shows its concentration. A decrease in the mass of the liquid phase intensifies the process of redistribution.

Figure 56g shows the composition of the equilibrium vapor phase. Within the whole range of conditions, it is strongly dominated by water vapor. Minor components are (in descending order) H_2, H_2S, CO_2, and, at the initial stage of boiling, CH_4. The molar fraction of these substances is 0.n% at low degrees of evaporation and declines with decreasing total pressure to 0.0n%. An exception is methane, whose concentration in the vapor phase decreases to 10^{-5}% owing to oxidation. The acid gases considered in the problem, HCl and SO_2, show very low equilibrium concentrations and have a negligible influence on the character of the process.

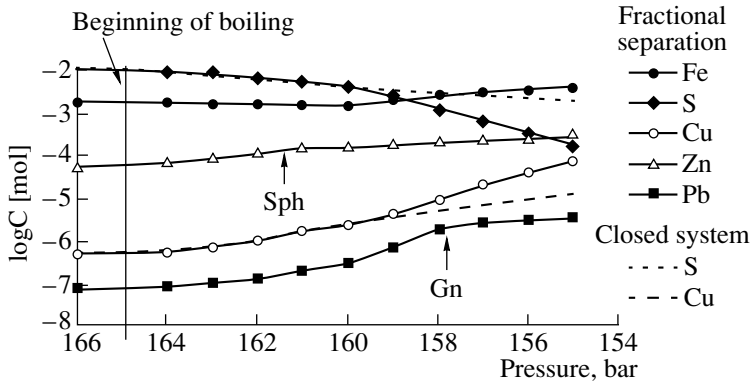

Fig. 57. Concentration of ore elements in solution during the fractional separation of the vapor phase at $T = 350°C$ and $R/W = 0.1$. For the sake of comparison, the data on S and Cu behavior during boiling in a closed system are shown by dashed lines. The arrows mark the disappearance of sulfide minerals.

The most interesting question in the numerical simulation is the behavior of ore elements. Figure 56f displays the concentrations of ore elements in the liquid phase. This diagram reveals the main tendency in the boiling process: the ore metals are rapidly accumulated in the liquid phase during boiling. The analysis of the model results suggests that different factors are responsible for the increase in the concentrations of various metals. The main carriers of iron in the model system are chlorite, epidote, and actinolite, and the increase in total iron concentration in the solution is explained by its enhanced complexation with chloride owing to an increase in solution mineralization. Before the beginning of boiling, the behavior of chalcophile elements (Cu, Zn, and Pb) is controlled by the presence of hydrogen sulfide through sulfide solubilities. The increase in their concentrations during boiling is related to the removal of H_2S into the vapor phase (mechanism of the loss of precipitant). This effect varies from element to element. Zinc is characterized by the highest mobility in the model system and is completely extracted into the solution at only a small degree of evaporation (≈10%). The disappearance of sphalerite from the equilibrium assemblage produces an inflection in the Zn concentration trend (Fig. 56f), and its subsequent accumulation is related to the boiling off of the liquid phase. Lead concentration increases owing to a combined effect of the loss of precipitant (hydrogen sulfide) and the enhancement of complexation. The effect of boiling is most pronounced for the copper concentration. In addition to the loss of precipitant and stronger complexation, the behavior of copper is influenced by a decrease in Fe^{++} activity due to the oxidation of the system. At $P = 130$ bar, about 1/3 of the total amount of copper occurring in the system migrates into solution. If we compare the states of the system before the onset of boiling (calculation for 166 bar) and after extensive boiling off (130 bar), the total mineralization of the solution increases by a factor of about 10, the concentration of H_2S decreases by a factor of eight, Fe and Zn increase by a factor of 30, Pb increases by a factor of 150, and Cu increases by a factor of 700. The initial rock suffered almost complete leaching of sulfides. Thus, phase separation appears to be most important for the least mobile ore metal, copper.

The results presented here on the influence of boiling on the properties of isothermal systems cannot be directly correlated with the sequential development of a natural process, because gradual decompression in a closed system could hardly be expected in nature. A decrease in hydrostatic pressure owing to tectonic processes is much slower than the formation of hydrothermal sedimentary ores. In contrast, pressure changes due to opening of channels for solution flow or boiling in a liquid column must have catastrophic consequences similar to phreatic explosions. The model results obtained here should be regarded as a qualitative assessment of the influence of boiling on the transportation of metals by solutions formed in the high-temperature focus of a hydrothermal system.

6.4.2. Phase separation in contact with a rock (open system)

The gradual separation of a vapor phase from a solution (stepwise distillation) is known to be a more efficient fractionation mechanism. The Rayleigh distillation law is widely used for the description of various geochemical processes. As to the multicomponent system addressed in this study, the Rayleigh distillation equation cannot be directly used because of the variability of fractionation coefficients due to phase transitions in the mineral part of the system. We performed, therefore, numerical simulation of phase separation with a pressure increment of 1 bar. The fraction of the vapor phase generated and released at such a pressure increment is only about 10% (thus, this process is not much different from the continuous Rayleigh model). The composition of the model system at a given step was equal to the composition of solution from the previous step. Such a scenario can be viewed as a slow

ascent of boiling liquid accompanied by gradual phase separation within the high-temperature zone of the system. At each step 10 g of fresh rock per one kilogram of initial fluid were added to the system. This addition is sufficient to buffer the pH value of fluid but is still too low to change the metasomatic mineral assemblage (Ab + Ep + Chl + Act) through an increase in *R*/*W*.

The simulation of the influence of phase separation on the behavior of metals in boiling hydrothermal solutions is shown in Fig. 57. In accordance with the theory, the gradual separation of the vapor phase efficiently removes H_2S from the liquid phase. Already at $P = 155$ bar and a degree of evaporation of 50%, the liquid phase retains only 0.8% of the initial amount of sulfide sulfur (8.4% in the above-described closed-system model). Correspondingly, the ore metals are also mobilized at significantly lower pressures. Zn is completely extracted from the rock at $P = 161$ bar (at a water loss of 9%); and Pb, at $P = 157$ bar (at a water loss of 32%). When the concentration of the solution increases by a factor of two ($P = 155$ bar), 26% Cu is removed from the rock, whereas the same degree of boiling off in a closed system corresponds to the very beginning of copper mobilization. It can be clearly seen in Fig. 57 that the concentrations of H_2S and Cu change much more drastically when the vapor phase is removed than in a closed system. The concentrations of zinc appeared to be practically identical, because this element was completely extracted into solution in both scenarios. The concentrations of Fe are always controlled by solid-phase assemblages and are insensitive to volatile loss.

Hydrogen and methane also escape much more rapidly from solution in the scenario with phase fractionation. However, the pH_T value of the solution is practically constant (6.4 ± 0.05) within the range of model conditions owing to the buffering effect of solid phases.

Thus, boiling accompanied by the removal of the gas phase can lead to extensive heavy metal mobilization from the rock. This result agrees with the conclusion by Drummond and Ohmoto (1985).

6.4.3. Adiabatic cooling of two-phase fluid

The rapid movement of hydrothermal solutions in the upwelling limb of the convection cell, which is established from many observations (Chapter 3), minimizes heat exchange between the solution and channel walls, and the *T–P–x* parameters of solution vary nearly adiabatically. Because the conduit is open and the solution can expand freely, this process can be regarded as isentropic (Bischoff and Pitzer, 1985): hydrothermal fluid expands during decompression and the energy for work against external pressure and the latent energy of phase transformations are supplied by the system cooling without any external heat sources. In such a rapid process, chemical interactions between the heterogeneous fluid and wallrocks can be ignored and only mineral deposition from the cooling solution needs to be considered.

Pressure is the only independent parameter of this model, and all other parameters can be expressed as functions of pressure through the condition of entropy conservation in the system. Such problems cannot be easily simulated using programs designed for the calculation of isobaric–isothermal equilibria (such as GIBBS, GBFLOW, and PENG), especially if boiling occurs in the model. A simple method for the approximate solution of isenthalpic problems was proposed by Bychkov and Grichuk (1991). In this method, an isothermal series of states of the system is calculated, and a state showing the target value of thermodynamic potential (*H* or *S*) is selected from them.

The entropy of a heterogeneous system is an additive function of the masses of phases:

$$S = m_l S_l + m_v S_v,$$

where the subscripts l and v denote liquid and vapor, respectively. The entropies of phases depend on their compositions. Their direct calculation would make the problem cumbersome and inefficient, because most of the substances in this problem are trace components, which make negligible contributions to the bulk entropy of the system. The H_2O–NaCl system (Bischoff and Pitzer, 1985) is a suitable prototype for the model of hydrothermal solution boiling, which allows us to simplify the task. Given the properties of the binary system, the mass proportions of phases providing the target value of the entropy of the system can be calculated, and then a state of the multicomponent system with the same phase proportions can be found.

The thermal properties of the H_2O–NaCl system along the boiling surface at temperatures up to 300°C were tabulated by Haas (1976a, 1976b), and the entropies of phases under higher parameters of state were reported by Tanger and Pitzer (1989). The results of calculations of isothermal boiling in contact with a rock at 350°C and pressures of 160 and 150 bar (compositions *1* and *2* in Table 31) were used as initial states for the simulation of adiabatic cooling.

The calculated parameters of adiabatic cooling with a temperature step of 50°C for model solutions *1* and *2* are shown in Table 32. These calculations revealed an interesting feature of adiabatic cooling in a water–salt system. Composition *1* initially contained 20 wt % of the vapor phase, and adiabatic decompression resulted in an increase in the amount of vapor up to 40%, i.e., boiling continued in the heterogeneous system during its ascent. The same change in pressure increased the fraction of liquid in composition *2*, i.e., partial vapor condensation occurred in that case. This seemingly paradoxical result is related to the high initial content of vapor in composition *2*, about 70 wt %. The gas phase expands considerably as the pressure decreases (at 200°C it occupies up to 99.4% of the system volume). The work of vapor expansion results in its partial con-

densation (mass fraction of vapor decreases from 70 to 60%).

The results of the thermodynamic modeling of changes in the composition of solution during isentropic cooling are shown in Fig. 58. These results indicate that isentropic cooling is accompanied by the deposition of ore minerals (Fig. 58a): pyrite, sphalerite, and chalcopyrite. The sulfides are deposited despite a twofold increase in the fraction of the vapor phase in the model within the cooling interval (Fig. 58b), and the continuous partitioning of hydrogen sulfide into the vapor phase (Fig. 58c). Simultaneously, the amount of iron in the solution decreases by a factor of two; zinc, by an order of magnitude; and copper, by two orders of magnitude (Figs. 58c, 58d). The concentration of lead does not change, and the system remains unsaturated with respect to galena. These changes are accompanied by a significant decrease in pH_T from 6.5 to 3.9 (Fig. 58e) and a decrease in H_2 activity from 8×10^{-3} to 1×10^{-5}. The characteristic maximum of pyrite deposition at 200°C is related to the fact that the concentration of Fe in the residual solution becomes higher than that of H_2S below this temperature. Note that the total amount of hydrogen sulfide in the heterogeneous system does not vary considerably.

Similar results were obtained for the adiabatic cooling of initial composition *2*, which was produced by isothermal boiling at a pressure of 150 bar (Fig. 59c). Pyrite is again the most abundant phase. A specific feature of mineral formation for this vapor-rich initial composition is that sphalerite saturation is achieved only after cooling to 150°C.

Figures 59a–59c compare the results of simulation of mineral formation during the stepwise cooling of a homogeneous solution and heterogeneous fluids. Figure 59a shows a cooling path of the model solution that was produced in the simulation of isothermal boiling at 350°C (Section 6.4.1) and $P > P_{boiling}$ (166 bar). The *T*–*P* parameters during cooling of this composition were varied along the boiling line within the homogeneous field, and the calculation procedure corresponded to the slow cooling scenario (Section 4.3.1). Figures 59b and 59c display the results of the adiabatic cooling of heterogeneous fluids described above. It can be seen that the adiabatic cooling of initially heterogeneous fluids yields much larger volumes of ore precipitates (in the cases considered, by a factor of 6, on average). The main contribution is that of pyrite, while sphalerite content shows only a twofold increase. Compared with the case of a homogeneous solution, the mass of chalcopyrite deposited during the cooling of heterogeneous fluid increases by factors of 5 and 20 for compositions *1* and *2*, respectively. In the homogeneous model, the mass fraction of chalcopyrite in the bulk precipitate was 0.36%, whereas this value is 0.38% for composition *1* (showing a fivefold increase of the total mass of sulfides) and 1.5% for composition *2*.

Table 31. Initial compositions of hydrothermal fluids in the model of adiabatic cooling obtained by the calculation of isothermal boiling in contact with rock at T = 350°C, $\Sigma R/W$ = 0.596, and wave no. 1

Composition no.	*1*	*2*
P_{init}	160	150
Gas/liquid, mass ratio	0.253	2.22
Liquid phase		
Mass, kg	0.810	0.315
Salinity, g/kg	40.72	103.3
pH_T	6.47	6.60
Amount of component, mole		
H	0.035424	0.008811
O	0.023567	0.007291
K	0.032676	0.032676
Na	0.450453	0.4481
Ca	0.030586	0.031363
Mg	1.21×10^{-8}	7.52×10^{-9}
Fe	0.001459	0.00214
Al	1.17×10^{-5}	6.43×10^{-6}
Si	0.004528	0.001152
C	0.001405	0.000169
S	0.0031	0.000445
Cl	0.545898	0.54589
Cu	2.07×10^{-6}	9.7×10^{-6}
Zn	0.000135	0.000135
Pb	2.28×10^{-7}	8.45×10^{-7}
H_2O*	43.11551	15.65974
Gas phase		
Mass, kg	0.205	0.699
Amount of component, mole		
H	22.73958	77.67893
O	11.33757	38.80279
C	0.006169	0.007405
S	0.007144	0.009805
Cl	2.15×10^{-6}	1.02×10^{-5}
Equilibrium mineral association	Gn, Bn, Ab, Ep75, Ep60, Chl75, Act80	Bn, Ab, Ep75, Ep60, Chl50, Chl75, Act80

The main reason for the enhancement of ore deposition from heterogeneous fluids is the higher initial metal content in them compared with homogeneous fluid. This can be seen in Fig. 56f, which displays the concentrations of ore components in the initial solutions that subsequently underwent cooling in the model. The considerable loss of metals from solution

Table 32. Parameters of the adiabatic cooling of solutions

Temperature, °C	Pressure, bar	Masses of phases, g		Bulk entropy of system, J/K	Salinity of liquid, g/kg
		liquid	gas		
Adiabat for composition *1* (Table 31); mass of system 1014.3 g and salt content 32.97 g					
350	160.56*	809.7	204.6	3961.591	40.72
300**	83.38	693.2	321.1	3961.601	47.56
300***	83.18	703.3	311.0	3961.597	46.88
Average	83.28	698.2	316.0	3961.599	47.22
250	38.58	675.5	338.7	3961.585	48.81
200	15.05	627.6	386.7	3961.594	52.54
150	4.59	583.4	430.9	3961.587	56.52
Adiabat for composition *2* (Table 31); mass of system 1014.0 g and salt content 32.50 g					
350	153.66*	314.6	699.4	4796.890	103.3
300**	80.87	369.4	644.5	4796.888	88.0
300***	80.84	373.6	640.4	4796.881	87.0
Average	80.85	371.5	642.5	4796.885	87.48
250	37.81	424.1	589.9	4796.899	76.63
200	14.79	426.0	588.0	4796.898	76.29
150	4.52	417.4	596.6	4796.897	77.86

* Calculated pressure for the H_2O–NaCl system for the gas/liquid ratio obtained for the initial composition by the simulation of a multicomponent system.

** Calculated using the data by Haas (1976a, 1976b).

*** Calculated using the data by Tanger and Pitzer (1989).

suggest that temperature is a more significant factor for the behavior of ore elements than hydrogen sulfide partitioning into the vapor phase. On the other hand, a comparison of residual concentrations in ore-forming solutions shows that phase separation is favorable for metal transportation by hydrothermal solutions. Within the whole temperature interval, the concentrations of metals in the liquid phase of heterogeneous systems were higher than those in the homogeneous system, and their temperature dependencies were less steep. This is especially pronounced for Zn concentrations (Fig. 59d).

However, in order to estimate the applicability of the model results to natural objects and the role of adiabatic cooling in ore formation to convective systems in general, it is necessary to evaluate the thermal and hydrodynamic aspects of this process. It is known that thermal convection is driven by the difference of hydrostatic pressures generated by water columns in the downwelling and upwelling limbs. This difference arises from the density contrast between cold and hot water. Phase separation results in a dramatic decrease in bulk fluid density owing to the large molar volume of the vapor phase. According to the data of Haas (1976a, 1976b), at 300°C and a bulk NaCl content of 0.5 mol/kg, the densities of homogeneous solution and two-phase systems with 20 and 70 wt % of vapor are 0.744, 0.180, and 0.059 g/cm^3, respectively. Consequently, the formation of a boiling zone in the upwelling limb and the focus of a hydrothermal system must strongly intensify solution circulation. Some hydrodynamic aspects of this problem were discussed by Cathles (1977) and Brikovski and Norton (1989). The hydrostatic pressure of the heterogeneous fluid column in the channel is small compared with the seawater pressure at the mouth of the channel. For a vertical channel size of 1 km, an ocean depth above the channel mouth of 1.6 km, a temperature of 350°C, and a vapor fraction of 20 wt %, its contribution will be only 30 bar as compared with 103 bar for cold seawater. As a result, the channel filled with ascending boiling fluid serves as an efficient intake manifold. The reduced pressure in the channel will inevitably intensify the lateral influx of colder water from fractures in the country rocks and subsurface mixing. This factor must strongly limit the development of boiling zones, because even a small addition of cold water will promote vapor condensation and cessation of boiling.

On the other hand, the adiabatic cooling of heterogeneous fluid from 350 to 300°C corresponds to a pressure decrease from 165–150 to 85–80 bar (Table 32). Given a density of the heterogeneous mixture of 0.2–0.3 g/cm^3, the length of the ascending flow channel must be 2–4 km. This is close to the maximum possible value for oceanic hydrothermal systems (perhaps also for ancient hydrothermal systems producing massive

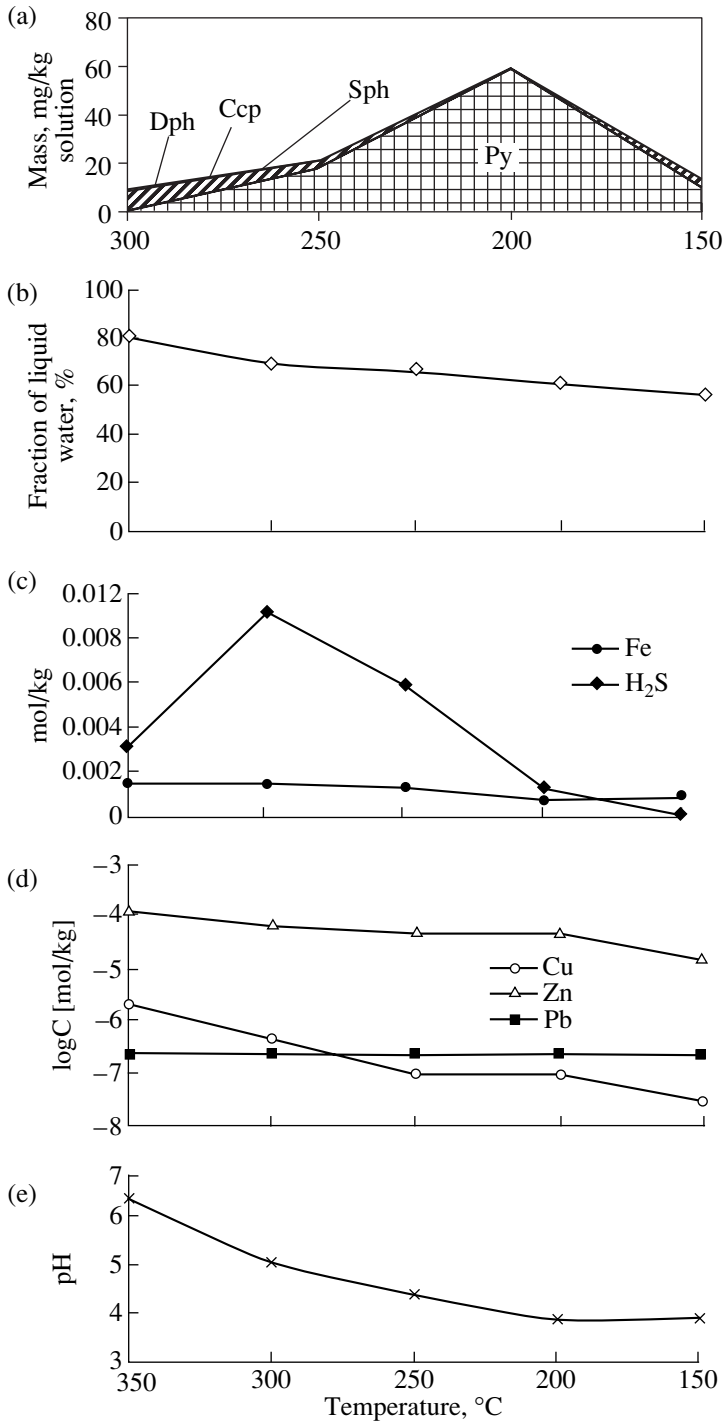

Fig. 58. Compositions of hydrothermal solutions during the adiabatic (isentropic) cooling of a heterogeneous fluid. The initial composition of solution is given in Table 31 (no. 1), and the adiabat parameters are listed in Table 32. (a) The deposition of minerals during adiabatic cooling; (b) the degree of water evaporation, %; (c) iron and sulfur in solution; (d) heavy metals in solution; and (e) solution pH_T.

sulfide deposits). The lengths of real vertical channels correspond to temperature variations of only 15–25°C during adiabatic discharge. These values are similar to the estimates obtained by Bischoff and Pitzer (1985). The model calculations showed that the maximum ore deposition from heterogeneous fluids occurs at much lower temperatures and more extensive cooling. The natural scales of adiabatic cooling allow rapid ascent of heterogeneous solutions through the conduit almost without loss of ore components.

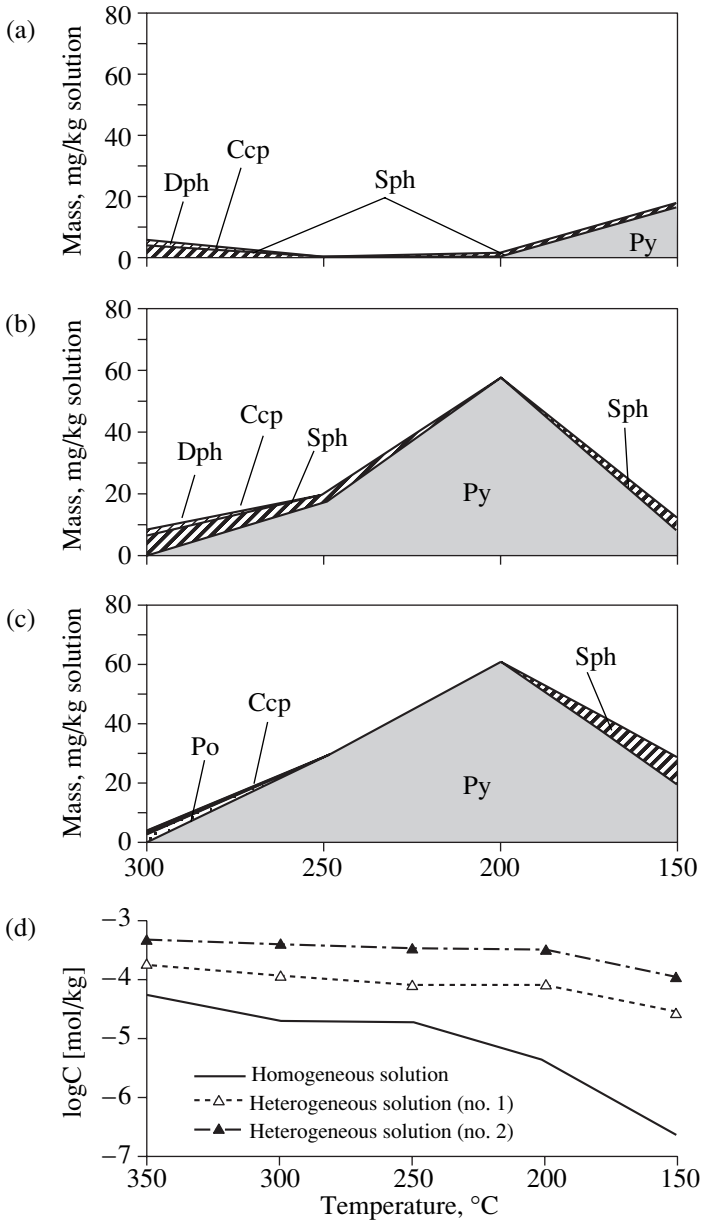

Fig. 59. Compositions of ore precipitates and hydrothermal solutions during the cooling of homogeneous and heterogeneous fluids. (a) Homogeneous initial solution, (b) 20% of vapor phase, (c) 70% of vapor phase; and (d) residual concentrations of zinc in solution during fluid cooling.

Thus, the model of an adiabatic (isentropic) cooling has limited applications for the reproduction of ore formation in the ocean. The natural process either does not follow an adiabatic path (owing to subsurface mixing) or produces no significant deposition of ore matter.

6.4.4. Condensation of two-phase fluid during rapid discharge and ore deposition

As was shown in Section 4.3.1, ore deposition during rapid discharge of hydrothermal fluids can be reproduced in the scenario of instantaneous cooling of hydrothermal solution without any chemical interaction with seawater. The cooling of a heterogeneous fluid will be accompanied by the condensation of the vapor phase and the interaction of vapor-borne substances with components from the liquid phase. That this case is realistic is suggested by the fact that fluid heterogeneity was never visually observed during the discharge of solutions in black smokers with definite evidence of boiling.

Within the scenario of instantaneous cooling, model calculations were performed for heterogeneous fluid formed (a) in the case of isothermal boiling without

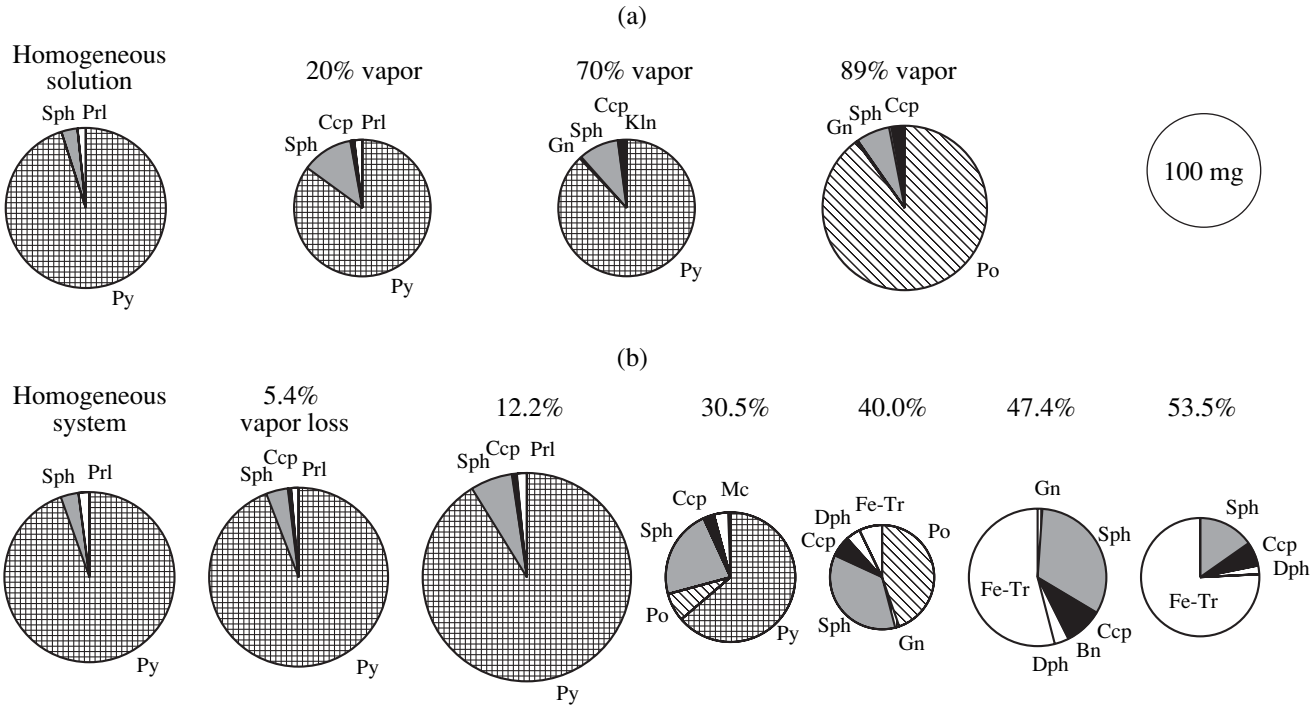

Fig. 60. Compositions of ore precipitates obtained during the rapid cooling of a heterogeneous fluid. The initial compositions of fluids were obtained by the simulation of boiling in contact with a rock at $T = 350°C$ (Figs. 56, 57). (a) Cooling after boiling without phase separation (initial compositions were obtained at P of 166, 160, 150, and 130 bar); and (b) boiling with phase separation (initial compositions were calculated at P of 166, 162, 160, 158, 157, 156, and 155 bar). Circle area is proportional to the mass of precipitated matter for 1 kg of fluid.

phase separation (Section 6.4.1, Fig. 56) at a varying fraction of the gas phase and pressures of 166, 160, 150, and 130 bar; and (b) in the case with phase separation (Section 6.4.2) for various degrees of boiling off.

The temperature of cooling was taken to be 150°C, similar to the calculations presented in Section 4.3.1. The pressure at this temperature was taken to be 100 bar in order to provide the complete condensation of the vapor phase.

The results of fluid cooling simulation without phase separation are shown in Fig. 60a together with the cooling of the homogeneous solution that was produced in the isothermal model at $P = 166$ bar. As can be seen in this diagram, within a wide range of vapor content (20–70 wt %), the cooling and condensation of heterogeneous fluid do not significantly affect the mass of precipitate but change its mineral composition toward a higher content of heavy metal sulfides. The fraction of sphalerite in the precipitate is 3% in the case of homogeneous solution and increases up to 10–13% during the cooling of heterogeneous fluids; the content of chalcopyrite increases by a factor of 20, from 0.06 to 1.3%. Similarly, the precipitate from a heterogeneous fluid contains up to 0.13% galena as compared with 0.01% calculated for a homogeneous solution. This enrichment is related to an increase in the concentrations of heavy metals in hydrothermal fluids owing to phase separation (Section 6.4.1, Fig. 56f). An interesting effect was observed during the cooling of fluid with the maximum vapor fraction (89 wt %). In that case, pyrite, which was predominant in all other cases, was replaced by pyrrhotite. The phenomenon is connected with the strong partitioning of H_2 into the vapor phase during boiling in the focus of the hydrothermal system (Fig. 56g). Although the molar fraction of hydrogen in the vapor phase is not high (about 0.1%), the vapor phase is abundant in this model. In the bulk system, the amount of H_2 increases up to 49 mmol as compared with 14 mmol in the homogeneous case. The condensation of such a gas phase results in the precipitation of a more reduced phase, pyrrhotite. This process also produced the maximum chalcopyrite fraction of 3%.

Thus, the condensation of heterogeneous fluids is accompanied by the precipitation of ore minerals, and the main feature distinguishing this case from the cooling of homogeneous hydrothermal solutions (without boiling) is the elevated fraction of heavy metals, Cu, Zn, and Pb.

Interesting results were obtained from the simulation of rapid cooling of solutions that suffered fractional separation during boiling (Fig. 60b). A minor vapor loss (5–10% of the mass of water) increases the amount of ore precipitate, but a high degree of boiling off has the opposite effect. This is surprising, because the concentrations of ore metals in the solution increase during phase separation (Fig. 57). The reason for this

effect is related to the deficit of sulfide sulfur: H_2S is eliminated with vapor during phase separation. Already at 20% evaporated, the residual H_2S concentration becomes equal to the total content of iron and heavy metals, and the advanced phase separation generates an S^{II} deficit in the solution. Because of this, at large degrees of evaporation, the amount of sulfides produced by cooling of the residual solutions decreases continuously. Pyrite is replaced by pyrrhotite (although the environment does not become more reducing than in the beginning of boiling) and later by Fe-chlorite and Fe-actinolite. The preservation of Zn and Cu sulfides in the precipitate suggests that they are less soluble than iron sulfides under such conditions. After 50% evaporation, cooling of the solution produces sphalerite, chalcocite, and gangue minerals.

6.4.5. Verification of the model

A comparison of the data obtained by the simulation of boiling in the interiors of hydrothermal systems with natural observations shows that the model provides an adequate description of the main properties of hydrothermal solutions that are usually connected with boiling. The model implies extensive partitioning of volatile components into the vapor phase during boiling. The liquid phase is simultaneously enriched in iron and heavy metals; this effect is related not only to evaporative concentration but also (and to a larger extent) to metal mobilization from the country rock. This results in a positive correlation of iron and heavy metal contents with chloride and a negative correlation with H_2S. Such relationships exist in natural hydrothermal systems (Section 6.2). The concentrations of metals in model solutions are of the same orders of magnitude as those in the natural prototypes: from *n* mmol/kg to 20 mmol/kg of Fe; 0.*n* mmol/kg of Zn; 0.0*n* mmol/kg of Cu, and 0.00*n* mmol/kg of Pb (Figs. 52, 56, 57). Exact quantitative correspondence between the model and the natural prototypes could hardly be expected, because the temperature of our simulation (350°C) is lower than that in the interiors of oceanic hydrothermal systems (370–400°C). Nonetheless, the calculated and observed trends in the development of boiling processes are evidently identical.

6.5. Conclusions

Analysis of the results of simulated boiling in oceanic hydrothermal systems showed that this factor is favorable for the transfer of metals in hydrothermal systems. Phase separation in solutions results in the partitioning of metals and hydrogen sulfide into different phases and a significant increase in the solubility of sulfides in heterogeneous systems. This effect corresponds to the action of the mechanism of precipitant loss. It must evidently influence not only the elements considered in our simulation (Fe, Cu, Zn, and Pb) but also any element with a sulfide form of precipitation and a nonsulfide form of migration in solutions. Among the elements considered in our model, copper is most sensitive to boiling, followed by zinc and lead. Boiling in the interior of a hydrothermal system can increase the concentrations of these metals in solution by up to two orders of magnitude. If the residual brine and vapor are spatially isolated, the mobilization of metals from the rock will further increase. Consequently, boiling increases the potential of hydrothermal systems with respect to base metal ore formation.

The cooling of heterogeneous solutions accompanied by condensation (during submarine discharge) can yield considerable amounts of sulfide precipitates. They will be enriched in heavy metals relative to the ores formed by the cooling of homogeneous fluids.

CHAPTER 7. POSSIBLE ROLE OF MAGMATIC FLUID: A COMBINED EXHALATION–RECYCLING MODEL

7.1. Problem Formulation

Magmatic fluids are traditionally regarded by geologists as the main ore generating agent in hydrothermal deposits. This point concerns, in particular, massive sulfide deposits. Starting from the pioneering studies by Zavaritskii (1943), a volcanic exhalation hypothesis and its modifications have been used in genetic reconstructions by many authors. However, an analysis of the literature on this problem shows that this concept is based on the observations of spatial and temporal links between magmatism and ore mineralization, whereas there are no direct lines of evidence for the formation of massive sulfide ores from magmatic gases. The finding and investigation of modern ore-forming systems on the ocean floor resulted in the development of an alternative recycling concept for the genesis of massive sulfide ores (Rona, 1984; Krivtsov, 1987; etc.). Seawater circulating in heated rocks is regarded as the main ore-forming agent in this concept. Both heat and ore components are supplied to the hydrothermal system from the country rocks. The exhalation and recycling concepts are not mutually exclusive; a superposition of these processes can be expected during functioning of a magma-related hydrothermal system. Hence, there is a need for indicators of the exhalation and recycling mechanisms which would allow us to distinguish their contributions to the formation of massive sulfide deposits.

The investigations of modern hydrothermal systems in oceans have not yet provided unambiguous evidence for the presence of a significant exhalation component in the ore-forming process (Chapter 3). However, almost all the oceanic hydrothermal systems studied to date are associated with divergent plate boundaries, and the melts reaching the crust in these regions are usually water-poor. According to the results of geodynamic reconstructions, most ancient massive sulfide deposits were formed in island-arc settings with a different style

of magmatism, a different type of magma chambers (central-type volcanoes rather than fissure eruptions), and magmas richer in water. Therefore, it would be inappropriate to extend the conclusions obtained for oceanic hydrothermal systems to ancient massive sulfide systems.

A paradoxical situation is revealed by the analysis of the literature on the problem of the volcanic exhalation origin of massive sulfide ores: the researchers never addressed the problem of quantitative estimation of the chemical effect of magmatic gases on the wall-rocks of massive sulfide deposits and characterization of the ores that could be formed during magmatic fluid ejection on the seafloor. One reason for this paradox is the lack of methods allowing for such quantification. Therefore, a search for new ways to tackle this problem is very important. The thermodynamic modeling of ore-forming processes is a promising approach.

In this section we address calculation of the thermodynamic model of a submarine hydrothermal system whose evolution included the stages of magmatic exhalation and convective recycling. This simulation was aimed at estimating the relative contributions of these mechanisms to the formation of submarine massive sulfide deposits.

7.2. Characteristics of the Exhalation Convective Model

The caldera of a submarine volcano filled with basic extrusive rocks and underlain by a magma chamber was regarded as a geologic prototype of the model (Fig. 61). During the first (magmatic) stage of development, the hydrothermal system is fed by the fluid released from the magma. As the fluid ascends toward the surface, it reacts with the country rocks forming a footwall channel, and ore minerals are deposited during fluid discharge on the ocean floor. The second (convection) stage produces a recycling hydrothermal system within the volcano supplied by seawater. This system inherits the discharge conduit of the magmatic stage, and the ore-forming process is superposed on the products of previous hydrothermal activity. Since there is no geological information on the mechanism of the change of system supply, the stage of a mixed magmatic–recycling source is not considered in the model, which simplifies the interpretation.

Model parameters are the compositions of rocks, magmatic gas, and seawater; temperature and pressure in the downwelling limb of the convection cell, feeder channel, and ore deposition zone; intensities of solution interaction with the country rocks (specified by the rock/water ratio); production of the system during the magmatic and recycling stages; and durations of these stages.

The model composition of the country rocks was approximated by the average composition of calc-alkaline basalts, and present-day seawater composition was used in the calculations. The estimation of the composition of magmatic gas is discussed below. For the sake of comparison, the ranges of temperature, pressure, *R*/*W* ratio, and discharge rate of the hydrothermal system were taken to be identical to those used in Chapter 4.

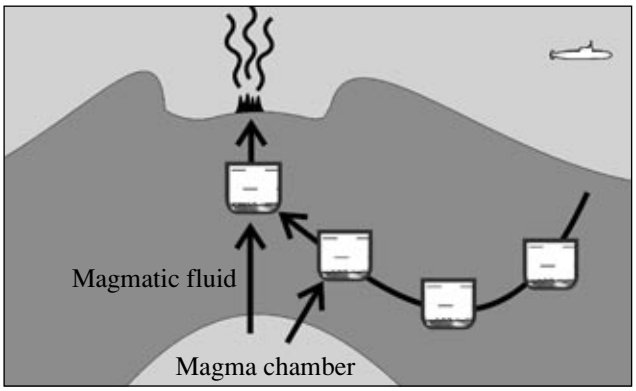

Fig. 61. Principal scheme of the model of a convective system involving magmatic fluids.

The mass proportions of magmatic and recycled fluids can be estimated from the heat balance of the hydrothermal systems, by calculating the amount of seawater required to cool the unit mass of magmatic melt and comparing it with the abundance of water dissolved in this melt. The heat released during the formation of igneous rocks includes the latent heat of crystallization and thermal effects of solid rock cooling. The procedure of heat balance calculation is similar to that described in Chapter 3, but the two contributions are considered separately:

$$M_{H_2O} = \frac{0.4}{370 \times 0.0044} + \frac{0.75}{370 \times 0.0044}$$

$$= 0.25 + 0.46 = 0.71 \text{ g } H_2O/\text{g rock}.$$

The concentration of water in the initial island-arc melt was taken to be 1% or 0.01 g per one gram of basalt. If this water is completely released during crystallization (which is certainly an overestimation) and there is no explosive degassing, the mass proportion of magmatic and convective components will be 1 : 70. It should be kept in mind that this proportion is valid for the whole period of magma chamber cooling. Cann *et al.* (1985/1986) calculated that hydrothermal activity is vigorous when melt is present in the magma chamber and attenuates gradually after melt disappearance. Therefore, the effective mass proportion will be less contrasting during the active phase of the process (but no higher than 1 : 25).

The discharge rate of the system in the convection stage was taken to be 10 kg/s, which is equal to that of the model described in Section 4.3.2. In order to facilitate comparison, the same discharge rate was assigned to the magmatic stage, which is not constrained by natural data. Therefore, the proportion of the durations of the magmatic and recycling stages corresponded to the ratio of solution masses (no less than 1 : 25).[34] The sim-

[34] An increase in the prescribed discharge rate value makes the magmatic stage shorter without changing the mass of released fluid and the corresponding mass of transported ore matter.

Table 33. Compositions of fluids used in the model, mol/kg

Component	Volcanic gas (Taran *et al.*, 1995)		Convecting solution (calculated for the downwelling limb)	
	initial composition	composition corrected to a degassing pressure of 500 bar	beginning of convection (calculation step no. 200)	end of convection (calculation step no. 900)
H	1.626999	3.436776	0.071243	0.071482
O	3.747455	1.201559	0.072429	0.072470
K	0.001400	0.001400	0.019807	0.005699
Na	0.002500	0.002500	0.476855	0.471885
Ca	0.026262	0.026262	0.023889	0.033377
Mg	0.000020	0.000020	0.000010	0.000016
Fe	0.000131	0.000980	0.001194	0.001393
Al	0.069808	0.069808	0.000008	0.000007
Si	9×10^{-8}	9×10^{-8}	0.014545	0.015788
C	0.9371	0.937100	0.004330	0.002624
S	1.030381	0.189000	0.001188	0.000480
Cl	0.252391	0.252391	0.545900	0.545900
Cu	0.000004	0.000004	0.000012	0.000031
Zn	0.000047	0.000047	0.000122	0.000033
Pb	0.000006	0.000006	0.000002	0.000001
H_2O	49.14576	48.200000	55.327085	55.405107

ulation was carried out with a time increment of 10^8 s (about 3 y), and the lifetime of the model system was $n \times 1000$–$n \times 10\,000$ y. The product of the discharge rate and the lifetime of the system is equal to the total output from the system, which controls the final size of the growing ore body.

Given the approximate character of many parameters, only those that affect the qualitative results of simulation are of real significance. An analysis of our simulation distinguishes a limited number of such model parameters: the maximum temperature in the interior part of the system, $\Sigma R/W$ value in the downwelling limb, and relationships of the discharge rate of the system and the duration of the process. Variations in other parameters influence the quantitative results of simulation but do not change the general qualitative patterns.

Initial composition of magmatic gas. The determination of the initial composition of magmatic fluid is a considerable challenge, because there is no direct evidence for massive sulfide deposits. The composition of volcanic gases from island-arc volcanoes can be used as a proxy. The most comprehensive and reliable results on the composition of volcanic gases were recently obtained for Kudryavyi Volcano (Iturup Island, Kurils) by Taran *et al.* (1995). These authors managed to sample fumaroles with a temperature of up to 940°C. The gas from these events changed negligibly after its separation from a melt. The roof of the magma chamber of Kudryavyi Volcano is probably situated only 200–300 m below the bottom of the crater. The composition of magmatic gas from this volcano is shown in Table 33.

It appeared, however, that simulation with magmatic fluid of such a composition does not produce massive sulfide ores. Reconnaissance calculations yielded mineral assemblages containing considerable amounts of anhydrite and elemental sulfur, which are common in subaerial exhalative volcanic deposits. This result is due to the SO_2-rich composition of gas from Kudryavyi Volcano. The reason for this effect lies in the conditions of gas separation from magma. Wallace and Carmichael (1994) showed that the relationships of oxidized and reduced sulfur species in a gas equilibrated with magma depend on the redox conditions and total pressure in the system. The equilibrium constant of the reaction

$$SO_2 + 3H_2 \longleftrightarrow H_2S + 2H_2O \quad (59)$$

gives

$$X_{H_2S}/X_{SO_2} = K_{59}P_{tot}(X^3_{H_2}/X^2_{H_2O}). \quad (60)$$

In order to take this factor into account, we refined the composition of magmatic fluid. It was assumed that gas separating from the melt at a temperature of 1100°C is in thermodynamic equilibrium with the *QFMP* (quartz–fayalite–magnetite–pyrrhotite) buffer. The composition of gas from Kudryavyi Volcano in the H–O–C–S–Fe–SiO_2 system was used for simulation (with excess solid buffer phases). The calculations were performed by the GBGAS program using the approximation of ideal mixing of real gases, and the thermodynamic properties of substances were taken from the UNITHERM data bank. Figure 62 shows the results of the simulation, indicating that an increase in the degassing pressure strongly reduces the molar fraction of SO_2 in the gas, whereas the molar fraction of H_2S remains constant. Hence, the SO_2/H_2S ratio in a deep magma chamber will be lower than that observed in volcanoes. The simulation of the formation of a massive sulfide system was carried out using the model composition of magmatic gas, whose major-component concentrations were corrected to a degassing pressure of 500 bar.[35] This composition is given in Table 1.

The interaction of magmatic fluid and convecting seawater with the walls of a feeder conduit was calculated by the procedure described in Section 4.2. The formation of an ore body was simulated by the method similar to that used in Section 4.3.2, except that during the first 100 steps of calculation, magmatic gas was introduced into the channel and altered seawater from the downwelling limb (its composition was calculated by the method described in Sections 2.2 and 4.1.2) was used in subsequent steps.

7.3. Results of Simulation

7.3.1. Formation of footwall metasomatic zoning

According to our simulation, the interaction of magmatic fluid with the walls of the feeder channel corresponds to acid leaching. The back zones of resulting columns (Fig. 63) are made up of the Prl + Py and Qtz + Prl + Py associations. Away from the channel wall, chlorite and talc appear and are further joined by actinolite, epidote, wairakite, and albite. The front zones are composed of assemblages typical of rocks affected by propylitic alteration: Chl + Ep + Act + Ab sulfides at 350°C, and carbonates occur instead of epidote and wairakite at 300 and 250°C. Another notable feature of the calculated columns is the magnesian chlorite composition (clinochlore) in their assemblages. Copper is fixed as chalcopyrite in the Qtz + Prl + Py zone, whereas zinc and lead form sphalerite and galena, respectively, in the clinochlore-bearing zone.

The results of simulation shed light on the nature of metasomatic zone boundaries and the regime of components within the column. Figure 64 gives some data

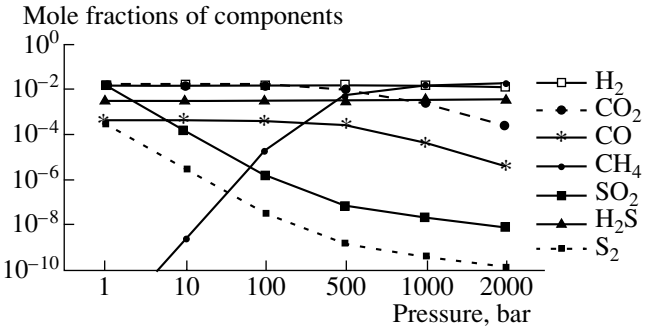

Fig. 62. Calculated composition of a magmatic gas phase in equilibrium with the *QFMP* buffer at various pressures and $T = 1100$°C.

on the composition of solutions moving through the model metasomatic column at a temperature of 350°C. The back zones of the column, including the Qtz + Prl + Py zone, are formed in contact with acid solutions showing pH_T 1.5–1.7. The transition to propylite assemblages is associated with the neutralization of the acid magmatic fluid by the country rocks (up to pH_T 4.5–4.6). Sulfide sulfur is efficiently transported by the fluid up to the frontal zone of propylites and strongly prevails over ore metals. The sequence of element mobility in the metasomatic halo is S > Fe, Zn > Cu.

These results are fundamentally different from those obtained in the convection model (Section 4.2, Fig. 28). Altered seawater produces chloritization and albitization in the country rocks. The resulting chlorite has an iron-rich ferromagnesian composition. The pH_T value (about 5.4) and proportions of ore elements in the percolating solution are practically invariable. The hydrothermal fluid of an exogenous origin passing through the convective system weakly reacts with basalt, because it equilibrated with the country rocks in the downwelling limb. Only a small shift from the equilibrium state takes place in the feeder channel owing to changes in *T* and *P*. The formation of a distinct footwall metasomatic zoning is obviously impossible in this case.

Consider now what happens when recycling overprints the metasomatic column formed by a magmatic fluid, i.e., a two-stage model. Figure 65 illustrates the simulation of the passage of 100 portions of magmatic gas through the metasomatic column (this case is shown in Fig. 64) followed by 100 portions of recycled solution from the downwelling limb ($T_{max} = 350$°C and $\Sigma R/W = 0.47$). The main effect of such a superposition is the formation of sericite during the percolation of recycled solution. This produces the typical metasomatic zoning of massive sulfide deposits: Qtz + Ser + Py → Qtz + Ser + Chl + Py → propylite.

[35] The concentrations of chlorides and ore metals were not corrected.

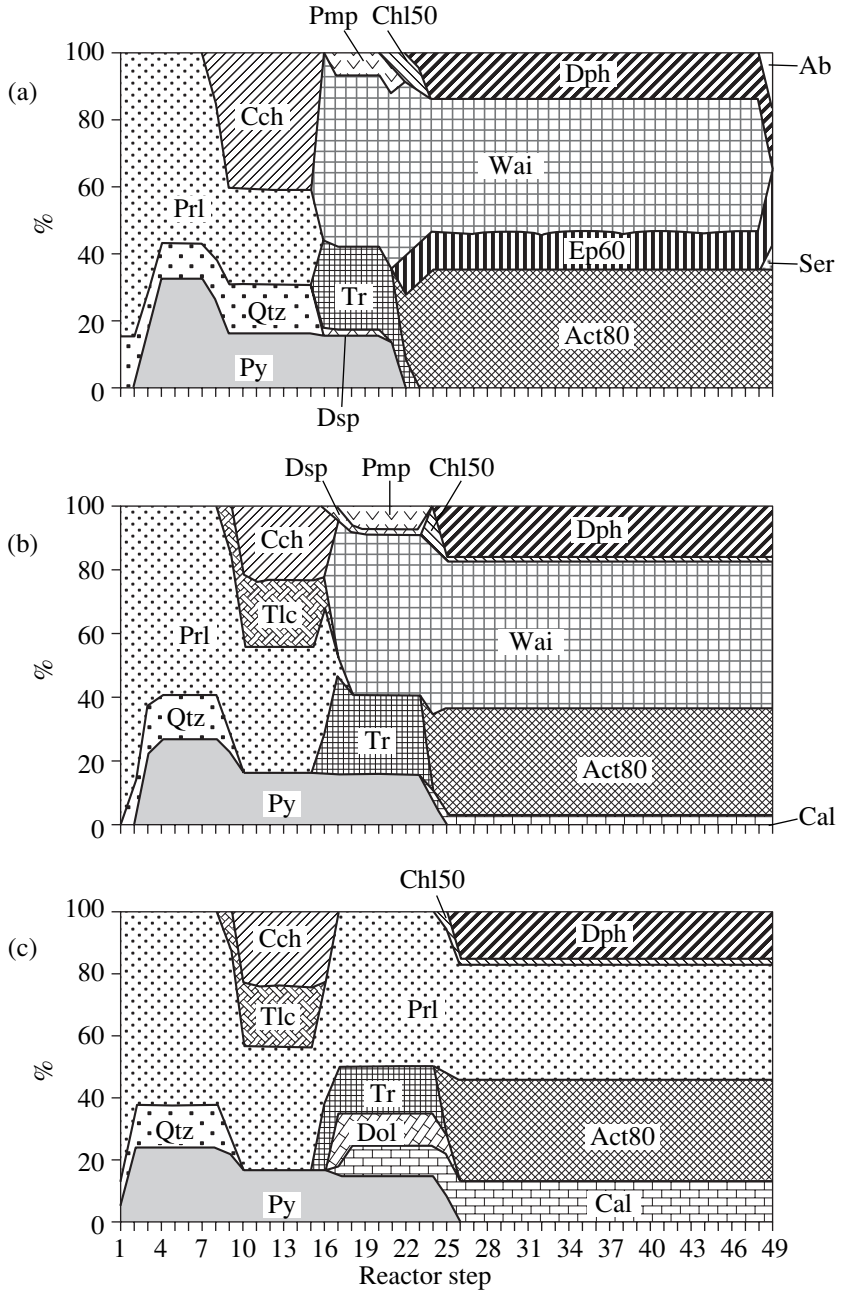

Fig. 63. Mineral composition of metasomatic columns developing around a feeder channel under the influence of magmatic fluid at (a) 350°C, (b) 300°C, and (c) 250°C and P = 500 bar.

7.3.2. Chemical evolution of the ore body in the combined exhalation–recycling model

The calculations presented in this section were performed for the following scenario of ore-forming processes. During the first (exhalative) stage, an ore body was formed at the expense of magmatic fluid discharge (ejection) on the ocean floor (its composition is shown in Table 33, column 2). This stage lasted 100 computation steps, with a discharge fluid rate of 10 kg/s, which corresponds to the degassing of a magma body, about 4 km^3 in volume, within 300 y. During the second stage, degassing ceased and a convection system was launched. This system had the same discharge rate, and its activity lasted 2500 steps (about 8 ky).[36]

Figures 66a and 67 show the structure and bulk composition of the ore body formed by the end of the magmatic stage (after 100 computation steps). The calculations suggest that the body has a pyritic composi-

[36] The proportion of the durations of the two stages, 1 : 25, was determined above from heat balance conditions.

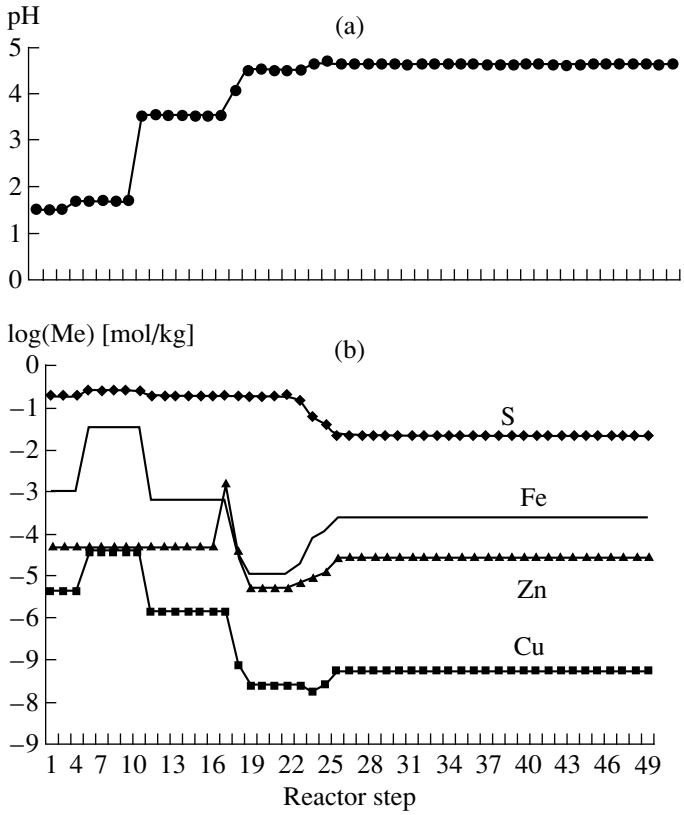

Fig. 64. Composition of solution generated during the formation of a metasomatic column corresponding to Fig. 63a at $T = 350°C$ and $P = 500$ bar (computation step no. 20). (a) pH and (b) concentrations of dissolved components (logarithmic scale).

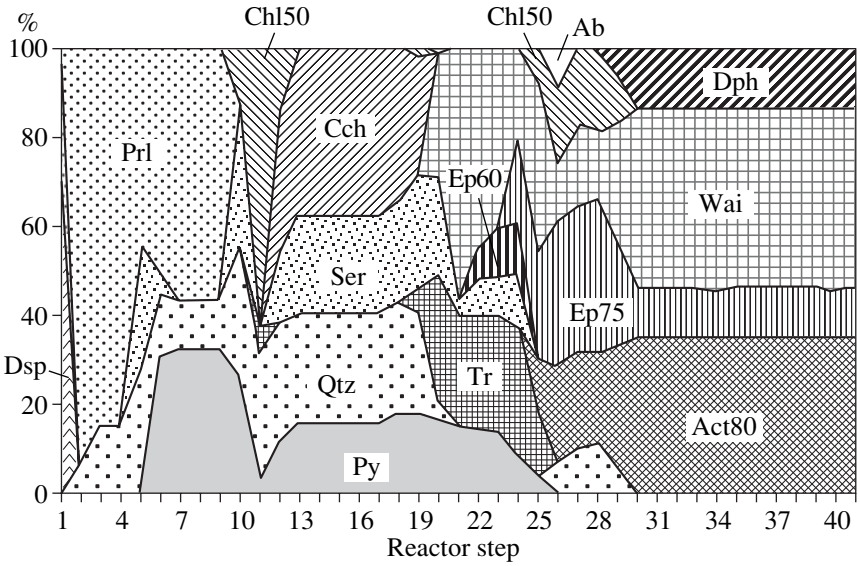

Fig. 65. Mineral composition of metasomatic rocks formed around a feeder channel in the combined exhalation–recycling model at $T = 350°C$, $P = 500$ bar, $\Sigma R/W = 0.47$, after the passage of 100 portions of magmatic fluid followed by 50 portions of recycled seawater.

tion. It grows rapidly and reaches about 1 Mt by the end of this stage. The concentrations of zinc and copper in the body are not high, no more than 0.7% Zn and 0.04% Cu. This base metal deficiency in the ore body is a consequence of the increased solution acidity. Magmatic fluids exiting from the channel show pH_T values of about 1.5 and are, therefore, undersaturated with respect to base metal sulfides, despite the rather high

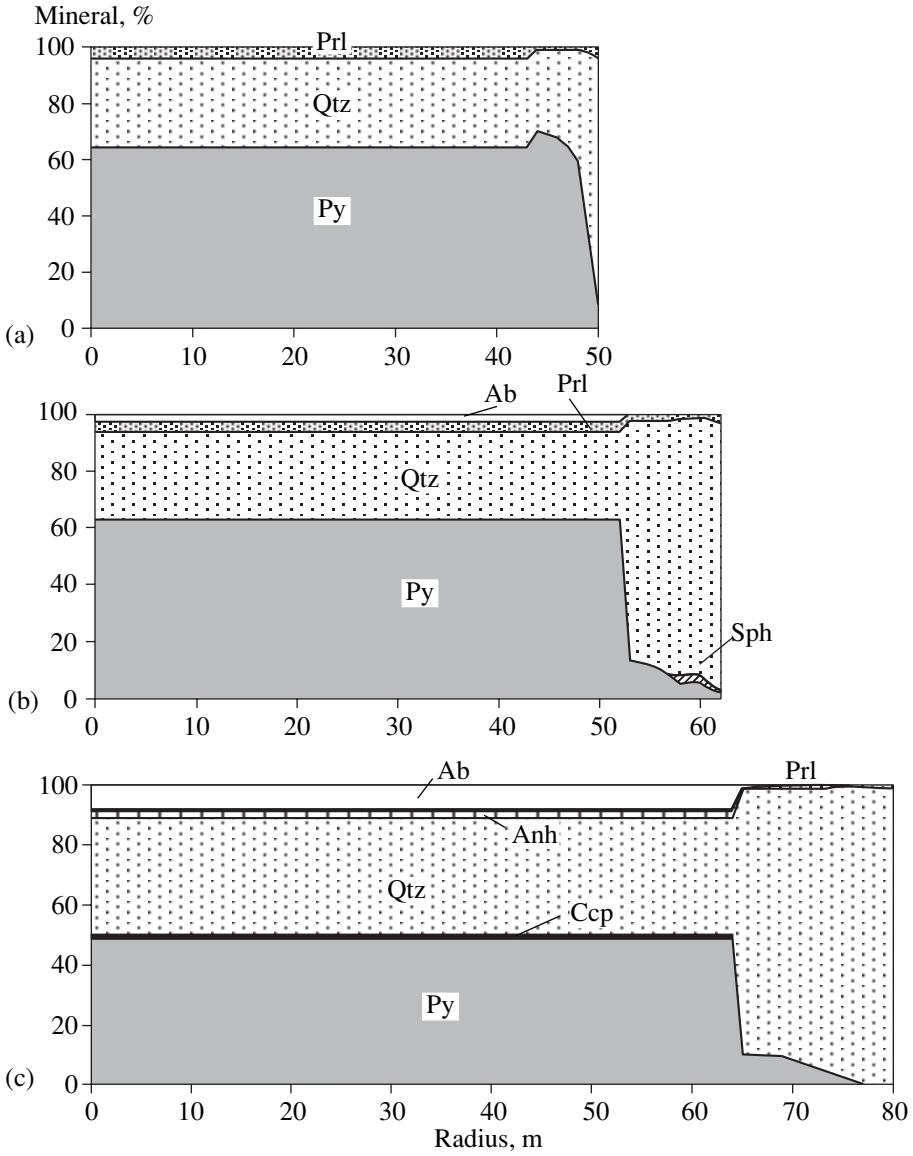

Fig. 66. Proportions of minerals in the radial cross-section of an ore body during various stages of its growth. (a) The end of the magmatic stage (computation step no. 100); (b) the beginning of the convective stage (computation step no. 300); and (c) the end of the convective stage (computation step no. 950).

concentrations of copper, zinc and sulfide sulfur in the solutions. The precipitation of these components begins only after considerable dilution of the fluid with seawater.[37]

When the ore-forming fluid changes from a magmatic to a recycling source, the character of the ore process also changes. The ore body grows several times more slowly during the recycling stage (Fig. 67a), and its composition changes dramatically. During computation step nos. 100–350, the ore body rapidly accumulates zinc extracted from the downwelling limb of the convection cell, and copper gain begins at step no. 720. Figures 66b and 66c show the composition of the ore body in the course of its growth. Zinc is mainly precipitated in the peripheral part of the ore body (Fig. 66b), whereas copper is accumulated in its hottest central zone. During the mature stage of development, zinc is gradually removed from the ore edifice, and magnetite appears near the channel mouth. Figure 66c shows zoning formed in the ore body by step no. 950.

7.4. Discussion

The simplified model developed in this chapter is based on a number of very approximate parameters, and the results of our simulation should be considered

[37] Another possible mechanism of neutralization is the metasomatic alteration of calcareous bottom sediments, but it is not considered in our model.

preliminary. Nonetheless, the following conclusions can be drawn from the qualitative results of calculations.

(1) Hydrothermal systems with different fluid sources will probably be significantly different in the character of metasomatic zoning around the feeder conduit. It should be least pronounced in the convective systems with small contributions from magmatic fluids.

The interaction of magmatic gas with country rocks forms a classic metasomatic column of acid leaching. Such columns are not common in massive sulfide deposits and were never reported from modern oceanic hydrothermal systems.

The mineral assemblages of ancient massive sulfide deposits were reproduced only when the model column of acid leaching was overprinted by the action of altered seawater.

(2) The magmatic and convection stages of ore body formation produce substantially different ore materials. The acid solutions of the magmatic stage rapidly form a pyrite–silica ore body, and the growth rate decreases significantly during the convection stage, when copper and, to a lesser extent, zinc are accumulated within the body.

In general, the available data do not contradict these conclusions, although there are some discrepancies.

As was noted in Section 4.2, there are only minor metasomatic alterations beneath the ore edifices on the oceanic floor, which is in agreement with the results of simulation. Drilling at the TAG hydrothermal site revealed a small zone of paragonitization directly beneath the body (Humphris *et al.*, 1998; Hannington *et al.*, 1998). Paragonite was never obtained in the model. Its development at the TAG field is probably related to the extensive process of subsurface mixing, which was not taken into account in the model. The zones of paragonite development were not documented in ancient massive sulfide occurrences.

The calculation of the model with magmatic fluids yielded pyrophyllite-bearing metasomatic assemblages. In natural deposits such assemblages are indicative of the conditions of intense acid leaching (*Metasomatism of...*, 1998). Pyrophyllite occurs sporadically as a minor component in ancient massive sulfide deposits, and its appearance is often connected with the presence of silicic rocks.

Monomineralic pyrite bodies deposited from acid solutions have not been found on the ocean floor. Such objects are known in ancient deposits (Franklin *et al.*, 1981). The sequential deposition of pyrite and base metal sulfides was suggested by many authors for massive sulfide deposits (e.g., Smirnov, 1982), but this problem is yet not fully resolved because of the difficulties of reconstructing ancient ore-forming processes.

The results of simulation allow us to suppose the following.

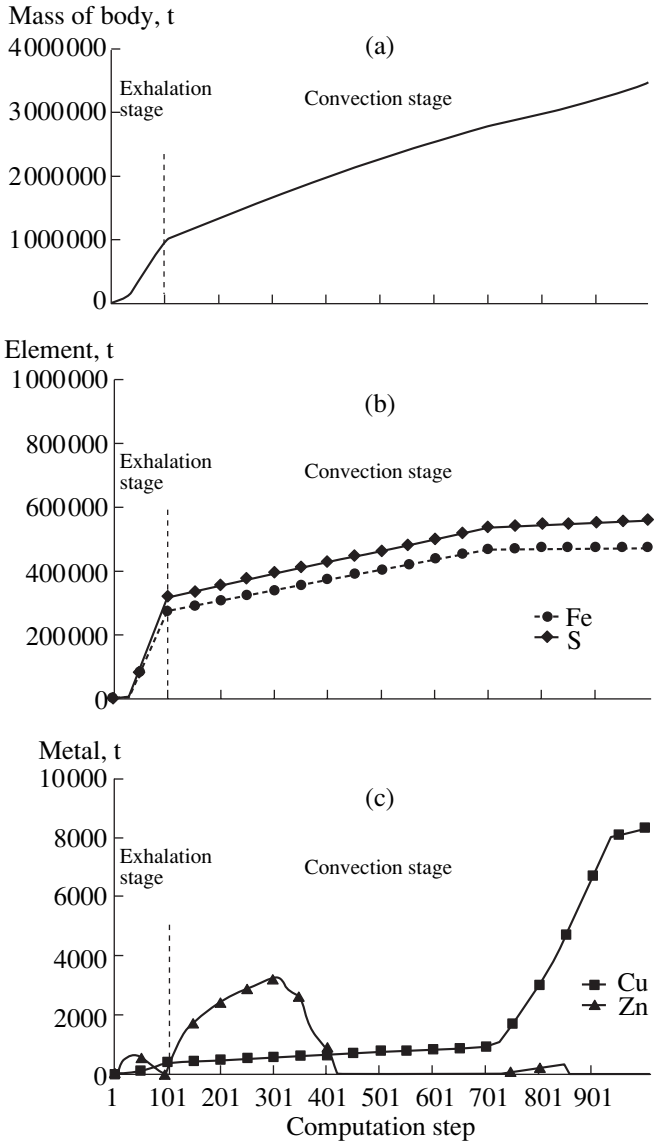

Fig. 67. Mass of a model ore body and quantitties of ore elements. (a) Total mass, (b) amounts of iron and sulfur, and (c) amounts of base metals.

(1) The footwall zoning of massive sulfide deposits could only be formed by the superposition of seawater convection on the products of the magmatic stage of system development. No single solution source (neither magmatic nor exogenous) could produce such a zoning in submarine hydrothermal systems.

(2) During the stage of exhalation activity, the ore body has a pyrite composition. Base metals are accumulated within it by the superposition of a convective recycling process. On the other hand, the major portion of sulfides is introduced into massive sulfide deposits during the magmatic stage.

These suggestions can be used as a starting point for future investigations of submarine hydrothermal systems with a combined fluid source.

CONCLUSIONS

The results obtained in Chapters 4 and 6 suggest that the ore-forming potential of hydrothermal systems depends on the concentration of ore elements in the solutions formed within them. The question of the factors controlling these concentrations is pivotal for the understanding of the geochemistry of oceanic ore mineralization.

The metal content of hydrothermal systems depends on diverse factors which may be interdependent. It is therefore difficult to discriminate the contributions of individual processes by the empirical generalization of natural data. Let us consider how such a problem can be resolved by a combined analysis of results obtained from the examination of natural objects, experimental data, and thermodynamic modeling.

The analysis of the logical scheme of oceanic hydrothermal systems (Section 3.2) showed that the main process responsible for the accumulation of ore elements in hydrothermal solutions is solution interaction with the country rocks. Hence, the conditions of water–rock interaction are the main factors that control the metal content in oceanic hydrothermal systems. The most important parameters are temperature, pressure, and the intensity of interaction (specified by the R/W ratio). The results of simulation (Section 4.1.2) suggest that the character of water–rock interaction changes during the evolution of a hydrothermal system, and, consequently, the lifetime of the system (τ) is also a very important factor. The occurrence of boiling within hydrothermal systems also influences the behavior of metals in solutions (Section 6.2), and the fraction of released gas (η) is a factor of metal concentration in such systems.

In addition to the aforementioned factors, a number of other parameters that could affect the behavior of metals in oceanic hydrothermal systems have been discussed in the literature. The possible role of magmatic gases in the supply of metals was addressed in Section 3.2, where we showed that this contribution is negligible in the hydrothermal systems of mid-ocean ridges. The composition of hydrothermal solutions can be affected by the composition of oceanic crustal materials. In the majority of oceanic hydrothermal systems studied, water reacts with rather homogeneous sequences of tholeiitic basalts, which show little chemical variation.[38]

Each of the three sources of information (natural data, experiments, and computer simulation) relevant to the problem considered has certain advantages and disadvantages.

Observations of natural objects provide the most valuable evidence. A considerable body of data has been accumulated to date on the chemical composition of hydrothermal solutions from submarine systems. The interpretation of these data must allow for the fact that only solutions discharged on the ocean floor are available for analysis, whereas the metals are extracted from rocks into the solution in deep parts of the system. The solution may lose some of its ore components on the way to the surface. The contributions of these factors cannot be directly measured, because they operate in the interior part of the system. They have to be reconstructed, and while such reconstructions are reliable for T and R/W, other factors require some assumptions.

The experimental simulation of seawater–basalt interaction allows characterization of the process under controlled conditions (T, P, and η). This approach provides unbiased data independent of the knowledge of the interaction mechanism. The experimental equipment that was used in the majority of recent studies (autoclaves allowing liquid sampling during the experiment) minimizes systematic errors. However, the interpretation of experimental data must account for the following points: (a) the time span of the natural process (τ) cannot be reproduced in experiments; (b) the available equipment is designed for static experiments, whereas the natural hydrothermal systems are of a flow-through character; and (c) the experimental results do not always correspond to the target R/W values, and the synthetic assemblages of secondary minerals are not fully consistent with natural ones (Section 3.2).

The thermodynamic modeling of hydrothermal systems provides unique opportunities for solving the problem, because all the factors in question are prescribed as model parameters. It allows the evaluation of the role of each factor separately, while keeping all other parameters constant, which is practically impossible by other methods. However, thermodynamic modeling is most sensitive to the completeness and quality of our knowledge on the geochemical processes occurring in hydrothermal systems. Nonetheless, a comparison of the results obtained by computer simulation with the characteristics of natural objects showed adequate agreement with respect to a wide range of parameters (Section 4.4).

From the above considerations, it is evident that the possible shortcomings and difficulties of interpretation of various sources of information are mutually independent and uncorrelated. An important consequence of this result is that the robustness of a conclusion increases substantially if it is drawn by fundamentally different methods.

Influence of temperature on the concentration of metals in oceanic hydrothermal systems. According to natural observations, the highest concentrations of ore elements are characteristic of the hottest black smokers (Table 6), whose measured discharge temperature is almost always higher than 300°C. Colder white and transparent smokers with temperatures below 300°C show much lower concentrations of ore metals. How-

[38] The role of hydrothermal solution interaction with sedimentary rocks overlying basaltic sequences and the participation of ultrabasic rocks in the generation of metal concentrations in hydrothermal systems should be addressed in future studies.

ever, this relationship does not necessarily reflect the character of processes in the interior part of hydrothermal systems but may be related to the discharge conditions on the ocean floor. White and black smokers often occur in close proximity and probably have a common deep source. Strictly speaking, the natural data are only indicative of the decreasing transportation capacity of hydrothermal solutions during their cooling. However, since the transportation of hydrogen sulfide together with heavy metals in a hydrothermal solution is possible only at high temperatures, extensive ore generation can be achieved only in high-temperature systems (probably, higher than 300°C in the interior parts).

The experimental investigation of seawater–basalt interaction provides compelling evidence that an increase in T intensifies the mobilization of ore metals from rocks. Figure 68a shows the experimental results by Seyfried and Janecky (1985), which were obtained holding all other interaction factors constant (P = 400 bar and R/W = 1). The concentrations of ore metals in the experimental fluids appeared to be similar to those of natural hydrothermal solutions at T = 375–400°C.

The results of simulation (Fig. 68b) support this inference. At high R/W, while sulfides are present in the solid phase, the equilibrium concentrations of heavy metals in the model solutions increase with increasing temperature.

There is no such effect at low R/W, because base metals are completely extracted from the basalts and their concentrations are functions of R/W only (however, the low-R/W range probably does not play a significant role in the formation of ore-forming solutions in the natural systems considered).

The explanation of the temperature dependency of ore metal concentrations is straightforward. At high temperatures the degree of base metal complexation (primarily with the chloride ion) rises and this enhances the solubility of sulfides and the mobility of heavy metals.

Influence of pressure. Natural observations are not sufficient to reveal the influence of this factor. Most of the hydrothermal systems studied are situated at the axis of the EPR, where the ocean is about 2.5 km deep, and their magma chambers probably occur at approximately equal depths. This parameter is different for the systems of the Mid-Atlantic Ridge (about 3.6 km deep) and Axial Seamount of the Juan de Fuca Ridge (about 1.5 km deep), but these systems are distinguished from those of the EPR by other important characteristics. In particular, the hydrothermal system of Axial Seamount shows evidence of boiling.

Experimental data indicate that, in general, pressure has a relatively weak effect on water–basalt interaction, except for the P–T region near the critical point of water (T = 370–400°C and P < 500 bar). According to the experiments by Seyfried and Janecky (1985), a pressure decrease within this region provides extensive mobilization of heavy metals. Figure 69a shows experimental

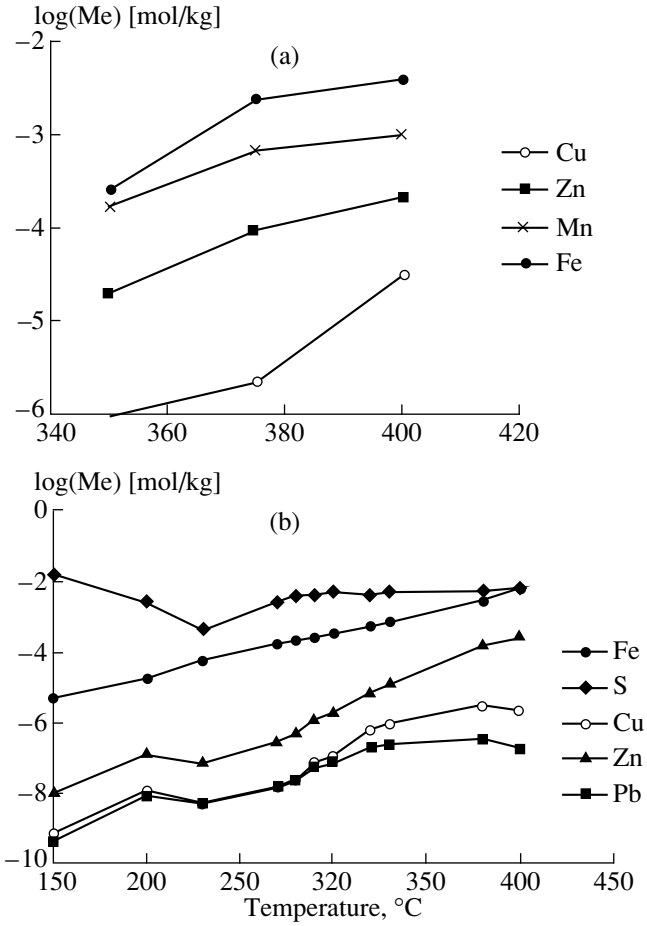

Fig. 68. Influence of temperature on the concentration of ore elements in solutions from the interior part of a hydrothermal system. (a) The experiments of Seyfried and Janecky (1985) at P = 400 bar and R/W = 1 and (b) the results of calculations at P = 500 bar and R/W = 0.3.

results (Mottl *et al.*, 1979; Rosenbauer and Bischoff, 1983; Seyfried and Janecky, 1985) obtained at various pressures holding other experimental parameters constant (T = 400°C and R/W =1).

The results of thermodynamic modeling (Fig. 69b) reveal the same tendency for Fe and Zn.[39]

This correlation is related to a dramatic change in the physicochemical properties of water (primarily, its dielectric constant) in the near-critical region. The decrease of the dielectric constant toward P_{cr} stabilizes complex compounds in the solution (Ryzhenko, 1981). As a result, the solubility of heavy metal sulfides increases strongly. Far from the critical point, the influence of P on the properties of water is negligible.

Influence of the rock/water ratio. The R/W values of the hydrothermal systems studied vary over a relatively

[39] The pressure dependency of the thermodynamic properties of Cu and Pb compounds is not well constrained at high temperatures.

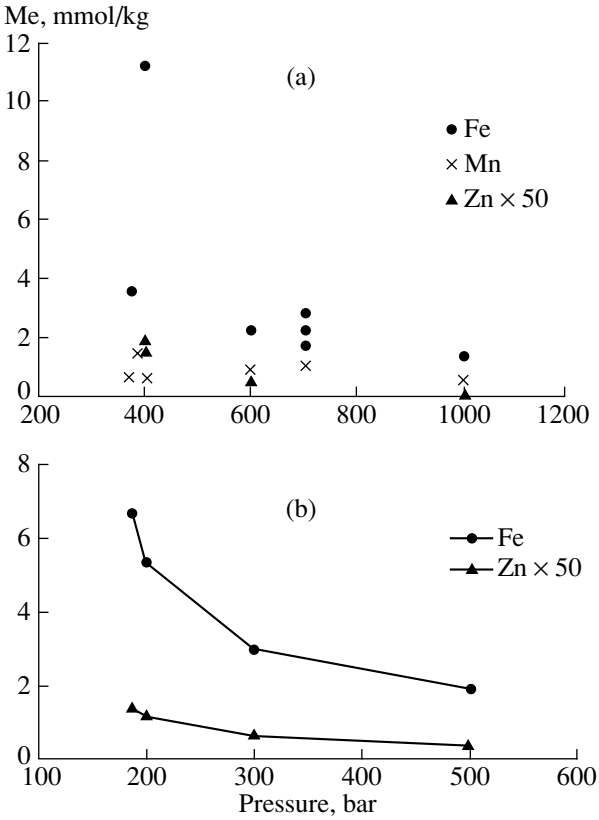

Fig. 69. Effect of pressure on the concentration of ore elements in hydrothermal solutions. (a) The experiments of Mottl *et al.* (1979), Rosenbauer and Bischoff (1983), and Seyfried and Janecky (1985) at $T = 400°C$ and $R/W = 1$; and (b) the results of calculations at $T = 400°C$ and $R/W = 0.6$.

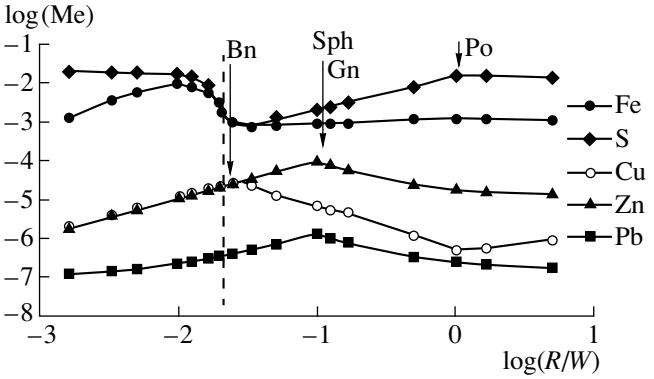

Fig. 70. Concentrations of ore elements as functions of the bulk rock/water ratio. Thermodynamic calculations at $T = 350°C$ and $P = 500$ bar. The dashed line shows the change from metasomatic assemblage I (oxidized, Mg-Chl + Hem + Anh + Qtz) to assemblage II (reduced, Ep + Fe-Chl + Act + Ab +…), and the arrows mark the appearance of ore metal sulfides in the assemblage.

narrow range from 0.5 to 2.0 (Tables 16, 17). The *R*/*W* estimates for individual systems differ, but the uncertainties of these estimates are comparable with the variations between the systems. The influence of this factor on the metal content of hydrothermal systems cannot yet be estimated from natural observations. According to Bowers *et al.* (1988), the compositions of solutions in the systems studied are independent of *R*/*W*, because they are buffered by the mineral associations of the country rocks in high-temperature zones (rock-dominated systems).

In an early experimental study, Seyfried and Mottl (1982) demonstrated that the concentrations of ore metals depend on the regime of water–basalt interaction. Low *R*/*W* values in water-dominated systems result in a higher metal content compared with those generated in rock-dominated systems with high *R*/*W*. According to their results, the boundary between the two regimes lies at an *R*/*W* value between 0.02 and 0.1. Most of the subsequent experimental studies were performed at higher *R*/*W* values (>0.1), which are closer to the conditions in active hydrothermal systems. The studies that included a series of kinetic experiments showed that the concentrations of heavy metals were high at the beginning of experiments (when the effective *R*/*W* was small) and decreased toward the steady-state stage. However, it is still unclear what the role is of sorption and incongruent dissolution of solid phases during the initial stage, and what can these results tell us about the conditions of natural processes?

The thermodynamic modeling supported the conclusions of Seyfried and Mottl (1982). Figure 70 shows the calculated dependency of the concentrations of ore metals on the cumulative *R*/*W* ratio during water–basalt interaction. In the model with low *R*/*W*, the metals are completely mobilized owing to oxidation processes. Their concentrations in the solution show a positive correlation with the amount of rock participating in the reaction. When the system reaches a certain *R*/*W* value, it becomes reduced, and H_2S appears in the solution and precipitates heavy metal sulfides. This results in a negative correlation between metal concentrations and *R*/*W* at high *R*/*W* values. Thus, the concentration of heavy metals passes through a maximum at *R*/*W* = 0.03–0.1. The concentration of iron in the solution also reaches a maximum value when assemblage I (hematite + chlorite + …) is changed to assemblage II (epidote + Fe-chlorite + actinolite + …). In contrast, the bulk sulfur content shows a minimum corresponding to the change of its migration forms from S^{VI} at low $\Sigma R/W$ to S^{II} at high $\Sigma R/W$. The results of our simulation suggest that each chalcophile element shows a change in the character of *R*/*W* dependency when its own sulfide appears in the phase association. Thus, the concentrations of these elements in solution are indirectly related to the type of the system (fluid-dominated or rock-dominated), through H_2S accumulation in the solution.

Influence of the lifetime of a hydrothermal system. As was noted in Section 3.1, the investigation of oceanic hydrothermal ores (Krasnov, 1990; *Hydrothermal Sulfide…*, 1992) showed that small, short-lived sulfide edifices are usually significantly enriched in Zn,

whereas large long-lived bodies comprising megatons of sulfides are distinguished by high copper concentrations. However, the available natural observations are not sufficient to reliably estimate the influence of the lifetime of a hydrothermal system on the composition of its solutions. For instance, the major-element composition of solutions from a long-lived hydrothermal system of the TAG field is similar to that of solutions from the EPR systems (Table 6).

There is no experimental evidence for the influence of the lifetime of systems on the composition of their solutions.

Our thermodynamic modeling showed that heavy metals are fractionated during prolonged convective circulation owing to metasomatic phenomena in the interior parts of hydrothermal systems (Section 4.1.2). The more mobile Zn and Pb are intensely removed by the first hydrothermal solutions (Fig. 27), whereas Cu is retained in the rock in relatively less soluble sulfides (chalcopyrite and bornite). In the course of prolonged system evolution, the mobility of Cu begins to increase in response to S^{II} removal from the rock, and the late portions of hydrothermal solutions are copper-rich. This model result is in agreement with the aforementioned correlation between the geochemical signature of sulfide bodies and the lifetime of hydrothermal systems. It is also supported by the relative Cu enrichment in the solutions from the long-lived TAG system (Edmond *et al.*, 1995).

Influence of boiling. As was shown in Section 6.2, the available natural data indicate that boiling within hydrothermal systems increases the concentrations of ore metals in hydrothermal solutions (Fig. 52). Low-salinity hydrothermal vents are formed simultaneously. They are enriched in hydrogen sulfide and other volatiles and depleted in metals. These phenomena are related to phase separation in the interior parts of the system. The metal-rich smokers discharge residual brine, and the freshened solutions contain an admixture of the condensed vapor phase.

Boiling in contact with a rock was experimentally studied by Bischoff and Rosenbauer (1987) under *P–T* conditions similar to those of oceanic hydrothermal systems (Table 25). The results of their experiments showed that boiling promotes extensive mobilization of chalcophile elements from rocks.

Our thermodynamic modeling of boiling hydrothermal solutions in the focus of a hydrothermal system is in agreement with these experiments. As can be seen from the results of the simulation of isothermal boiling in contact with a rock (Section 6.4.1), an increase in the fraction of the vapor phase is accompanied by sulfide dissolution in the rock and metal accumulation in the solution. The analysis of our model results suggests that the main reason for the mobilization of chalcophile elements is H_2S partitioning from solution into the vapor phase and the corresponding shift of sulfide equilibria to dissolution.

Table 34. Influence of various factors on the metal concentrations in oceanic hydrothermal systems

Factor	Natural observations	Experiments	Thermodynamic modeling
Temperature	+	+	+
Pressure (outside the boiling zone)	i.i.	–	–
Boiling	Fe, Zn+	Cu, Zn+	+
Rock/water ratio			
—outside the boiling zone	i.i.	maximum between 0.02 and 0.1	maximum between 0.025 and 0.1
—during boiling	i.i.	i.i.	+
Lifetime of the hydrothermal system	(+)	i.i.	Cu+ Zn, Pb, S–

Note: The plus and minus signs denote an increase and a decrease in metal content in response to the increase of the factor, respectively; i.i. means insufficient information; and values in parentheses show estimates.

An important feature of the thermodynamic model including boiling is the change of the role of the *R*/*W* ratio. If there is no boiling, the equilibrium concentrations of heavy metals decrease in the solution with increasing *R*/*W* (at $R/W > 0.1$) owing to the accumulation of H_2S in it (Fig. 70). This effect is completely eliminated by boiling owing to H_2S partitioning into the vapor phase. The larger the amount of rock interacting with heterogeneous fluid (vapor + water), the higher the degree of ore metal mobilization. Therefore, the metal content of hydrothermal solutions from boiling systems must increase with increasing *R*/*W* value.

Thus, the comparative analysis of natural and experimental data and computer simulation allowed us to evaluate the influence of *T*, *P*, *R*/*W*, τ, and η on the metal concentrations in oceanic hydrothermal systems. The results of this analysis are summarized in Table 34.

As can be seen in this table, all the aforementioned sources of information give identical results. Since all the methods are mutually independent and the possible uncertainties of these methods are uncorrelated, such an agreement supports the reliability of the results. This allows us to state the following.

(1) An increase in temperature within the system is favorable for the accumulation of ore metals in the hydrothermal solutions.

(2) If near critical conditions are maintained in the interior parts, the metal content is higher in lower pressure systems (and other parameters are equal), i.e., when the roof of the magma chamber is situated at shallower levels.

(3) The maximum removal of metals from basalts is attained at $R/W \approx 0.03$. An increase in *R*/*W* above 0.1 reduces the mobility of ore metals.

(4) Boiling in the interior parts of hydrothermal systems enhances the removal of heavy metals.

(5) An increase in the duration of hydrothermal activity must result in a relative copper enrichment in the solutions, which is reflected in the geochemical signature of the ore bodies.

It should be noted that the method of thermodynamic modeling appeared to be the most informative among the approaches used to distinguish the factors of metal accumulation in hydrothermal systems (Table 34).

The following **general conclusions** were drawn from the results of this study.

(1) A complex method for thermodynamic modeling was developed in this study on the basis of the principle of a step flow reactor. This method allows for the description of all major geochemical processes in submarine hydrothermal systems. A comprehensive geochemical model was constructed for an ore-forming oceanic system from the formation of hydrothermal solution in the downwelling limb of the convection cell to ore deposition during solution discharge on the ocean floor. The results of computer simulation are consistent with the natural prototypes in a variety of characteristics, including metasomatic and ore mineral assemblages and the chemical and isotopic compositions of solutions. This enables the use of our model for the prediction of the behavior of elements in natural systems.

(2) The alteration of seawater in the downwelling limb of the convection cell occurs when water passes through the regions of two mineral assemblages: (I) oxidized (chlorite + hematite + anhydrite + quartz + …) and (II) reduced (chlorite + epidote + actinolite + albite + sulfides + …), which show fundamentally different behaviors of major and trace elements. The position of the boundary between these regions depends on the input–output budget of the components. A prolonged influx of seawater into the system changes its bulk chemical composition and shifts the oxidation front to higher temperatures, which results in the time evolution of hydrothermal solutions produced by the system.

(3) The ore metals are extensively extracted from the region of assemblage I and are weakly mobile in the region of assemblage II because of sulfide precipitation. The sequence of element mobility in oceanic hydrothermal environments is $S^{II} > Pb > Zn > Cu > Fe$. The metallogenic signature of solutions changes during their evolution from Zn > Cu to Cu > Zn. The reason for this inversion is the different rates of Zn and Cu removal from the interior parts of the system. This explains the observed discrimination of sulfide edifices on the ocean floor into zinc- and copper-dominated ones and the confinement of the latter to long-lived systems in slow-spreading ridges and volcanic seamounts.

(4) The physicochemical mechanism of formation of large sulfide bodies includes (a) the evolution of parent solutions, (b) ore deposition during mixing with seawater, and (c) the metasomatic redeposition of matter within the edifice. Such a scenario produces a zoned ore body, whose structure and metallogenic signature change with time. The early stages of this evolution correspond to the known active vents on the ocean floor. The mature stages of evolution yield massive sulfide ore bodies, whose structures and compositions are similar to those of ancient ore occurrences on continents.

(5) A thermodynamic model was constructed on the basis of the method of an isotopic chemical system for sulfur isotopes. It showed that the sulfur isotopic systematics of convective hydrothermal systems in the ocean are controlled by the mixing of sulfur from two isotopically different sources, seawater and basalt. The main characteristic is the regular increase in the $\delta^{34}S$ value of a solution over the lifetime of the system. This explains the observed variations in the isotopic compositions of oceanic sulfides, including the different isotopic signatures of small and large ore bodies and the ^{34}S enrichment of dissolved hydrogen sulfide compared with sulfides from the ore body.

(6) Boiling within oceanic hydrothermal systems is favorable for the concentration of metals in hydrothermal solutions. Phase separation in solution results in the partitioning of metals and hydrogen sulfide into different phases and an increase in the solubility of sulfides in heterogeneous systems (mechanism of precipitant loss). This effect must evidently be manifested for any elements with a sulfide form of precipitation and nonsulfide forms of solution transfer. Hence, boiling increases the ore-generating potentials of hydrothermal systems. The cooling and condensation of heterogeneous fluids during their submarine discharge can produce considerable amounts of sulfide deposits. They differ from the ores formed by cooling of homogeneous fluids in having a higher fraction of heavy metals.

In accordance with the classification of simulation problems proposed in Section 1.1, conclusion (1) corresponds to type II problems (internal with respect to the method), and conclusions (2)–(6) are related to type II problems (external with respect to the method). Conclusions (3)–(5) provide solutions to the problems of functional relationships between the known properties of the object studied, and conclusions (2) and (6) predict the properties of natural objects. We believe that further progress in the thermodynamic modeling of natural geochemical processes will result in a higher fraction of predictive results, which are most valuable for the development of geochemistry.

REFERENCES

1. E. E. Abramova and D. V. Grichuk, "Computational Thermodynamic Model of the Recycled Hydrothermal System," Rudy Metally, No. 2, 36–44 (1994).
2. V. A. Akimtsev, V. N. Sharapov, V. Yu. Kolobov, *et al.*, "Hydrothermal Mineralization of Mid-Atlantic Ridge

in the Zone of Its Junction with the Green Cape Transform Fault," Geol. Geofiz., No. 8, 32–37 (1991).

3. N. N. Akinfiev, "A Method for the Computation of Ore Deposition from Boiling Fluid: Accounting for Dielectric Constant," Geokhimiya, No. 10, 1465–1478 (1994).
4. F. Albarede, A. Michard, J. F. Minster, and G. Michard, "$^{87}Sr/^{86}Sr$ Ratios in Hydrothermal Waters and Deposits from the East Pacific Rise at 21° N," Earth Planet. Sci. Lett. **55**, 229–236 (1981).
5. V. A. Alexeyev, "Dynamic Model of Infiltration Metasomatism Based on the Calculation of Local Equilibria," Geokhimiya, No. 9, 1311–1320 (1985).
6. A. I. Almukhamedov, G. L. Kashintsev, and V. V. Matveenkov, *Evolution of Basaltic Volcanism in the Red Sea Region* (Nauka, Novosibirsk, 1985) [in Russian].
7. J. C. Alt, "The Chemistry and Sulfur Isotopic Composition of Massive Sulfide and Associated Deposits on Green Seamount, Eastern Pacific," Econ. Geol. **83**, 1026–1033 (1988).
8. J. C. Alt and W. C. Shanks, III, "Serpentinization of Abyssal Peridotites from the MARK Area, Mid-Atlantic Ridge: Sulfur Geochemistry and Reaction Modeling," Geochim. Cosmochim. Acta **67**, 641–653 (2003).
9. J. C. Alt, J. Honnorez, H.-W. Hubberten, and E. Saltzman, "Occurrence and Origin of Anhydrite from Deep Sea Drilling Project Leg 70, Hole 504B, Costa Rica Rift," Deep Sea Drill. Project: Initial Rep. **69**, 547–550 (1983).
10. J. C. Alt, P. Lonsdale, R. Haymon, and K. Muechlenbachs, "Hydrothermal Sulfide and Oxide Deposits on Seamounts near 21° N, East Pacific Rise," Bull. Geol. Soc. Am. **98**, 157–168 (1987).
11. J. C. Alt, T. E. Anderson, and L. Bonell, "The Geochemistry of Sulfur in a 1.3 km Section of Hydrothermally Altered Oceanic Crust, DSDP Hole 504B," Geochim. Cosmochim. Acta **53**, 1011–1023 (1989).
12. J. Alvarez, R. Crovetto, and R. Fernandez-Prini, "The Dissolution of N_2 and H_2 in Water from Room Temperature to 640 K," Ber. Bunsen-Ges. Phys. Chem. **92**, 935–940 (1988).
13. R. N. Anderson, J. C. Alt, J. Malpas, *et al.*, "Geochemical Well Logging in Basalts: The Palisades Sill and the Oceanic Crust of Hole 504B," J. Geophys. Res. **95**, 9265–9292 (1990).
14. M. Arnold and S. M. F. Sheppard, "East Pacific Rise at Latitude 21° N: Isotopic Composition and Origin of the Hydrothermal Sulfur," Earth Planet. Sci. Lett. **56**, 148–156 (1981).
15. Yu. A. Averkin, "Dynamics of Sulfide Deposition from Hydrothermal Solution in the Process of CO_2 Boiling off," Geokhimiya, No. 11, 1580–1586 (1987).
16. R. D. Ballard and J. Francheteau, "The Relationship between Active Sulfide Deposition and the Axial Processes of the Mid-Ocean Ridge," Mar. Technol. Soc. Japan **16** (3), 8–22 (1982).
17. L. A. Bannikova, *Organic Matter in Hydrothermal Ore Formation* (Nauka, Moscow, 1990) [in Russian].
18. L. A. Bannikova and B. N. Ryzhenko, "Isotopic Ratios of Carbon and Sulfur in the Products of Redox Reactions inunder Hydrothermal Conditions: The System CH_4–Na_2SO_4–NaCl–H_2O," Geokhimiya, No. 9, 1268–1281 (1984).
19. L. A. Bannikova, D. V. Grichuk, and B. N. Ryzhenko, "Calculation of Chemical and Isotopic Equilibria in the C–H–O System and Their Application to a Study of Redox Reactions in Hydrothermal Systems," Geokhimiya, No. 3, 416–428 (1987).
20. Vikt. L. Barsukov and M. V. Borisov, "Simulation of Geochemical Consequences of Selfmixing Hydrothermal Solutions: 1. Mass Transfer at the Spreading Areas of Flows of Hydrothermal Solutions," Geokhimiya, No. 8, 1108–1123 (1982a).
21. Vikt. L. Barsukov and M. V. Borisov, "Simulation of Geochemical Consequences of Selfmixing Hydrothermal Solutions: 2. Mass Transfer at the Areas of Constriction of Flows of Hydrothermal Solutions," Geochem. Int. **19** (5), 26–36 (1982b).
22. R. Becker, M. G. Langseth, R. P. Von Herzen, and R. N. Anderson, "Deep Crustal Geothermal Measurements, Hole 504B, Costa Rica Rift," J. Geophys. Res. **88**, 3447–3457 (1983).
23. V. M. Belyi, A. A. Migdisov, N. V. Barskaya, and V. A. Grinenko, "Redistribution of Sulfur and Its Isotopes in Hydrothermally Altered Oceanic Basalts, Costa Rica Rift, Hole 504B," Geokhimiya, No 3, 390–402 (1984).
24. M. E. Berndt and W. E. Seyfried, Jr., "Boron, Bromine, and Other Trace Elements as Clues to the Fate of Chlorine in Mid-Ocean Ridge Vent Fluids," Geochim. Cosmochim. Acta **54**, 2235–2245 (1990).
25. M. E. Berndt and W. E. Seyfried, Jr., "Calibration of Br/Cl Fractionation during Subcritical Phase Separation of Seawater: Possible Halite at 9 to 10° N East Pacific Rise," Geochim. Cosmochim. Acta **61**, 2849–2854 (1997).
26. D. Bideau, Y. Fouquet, and R. Hekinian, "Decouverte de basaltes metamorphises dans le graben axial de la dorsale Est-Pacifique a 12°50′ N," Soc. Geol. Fr. Bull. **1**, 905–913 (1985).
27. R. A. Binns and S. D. Scott, "Actively Forming Polymetallic Sulfide Deposits Associated with Felsic Volcanic Rocks in the Eastern Manus Back-Arc Basin, Papua New Guinea," Econ. Geol. **88**, 2226–2236 (1993).
28. D. K. Bird and H. C. Helgeson, "Chemical Interaction of Aqueous Solutions with Epidote–Feldspar Mineral Assemblages in Geological Systems: I. Thermodynamic Analysis of Phase Relations in the System CaO–FeO–Fe_2O_3–Al_2O_3–SiO_2–H_2O–CO_2," Am. J. Sci. **280**, 907–910 (1980).
29. J. L. Bischoff and F. W. Dickson, "Seawater–Basalt Interaction at 200°C and 500 bars: Implication for Origin of Sea-Floor Heavy-Metal Deposits and Regulation of Seawater Chemistry," Earth Planet. Sci. Lett. **25**, 385–397 (1975).
30. J. L. Bischoff and K. S. Pitzer, "Phase Relations and Adiabats in Boiling Seafloor Geothermal Systems" Earth Planet. Sci. Lett. **75**, 327–338 (1985).
31. J. L. Bischoff and K. S. Pitzer, "Liquid–Vapor Relations for the System NaCl–H_2O: Summary of the *P–T–x* Surface from 300° to 500°C," Am. J. Sci. **289**, 217–248 (1989).

32. J. L. Bischoff and R. J. Rosenbauer, "Phase Separation in Seafloor Geothermal Systems: An Experimental Study of the Effects on Metal Transport," Am. J. Sci. **287**, 953–978 (1987).
33. J. L. Bischoff and R. J. Rosenbauer, "Liquid–Vapor Relation in the Critical Region of the System NaCl–H_2O from 380° to 415°C: A Refined Determination of the Critical Point and Two-Phase Boundary of Seawater," Geochim. Cosmochim. Acta **52**, 2121–2126 (1988).
34. J. L. Bischoff and R. J. Rosenbauer, "Phase Separation in Seafloor Geothermal Systems by Layered Double-Diffusive Convection," J. Geol. **97**, 613–623 (1989).
35. J. L. Bischoff and W. E. Seyfried, Jr., Hydrothermal Chemistry of Seawater from 25° to 350°C", Am. J. Sci. **278**, 838–860 (1978).
36. J. L. Bischoff, A. S. Radtke, and R. J. Rosenbauer, "Hydrothermal Alteration of Graywacke by Brine and Seawater: Roles of Alteration and Chloride Complexing on Metal Solubilization at 200° and 350°C," Econ. Geol. **76**, 659–676 (1981).
37. J. L. Bischoff, R. J. Rosenbauer, and K. S. Pitzer, "The system NaCl–H_2O: Relation of Vapor–Liquid near the Critical Temperature of Water and of Vapor–Liquid–Halite from 300° to 500°," Geochim. Cosmochim. Acta **50**, 1437–1444 (1986).
38. J. L. Bischoff, R. J. Rosenbauer, and R. O. Fournier, "The Generation of HCl in the System $CaCl_2$–H_2O: Vapor–Liquid Relations from 380° to 500°C," Geochim. Cosmochim. Acta **60**, 7–16 (1996).
39. C. W. Blownt and F. W. Dickson, "The Solubility of Anhydrite ($CaSO_4$) in NaCl–H_2O from 100 to 450°C and 1 to 1000 bars," Geochim. Cosmochim. Acta **33**, 227–245 (1969).
40. G. J. Bluth, and H. Ohmoto, "Sulfide–Sulfate Chimneys on the East Pacific Rise, 11° and 13° N Latitudes: II. Sulfur Isotopes," Can. Mineral. **26**, 505–515 (1988).
41. Yu. A. Bogdanov, *Hydrothermal Deposits of the Mid-Atlantic Ridge Rifts* (Nauchnyi Mir, Moscow, 1997) [in Russian].
42. Yu. A. Bogdanov, N. S. Bortnikov, I. V. Vikent'ev, *et al.*, "A New Type of Modern Mineral-Forming System: Black Smokers of the Hydrothermal Field at 14°45′ N Latitude, Mid-Atlantic Ridge," Geol. Rudn. Mestorozhd. **39**, 58–78 (1997a) [Geol. Ore Depos. **39**, 68–90 (1997a)].
43. Yu. A. Bogdanov, N. S. Bortnikov, and A. P. Lisitsin, "The Origin of Hydrothermal Sulfide Ores in the Axial Parts of the Mid-Atlantic Ridge," Geol. Rudn. Mestorozhd. **39**, 351–370 (1997b) [Geol. Ore Depos. **39**, 409–429 (1997b)].
44. M. V. Borisov, "Geochemical and Thermodynamic Models for the Genesis of Low and Medium Temperature Vein Mineralization and Metasomatism in Wall Rocks," Geochem. Int. **41** (Suppl. 2), S145–S312 (2003).
45. M. V. Borisov and I. L. Khodakovskii, "On the Problem of Error Identification in Physicochemical Modeling," Geokhimiya, No. 6, 907–908 (1989).
46. M. V. Borisov and Yu. V. Shvarov, *Thermodynamics of Geochemical Processes* (Mosk. Gos. Univ., Moscow, 1992) [in Russian].
47. N. S. Bortnikov, D. T. Fedorov, and K. G. Muraviov, "Mineral Composition and Formation Conditions of Sulfide Deposits in the Lau Basin, Southwestern Pacific," Geol. Rudn. Mestorozhd. **35**, 528–544 (1993).
48. Y. Bottinga and M. Javoy, "MORB Degassing: Evolution of CO_2," Earth Planet. Sci. Lett. **95**, 215–225 (1989).
49. T. S. Bowers, "Stable Isotope Signatures of Water–Rock Interaction in Mid-Ocean Ridge Hydrothermal Systems: Sulfur, Oxygen, and Hydrogen," J. Geophys. Res. **94**, 5775–5786 (1989).
50. T. S. Bowers, "The Deposition of Gold and Other Metals: Pressure-Induced Fluid Immiscibility and Associated Stable Isotope Signatures," Geochim. Cosmochim. Acta **55**, 2417–2434 (1991).
51. T. S. Bowers and H. P. Taylor, "An Integrated Chemical and Stable-Isotope Model of the Origin of Mid-Ocean Ridge Hot Spring Systems," J. Geophys. Res. **90**, 12 583–12 606 (1985).
52. T. S. Bowers, K. L. Von Damm, and J. M. Edmond, "Chemical Evolution of Mid-Ocean Ridge Hot Springs," Geochim. Cosmochim. Acta **49**, 2239–2252 (1985).
53. T. S. Bowers, A. C. Campbell, C. I. Measures, *et al.*, "Chemical Controls on the Composition of Vent Fluids at 13°–11° N and 21° N, East Pacific Rise," J. Geophys. Res. **93**, 4522–4536 (1988).
54. T. Brikovski and D. Norton, "Influence of Magma Chamber Geometry on Hydrothermal Activity at Mid-Ocean Ridges," Earth Planet. Sci. Lett. **93**, 241–255 (1989).
55. O. V. Bryzgalin, "Some Strong Electrolytes in the Supercritical Field: Estimation of Dissociation Constants Based of the Electrostatic Model," Geokhimiya, No. 8, 1184–1195 (1985).
56. D. A. Butterfield and G. J. Massoth, "Geochemistry of North Cleft Segment Vent Fluids: Temporal Changes in Chlorinity and Their Possible Relation to Recent Volcanism," J. Geophys. Res. **99**, 4951–4968 (1994).
57. D. A. Butterfield, G. J. Massoth, R. E. McDuff, *et al.*, "Geochemistry of Hydrothermal Fluids from Axial Seamount Hydrothermal Emission Study Vent Field, Juan De Fuca Ridge: Subseafloor Boiling and Subsequent Fluid–Rock Interaction," J. Geophys. Res. **95**, 12 895–12 921 (1990).
58. D. A. Butterfield, R. E. McDuff, M. J. Mottl, *et al.*, "Gradients in the Composition of Hydrothermal Fluids from the Endeavour Segment Vent Field: Phase Separation and Brine Loss," J. Geophys. Res. **99**, 9561–9583 (1994).
59. G. Yu. Butuzova, "On the Sources of Substances in the Hydrothermal–Sedimentary Ore Formation: I. Sources of Water, Gases, Sulfur, and the Generation of Major Salt Composition of Ore-Forming Solutions," Litol. Polezn. Iskop., No. 5, 3–18 (1986a).
60. G. Yu. Butuzova, "On the Sources of Substances in the Hydrothermal–Sedimentary Ore Formation: II. Sources of Ore-Forming Elements," Litol. Polezn. Iskop., No. 6, 3–18 (1986b).
61. A. Yu. Bychkov, Candidate's Dissertation in Geology and Mineralogy (MGU, Moscow, 1995).

62. A. Yu. Bychkov and D. V. Grichuk, "A Thermodynamic Model for the Sb–As Mineralization in the Uzon Caldera," Geokhimiya, No. 4, 527–538 (1991).

63. C. D. Byers, D. W. Muenow, and M. D. Garcia, "Volatiles in Basalts and Andesites from the Galapagos Spreading Center, 85 to 86° W," Geochim. Cosmochim. Acta **47**, 1551–1558 (1983).

64. C. D. Byers, D. M. Christie, D. W. Muenow, and J. M. Sinton, "Volatile Contents and Ferric–Ferrous Ratios of Basalt, Ferrobasalt, Andesite, and Rhyodacite Glasses from the Galapagos 95.5° W Propagating Rift," Geochim. Cosmochim. Acta **48**, 2239–2245 (1984).

65. C. D. Byers, M. D. Garcia, and D. W. Muenow, "Volatiles in Basaltic Glasses from the East Pacific Rise at 21° N: Implications for MORB Sources and Submarine Lava Flow Morphology," Earth Planet. Sci. Lett. **79**, 9–20 (1986).

66. A. C. Campbell and J. M. Edmond, "Halide Systematics of Submarine Hydrothermal Vents," Nature **342**, 168–170 (1989).

67. A. C. Campbell, T. S. Bowers, C. I. Measures, *et al.*, "A Time Series of Vent Fluid Compositions From 21° N, East Pacific Rise (1979, 1981, 1985), and the Guaymas Basin, Gulf of California (1982, 1985)," J. Geophys. Res. **93**, 4537–4549 (1988a).

68. A. C. Campbell, M. R. Palmer, G. P. Klinkhammer, *et al.*, "Chemistry of Hot Springs on the Mid-Atlantic Ridge," Nature **335**, 514–519 (1988b).

69. J. R. Cann and M. R. Strens, "Black Smokers Fueled by Freezing Magma," Nature **298**, 147–149 (1982).

70. J. R. Cann, M. R. Strens, and A. Rise, "A Simple Magma-Driven Thermal Model for Formation of Volcanogenic Massive Sulfides," Earth Planet. Sci. Lett. **76**, 123–134 (1985/1986).

71. J. J. Carroll and A. E. Mather, "Phase Equilibrium in the System Water–Hydrogen Sulfide: Modeling the Phase Behavior with an Equation of State," Can. J. Chem. Eng. **67**, 999–1003 (1989).

72. L. M. Cathles, "An Analysis of the Cooling of Intrusives by Groundwater Convection which Includes Boiling," Econ. Geol. **72**, 804–826 (1977).

73. J.-P. Charlou, Y. Fouquet, J. P. Donval, *et al.*, "Mineral and Gas Chemistry of Hydrothermal Fluids on an Ultrafast Spreading Ridge: East Pacific Rise, 17–19° S (Naudir Cruise, 1993) Phase Separation Processes Controlled by Volcanic and Tectonic Activity," J. Geophys. Res. **101**, 15 889–15 919 (1996).

74. J. L. Charlou, J. P. Donval, E. Douville, *et al.*, "Compared Geochemical Signatures and the Evolution of Menez Gwen (37°50′ N) and Lucky Strike (37°17′ N) Hydrothermal Fluids, South of the Azores Triple Junction on the Mid-Atlantic Ridge," Chem. Geol. **171**, 49–75 (2000).

75. J. L. Charlou, J. P. Donval, Y. Fouquet, *et al.*, "Geochemistry of High H_2 and CH_4 Vent Fluids Issuing from Ultramafic Rocks at the Rainbow Hydrothermal Field (36°14′ N, MAR)," Chem. Geol. **191**, 345–359 (2002).

76. J. H. Chen, "U, Th and Pb Isotopes in Hot Springs on the Juan de Fuca Ridge," J. Geophys. Res. **92**, 11 411–11 415 (1987).

77. J. H. Chen, G. J. Wasserburg, K. L. Von Damm, and J. M. Edmond, "The U–Th–Pb Systematics in Hot Springs on the East Pacific Rise at 21° N and Guaymas Basin," Geochim. Cosmochim. Acta **50**, 2467–2479 (1986).

78. J. S. Cline, R. J. Bodnar, and J. D. Rimstidt, "Numerical Simulation of Fluid Flow and Silica Transport and Deposition in Boiling Hydrothermal Solution: Application to Epithermal Gold Deposits," J. Geophys. Res. **97**, 9085–9103 (1992).

79. R. G. Coleman, *Ophiolites* (Springer-Verlag, Berlin, 1977).

80. D. R. Converse, H. D. Holland, and J. M. Edmond, "Flow Rates in the Axial Hot Springs of the East Pacific Rise (21° N): Implication for the Heat Budget and the Formation of Massive Sulfide Deposits," Earth Planet. Sci. Lett. **69**, 159–175 (1984).

81. H. Craig, Y. Horibe, K. A. Farley, *et al.*, "Hydrothermal Vents in the Mariana Trough: Results of the First Alvin Dives," EOS, Trans. Am. Geophys. Union **68**, 1531 (1987).

82. K. Crane, "The Distribution of Geothermal Fields along the Mid-Ocean Ridge: An Overview," in *Hydrothermal Vents in the East Pacific*, Bull. Biol. Soc. Washington, No. 30, 3–18 (1985).

83. C. G. Cunningham, "Characteristics of Boiling-Water-Table and Carbon Dioxide Models for Epithermal Gold Deposition," US Geol. Surv. Bull., No. 1646, 43–46 (1985).

84. A. S. Davis and D. A. Clague, "Geochemistry, Mineralogy, and Petrogenesis of Basalt from the Gorda Ridge," J. Geophys. Res. **92**, 10 467–10 483 (1987).

85. E. E. Davis, W. D. Goodfellow, B. D. Bornhold, *et al.*, "Massive Sulfides in a Sediment Rift Valley, Northern Juan de Fuca Ridge," Earth Planet. Sci. Lett. **82**, 49–61 (1987).

86. E. E. Davis, M. J. Mottl, A. T. Fisher, *et al.*, Proceedings of the Ocean Drilling Program. *Initial Reports* (1992), Vol. 139.

87. J. R. Delaney and B. A. Cosens, "Boiling and Metal Deposition in Submarine Hydrothermal Systems," J. Mar. Technol. Soc. **16** (3), 62–66 (1982).

88. J. R. Delaney, R. E. McDuff, M. K. Tivey, and J. E. Lupton, "Measurements of 400°C Hydrothermal Fluids and Temporal Variability in the Endeavour Vent Field," EOS, Trans. Am. Geophys. Union **70**, 1163 (1989).

89. C. G. Denbig, *Theory of Chemical Reactors* (Nauka, Moscow, 1968) [in Russian].

90. R. S. Detrick, J. Honnorez, *et al.*, "Mid-Atlantic Bare-Rock Drilling and Hydrothermal Vents," Nature **321**, 14–15 (1986).

91. F. W. Dickson, "The Role of Rhyolite–Seawater Reaction in the Genesis of Kuroko Ore Deposits," in *Proceedings of the 2nd International Symposium on Water–Rock Interaction, Sec. 4* (Strasbourg, 1977), pp. 181–190.

92. B. R. Doe, "Zinc, Copper, and Lead in Mid-Ocean Ridge Basalts and the Source Rock Control on Zn/Pb in Ocean-Ridge Hydrothermal Deposits," Geochim. Cosmochim. Acta **58**, 2215–2223 (1994).

93. P. I. Dorogokupetz and I. K. Karpov, *Thermodynamics of Minerals and Mineral Equilibria* (Nauka, Novosibirsk, 1984) [in Russian].
94. E. Douville, J. L. Charlou, E. H. Oelkers, *et al.*, "The Rainbow Fluids (36°14′ N, MAR): The Influence of Ultramafic Rocks and Phase Separation on Trace Metal Content in Mid-Atlantic Ridge Hydrothermal Fluids," Chem. Geol. **184**, 37–48 (2002).
95. S. E. Drummond and H. Ohmoto, "Chemical Evolution and Mineral Deposition in Boiling Hydrothermal Systems," Econ. Geol. **80**, 126–147 (1985).
96. F. Duennebier and G. Blackington, "A Man-Made Hot Spring on the Ocean Floor," Deep Sea Drill. Project: Initial Rep. **65**, 357–359 (1983).
97. J. Dymond, R. Cobler, L. Gordon, *et al.*, "^{226}Ra and ^{222}Rn Contents of Galapagos Rift Hydrothermal Waters: The Importance of Low-Temperature Interactions with Crustal Rocks," Earth Planet. Sci. Lett. **64**, 417–429 (1983).
98. J. M. Edmond, C. Measures, B. Mangum, *et al.*, "The Formation of Metal-Rich Deposits at Ridge Crests," Earth Planet. Sci. Lett. **46**, 19–30 (1979).
99. J. M. Edmond, K. L. Von Damm, R. E. McDuff, and C. J. Measures, "Chemistry of Hot Springs on the East Pacific Rise and Their Effluent Dispersal," Nature **297**, 187–191 (1982).
100. J. M. Edmond, A. C. Campbell, M. R. Palmer, *et al.*, "Time Series Studies of Vent Fluids from the TAG and MARK Sites (1986, 1990), Mid-Atlantic Ridge: A New Solution Chemistry Model and a Mechanism for Cu/Zn Zonation in Massive Sulfide Orebodies," in *Hydrothermal Vents and Processes*, Ed. by L. M. Parson, C. L. Walker, and D. P. Dixon (Geol. Soc. Spec. Publ., London, 1995), No. 87, pp. 77–86.
101. H. Edmonds and J. M. Edmond, "A Three-Component Mixing Model for Ridge-Crest Hydrothermal Fluids," Earth Planet. Sci. Lett. **134**, 53–67 (1995).
102. A. J. Ellis, "Explored Geothermal Systems," in *Geochemistry of Hydrothermal Ore Deposits*, Ed. by H. Barnes, 2nd ed. (Wiley, New York, 1979), pp. 632–737.
103. R. W. Embley, I. R. Jonasson, M. R. Perfit, *et al.*, "Submersible Investigation of an Extinct Hydrothermal System on the Galapagos Ridge: Sulfide Mounds, Stockwork Zone, and Differentiated Lavas," Can. Mineral. **26**, 517–539 (1988).
104. T. Erdey-Gru, *Transport Phenomena in Aqueous Solutions* (Akadémiai Kiadó, Budapest, 1974).
105. W. C. Evans, L. D. White, and J. B. Rapp, "Geochemistry of Some Gases in Hydrothermal Fluids from the Southern Juan de Fuca Ridge," J. Geophys. Res. **93**, 15 305–15 313 (1988).
106. G. Faure, *Principles of Isotope Geology*, 2nd ed. (Wiley, New York, 1986; Mir, Moscow, 1989).
107. R. A. Feely, T. L. Geiselman, E. T. Baker, and G. J. Massoth, "Distribution and Composition of Hydrothermal Plume Particles from the ASHES Vent Field of Axial Volcano, Juan de Fuca Ridge," J. Geophys. Res. **95**, 12 855–12 873 (1990).
108. U. Fehn and L. M. Cathles, "Hydrothermal Convection at Slow-Spreading Mid-Ocean Ridges," Tectonophysics **55**, 239–260 (1979).
109. R. Fernandez-Prini and R. Crovetto, "A Critical Evaluation of the Solubility of Simple Inorganic Gases in Water at High Temperature," AIChE J. **31**, 513–516 (1985).
110. R. Fernandez-Prini and R. Crovetto, "Evaluation of Data on Solubility of Simple Apolar Gases in Light and Heavy Water at High Temperature," J. Phys. Chem. Refer. Data **18**, 1231–1243 (1989).
111. T. Finlow-Bates and D. E. Large, "Water Depth as a Major Control on the Formation of Submarine Exhalative Ore Deposits," Geol. Jahrb. **30**, 27–39 (1978).
112. A. T. Fisher and T. N. Narasimhan, "Numerical Simulation of Hydrothermal Circulation Resulting from Basalt Intrusion in a Buried Spreading Centers," Earth Planet. Sci. Lett. **103**, 100–115 (1991).
113. D. E. Fisher and M. R. Perfit, "Evidence from Rare Gases for Magma-Chamber Degassing of Highly Evolved Mid-Ocean-Ridge Basalt," Nature **343**, 450–452 (1990).
114. D. J. Fornari, T. Shank, K. L. Von Damm, *et al.*, "Time-Series Temperature Measurements at High-Temperature Hydrothermal Vents, East Pacific Rise 9°49′–51′ N: Evidence for Monitoring a Crustal Cracking Event," Earth Planet. Sci. Lett. **160**, 419–431 (1998).
115. A. M. Fouillac and M. Javoy, "Oxygen and Hydrogen Isotopes in the Volcano–Sedimentary Complex of Huelva (Iberian Pyrite Belt): Example of Water Circulation through a Volcano–Sedimentary Sequence," Earth Planet. Sci. Lett. **87**, 473–484 (1988).
116. C. Fouillac, G. Michard, and G. Bocquier, "Une Methode de Simulation de l'Evolution des Profils d'Alteration," Geochim. Cosmochim. Acta **41**, 207–213 (1977).
117. Y. Fouquet, G. Auclair, P. Cambon, and J. Etoubleau, "Geological Setting and Geochemical Investigations on Sulfide Deposits near 13° N on the East Pacific Rise," Mar. Geol. **84**, 143–178 (1988).
118. Y. Fouquet, U. Von Stackelberg, J. L. Charlou, *et al.*, "Metallogenesis in Back-Arc Environments: The Lau Basin Example," Econ. Geol. **88**, 2154–2181 (1993).
119. Y. Fouquet, R. Knott, P. Cambon, *et al.*, "Formation of Large Sulfide Mineral Deposits along Fast Spreading Ridges: Examples from Off-Axial Deposits at 12°43′ N on the East Pacific Rise," Earth Planet. Sci. Lett. **144**, 147–162 (1996).
120. C. G. Fox, "Consequences of Phase Separation on the Distribution of Hydrothermal Fluids at ASHES Vent Field, Axial Volcano, Juan de Fuca Ridge," J. Geophys. Res. **95**, 12 923–12 926 (1990).
121. R. D. Francis, "Sulfide Globules in Mid-Ocean Ridge Basalts (MORB), and the Effect of Oxygen Abundance in Fe–S–O Liquids on the Ability of These Liquids to Partition Metals from MORB and Komatiite Magmas," Chem. Geol. **85**, 199–213 (1990).
122. J. M. Franklin, J. W. Lydon, and D. F. Sangster, "Volcanic-Associated Massive Sulfide Deposits," Econ. Geol. **75**, 485–627 (1981).
123. I. Friedman and J. R. O'Neil, "Compilation of Stable Isotope Fractionation Factors of Geochemical Interest," in *Data of Geochemistry*, 6th ed. US Geol. Surv. Prof. Pap., No. 440 (1977).

124. B. Fritz, "Etude thermodynamique et simulation des reactions entre mineraux et solutions: application a la geochimie des alterations et des eaux continentales," Memoire Sci. Geol., No. 41 (1975).

125. B. Fritz, "Etude thermodinamique et modelisation des reactions hydrothermales et diagenetiques," Memoir Sci. Geol., No. 65 (1981).

126. W. S. Fyfe, N. J. Price, and A. B. Thompson, *Fluids in the Earth Crust* (Elsevier, Amsterdam, 1978).

127. T. Gamo, H. Sakai, E.-S. Kim, *et al.*, "High Alkalinity Due to Sulfate Reduction in the CLAM Hydrothermal Field, Okinawa Trough," Earth Planet. Sci. Lett. **107**, 328–338 (1991).

128. T. Gamo, K. Okamura, J.-L. Charlou, *et al.*, "Acidic and Sulfate-Rich Hydrothermal Fluids from the Manus Back-Arc Basin, Papua New Guinea," Geology **25**, 139–142 (1997).

129. T. Gamo, H. Chiba, T. Yamanaka, *et al.*, "Chemical Characteristics of Newly Discovered Black Smoker Fluids and Associated Hydrothermal Plumes at the Rodrigues Triple Junction, Central Indian Ridge," Earth Planet. Sci. Lett. **193**, 371–379 (2001).

130. R. M. Garrels and C. L. Christ, *Solutions, Minerals, and Equilibria* (Freeman Cooper, San Francisco, 1965).

131. M. O. Garcia, D. W. Muenow, and K. E. Aggrey, "Major Element, Volatile, and Stable Isotope Geochemistry of Hawaiian Submarine Tholeiitic Glasses," J. Geophys. Res. **94**, 10525–10538 (1989).

132. J. B. Gemmell and R. Sharpe, "Detailed Sulfur-Isotope Investigation of the TAG Hydrothermal Mound and Stockwork Zone, 26° N, Mid-Atlantic Ridge," Proc. Ocean Drill. Program: Sci. Results **158**, 71–84 (1998).

133. *General Chemical Technology,* Ed. by A. G. Amelin (Khimiya, Moscow, 1977) [in Russian].

134. *Geophysics of the Ocean*, Vol. 2: *Geodynamics,* Ed. by O. G. Sorokhtin (Nauka, Moscow, 1979) [in Russian].

135. T. M. Gerlach, "Exsolution of H_2O, CO_2, and S during Eruptive Episodes at Kilauea Volcano, Hawaii," J. Geophys. Res. **91**, 12177–12185 (1986).

136. T. M. Gerlach, "CO_2 from Magma-Chamber Degassing," Nature **337**, 124 (1989).

137. H. A. Gild and S. M. F. Sheppard, "Hydrogen Isotope Fractionation between Kaolinite and Water Revisited," Geochim. Cosmochim. Acta **60**, 529–533 (1996).

138. K. M. Gillis, "Controls on Hydrothermal Alteration in a Section of Fast-Spreading Oceanic Crust," Earth Planet. Sci. Lett. **134**, 473–489 (1995).

139. K. M. Gillis and P. T. Robinson, "Pattern and Processes of Alteration in the Lavas and Dykes of the Troodos Ophiolite, Cyprus," J. Geophys. Res. **95**, 21 523–21 548 (1990).

140. U. Ginster, M. J. Mottl, and R. P. Von Herzen, "Heat Flux from Black Smokers on the Endeavour and Cleft Segments, Juan de Fuca Ridge," J. Geophys. Res. **99**, 4937–4950 (1994).

141. E. Gitlin, "Sulfide Remobilization during Low Temperature Alteration of Seafloor Basalt," Geochim. Cosmochim. Acta **49**, 1567–1579 (1985).

142. G. P. Glasby and K. Notsu, "Submarine Hydrothermal Mineralization in the Okinawa Trough, SW of Japan: An Overview," Ore Geol. Rev. **23**, 299–339 (2003).

143. S. I. Golyshev, V. A. Grinenko, and N. L. Padalko, "Thermodynamic Isotope Effects for Sulfur and Oxygen in the System Solution–Sulfate Mineral," Geokhimiya, No. 10, 1379–1390 (1983).

144. W. D. Goodfellow and B. Blaise, "Sulfide Formation and Hydrothermal Alteration of Hemipelagic Sediment in Middle Valley, Northern Juan de Fuca," Can. Mineral. **26**, 675–696 (1988).

145. W. D. Goodfellow and J. M. Franklin, "Geology, Mineralogy, and Chemistry of Sediment-Hosted Clastic Massive Sulfides in Shallow Cores, Middle Valley, Northern Juan de Fuca Ridge," Econ. Geol. **88**, 2037–2068 (1993).

146. N. S. Gorbachev and G. A. Kashirtseva, "Fluid–Magmatic Differentiation of Basaltic Magmas and Magmatic Sulfide Formation," in *Experiment in the Solution of Important Geological Problems* (Nauka, Moscow, 1986), pp. 98–119 [in Russian].

147. S. Goto, M. Kinoshita, O. Matsubayashi, and R. P. Von Herzen, "Geothermal Constraints on the Hydrological Regime of the TAG Active Hydrothermal Mound, Inferred from Long-Term Monitoring," Earth Planet. Sci. Lett. **203**, 149–163 (2002).

148. U. M. Graham, G. J. Bluth, and H. Omoto, "Sulfide–Sulfate Chimneys on the East Pacific Rise, 11 and 13° N Latitudes: I. Mineralogy and Paragenesis," Can. Mineral. **26**, 487–504 (1988).

149. D. V. Grichuk, "Estimation of Gibbs Free Energies for Isotopic Forms of Compounds," Geokhimiya, No. 2, 178–191 (1987).

150. D. V. Grichuk, "An Isotopic–Chemical Thermodynamic Model of a Hydrothermal System," Dokl. Akad. Nauk SSSR **298**, 1222–1225 (1988).

151. D. V. Grichuk, "Ore Elements in a Mid-Ocean Ridge Hydrothermal System," Geokhimiya, No. 7, 650–672 (1996) [Geochem. Int. **34**, 586–606 (1996)].

152. D. V. Grichuk, "Estimation of the Isotopic–Chemical Cross Effect," in *Abstracts of XV Symposium on Isotope Geochemistry* (Moscow, 1998), p. 81.

153. D. V. Grichuk and M. V. Borisov, "Thermodynamic Model of a Hydrothermal System in the Oceanic Crust," Dokl. Akad. Nauk SSSR **270**, 424–427 (1983).

154. D. V. Grichuk and S. G. Krasnov, "Sources of Ore Elements in Present-Day Hydrothermal Systems of the Ocean Floor," Litol. Polezn. Iskop., No. 1, 105–113 (1989).

155. D. V. Grichuk and A. Yu. Lein, "Evolution of an Oceanic Hydrothermal System and Sulfur Isotope Composition of Sulfides," Dokl. Akad. Nauk SSSR **318**, 422–425 (1991).

156. D. V. Grichuk and Yu. V. Shvarov, "Boiling as a Factor of Metal Mobilization in Hydrothermal Systems," in *Abstracts of II International Symposium on Thermodynamics of Natural Processes* (Novosibirsk, 1992), p.24.

157. D. V. Grichuk and Yu. V. Shvarov, "Comparative Analysis of Techniques Used in the Equilibrium–Dynamic Simulations of Infiltration Metasomatic Zoning," Petrologiya **10**, 654–667 (2002) [Petrology **10**, 580–592 (2002)].

158. D. V. Grichuk, M. V. Borisov, and G. L. Mel'nikova, "Thermodynamic Modeling of Seawater–Basalt and Seawater–Peridotite Interactions under Hydrothermal

Conditions," in *Abstracts of V All-Union School on Marine Geology: Geology of Seas and Oceans* (1982), Vol. 3, pp. 166–168.

159. D. V. Grichuk, M. V. Borisov, and G. L. Mel'nikova, "Thermodynamic Modeling of a Hydrothermal System in Oceanic Crust: Evolution of Fluid Composition," Int. Geol. Rev. **27**, 1097–1115 (1985).
160. D. V. Grichuk, N. M. Sushchevskaya, Yu. V. Vasyuta, and N. N. Kononkova, "On the Role of Magmatic Fluids in the Formation of the Chemical Composition of Hydrothermal Waters of Mid-Ocean Ridges," Geokhimiya, No. 12, 1741–1750 (1988).
161. D. V. Grichuk, E. E. Abramova, and A. V. Tutubalin, "A Thermodynamic Model of Submarine Massive Sulfide Formation in a Convecting Hydrothermal System," Geol. Rudn. Mestorozhd., No. 1, 1–15 (1998) [Geol. Ore Depos. **40**, 1–15 (1998)].
162. D. Grimaud, J. Ishibashi, J. M. Auzende, and T. Urabe, "The Chemistry of the Hot Springs at 17° S on the North Fiji Basin Axis (SW Pacific)," EOS, Trans. Am. Geophys. Union **70**, 1398 (1989).
163. L. N. Grinenko, V. A. Grinenko, G. D. Zagryaiskaya, and Yu. M. Stolyarov, "Isotopic Composition of Sulfur in Sulfides and Sulfates from the Levikha Massive Sulfide Deposits with Applications to Their Genesis," Geol. Rudn. Mestorozhd., No. 3, 26–38 (1969).
164. V. A. Grinenko and H. G. Thode, "Sulfur Isotope Effects in Volcanic Gas Mixtures," Can. J. Earth Sci. **7**, 1402–1409 (1970).
165. A. A. Gurenko, A. V. Sobolev, and N. N. Kononkova, "Petrology of the Primary Melt of Rift Tholeiites from the Reikjanes Peninsula, Iceland," Geokhimiya, No. 8, 1137–1150 (1990).
166. J. L. Haas, Jr., "Physical Properties of the Coexisting Phases and Thermochemical Properties of the H_2O Component in Boiling NaCl Solutions: Preliminary Steam Tables for NaCl Solutions," Geol. Surv. Bull., No. 1421-A (1976a).
167. J. L. Haas, Jr., "Thermodynamic Properties of the Coexisting Phases and Thermochemical Properties of the NaCl Component in Boiling NaCl Solutions: Preliminary Steam Tables for NaCl Solutions," Geol. Surv. Bull., No. 1421-B (1976b).
168. A. Hajash, "Hydrothermal Processes along Mid-Ocean Ridges: An Experimental Investigation," Contrib. Mineral. Petrol. **53**, 205–226 (1975).
169. A. Hajash and G. W. Chandler, "An Experimental Investigation of High-Temperature Interactions between Seawater and Rhyolite, Andesite, Basalt and Peridotite," Contrib. Mineral. Petrol. **78**, 240–254 (1981).
170. P. Halbach, K. Nakamura, M. Washner, *et al.*, "Probable Modern Analogue of Kuroko-Type Massive Sulfide Deposits in the Okinawa Trough Back-Arc Basin," Nature **338**, 496–499 (1989).
171. P. Halbach, B. Pracejus, and A. Marten, "Geology and Mineralogy of Massive Sulfide Ores from the Central Okinawa Trough, Japan," Econ. Geol. **88**, 2210–2225 (1993).
172. *Handbook on Heat Transfer*, Ed. by B. S. Petukhov and V. K. Shikov (Energoatomizdat, Moscow, 1987) [in Russian].
173. M. D. Hannington and S. D. Scott, "Mineralogy and Geochemistry of a Hydrothermal Silica–Sulfide–Sulfate Spire in the Caldera of Axial Seamount, Juan de Fuca Ridge," Can. Mineral. **26**, 603–625 (1988).
174. M. Hannington, P. Herzig, S. Scott, *et al.*, "Comparative Mineralogy and Geochemistry of Gold-Bearing Sulfide Deposits on the Mid-Ocean Ridges," Mar. Geol. **101**, 217–248 (1991).
175. M. D. Hannington, A. G. Galley, P. M. Herzig, and S. Petersen, "Comparison of the TAG Mound and Stockwork Complex with Cyprus-Type Massive Sulfide Deposits," Proc. Ocean Drill. Program: Sci. Results **158**, 389–416 (1998).
176. M. Hannington, P. Herzig, P. Stoffers, *et al.*, "First Observations of High-Temperature Submarine Hydrothermal Vents and Massive Anhydrite Deposits off the North Coast of Iceland," Mar. Geol. **177**, 199–220 (2001).
177. R. Haymon, "The Growth History of Hydrothermal 'Black Smoker' Chimneys," Nature **301**, 695–698 (1983).
178. R. M. Haymon, R. A. Koski, and M. J. Abrams, "Hydrothermal Discharge Zones beneath Massive Sulfide Deposits Mapped in the Oman Ophiolite," Geology **17**, 531–535 (1989).
179. C. A. Heinrich, "The Chemistry of Hydrothermal Tin (-Tungsten) Ore Deposition," Econ. Geol. **85**, 457–481 (1990).
180. C. A. Heinrich, J. H. C. Bain, T. P. Mernagh, *et al.*, "Fluid and Mass Transfer during Metabasalt Alteration and Copper Mineralization at Mount Isa, Australia," Econ. Geol. **90**, 705–730 (1995).
181. H. Heinrichs, B. Schulz-Dobrick, and K. H. Wedepohl, "Terrestrial Geochemistry of Cd, Bi, Tl, Pb, Zn, and Rb," Geochim. Cosmochim. Acta **44**, 1519–1533 (1980).
182. R. Hekinian and Y. Fouquet, "Volcanism and Metallogenesis of Axial and Off-Axial Structures on the East Pacific Rise Near 13° N," Econ. Geol. **80**, 221–249 (1985).
183. R. Hekinian and D. Walker, "Diversity and Spatial Zonation of Volcanic Rocks from the East Pacific Rise near 21° N," Contrib. Mineral. Petrol. **96**, 265–280 (1987).
184. R. Hekinian, J. Francheteau, V. Renard, *et al.*, "Intense Hydrothermal Activity at the Axis of the East Pacific Rise Near 13° N: Submersible Witness of Growth of Sulfide Chimney," Mar. Geophys. Res. **6**, 1–14 (1983).
185. R. Hekinian, G. Thompson, and D. Bideau, "Axial and Off-Axial Heterogeneity of Basaltic Rocks from the East Pacific Rise at 12°35′ N–12°51′ N and 11°26′ N–11°30′ N," J. Geophys. Res. **94**, 17 437–17 463 (1989).
186. H. C. Helgeson, "Evaluation of Irreversible Reactions in Geochemical Processes Involving Minerals and Aqueous Solutions: I. Thermodynamic Relations," Geochim. Cosmochim. Acta **32**, 853–877 (1968).
187. H. C. Helgeson, "Mass Transfer among Minerals and Hydrothermal Solutions," in *Geochemistry of Hydrothermal Ore Deposits*, 2nd ed., Ed. by H. Barnes (Wiley, New York, 1979), pp. 568–610.
188. H. C. Helgeson and D. H. Kirkham, "Theoretical Prediction of the Thermodynamic Behavior of Aqueous

Electrolytes at High Pressures and Temperatures: II Debye–Hückel Parameters for Activity Coefficients and Relative Partial Molal Properties," Am. J. Sci. **274**, 1199–1261 (1974).

189. H. C. Helgeson, R. M. Garrels, and F. T. McKenzie, "Evaluation of Irreversible Reactions in Geochemical Processes Involving Minerals and Aqueous Solutions: II. Applications," Geochim. Cosmochim. Acta **33**, 455–481 (1969).
190. H. C. Helgeson, T. H. Brown, A. Nigrini, and T. A. Jones, "Calculation of Mass Transfer in Geochemical Processes Involving Aqueous Solutions," Geochim. Cosmochim. Acta **34**, 569–592 (1970).
191. H. C. Helgeson, J. M. Delany, H. W. Nesbitt, and D. K. Bird, "Summary and Critique of the Thermodynamic Properties of Rock-Forming Minerals," Am. J. Sci. **278-a**, 1–228 (1978).
192. H. C. Helgeson, D. H. Kirkham, and G. C. Flowers, "Theoretical Prediction of the Thermodynamic Behavior of Aqueous Electrolytes at High Pressures and Temperatures: IV. Calculation of Activity Coefficients, Osmotic Coefficients, and Apparent Molal and Standard and Relative Partial Molal Properties to 600°C and 5 Kb," Am. J. Sci. **281**, 1249–1516 (1981).
193. J. J. Hemley, G. L. Cygan, J. B. Fein, *et al.*, "Hydrothermal Ore-Forming Processes in the Light of Studies in Rock-Buffered Systems: I. Iron–Copper–Zinc–Lead Sulfide Solubility Relations," Econ. Geol. **87**, 1–22 (1992).
194. P. M. Herzig, M. D. Hannington, and A. J. Arribas, "Sulfur Isotopic Composition of Hydrothermal Precipitates from the Lau Back Arc: Implication for Magmatic Contributions to Seafloor Hydrothermal Systems," Miner. Deposita **33**, 226–237 (1998a).
195. P. M. Herzig, S. E. Humphris, D. J. Miller, and R. A. Zierenberg, Proc. Ocean Drill. Program: Sci. Results **158**, 389–416 (1998).
196. P. M. Herzig, S. Petersen, and M. D. Hannington, "Geochemistry and Sulfur-Isotopic Composition of the TAG Hydrothermal Mound, Mid-Atlantic Ridge, 26° N," Proc. Ocean Drill. Program: Sci. Results **158**, 47–70 (1998b).
197. H. D. Holland and S. D. Malinin, "The Solubility and Occurrence of Non-Ore Minerals," in *Geochemistry of Hydrothermal Ore Deposits*, 2nd ed., Ed. by H. L. Barnes (Wiley, New York, 1979), pp. 461–508.
198. J. R. Holloway, "Magmatic Fluids," in *Thermodynamic Modeling of Geological Materials: Minerals, Fluids, and Melts*, Vol. 17 of *Reviews in Mineralogy*, Ed. by I. S. E. Carmichael and H. P. Eugster (1987).
199. J. Honnorez, L. C. Alt, B.-M. Honnorez-Guerstein, *et al.*, "Stockwork-Like Sulfide Mineralization in Young Oceanic Crust: Deep Sea Drilling Project Hole 504B," Deep Sea Drill. Project: Initial Rep. **83**, 263–282 (1985).
200. *Hot Brines and Recent Heavy Metal Deposits in the Red Sea*, Ed. by E. T. Degens and D. A. Ross (Springer-Verlag, Berlin, 1969).
201. S. E. Humphris, P. M. Herzig, D. J. Miller, *et al.*, "The Internal Structure of an Active Sea-Floor Massive Sulfide Deposit," Nature **377**, 713–716 (1995).
202. S. E. Humphris, J. C. Alt, D. A. H. Teagle, and J. J. Honnorez, "Geochemical Changes during Hydrothermal Alteration of Basement in the Stockwork beneath the Active TAG Hydrothermal Mound," Proc. Ocean Drill. Program: Sci. Results **158**, 255–276 (1998).
203. S. F. Humphris and G. Thompson, "Hydrothermal Alteration of Oceanic Basalts by Seawater," Geochim. Cosmochim. Acta **42**, 107–125 (1978).
204. *Hydrothermal Sulfide Ores and Metalliferous Sediments in the Ocean,* Ed. by I. S. Gramberg and A. I. Ainemer (Nedra, St. Petersburg, 1992) [in Russian].
205. R. D. Hyndman and M. J. Drury, "The Physical Properties of Oceanic Basement Rocks from Deep Drilling on the Mid-Atlantic Ridge," J. Geophys. Res. **81**, 4042–4052 (1976).
206. S. A. Igumnov, V. A. Grinenko, and N. B. Poner, "Temperature Dependence of Sulfur Isotope Partition Coefficients between Hydrogen Sulfide and Dissolved Sulfate at 260–400°C," Geokhimiya, No. 7, 1085–1087 (1977).
207. R. P. Ilchik and M. D. Barton, "An Amagmatic Origin of Carlin-Type Gold Deposits," Econ. Geol. **92**, 269–288 (1997).
208. J. I. Ishibashi, Y. Sano, H. Wakita, *et al.*, "Helium and Carbon Geochemistry of Hydrothermal Fluids from the Mid-Okinawa Trough Back Arc Basin, Southwest of Japan," Chem. Geol. **123**, 1–15 (1995).
209. E. Ito, D. M. Harris, and A. T. Anderson, "Alteration of Oceanic Crust and Geological Cycling of Chlorine and Seawater," Geochim. Cosmochim. Acta **47**, 1613–1624 (1983).
210. I. P. Ivanov and M. V. Borisov, "Estimation of the Composition of Initial Solution for the Process of Metasomatic Replacement of Rocks," Geokhimiya, No. 12, 1797–1806 (1980).
211. R. H. James, H. Elderfield, and M. R. Palmer, "The Chemistry of Hydrothermal Fluids from the Broken Spur Site, 29° N Mid-Atlantic Ridge," Geochim. Cosmochim. Acta **59**, 651–659 (1995).
212. D. R. Janecky and W. E. Seyfried, Jr., "Formation of Massive Sulfide Deposits on Oceanic Ridge Crests: Incremental Reaction Models for Mixing between Hydrothermal Solutions and Seawater," Geochim. Cosmochim. Acta **48**, 2723–2738 (1984).
213. D. R. Janecky and W. E. Seyfried, Jr., "Hydrothermal Serpentinization of Peridotite within the Oceanic Crust: Experimental Investigation of Mineralogy and Major Element Chemistry," Geochim. Cosmochim. Acta **50**, 1357–1378 (1986).
214. D. R. Janecky and W. C. Shanks, III, "Computational Modeling of Chemical and Sulfur Isotopic Reaction Processes in Seafloor Hydrothermal Systems: Chimneys, Massive Sulfides, and Subjacent Alteration Zones," Can. Mineral. **26**, 603–625 (1988).
215. M. L. Japas and J. M. H. Levelt Sengers, "Gas Solubility and Henry's Law Near the Solvent's Critical Point," AIChE J. **35**, 705–713 (1989).
216. P. Jean-Baptiste, H. Bougault, A. Vangriesheim, *et al.*, "Mantle ^{3}He in Hydrothermal Vents and Plume of the Lucky Strike Site (MAR 37°17′ N) and Associated Geothermal Heat Flux," Earth Planet. Sci. Lett. **157**, 69–77 (1998).

217. Ph. Jean-Baptiste, A. Dapoigny, M. Stievenard, *et al.*, "Helium and Oxygen Isotope Analyses of Hydrothermal Fluids from the East Pacific Rise between 17° S and 19° S," Geo-Mar. Lett. **17**, 213–219 (1997a).

218. Ph. Jean-Baptiste, J. L. Charlou, and M. Stievenadr, "Oxygen Isotope Study of Mid-Ocean Ridge Hydrothermal Fluids: Implication for the Oxygen-18 Budget of the Ocean," Geochim. Cosmochim. Acta **61**, 2669–2677 (1997b).

219. Ph. Jean-Baptiste, J. L. Charlou, M. Stievenard, *et al.*, "Helium and Methane Measurements in Hydrothermal Fluids from the Mid-Atlantic Ridge: The Snake Pit Site at 23° N," Earth Planet. Sci. Lett. **106**, 17–28 (1991).

220. J. Jedwab and J. Boulegue, "Graphite Crystals in Hydrothermal Vents," Nature **310**, 41–43 (1984).

221. J. W. Johnson, E. H. Oelkers, and H. C. Helgeson, "SUPCRT 92: A Software Package for Calculating the Standard Molal Thermodynamic Properties of Minerals, Gases, Aqueous Species, and Reactions from 1 to 5000 Bars and 0 to 1000°C," Comput. Geosci. **18**, 899–947 (1992).

222. J. Jonasson, R. Embley, T. Francis, *et al.*, "Exposure of the Alteration Zone beneath the Galapagos Massive Sulfide Deposit," EOS, Trans. Am. Geophys. Union **67**, 86 (1986).

223. D. Kadko and W. Moore, "Radiochemical Constraints on the Crustal Residence Time of Submarine Hydrothermal Fluids: Endeavour Ridge," Geochim. Cosmochim. Acta **52**, 659–668 (1988).

224. Y. Kajiwara, "Sulfur Isotope Study of the Kuroko Ores of Shakanai No. 1 Deposits, Akita Prefecture, Japan," Geochem. J. **4**, 157–181 (1971).

225. V. S. Kamenetsky, P. Davidson, T. P. Mernagh, *et al.*, "Fluid Bubbles in Melt Inclusions and Pillow-Rim Glasses: High-Temperature Precursors to Hydrothermal Fluids?" Chem. Geol. **183**, 349–364 (2002).

226. E. S. Kappel and J. M. Franklin, "Relationship between Geologic Development of Ridge Crests and Sulfide Deposits in the Northeast Pacific Ocean," Econ. Geol. **84**, 485–505 (1988).

227. I. K. Karpov, *Physicochemical Computer Modeling in Geochemistry* (Nauka, Novosibirsk, 1981) [in Russian].

228. I. K. Karpov, A. I. Kiselev, and F. A. Letnikov, *Computer Modeling of Natural Mineral Formation* (Nedra, Moscow, 1976) [in Russian].

229. K. Kase, M. Yamamoto, and T. Shibata, "Copper-Rich Sulfide Deposit Near 23° N, Mid-Atlantic Ridge: Chemical Composition, Mineral Chemistry, and Sulfur Isotopes," Proc. Ocean Drill. Program: Sci. Results **106/109**, 163–177 (1990).

230. S. A. Kashik, *Formation of Mineral Zoning in Alteration Residues* (Nauka, Novosibirsk, 1989) [in Russian].

231. S. A. Kashik and I. K. Karpov, *Physicochemical Theory of Zoning Formation in the Alteration Residues* (Nauka, Novosibirsk, 1978) [in Russian].

232. M. Kastner, H. Craig, and A. Sturz, "Hydrothermal Deposition in the Mariana Trough: Preliminary Mineralogical Investigation," EOS, Trans. Am. Geophys. Union **68**, 1531 (1987).

233. H. Kawahata and S. D. Scott, "Strontium Isotopes and Water–Rock Interactions of the Agrokipia "B" Stockwork Deposit in the Troodos Ophiolite, Cyprus: A Fossil Subseafloor Ore Body," Geochem. J. **24**, 349–356 (1990).

234. H. Kawahata and N. Shikazono, "Sulfur Isotope and Total Sulfur Studies of Basalts and Greenstones from DSDP Hole 504B, Costa Rica Rift: Implications for Hydrothermal Alteration," Can. Mineral. **26**, 555–565 (1988).

235. D. S. Kelley and J. R. Delaney, "Two Phase Separation and Fracturing in Mid-Ocean Ridge Gabbros at Temperatures Greater than 700°C," Earth Planet. Sci. Lett. **83**, 53–66 (1987).

236. D. S. Kelley, J. A. Karson, D. K. Blackman, *et al.*, "Discovery of Lost City: An Off-Axis Hydrothermal Vent Field Near the Mid-Atlantic Ridge at 30° N," Nature **412**, 145–149 (2001).

237. J. F. Kerridge, R. M. Haymon, and M. Kastner, "Sulfur Isotope Systematics at the 21° N Site, East Pacific Rise," Earth Planet. Sci. Lett. **66**, 91–100 (1983).

238. I. L. Khodakovsky, V. P. Volkov, Yu. I. Sidorov, and M. V. Borisov, "Preliminary Prediction of the Mineral Composition of Surface Rocks and the Hydration and Oxidation Processes of the Venus Outer Shell," Geokhimiya, No. 12, 1821–1835 (1978).

239. H. C. Kim and G. M. McMurtry, "Radial Growth Rates and ^{210}Pb Ages of Hydrothermal Massive Sulfides from the Juan de Fuca Ridge," Earth Planet. Sci. Lett. **104**, 299–314 (1991).

240. K.-R. Kim, J. A. Welhan, and H. Craig, "The Hydrothermal Vent Fields at 13° and 11° N on the East Pacific Rise: Alvin Results," EOS, Trans. Am. Geophys. Union **65**, 973 (1984).

241. R. Knott, Y. Fouquet, J. Honnorez, *et al.*, "Petrology of Hydrothermal Mineralization: A Vertical Section through the TAG Mound," Proc. Ocean Drill. Program: Sci. Results **158**, 5–26 (1998).

242. G. R. Kolonin, G. A. Palyanova, G. P. Shironosova, and K. G. Morgunov, "Thermodynamic Model of Potential Gold-Bearing High-Temperature Water–Carbon Dioxide Fluid," Geokhimiya, No. 12, 1725–1734 (1994).

243. M. Yu. Korotaev, A. A. Pek, and M. N. Kim, "Infiltration Metasomatism in Gradient Field: Modeling of Metasomatic Vein Formation," Geokhimiya, No. 1, 20–35 (1992).

244. D. S. Korzhinskii, "General Properties of the Infiltration Metasomatic Zoning," Dokl. Akad. Nauk SSSR **78** (1), 95–98 (1951).

245. D. S. Korzhinskii, *Theory of Metasomatic Zoning* (Nauka, Moscow, 1969; Clarendon, Oxford, UK, 1970).

246. D. S. Korzhinskii, "Conventional Stationary Systems," Zap. Vses. Mineral. O–va **108**, 522–523 (1979).

247. R. Koski, P. Lonsdale, W. C. Shanks, III, *et al.*, "Mineralogy and Geochemistry of a Sediment-Hosted Hydrothermal Sulfide Deposit from the Southern Trough of Guaymas Basin, Gulf of California," J. Geophys. Res. **90**, 6695–6707 (1985).

248. R. Koski, W. C. Shanks, III, W. A. Bohrson, and R. L. Oscarson, "The Composition of Massive Sulfide Deposits from the Sediment-Covered Floor of Escanaba Trough, Gorda Ridge: Implications for Depositional Processes," Can. Mineral. **26**, 655–673 (1988).

249. S. G. Krasnov, "On the Minimum Depth of Massive Sulfide Ore Formation on the Ocean Floor," Dokl. Akad. Nauk SSSR **296**, 1188–1191 (1987).

250. S. G. Krasnov, "Geochemical Specialization of Oceanic Sulfide Ores," Dokl. Akad. Nauk SSSR **313**, 962–966 (1990).

251. S. G. Krasnov, Doctoral Dissertation in Geology and Mineralogy (St. Petersburg, 1993).

252. S. G. Krasnov and T. V. Stepanova, "The Formation of a Large Oceanic Massive Sulfide Ore Body (Middle Valley, Endeavour Ridge): Evidence from Geochemical Study of the Cores," Geochem. Int., No. 9, 768–789 (1996).

253. S. G. Krasnov, A. I. Ainemer, and T. V. Stepanova, "Geochemistry and Genesis of Sulfide Ores in the Pacific," in *Geology of Seas and Oceans* (Nauka, Moscow, 1988), pp. 129–140 [in Russian].

254. S. G. Krasnov, D. V. Grichuk, and T. V. Stepanova, "Hydrothermal Mineral Formation in the Ocean," Zap. Vses. Mineral. O–va **116**, 23–32 (1990).

255. S. Krasnov, T. Stepanova, and M. Stepanov, "Chemical Composition and Formation of a Massive Sulfide Deposit, Middle Valley, Northern Juan de Fuca Ridge (Site 856)," Proc. Ocean Drill. Program: Sci. Results **139**, 353–372 (1994).

256. A. I. Krivtsov, "Qualitative Aspects of the Problem of Ore Matter Sources," Geol. Rudn. Mestorozhd. **23** (5), 3–18 (1981).

257. A. I. Krivtsov, "Environments and Conditions of Ancient and Modern Massive Sulfide Ore Formation," Geol. Rudn. Mestorozhd., No. 3, 3–17 (1987).

258. V. B. Kurnosov, *Hydrothermal Alteration of Basalts in the Pacific Ocean and Metalliferous Sediments: Evidence from Deep-Sea Drilling Data* (Nauka, Moscow, 1986) [in Russian].

259. M. Kusakabe, S. Mayeda, and E. S. Nakamura, "O and Sr Isotope Systematics of Active Vent Materials from the Mariana Backarc Basin Spreading Axis at 18° N," Earth Planet. Sci. Lett. **100**, 275–282 (1990).

260. T. K. Kyser and J. R. O'Neil, "Hydrogen Isotope Systematics of Submarine Basalts," Geochim. Cosmochim. Acta **48**, 2123–2133 (1984).

261. C. Lalou, J.-L. Reyss, and E. Brichet, "Actinide-Series Disequilibrium as a Tool to Establish the Chronology of Deep-Sea Hydrothermal Activity," Geochim. Cosmochim. Acta **57**, 1221–1231 (1993).

262. C. Lalou, J.-L. Reyss, E. Brichet, *et al.*, "Hydrothermal Activity on a 10^5-Year Scale at a Slow Spreading Ridge, TAG Hydrothermal Field, Mid-Atlantic Ridge 26° N," J. Geophys. Res. **100**, 17 855–17 862 (1995).

263. R. R. Large, "Chemical Evolution and Zonation of Massive Sulphide Deposits in Volcanic Terrains," Econ. Geol. **72**, 549–572 (1977).

264. A. C. Lasaga, "Rate Laws of Chemical Reactions," in *Kinetics of Geochemical Processes*, Vol. 8 of *Reviews in Mineralogy* (1981), pp. 1–68.

265. A. Yu. Lein, "Sulfur and Carbon Isotopes in Hydrothermal Fields of the Mid-Atlantic Ridge," Geokhimiya, No. 11, 1162–1173 (2001) [Geochem. Int. **39**, 1066–1077 (2001)].

266. A. Yu. Lein, V. F. Gal'chenko, V. A. Grinenko, *et al.*, "Mineral Composition and Geochemistry of Rocks with Bacterial Overgrowths from Submarine Hydrothermal Structures," Geokhimiya, No. 9, 1235–1248 (1988).

267. A. Yu. Lein, N. V. Ul'yanova, V. A. Grinenko, and A. P. Lisitsin, "Geochemistry of the Hydrothermal Sulfide Ores of the Mid-Atlantic Ridge (26° N)," Geokhimiya, No. 3, 307–319 (1991).

268. A. Yu. Lein, N. V. Ul'yanova, V. A. Grinenko, *et al.*, "Mineralogical and Geochemical Peculiarities of Hydrothermal Sulfide Ores from the Manus Basin (Bismark Sea)," Geokhimiya, No. 4, 524–537 (1993).

269. A. Yu. Lein, D. V. Grichuk, E. G. Gurvich, and Yu. A. Bogdanov, "New Type of the Hydrothermal Fluid Enriched in H_2 and CH_4 at the Rift Zone of the Mid-Atlantic Ridge," Dokl. Akad. Nauk **375**, 380–383 (2000) [Trans. Russ. Acad. Sci., Earth Sci. Sec. **375**, 1391–1394 (2000)].

270. A. Yu. Lein, G. A. Cherkashev, A. A. Ul'yanov, *et al.*, "Mineralogy and Geochemistry of Sulfide Ores from the Logatchev-2 and Rainbow Fields: Similar and Distinctive Features," Geokhimiya, No. 3, 304–328 (2003) [Geochem. Int. **41**, 271–294 (2003)].

271. A. Yu. Lein, Yu. A. Bogdanov, A. M. Sagalevich, *et al.*, "A New Type of Hydrothermal Field in the Mid-Atlantic Ridge (Lost City Field, 30° N)," Dokl. Akad Nauk. **394**, 380–383 (2004) [Trans. Russ. Acad. Sci., Earth Sci. Sec. **394**, 92–95 (2004)].

272. P. C. Lichtner and V. N. Balashov, "Metasomatic Zoning: Appearance of Ghost Zones in the Limit of Pure Advective Mass Transport," Geochim. Cosmochim. Acta **57**, 369–387 (1993).

273. A. P. Lisitsin, Yu. A. Bogdanov, and E. G. Gurvich, *Hydrothermal Deposits in Oceanic Rift Zones* (Nauka, Moscow, 1990) [in Russian].

274. A. P. Lisitsin, R. A. Binns, Yu. A. Bogdanov, *et al.*, "Recent Hydrothermal Activity of Franklin Seamount, Western Woodlark Sea (Papua New Guinea)," Izv. Akad. Nauk SSSR, Ser. Geol., No. 8, 125–140 (1991).

275. A. P. Lisitsin, K. Crook, Yu. A. Bogdanov, *et al.*, "Hydrothermal Field of a Rift Zone in the Manus Basin," Izv. Akad. Nauk SSSR, Ser. Geol., No. 10, 34–55 (1992).

276. C. R. B. Lister, "On the Thermal Balance of a Mid-Ocean Ridge," Geophys. J. R. Astron. Soc. **26**, 515–535 (1972).

277. C. R. B. Lister, "On the Penetration of Water into Hot Rock," Geophys. J. R. Astron. Soc. **39**, 465–509 (1974).

278. C. R. B. Lister, "Heat Flow and Hydrothermal Circulation," Annu. Rev. Earth Planet. Sci. **8**, 95–117 (1980).

279. S. A. Little, K. D. Stolzenbach, and R. P. Von Herzen, "Measurements of Plume Flow from Hydrothermal Vent Field," J. Geophys. Res. **92**, 2587–2596 (1987).

280. R. P. Lowell, "Circulation in Fractures, Hot Springs, and Convective Heat Transport on Mid-Ocean Ridge Crests," Geophys. J. R. Astron. Soc. **40**, 351–369 (1975).

281. K. C. Macdonald and P. J. Fox, "The Axial Summit Graben and Cross-Sectional Shape of the East Pacific Rise as Indicators of Axial Magma Chambers and Recent

Volcanic Eruptions," Earth Planet. Sci. Lett. **88**, 119–131 (1988).

282. K. C. Macdonald, K. Becker, F. N. Spiess, and R. D. Ballard, "Hydrothermal Heat Flux of the 'Black Smoker' Vents on the East Pacific Rise," Earth Planet. Sci. Lett. **48**, 1–7 (1980).
283. V. I. Mal'kovskii and A. A. Pek, "The influence of a Highly Permeable Fault on the Structure of Thermal Convection Flow in Ocean Floor Spreading Zones," Dokl. Akad. Nauk **354**, 787–789 (1997) [Trans. Russ. Acad. Sci., Earth Sci. Sec. **355**, 672–675 (1997)].
284. K. Marumo and K. H. Hattori, "Seafloor Hydrothermal Clay Alteration at Jade in the Back-Arc Okinawa Trough: Mineralogy, Geochemistry and Isotope Characteristics," Geochim. Cosmochim. Acta **63**, 2785–2804 (1999).
285. V. V. Maslennikov, *Sedimentogenesis, Halmyrolysis, and Ecology of Massive Sulfide-Bearing Paleohydrothermal Fields: Evidence from the Southern Urals* (Geotur, Miass, 1999) [in Russian].
286. J. J. Massoth, D. A. Butterfield, J. E. Lupton, *et al.*, "Submarine Venting of Phase-Separated Hydrothermal Fluids at Axial Volcano, Juan de Fuca Ridge," Nature **340**, 702–705 (1989).
287. J. S. McClain, J. A. Orcutt, and M. Burnett, "The East Pacific Rise in Cross Section: A Seismic Model," J. Geophys. Res. **90**, 8627–8639 (1985).
288. M. T. McCulloch, R. T. Gregory, G. J. Wasserburg, and H. P. Taylor, "A Neodymium, Strontium, and Oxygen Isotopic Study of the Cretaceous Samail Ophiolite and Implications for the Petrogenesis and Seawater–Hydrothermal Alteration of Oceanic Crust," Earth Planet. Sci. Lett. **46**, 201–211 (1980).
289. I. A. Menyailov, L. P. Nikitina, and V. N. Shapar, "Geochemical Pecularities of Volcanic Gases," in *Great Fissure Tolbachik Eruption* (Nauka, Moscow, 1984), pp. 285–309 [in Russian].
290. L. Merlivat, C. Andrie, and P. Jean-Baptiste, "Distribution des isotopes de l'hydrogene, de l'oxygene et de l'helium dans les sources hydrothermales sous-marines de la ride Est-Pacifique, 13° N," C. R. Acad. Sci., Ser. II **299**, 1191–1196 (1984).
291. L. Merlivat, F. Pineau, and M. Javoy, "Hydrothermal Vent Waters at 13° N on the East Pacific Rise: Isotopic Composition and Gas Concentration," Earth Planet. Sci. Lett. **84**, 100–108 (1987).
292. *Metasomatism and Metasomatic Rocks*, Ed. by V. A. Zharikov and V. L. Rusinov (Nauchniy Mir, Moscow, 1998) [in Russian].
293. *Methods of Geochemical Modelling and Forecasting in Hydrogeology*, Ed. by S. R. Krainov (Nedra, Moscow, 1988) [in Russian].
294. S. Metz and J. H. Trefry, "Chemical and Mineralogical Influences on Concentrations of Trace Metals in Hydrothermal Fluids," Geochim. Cosmochim. Acta **64**, 2267–2279 (2000).
295. G. Michard, F. Albarede, A. Michard, *et al.*, "Chemistry of Solutions from the 13° N East Pacific Rise Hydrothermal Site," Earth Planet. Sci. Lett. **67**, 297–307 (1984).
296. M. V. Mironenko and A. A. Kosorukov, "Calculation of the Phase Composition of Fluid Systems," Geokhimiya, No. 8, 1195–1200 (1990).
297. M. J. Mottl, "Metabasalts, Axial Hot Springs, and the Structure of Hydrothermal Systems at Mid-Ocean Ridges," Geol. Soc. Am. Bull. **94**, 161–180 (1983).
298. M. J. Mottl and H. D. Holland, "Chemical Exchange during Hydrothermal Alteration of Basalt by Seawater: I. Experimental Results for Major and Minor Components of Seawater," Geochim. Cosmochim. Acta **42**, 1103–1115 (1978).
299. M. J. Mottl and W. E. Seyfried, Jr., "Sub-Seafloor Hydrothermal Systems: Rock vs. Seawater Dominated," in *Seafloor Spreading Centers of Hydrothermal Systems*, Benchmark Pap. Geol. **56**, 66–82 (1980).
300. M. J. Mottl, H. D. Holland, and R. F. Corr, "Chemical Exchange during Hydrothermal Alteration of Basalt by Seawater: II. Experimental Results for Fe, Mn, and Sulfur Species," Geochim. Cosmochim. Acta **43**, 869–884 (1979).
301. N. N. Mozgova, Yu. S. Borodaev, A. V. Efimov, *et al.*, "Silver Minerals in Oceanic Hydrothermal Ore Deposits (Manus and Woodlark Basins, Papua New Guinea Region)," Geol. Rudn. Mestorozhd. **35**, 333–343 (1993).
302. A. Yu. Namiot, *Solubilities of Gases in Water: A Handbook* (Nedra, Moscow) [in Russian].
303. P. Nehlig, T. Juteau, V. Bendel, and J. Cotteu, "The Root Zones of Oceanic Hydrothermal Systems: Constraints from the Samail Ophiolite (Oman)," J. Geophys. Res. **99**, 4703–4713 (1994).
304. G. V. Nesterenko and A. I. Almukhamedov, *Geochemistry of Differentiated Trapps* (Nauka, Moscow, 1973) [in Russian].
305. D. Norton and J. Knight, "Transport Phenomena in Hydrothermal Systems: Cooling Plutons," Am. J. Sci. **277**, 937–981 (1977).
306. H. Ohmoto, "Systematics of Sulfur and Carbon Isotopes in Hydrothermal Ore Deposits," Econ. Geol. **65**, 551–578 (1972).
307. H. Ohmoto and A. Lasaga, "Kinetics of Reactions between Aqueous Sulfates and Sulfides in Hydrothermal Systems," Geochim. Cosmochim. Acta **46**, 1727–1746 (1982).
308. H. Ohmoto and R. Rye, "Hydrogen and Oxygen Isotopic Composition of Fluid Inclusion in the Kuroko Deposits," Econ. Geol. **69**, 947–953 (1974).
309. H. Ohmoto and R. O. Rye, "Isotopes of Sulfur and Carbon," in *Geochemistry of Hydrothermal Ore Deposits*, 2nd ed., Ed. by H. Barnes (Wiley, New York, 1979), pp. 509–567.
310. H. Ohmoto, M. Mizukami, S. E. Drummond, *et al.*, "Chemical Processes of Kuroko Formation," in *The Kuroko and Related Volcanogenic Massive Sulfide Deposits*, Econ. Geol. Monogr. Ser. **5**, 570–604 (1983).
311. S. E. Oosting and K. L. Von Damm, "Bromide–Halide Fractionation in Seafloor Hydrothermal Fluids from 9–10° N East Pacific Rise," Earth Planet. Sci. Lett. **144**, 133–145 (1996).
312. H. Paulick, D. A. Vanko, and C. J. Yeats, "Drill Core-Based Facies Reconstruction of a Deep-Marine Felsic Volcano Hosting an Active Hydrothermal System (Pual

Ridge, Papua New Guinea, ODP Leg 193)," J. Volcanol. Geotherm. Res. **130**, 31–50 (2004).

313. M. R. Palmer and J. M. Edmond, "Cesium and Rubidium in Submarine Hydrothermal Fluids: Evidence for Recycling of Alkali Elements," Earth Planet. Sci. Lett. **95**, 8–14 (1989).
314. D. Y. Peng and D. B. Robinson, "A New Two-Constant Equation of State," Ind. Eng. Chem. Res. **15**, 59–64 (1976).
315. M. R. Perfit, D. J. Fornari, A. Malahoff, and R. W. Embley, "Geochemical Studies of Abyssal Lavas Recovered by DSRV Alvin from Eastern Galapagos Rift, Inca Transform, and Ecuador Rift: 3. Trace Element Abundances and Petrogenesis," J. Geophys. Res. **88**, 551–572 (1983).
316. J. M. Peter and W. C. Shanks, III, "Sulfur, Carbon, and Oxygen Isotope Variations in Submarine Hydrothermal Deposits of Guaymas Basin, Gulf of California, USA," Geochim. Cosmochim. Acta **56**, 2025–2040 (1992).
317. S. Petersen, P. M. Herzig, and M. D. Hannington, "Fluid Inclusion Studies as a Guide to the Temperature Regime within the TAG Hydrothermal Mound, 26° N, Mid-Atlantic Ridge," Proc. Ocean Drill. Program: Sci. Results **158**, 163–178 (1998).
318. R. A. Phinney and R. I. Odom, "Seismic Studies of Crustal Structure," Rev. Geophys. Space Phys. **21**, 1318–1332 (1983).
319. *Physical Properties of Rocks and Minerals: Handbook for Geophysics*, 2nd ed., Ed. by N. B. Dortman (Nedra, Moscow, 1984) [in Russian].
320. L. P. Plyusnina, *Experimental Studies of the Metamorphism of Basic Rocks* (Nedra, Moscow, 1983) [in Russian].
321. A. V. Plyasunov and I. P. Ivanov, "Solubility of Zinc Oxide in Sodium Chloride Solutions up to 600°C and 1000 bars," Geokhimiya, No. 11, 1605–1617 (1990).
322. *Principles of Chemical Technology,* 4th ed., Ed. by I. P. Mukhlenov, A. E. Gorenshtein, and E. S. Tumarkina (Vysshaya Shkola, Moscow, 1991) [in Russian].
323. *Prospecting for Copper Ore Deposits*, Ed. by M. B. Borodaevskaya, R. N. Volodin, A. I. Krivtsov, *et al.* (Nedra, Moscow, 1985) [in Russian].
324. R. P. Rafal'sky, *Water–Rock Interaction under Hydrothermal Conditions* (Nauka, Moscow, 1993) [in Russian].
325. M. H. Reed, "Calculation of Multicomponent Chemical Equilibria and Reaction Processes in Systems Involving Minerals, Gases, and an Aqueous Phase," Geochim. Cosmochim. Acta **46**, 513–528 (1982).
326. M. H. Reed, "Seawater–Basalt Reaction and the Origin of Greenstones and Related Ore Deposits," Econ. Geol. **78**, 446–485 (1983).
327. R. J. Ribando, K. E. Torrance, and D. L. Turcotte, "Numerical Models for Hydrothermal Circulation in the Oceanic Crust," J. Geophys. Res. **81**, 3007–3012 (1976).
328. C. J. Richardson, J. R. Cann, H. G. Richards, and J. G. Cowan, "Metal-Depleted Root Zones of the Troodos Ore-Forming Hydrothermal Systems, Cyprus," Earth Planet. Sci. Lett. **84**, 243–253 (1987).
329. J. D. Ridge, "Volcanic Exhalations and Ore Deposition in the Vicinity of the Seafloor," Miner. Deposita **8**, 332–348 (1973).
330. W. I. Ridley, M. R. Perfit, I. R. Jonesson, and M. F. Smith, "Hydrothermal Alteration in Oceanic Ridge Volcanoes: A Detailed Study at the Galapagos Fossil Hydrothermal Field," Geochim. Cosmochim. Acta **58**, 2477–2494 (1994).
331. H. Riedesel, J. A. Orcutt, K. C. Macdonald, and J. S. McClain, "Microearthquakes in the Black Smoker Hydrothermal Field, East Pacific Rise at 21° N," J. Geophys. Res. **87**, 613–623 (1982).
332. RISE Project Group: F. N. Spiess, K. C. Macdonald, T. Atwater, *et al.*, "East Pacific Rise: Hot Springs and Geophysical Experiments," Science **207**, 1421–1433 (1980).
333. B. E. Roberts and P. R. Tremaine, "Vapour Liquid Equilibrium Calculations for Dilute Aqueous Solutions of CO_2, H_2S, NH_3, and NaOH to 300°C," Can. J. Chem. Eng. **63**, 294–300 (1985).
334. R. A. Robie, B. S. Hemingway, and J. R. Fisher, "Thermodynamic Properties of Minerals and Related Substances at 298.15 K and 1 Bar (10^5 Pascals) Pressure and at High Temperatures," Geol. Surv. Bull., No. 1452 (1978).
335. P. A. Rona, "Hydrothermal Mineralization at Seafloor Spreading Centers," Earth Sci. Rev. **20**, 1–104 (1984).
336. P. Rona and S. D. Scott, "A Special Issue on Sea-Floor Hydrothermal Mineralization: New Perspectives. Preface," Econ. Geol. **88**, 1935–1976 (1993).
337. P. A. Rona, M. D. Hannington, C. V. Raman, *et al.*, "Active and Relict Sea-Floor Hydrothermal Mineralization at the TAG Hydrothermal Field, Mid-Atlantic Ridge," Econ. Geol. **88**, 1989–2017 (1993).
338. R. J. Rosenbauer and J. L. Bischoff, "Uptake and Transport of Heavy Metals by Heated Seawater: A Summary of the Experimental Results," in *Hydrothermal Processes at Seafloor Spreading Centers*, Ed. by P. A. Rona *et al.* (Springer-Verlag, New York, 1983), pp. 177–197.
339. K. Rubin, "Degassing of Metals and Metalloids from Erupting Seamount and Mid-Ocean Ridge Volcanoes: Observations and Predictions," Geochim. Cosmochim. Acta **61**, 3525–3542 (1997).
340. B. N. Ryzhenko, *Thermodynamics of Equilibria in Hydrothermal Solutions* (Nauka, Moscow, 1981) [in Russian].
341. H. Sakai, "Isotopic Properties of Sulfur Compounds in Hydrothermal Processes," Geochem. J. **2**, 29–49 (1968).
342. H. Sakai and O. Matsubaya, "Isotopic Geochemistry of the Thermal Waters of Japan and Its Bearing on the Kuroko Ore Solutions," Econ. Geol. **69**, 974–991 (1974).
343. H. Sakai, D. J. Des Marias, A. Ueda, and J. G. Moore, "Concentrations and Isotope Ratios of Carbon, Nitrogen, and Sulfur in Ocean Floor Basalts," Geochim. Cosmochim. Acta **48**, 3282–3294 (1984).
344. P. Sarda and D. Graham, "Mid-Ocean Ridge Popping Rocks: Implication for Degassing at Ridge Crests," Earth Planet. Sci. Lett. **97**, 268–289 (1990).

345. A. Sasaki, "Seawater Sulfate as a Possible Determinant for Sulfur Isotopic Compounds in Some Stratabound Sulfide Ores," Geochem. J. **4**, 41–51 (1970).

346. J. Seewald, A. Cruse, and P. Saccocia, "Aqueous Volatiles in Hydrothermal Fluids from the Main Endeavour Field, Northern Juan de Fuca Ridge: Temporal Variability Following Earthquake Activity," Earth Planet. Sci. Lett. **216**, 575–590 (2003).

347. J. C. Seitz, J. G. Blencoe, D. B. Joyce, and R. J. Bodnar, "Volumetric Properties of CO_2–CH_4–N_2 Fluids at 200°C and 1000 Bars: A Comparison of Equations of State and Experimental Data," Geochim. Cosmochim. Acta **58**, 1065–1071 (1994).

348. T. M. Seward, "The Formation of Lead (II) Chloride Complexes to 300°C: A Spectrophotometric Study," Geochim. Cosmochim. Acta **48**, 121–134 (1984).

349. W. Seyfried and J. L. Bischoff, "Hydrothermal Transport of Heavy Metals by Seawater: The Role of Seawater/Basalt Ratio," Earth Planet. Sci. Lett. **34**, 71–77 (1977).

350. W. E. Seyfried, Jr. and J. L. Bischoff, "Low Temperature Basalt Alteration by Seawater: An Experimental Study at 70°C and 150°C," Geochim. Cosmochim. Acta **43**, 1937–1947 (1979).

351. W. E. Seyfried, Jr. and W. E. Dibble, Jr., "Seawater–Peridotite Interaction at 300°C and 500 Bar: Implication for the Origin of Oceanic Serpentinites," Geochim. Cosmochim. Acta **44**, 309–321 (1980).

352. W. E. Seyfried, Jr. and D. R. Janecky, "Heavy Metal and Sulfur Transport during Subcritical and Supercritical Hydrothermal Alteration of Basalt: Influence of Fluid Pressure and Basalt Composition and Crystallinity," Geochim. Cosmochim. Acta **49**, 2545–2560 (1985).

353. W. E. Seyfried, Jr. and M. J. Mottl, "Hydrothermal Alteration of Basalt by Seawater under Seawater-Dominated Conditions," Geochim. Cosmochim. Acta **46**, 985–1002 (1982).

354. W. E. Seyfried, Jr., P. C. Gordon, and F. W. Dickson, "A New Reaction Cell for Hydrothermal Solution Equipment," Am. Mineral. **64**, 646–649 (1979).

355. W. E. Seyfried, Jr., D. R. Janecky, and M. J. Mottl, "Alteration of the Oceanic Crust: Implication for Geochemical Cycles of Lithium and Boron," Geochim. Cosmochim. Acta **48**, 557–569 (1984).

356. W. E. Seyfried, Jr., M. E. Berndt, and D. R. Janecky, "Chloride Depletions and Enrichments in Seafloor Hydrothermal Fluids: Constraints from Experimental Basalt Alteration Studies," Geochim. Cosmochim. Acta **50**, 469–475 (1986).

357. T. N. Shadlun, N. S. Bortnikov, Yu. A. Bogdanov, *et al.*, "Mineral Composition, Textures, and Formational Conditions of Modern Sulfide Ores in the Rift Zone of Manus Basin," Geol. Rudn. Mestorozhd. **34** (5), 3–21 (1992).

358. W. C. Shanks, III and W. E. Seyfried, Jr., "Stable Isotope Studies of Vent Fluids and Chimney Minerals. Southern Juan de Fuca Ridge: Sodium Metasomatism and Seawater Sulfate Reduction," J. Geophys. Res. **92**, 11 387–11 399 (1987).

359. V. N. Sharapov and V. A. Akimtsev, "Ore-Forming Magmatic Systems in the Mid-Oceanic Ridges," Geol. Geofiz. **38**, 1289–1304 (1997).

360. R. Shiraki, H. Sakai, M. Endoh, and N. Kishima, "Experimental Studies on Rhyolite– and Andesite–Seawater Interactions at 300°C and 1000 Bars," Geochem. J. **21**, 139–148 (1987).

361. E. L. Shock and H. C. Helgeson, "Calculation of the Thermodynamic and Transport Properties of Aqueous Species at High Pressures and Temperatures: Correlation Algorithms for Ionic Species and Equation of State Prediction to 5 Kb and 1000°C," Geochim. Cosmochim. Acta **52**, 2009–2036 (1988).

362. Yu. V. Shvarov, V. A. Zharikov, and T. B. Zhandarova, "Calculation of an Infiltrational Metasomatic Column on the Basis of the Local Equilibrium Principle," Geochem. Int., No. 11, 1041–1049 (2000).

363. G. Yu. Shvedenkov and A. V. Savinov, "Thermodynamic Calculation of the Critical Parameters of Hydrogen Sulfide–Water Mixtures," Geol. Geofiz. **35** (11), 3–12 (1994).

364. S. A. Silantyev, *Metamorphic Rocks of the Atlantic Ocean Floor* (Nauka, Moscow, 1984) [in Russian].

365. S. A. Silantyev, M. V. Mironenko, B. A. Bazylev, and Yu. V. Semenov, "Metamorphism Associated with Mid-Ocean Ridge Hydrothermal Systems: Thermodynamic Modeling," Geokhimiya, No. 7, 1015–1034 (1992).

366. R. Skirrow and M. L. Coleman, "Origin of Sulphur and Geothermometry of Hydrothermal Sulphides from the Galapagos Rift, 86° W," Nature **299**, 142–144 (1982).

367. N. S. Skripchenko, *Hydrothermal–Sedimentary Sulfide Ores of Basaltoid Associations* (Nedra, Moscow, 1972) [in Russian].

368. N. H. Sleep, "Hydrothermal Convection at Ridge Axes," in *Hydrothermal Processes of Seafloor Spreading Centers*, Ed. by P. A. Rona *et al.* (Springer-Verlag, New York, 1983), pp. 71–82.

369. V. I. Smirnov, *Geology of Mineral Deposits*, 4th ed. (Nedra, Moscow, 1982) [in Russian].

370. M. Solomon and D. Walshe, "The Formation of Massive Sulfide Deposits on the Sea Floor," Econ. Geol. **74**, 797–813 (1979).

371. M. A. Sommer and E. K. Gibson, "Volatile Concentrations of Submarine Glasses from the Juan de Fuca Ridge," EOS, Trans. Am. Geophys. Union **66**, 926 (1985).

372. E. T. S. Spooner, R. D. Beckinsale, P. C. England, and A. Senior, "Hydration, ^{18}O Enrichment and Oxidation during Ocean Floor Hydrothermal Metamorphism of Ophiolitic Metabasic Rocks from E. Liguria, Italy," Geochim. Cosmochim. Acta **41**, 875–871 (1977).

373. N. F. Spycher and M. H. Reed, "Fugacity Coefficients of H_2, CO_2, CH_4, H_2O, and of H_2O–CO_2–CH_4 Mixtures: A Virial Equation Treatment for Moderate Pressures Applicable to Calculations of Hydrothermal Boiling," Geochim. Cosmochim. Acta **52**, 739–749 (1988).

374. N. F. Spycher and M. H. Reed, "Evolution of a Broadlands-Type Epithermal Ore Fluid along Alternative *P–T* Paths: Implications for the Transport and Deposition of Base, Precious, and Volatile Metals," Econ. Geol. **84**, 328–359 (1989).

375. D. S. Stakes, J. W. Shervais, and C. A. Hopson, "The Volcanic–Tectonic Cycle of the FAMOUS and AMAR Valleys, Mid-Atlantic Ridge (36°47′ N): Evidence from Basalt Glass and Phenocryst Compositional Variations

for a Steady State Magma Chamber Beneath the Valley Midsections, AMAR3," J. Geophys. Res. **89**, 8995–7028 (1984).

376. C. I. Steefel and A. C. A. Lasaga, "Coupled Model for Transport of Multiple Chemical Species and Kinetic Precipitation/Dissolution Reactions with Application to Reactive Flow in Single Phase Systems," Am. J. Sci. **294**, 529–592 (1994).
377. Yu. M. Stolyarov, "Anhydrite and Gypsum in Massive Sulfide Deposits of the Urals and the Problem of Their Genesis," Geol. Rudn. Mestorozhd., No. 2, 107–113 (1965).
378. Yu. M. Stolyarov, "On the Sulfate Mineralization in Massive Sulfide Deposits of the Southern Urals," Zap. Vses. Mineral. O–va **101**, 352–355 (1972).
379. R. Stryjek and J. H. Vera, "PRSV: An Improved Peng–Robinson Equation of State for Pure Compounds and Mixtures," Can. J. Chem. Eng. **64**, 323–333 (1986).
380. M. M. Styrt, A. J. Brockman, H. D. Holland, *et al.*, "Mineralogy and the Isotopic Composition of Sulfur in Hydrothermal Sulfide–Sulfate Deposits on the East Pacific Rise, 21° N Latitude," Earth Planet. Sci. Lett. **53**, 382–390 (1981).
381. T. N. Surin, *Metasomatism and Massive Sulfide Formation. High-Ural Region* (Nauka, Yekaterinburg, 1993) [in Russian].
382. R. B. Symonds and M. H. Reed, "Calculation of Multicomponent Chemical Equilibria in Gas–Solid–Liquid Systems: Calculation Methods, Thermochemical Data, and Applications to Studies of High-Temperature Volcanic Gases with Examples from Mount St. Helens," Am. J. Sci. **293**, 758–864 (1993).
383. R. B. Symonds, M. H. Reed, and W. I. Rose, "Origin, Speciation and Fluxes of Trace Element Gases at Augustine Volcano, Alaska: Insights into Magma Degassing and Fumarolic Processes," Geochim. Cosmochim. Acta **56**, 633–657 (1992).
384. J. C. Tanger, IV and K. S. Pitzer, "Thermodynamics of NaCl–H_2O: A New Equation of State for the Near-Critical Region and Comparisons with Other Equations for Adjoining Regions," Geochim. Cosmochim. Acta **53**, 973–987 (1989).
385. Yu. A. Taran, J. W. Hedenquist, M. A. Korzhinsky, *et al.*, "Geochemistry of Magmatic Gases from Kudryavy Volcano, Iturup, Kuril Islands," Geochim. Cosmochim. Acta **59**, 1749–1761 (1995).
386. B. E. Taylor, "Carbon Dioxide and Methane in Hydrothermal Vent Fluids from Middle Valley, a Sediment-Covered Ridge Segment," EOS, Trans. Am. Geophys. Union **71**, 1569 (1990).
387. *Thermal Constants of Substances*, Ed. by V. P. Glushko (VINITI, Moscow, 1965–1979) [in Russian].
388. *Thermodynamic Properties of Pure Substances*, Ed. by V. P. Glushko (Nauka, Moscow, 1978–1982), Vols. 1–4 [in Russian].
389. E. C. Thornton and W. E. Seyfried, Jr., "Sediment–Seawater Interaction at 200 and 300°C, 500 Bars Pressure: The Role of Sediment Composition in Diagenesis and Low-Grade Metamorphism of Marine Clay," Bull. Geol. Soc. Am. **96**, 1287–1295 (1985).
390. E. C. Thornton and W. E. Seyfried, Jr., "Reactivity of Organic-Rich Sediment in Seawater at 350°C, 500 Bars: Experimental and Theoretical Constraints and Implications for Guaymas Basin Hydrothermal System," Geochim. Cosmochim. Acta **51**, 1997–2001 (1987).
391. P. P. Timofeev, V. N. Kholodov, and V. P. Zverev, "The Balance of Water in the Recent Sedimentation Process," Dokl. Akad. Nauk SSSR **287**, 1465–1469 (1986).
392. M. K. Tivey, "The Influence of Hydrothermal Fluid Composition and Advection Rates on Black Smoker Chimney Mineralogy: Insights from Modeling Transport and Reaction," Geochim. Cosmochim. Acta **59**, 1933–1949 (1995).
393. M. K. Tivey and R. E. McDuff, "Mineral Precipitation in the Walls of Black Smoker Chimneys: A Quantitative Model of Transport and Chemical Reaction," J. Geophys. Res. **95**, 12 617–12 637 (1990).
394. M. K. Tivey, L. O. Olson, V. W. Miller, and R. D. Light, "Temperature Measurements during Initiation and Growth of a Black Smoker Chimney," Nature **346**, 5–54 (1990).
395. M. K. Tivey, A. M. Bradley, T. M. Joyce, and D. Kadko, "Insights into Tide-Related Variability at Seafloor Hydrothermal Vents from Time-Series Temperature Measurements," Earth Planet. Sci. Lett. **202**, 693–707 (2002).
396. J. H. Trefry, D. B. Butterfield, S. Metz, *et al.*, "Trace Metals in Hydrothermal Solutions from Cleft Segment on the Southern Juan de Fuca Ridge," J. Geophys. Res. **99**, 4925–4935 (1994).
397. V. Tunnicliffe, M. Botros, M. E. de Burgh, *et al.*, "Hydrothermal Vents of Explorer Ridge, Northern Pacific," Deep-Sea Res. **33**, 401–412 (1986).
398. A. V. Tutubalin and D. V. Grichuk, "Coupled Hydrodynamic and Thermodynamic Model for a Convecting Hydrothermal System: 1. The Marker Method of Modeling," Geochem. Int., No. 11, 972–984 (1997a).
399. A. V. Tutubalin and D. V. Grichuk, "Coupled Hydrodynamic and Thermodynamic Model for a Convecting Hydrothermal System: 2. Self-Mixing of Solutions," Geochem. Int., No. 12, 1071–1082 (1997b).
400. A. V. Tutubalin, D. V. Grichuk, and V. I. Mal'kovskii, "A Complex Hydrodynamic and Thermodynamic Model of a Convective Hydrothermal System," in *Proceedings of 8th International Symposium on Water–Rock Interaction* (Balkema, Rotterdam, 1995), pp. 763–766.
401. D. A. Vanko, "Temperature, Pressure, and Composition of Hydrothermal Fluids, with Their Bearing on the Magnitude of Tectonic Uplift at Mid-Oceanic Ridges, Inferred from Fluid Inclusions in Oceanic Layer 3," J. Geophys. Res. **93**, 4595–4611 (1988).
402. L. N. Var'yash, "Experimental Study of Cu(I) Complex Formation in NaCl Solutions at 300 and 350°C," Geokhimiya, No. 8, 1166–1174 (1991).
403. A. P. Vinogradov, L. N. Grinenko, V. A. Grinenko, and Yu. M. Stolyarov, "Isotopic Composition of Sulfur in Sulfides and Sulfates from the Alekseevskii Copper Deposit (Middle Urals) and Some Problems of Its Genesis," Geokhimiya, No. 8, 915–926 (1968).
404. V. P. Volkov and G. I. Ruzaikin, "On Gas Equilibria and Methods of Their Computation with Application to Petrogenetic Problems," Geokhimiya, No. 8, 976–991 (1969).

405. K. L. Von Damm, "Seafloor Hydrothermal Activity: Black Smoker Chemistry and Chimneys," Annu. Rev. Earth Planet. Sci. **18**, 173–204 (1990).

406. K. L. Von Damm, "Chemistry of Hydrothermal Vent Fluids from 9°–10° N, East Pacific Rise: 'Time Zero', the Immediate Posteruptive Period," J. Geophys. Res. **105**, 11 203–11 222 (2000).

407. K. L. Von Damm and J. L. Bischoff, "Chemistry of Hydrothermal Solutions from the Southern Juan de Fuca Ridge," J. Geophys. Res. **92**, 11 334–11 346 (1987).

408. K. L. Von Damm, J. M. Edmond, B. Grant, *et al.*, "Chemistry of Submarine Hydrothermal Solutions at 21° N, East Pacific Rise," Geochim. Cosmochim. Acta **49**, 2197–2220 (1985).

409. K. L. Von Damm, S. E. Oosting, R. Kozlowski, *et al.*, "Evolution of East Pacific Rise Hydrothermal Vent Fluids Following a Volcanic Eruption," Nature **375**, 47–50 (1995).

410. K. L. Von Damm, G. Buttermore, S. E. Oosting, *et al.*, "Direct Observation of the Evolution of a Seafloor 'Black Smoker' from Vapor to Brine," Earth Planet. Sci. Lett. **149**, 101–111 (1997).

411. K. L. Von Damm, A. M. Bray, G. Buttermore, and S. E. Oosting, "The Geochemical Controls on Vent Fluids from the Lacky Strike Vent Field, Mid-Atlantic Ridge," Earth Planet. Sci. Lett. **160**, 521–536 (1998).

412. K. L. Von Damm, M. D. Lilley, W. C. Shanks III, *et al.*, "Extraordinary Phase Separation and Segregation in Vent Fluids from the Southern East Pacific Rise," Earth Planet. Sci. Lett. **206**, 365–378 (2003).

413. P. J. Wallace and I. S. E. Carmichael, "S Speciation in Submarine Basaltic Glasses as Determinated by Measurements of S$K\alpha$ X-ray Wavelength Shifts," Am. Mineral. **79**, 161–167 (1994).

414. J. V. Walther and B. J. Wood, "Mineral–Fluid Reaction Rates," in *Fluid–Rock Interactions during Metamorphism*, Vol. 5 of *Advances in Physical Geochemistry,* Ed. by J. V. Walther and B. J. Wood (Springer-Verlag, New York, 1986), pp. 194–213.

415. J. A. Welhan and H. Craig, "Methane, Hydrogen, and Helium in Hydrothermal Fluids at 21° N on the East Pacific Rise," in *Hydrothermal Processes at Seafloor Spreading Centers*, Ed. by P. A. Rona, *et al.* (Springer-Verlag, New York, 1983), pp. 391–409.

416. J. T. Wells and M. S. Ghiorso, "Coupled Fluid Flow and Reaction in Mid-Ocean Ridge Hydrothermal Systems: The Behavior of Silica," Geochim. Cosmochim. Acta **55**, 2467–2481 (1991).

417. W. S. D. Wilcock and J. R. Delaney, "Mid-Ocean Ridge Sulfide Deposits: Evidence for Heat Extraction from Magma Chambers Or Cracking Fronts?," Earth Planet. Sci. Lett. **145**, 49–64 (1996).

418. T. J. Wolery and N. H. Sleep, "Hydrothermal Circulation and Geochemical Flux at Mid-Ocean Ridges," J. Geol. **84**, 249–275 (1976).

419. B. J. Wood and J. V. Walther, "Rates of Hydrothermal Reactions," Science **222**, 413–415 (1983).

420. L. G. Woodruff and W. C. Shanks, III, "Sulfur Isotope Study of Chimney Minerals and Vent Fluids from 21° N, East Pacific Rise: Hydrothermal Sulfur Sources and Disequilibrium Sulfate Reduction," J. Geophys. Res. **93**, 4562–4572 (1988).

421. A. A. Yaroshevsky and T. I. Tsekhonya, "Petrochemical Types of Ocean Floor Magmatic Rocks: Pecularities in Their Associations and Distribution in Structural Zones," in *Magmatism in the Ocean: Evolution and Geologic Correlation* (Nauka, Moscow, 1986), pp. 95–103 [in Russian].

422. G. P. Zaraiskii, V. N. Balashov, and M. I. Lebedeva, "Macrokinetic Model of Metasomatic Zoning," Geokhimiya, No. 10, 1386–1395 (1989).

423. A. N. Zavaritskii, "On the Genesis of Volcanogenic Massive Deposits," Izv. Akad. Nauk SSSR, Ser. Geol., No. 3, 3–18 (1943).

424. V. V. Zaikov, *Volcanism and Sulfide Mounds of Paleooceanic Margins: Evidence from Massive Sulfide Deposits of the Urals and Siberia* (Nauka, Moscow, 1991) [in Russian].

425. R. A. Zierenberg, W. C. Shanks, III, and J. L. Bischoff, "Massive Sulfide Deposits at 21° N, East Pacific Rise: Chemical Composition, Stable Isotopes, and Phase Equilibria," Geol. Soc. Am. Bull. **95**, 922–929 (1984).

426. R. A. Zierenberg, R. A. Koski, J. L. Morton, *et al.*, "Genesis of Massive Sulfide Deposits on a Sediment-Covered Spreading Center, Escanaba Trough, Southern Gorda Ridge," Econ. Geol. **88**, 2069–2098 (1993).

427. A. Zindler and S. Hart, "Helium: Problematic Primordial Signals," Earth Planet. Sci. Lett. **79**, 1–8 (1986).

428. A. G. Zlotnik-Khotkevitch, "Diagenetic Transformation of Massive Sulphide Ores," Geol. Rudn. Mestorozhd. **34** (2), 83–98 (1992).

429. A. G. Zlotnik-Khotkevitch and N. A. Andriyanova, "Formation of Mineral Zoning in Volcanogenic Massive Sulfide Ores," Izv. Akad. Nauk SSSR, Ser. Geol., No. 8, 125–132 (1987).